# Measurements and Modeling of Nitric Oxide Formation in Counterflow, Premixed CH$_4$/O$_2$/N$_2$ Flames

D. Douglas Thomsen and Normand M. Laurendeau
Purdue University, West Lafayette, Indiana

National Aeronautics and
Space Administration

Glenn Research Center

Available from

TABLE OF CONTENTS

# LIST OF TABLES

LIST OF FIGURES

Figure            Page

Figure                                                        Page

Figure                                                                                      Page

NOMENCLATURE

<u>English Symbols</u>

| <u>Symbol</u> | <u>Description</u> | <u>Units</u> |
|---|---|---|
| $A$ | Einstein A coefficient for spontaneous emission | $s^{-1}$ |
| $A$ | Pre-exponential factor of modified Arrhenius rate expression | (cm-mol-atm) system |
| $A_{ul}$ | Einstein A coefficient for spontaneous emission | $s^{-1}$ |
| $b$ | Absorption rate ratio | -- |
| $c$ | Speed of light | cm/s |
| $C_b$ | Background interference signal | V/V |
| $E_a$ | Activation energy in modified Arrhenius rate expression | cal/gmol |
| $f$ | Ratio of off- and on-line calibration curve slopes | -- |
| $g$ | Degeneracy of the electronic level | -- |
| $G$ | Photomultiplier gain | V/W |
| $h$ | Planck constant | J·s |
| $I$ | Irradiance | W/cm$^2$ |
| $m$ | Slope of calibration curve | (V/V)/ppm NO |
| $n$ | Temperature power constant in modified Arrhenius rate expression | -- |
| $N$ | Population in rotational level | cm$^{-3}$ |
| $N_T$ | NO number density | cm$^{-3}$ |
| $N_l^0$ | Total population in system | cm$^{-3}$ |

| Symbol | Description | Units |
|--------|-------------|-------|
| $NO$ | NO concentration | ppm |
| $[NO]$ | NO number density | $cm^{-3}$ |
| $P$ | Pressure | atm |
| $P^0$ | Reference pressure in Eq. (5.1) | atm |
| $q$ | Quenching rate ratio | -- |
| $Q_e$ | Electronic quenching rate coefficient | $s^{-1}$ |
| $Q_r$ | Rotational relaxation rate coefficient | $s^{-1}$ |
| $Q_{ul}$ | Electronic quenching rate coefficient | $s^{-1}$ |
| $Q_v$ | Vibrational quenching rate coefficient | $s^{-1}$ |
| $R$ | Ideal gas constant | cal/gmol·K |
| $S$ | Laser-power corrected fluorescence signal | V/V |
| $S_L$ | Laminar flame speed | m/s |
| $S_L^0$ | Laminar flame speed at reference temperature and pressure | m/s |
| $S_{NO}$ | Corrected fluorescence signal for NO | V/V |
| $S_{X_j,i}$ | Sensitivity coefficient for species j, reaction i | (cm-mol-atm) system |
| $T$ | Temperature | K |
| $V$ | Voltage | V |
| $V_f$ | Fluorescence voltage | V |
| $V_{f,b}$ | Broadband fluorescence voltage | V |
| $V_l$ | Relative laser power voltage | V |
| $V_c$ | Fluorescence collection volume | $cm^3$ |
| $W_i$ | Rate coefficient for photoionization | $s^{-1}$ |
| $W_{lu}$ | Stimulated absorption rate coefficient | $s^{-1}$ |
| $W_{ul}$ | Stimulated emission rate coefficient | $s^{-1}$ |
| $X$ | Mole fraction | -- |

## Greek Symbols

| Symbol | Description | Units |
|---|---|---|
| $\alpha$ | Absorption coefficient per unit NO number density | $cm^2$ |
| $\beta$ | Detection efficiency of collection optics | -- |
| $\beta$ | Constant in Eq. (5.2) | -- |
| $\delta(\ )$ | Absolute uncertainty (95% confidence interval) | -- |
| $\varepsilon_f$ | Fluorescence emission | $W/(cm^3 \cdot sr)$ |
| $\varepsilon(\ )$ | Relative uncertainty (95% confidence interval) | -- |
| $\varepsilon(pdl)$ | Relative uncertainty in signal owing to pdl drift | -- |
| $\varepsilon(NO_b)$ | Relative uncertainty in calibration gas concentration | -- |
| $\varepsilon(NO_d)$ | Relative uncertainty owing to flamefront NO destruction | -- |
| $\varepsilon(C_{phi})$ | Relative uncertainty of background owing to shift with equivalence ratio or location | -- |
| $\varepsilon(b)$ | Relative uncertainty owing to Boltzmann fraction changes | -- |
| $\varepsilon(q)$ | Relative uncertainty owing to quenching rate variations | -- |
| $\lambda$ | Wavelength | nm |
| $\nu$ | Wavenumber | $cm^{-1}$ |
| $\sigma$ | One-photon absorption cross-section | $cm^2$ |
| $\Omega_c$ | Solid collection angle of detection optics | sr |

## Subscripts

| Symbol | Description | Units |
|---|---|---|
| $a$ | Accuracy | -- |
| $b$ | Refers to background | -- |
| $c$ | Refers to measurements at calibration conditions | -- |

| Symbol | Description | Units |
|--------|-------------|-------|
| $f$ | Fluorescence | -- |
| $f$ | Forward reaction rate | -- |
| $i$ | Reaction number | -- |
| $j$ | Species number | -- |
| $j,k,m,n$ | Specific rotational levels | -- |
| $l$ | Refers to lower rovibronic level | -- |
| $L$ | Laser | -- |
| $NO$ | Refers to portion from NO | -- |
| $p$ | Precision | -- |
| $r$ | Reverse reaction rate | -- |
| $u$ | Refers to upper rovibronic level | -- |
| $u$ | Refers to undoped condition in calibration plot | -- |
| $v'$ | Upper vibrational state quantum number | -- |
| $v''$ | Lower vibrational state quantum number | -- |

## Superscripts

| Symbol | Description | Units |
|--------|-------------|-------|
| $'$ | Refers to off-line excitation | -- |

ABSTRACT

Laser-induced fluorescence (LIF) measurements of NO concentration in a variety of $CH_4/O_2/N_2$ flames are used to evaluate the chemical kinetics of NO formation. The analysis begins with previous measurements in flat, laminar, premixed $CH_4/O_2/N_2$ flames stabilized on a water-cooled McKenna burner at pressures ranging from 1 to 14.6 atm, equivalence ratios from 0.5 to 1.6, and volumetric nitrogen/oxygen dilution ratios of 2.2, 3.1 and 3.76. These measured results are compared to predictions to determine the capabilities and limitations of the comprehensive kinetic mechanism developed by the Gas Research Institute (GRI), version 2.11. The model is shown to predict well the qualitative trends of NO formation in lean-premixed flames, while quantitatively underpredicting NO concentration by 30-50%. For rich flames, the model is unable to even qualitatively match the experimental results.

These flames were found to be limited by low temperatures and an inability to separate the flame from the burner surface. In response to these limitations, a counterflow burner was designed for use in opposed premixed flame studies. A new LIF calibration technique was developed and applied to obtain quantitative measurements of NO concentration in laminar, counterflow premixed, $CH_4/O_2/N_2$ flames at pressures ranging from 1 to 5.1 atm, equivalence ratios of 0.6 to 1.5, and an $N_2/O_2$ dilution ratio of 3.76.

The counterflow premixed flame measurements are combined with measurements in burner-stabilized premixed flames and counterflow diffusion flames to build a comprehensive database for analysis of the GRI kinetic mechanism. Pathways, quantitative reaction path and sensitivity analyses are applied to the GRI mechanism for these flame conditions. The prompt NO mechanism is found to severely underpredict the amount of NO formed in rich premixed and nitrogen-diluted diffusion flames. This underprediction is traced to uncertainties in the CH kinetics as well as in the nitrogen

oxidation chemistry. Suggestions are made which significantly improve the predictive capability of the GRI mechanism in near-stoichiometric, rich, premixed flames and in atmospheric-pressure, diffusion flames. However, the modified reaction mechanism is unable to model the formation of NO in ultra-rich, premixed or in high-pressure, non-premixed flames, thus indicating the need for additional study under these conditions.

# 1. INTRODUCTION

## 1.1 Background

Nitric oxide (NO) is an atmospheric pollutant that has been tied to both the destruction of the ozone layer and to the creation of photochemical smog. Because of these effects, current government emission standards have mandated that advanced gas turbines produce low $NO_x$ levels (<10 ppm @ 15% $O_2$, as corrected through the addition of dilution air). Since $NO_x$ production by nonpremixed combustion generates $\geq 100$ ppm (@ 15% $O_2$) for non-nitrogen bound fuels (Correa, 1992), the goal of lower $NO_x$ emissions will require partially or fully premixed combustion.

Lean, premixed combustion reduces thermal $NO_x$ by preventing the creation of high-temperature stoichiometric interfaces. However, $NO_x$ emissions are also intimately and inversely coupled to those of CO and unburned hydrocarbons (UHC). These restrictions result in a set of competing goals: the increase in pressure and temperature required to improve efficiency results in more $NO_x$, while leaning the mixture to reduce $NO_x$ will result in operation nearer the weak limit with a corresponding increase in CO. Hence, a more thorough understanding is needed of the chemical kinetics of pollutant formation in lean, premixed combustion. Of particular interest is the development of a simplified, high-pressure $NO_x$ model capable of predicting NO formation for practical gas turbine conditions. To achieve this goal, a complete understanding is needed of the chemical kinetics involved in the production of NO at high pressure. This knowledge, in turn, requires accurate *in situ* measurements of NO concentration to verify any proposed kinetic modeling scheme.

In response to these needs, laser-induced fluorescence (LIF) has recently been used (Reisel and Laurendeau, 1994a; Klassen *et al.*, 1995; Thomsen, 1996) to obtain

quantitative measurements of NO formation in laminar premixed flames stabilized upon a water-cooled McKenna burner at 1.0-14.6 atm. In fact, great strides have been made in both increasing the accuracy of these measurements (Thomsen *et al.*, 1997) and in broadening the conditions studied to different fuels and ever increasing pressures (Reisel and Laurendeau, 1994a; Reisel and Laurendeau, 1995; Klassen *et al.*, 1995; Kuligowski, 1997; Charleston-Goch, 1999). However, the flame geometry used in these studies is not without its limitations, both with respect to experimental application and ease of modeling. Most of these limitations center around the fact that the flamefront sits extremely close to the burner, especially at high pressures. Consequently, these flames are highly non-adiabatic and it becomes impossible to obtain experimental profiles of temperature and species concentrations through the flamefront or even to experimentally validate concentrations and temperatures upstream of the flame.

An alternate configuration that promises to provide this capability while retaining a one-dimensional structure for ease of modeling is that of counterflow premixed flames. Because such flames are stabilized by curvature effects rather than by heat loss to the burner, significant separations can exist between the flamefront and the burner surface. In addition, because less heat loss occurs to the burner surface, near adiabatic conditions may be obtained which allow for the study of leaner flames than can be stabilized on traditional flat-flame burners. This feature is clearly advantageous for the study of lean premixed combustion which is being pursued for $NO_x$ abatement in advanced gas turbines. However, to date, there have been no measurements of nitric oxide in counterflow premixed flames for use in chemical kinetic comparisons.

Nitric oxide formation in high-pressure flames is a research area of great practical interest owing to the high pressures which exist in all practical power-generation and propulsion engines. Unfortunately, those chemical kinetic codes available for prediction of NO formation in combustion systems were developed via comparisons with target flames at only atmospheric and sub-atmospheric pressures (Bowman *et al.*, 1995; Miller and Bowman, 1989; Glarborg *et al.*, 1986). Hence, the high-pressure flame conditions that

industry is most interested in understanding may not be well modeled by the kinetic mechanisms available to study them.

Recently, the Gas Research Institute (GRI) has supported the creation of a comprehensive reaction mechanism for the modeling of natural gas combustion (Bowman *et al.*, 1995). The current version of this mechanism (2.11) has been optimized against numerous measurements of flame speed, species concentrations and temperatures. However, few high-pressure targets have been included in this work. Hence, comparisons of predictions using this mechanism with measurements are still required over a wide range of high-pressure flames. The ultimate goal of such comparisons is the development of a truly accurate, comprehensive mechanism for NO production in methane/air flames that can be used as a basis for future work on the creation of a reduced mechanism for modeling NO formation in gas-turbine engines.

## 1.2 Contents of Thesis

In this study, previous LIF measurements of NO in flat, laminar, premixed, $CH_4/O_2/N_2$ flames at pressures ranging from 1 to 14.6 atm, equivalence ratios from 0.5 to 1.6, and nitrogen/oxygen dilution ratios of 2.2, 3.1 and 3.76 are first compared to modeling predictions to determine the capabilities and limitations of the GRI reaction mechanism for predicting NO formation in high-pressure, premixed flames. Subsequently, the design of a new counterflow burner is presented for chemical kinetic studies in counterflow premixed flames. The LIF technique is then extended to obtain measurements of NO concentration in a series of counterflow premixed flames at pressures ranging from 1.0 to 5.1 atm and equivalence ratios from 0.6 to 1.5. The results of the above studies are then used to analyze which elementary reactions within the GRI reaction mechanism are most important for determining NO formation in lean, premixed flames and to suggest possible improvements to the current kinetic model.

In Chapter 2, the basic theory is reviewed for laser-induced fluorescence (LIF). Results are discussed from other studies of NO formation in high-pressure flame

environments. A summary of the primary formation mechanisms for NO is presented, as well as a review of the literature regarding these mechanisms. Finally, the use of counterflow premixed flames is reviewed for a variety of combustion applications. Chapter 3 provides a description of the experimental apparatus used in performing the high-pressure LIF measurements of NO. A brief description is also presented of the modeling software and of the chemical kinetic mechanisms used for predicting NO formation in these flames.

A wide range of LIF measurements in flat, laminar, premixed, $CH_4/O_2/N_2$ flames is presented in Chapter 4. Modeling predictions using the GRI reaction mechanism (Bowman *et al.*, 1995) are also presented and compared to both the LIF results and predictions using an earlier NO mechanism (Drake and Blint, 1991). A major conclusion from this section is that while the GRI reaction mechanism accurately predicts the equivalence ratio and pressure trends of NO formation in lean, premixed flames, it is incapable of making even qualitatively correct predictions in moderately rich flames.

In Chapter 5, the development of a counterflow burner is presented for use in the high-pressure facility within the Flame Diagnostics Laboratory. Key issues in this design are discussed as they pertain to the current chemical kinetics study.

Chapter 6 presents LIF profiles of NO concentration in atmospheric pressure counterflow premixed flames. Modeling of these flames using the Sandia opposed diffusion flame code in conjunction with the GRI reaction mechanism is presented and compared to the LIF data. A comprehensive analysis is then undertaken to determine the key reactions within the GRI mechanism responsible for both its good and bad predictive capabilities.

The counterflow premixed studies are extended to higher pressures in Chapter 7. While certain limitations of the counterflow premixed geometry are observed, more data are obtained that contrast the relatively good predictive capability of the GRI mechanism in lean flames with its poor predictive capability in rich flames.

Chapter 8 brings together all of the measurements and modeling presented here, along with similar measurements in the counterflow diffusion flames of Ravikrishna

(1999), so as to make some definite conclusions regarding the strengths and weaknesses of the GRI reaction mechanism. Key reactions are identified for each NO formation pathway that are most sensitive to NO production. Suggestions are then made for improving the overall performance of this comprehensive NO mechanism. Finally, Chapter 9 presents the major conclusions gleaned from this investigation. Recommendations are also made for future work on NO kinetics in high-pressure flames.

# 2. THEORY AND LITERATURE REVIEW

## 2.1 Introduction

The goal of reduced emissions from gas-turbine engines has led to the study of NO formation in high-pressure, high-temperature regimes typically found in these engines. Most chemical kinetics models used for combustion studies were developed through the analysis of low-pressure, reaction-rate data. To evaluate the ability of these low-pressure models to predict NO in more realistic high-pressure regimes, it is necessary to obtain accurate NO measurements in high-pressure flames that can be compared to computer modeling.

In this chapter, a review is presented of the theory of laser-induced fluorescence (LIF), an optical technique that can be used to measure NO concentrations in the harsh environments found in practical combustors without disrupting the flowfield and kinetics within the combustor. The results of previous high-pressure NO studies using either LIF or other sampling techniques are also discussed. Next, a review of the relevant kinetics involved in NO formation in this regime is presented, with special emphasis on the kinetics responsible for NO formation via the prompt mechanism. Finally, the status of current research is examined for counterflow premixed flames and the utility of this flame configuration is discussed with respect to mechanistic modeling.

## 2.2 Laser-Induced Fluorescence Theory

Optical techniques are becoming increasingly important for determining species concentrations in combustion processes. They can withstand the harsh conditions of

Excited
Electronic      u
State
        A

$W_{lu}$        $W_{ul}$        $A_{ul}$        $Q_{ul}$

Ground
Electronic      l
State
        X
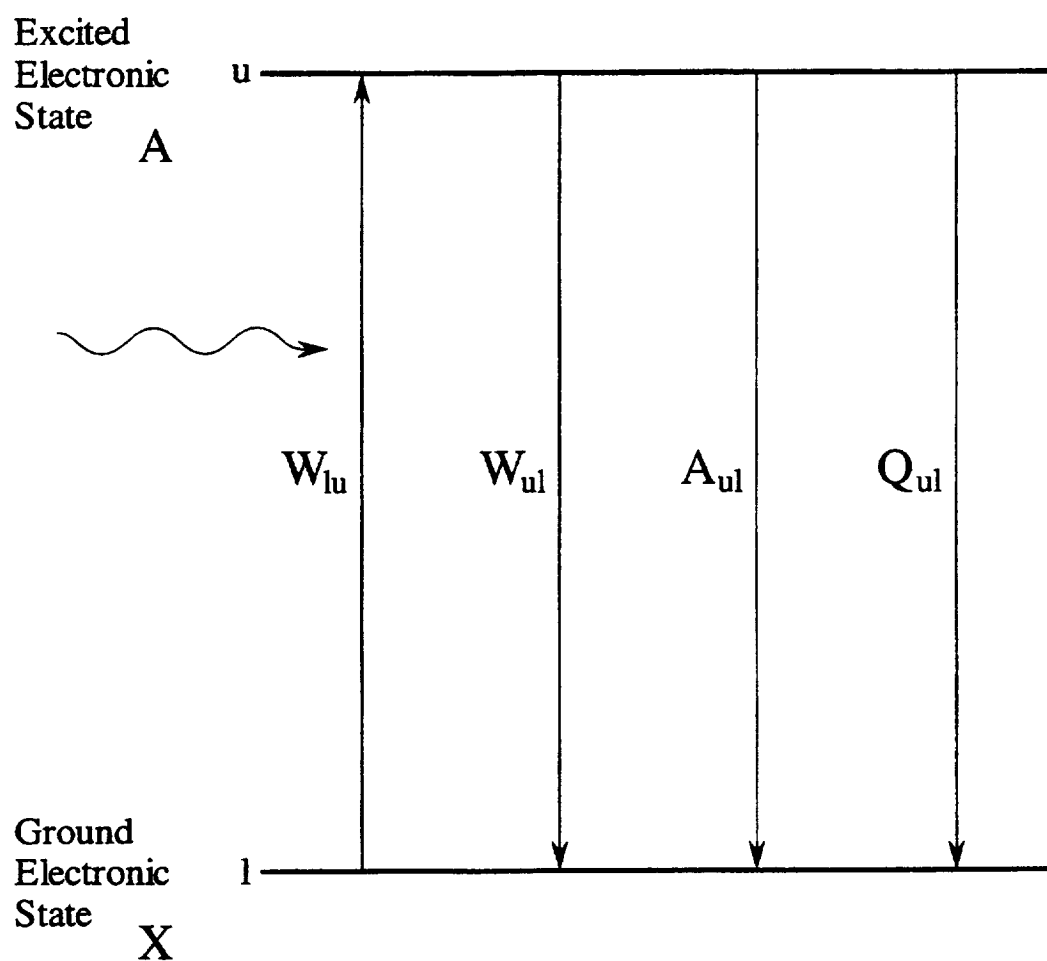
Figure 2.1:   Simplified, two-level model for LIF studies. Shown are the rate coefficients for absorption ($W_{lu}$), stimulated emission ($W_{ul}$), spontaneous emission ($A_{ul}$), and quenching ($Q_{ul}$).

combustive environments without disturbing either their flowfield or the resulting chemical kinetics. Laser-induced fluorescence is one such technique that has become important for the detection and measurement of a variety of radical species, such as NO, that are found in combustion systems. The fundamentals of the LIF technique can most easily be understood by studying the two-level model described by Laurendeau and Goldsmith (1989). However, broadband LIF measurements of NO require the inclusion of several rate processes not considered in the two-level model. To provide a complete yet clear presentation of the LIF technique, the two-level model will be presented and then these additional rate processes will be discussed and added to the model.

The two-level model is based on four simplifying assumptions (Laurendeau and Goldsmith, 1989):

1. The excitation beam is uniform and linearly polarized;

2. The entire population is assumed to be in the ground electronic state before laser excitation ($N_l + N_u = N_l^0$);

3. The fluorescence signal is measured at the peak of the emissive pulse where the upper level population is at steady state;

4. The fluorescence signal consists of a single wavelength corresponding to a single rovibronic transition.

Given these assumptions, the two-level model consists of four rate processes with their corresponding rate coefficients ($s^{-1}$). These processes and their coefficients, demonstrated in Figure 2.1, consist of absorption ($W_{lu}$), stimulated emission ($W_{ul}$), spontaneous emission ($A_{ul}$), and collisional quenching ($Q_{ul}$). A portion of the spontaneous emission, which radiates equally in all directions, is collected as the fluorescence signal.

Considering only the above four processes, rate equations can be written for the change in number density of each electronic level. These equations are

$$\frac{dN_l}{dt} = -N_l W_{lu} + N_u (W_{ul} + A_{ul} + Q_{ul}) \quad , \tag{2.1}$$

and

$$\frac{dN_u}{dt} = N_l W_{lu} - N_u (W_{ul} + A_{ul} + Q_{ul}) \quad . \tag{2.2}$$

At the peak of the laser pulse, where we have assumed steady state, the above two equations will both equal zero. Hence, we can solve either of them to obtain an equation for the ground state number density $N_l$. Noting that $N_l + N_u = N_l^0$ from our second assumption, we obtain

$$N_u = \frac{N_l^0}{\{(W_{ul} + A_{ul} + Q_{ul}) / W_{lu}\} + 1} \quad . \tag{2.3}$$

At this point, one of two simplifying assumptions can be made based on the experimental conditions. For large laser irradiances and lower pressures, stimulated emission and absorption dominate. In other words, both $W_{ul}$ and $W_{lu}$ are large compared to $A_{ul}$ and $Q_{ul}$. This condition is referred to as the laser-saturated fluorescence (LSF) regime. Thus, neglecting quenching and spontaneous emission, Eq. (2.3) becomes

$$N_u = \frac{W_{lu}}{W_{lu} + W_{ul}} N_l^0 \quad . \tag{2.4}$$

Now, the rate coefficients for stimulated emission and absorption are related by the degeneracies of the upper and lower levels ($g_u$ and $g_l$) according to

$$g_l W_{lu} = g_u W_{ul} \quad . \tag{2.5}$$

Combining Eqs. (2.4) and (2.5), we obtain for the LSF upper-level population,

$$N_u = \frac{g_u}{g_l + g_u} N_l^0 \quad . \tag{2.6}$$

The second possible simplification concerns the case for which the laser irradiance is much less than that required to saturate the transition. For high-pressure LIF, this is almost always the case. Here the simplifying assumption is that $W_{ul}$ and $W_{lu}$ are small compared to $A_{ul}$ and $Q_{ul}$. Thus, for this linear LIF regime, electronic quenching and spontaneous emission are the dominant processes. Based on this assumption, Eq. (2.3) becomes

$$N_u = \frac{W_{lu}}{A_{ul} + Q_{ul}} N_l^0 \quad . \tag{2.7}$$

It is important to note at this point that although the rate coefficients for electronic quenching and spontaneous emission are independent of laser power, the rate coefficient for stimulated absorption depends on laser power via the equation

$$W_{lu} = \frac{\sigma I_L}{hc\nu_L} ,$$ (2.8)

where $\sigma$ is the one-photon fluorescence cross-section of the molecule ($cm^2$), $I_L$ is the laser irradiance (W/$cm^2$), and $\nu_L$ is the wavenumber of the laser irradiance ($cm^{-1}$). Combining Eqs. (2.7) and (2.8), we obtain for the LIF upper-level population,

$$N_u = \frac{\left(\sigma I_L/hc\nu_L\right)}{A_{ul} + Q_{ul}} N_l^0 .$$ (2.9)

Considering Eqs. (2.6) and (2.9), we see that for LSF the upper level number density is independent of both laser power and collisional quenching, which is its major advantage. Unfortunately, for higher pressure studies, saturation cannot be achieved; thus, both laser power and quenching must be accounted for in such LIF measurements.

The fluorescence emission $\varepsilon_f$ (W/$cm^3$•sr) is related to the upper level number density through the relation (Laurendeau and Goldsmith, 1989)

$$\varepsilon_f = \frac{hc\nu_f A_{ul}}{4\pi} N_u .$$ (2.10)

where $\nu_f$ ($cm^{-1}$) represents the wavenumber at which the fluorescence occurs. For the simple two-level atomic model, $\nu_f = \nu_L$. Such is not the case for molecular LIF, as will be discussed later. The fluorescence signal depends on both the collection optics and detection electronics through

$$V_f = \beta G\Omega_c V_c \varepsilon_f ,$$ (2.11)

where $V_f$ is the fluorescence voltage, $\beta$ accounts for the efficiency of the collection optics, $G$ is the photomultiplier gain (V/W), $\Omega_c$ is the solid collection angle of the optics (sr), and $V_c$ is the fluorescence collection volume ($cm^3$). Combining Eqs. (2.10) and (2.11) with Eqs. (2.9) and (2.6), we obtain fluorescence signal expressions for each technique. For LSF, we find

$$V_f = \beta h c \nu_f G V_c \left(\frac{\Omega_c}{4\pi}\right)\left(\frac{g_u}{g_l + g_u}\right) A_{ul} N_l^0 \ . \qquad (2.12)$$

For linear LIF, we obtain

$$V_f = \beta \left(\frac{\nu_f}{\nu_L}\right) G V_c \sigma \left(\frac{\Omega_c}{4\pi}\right)\left(\frac{A_{ul}}{A_{ul} + Q_{ul}}\right) N_l^0 I_L \ . \qquad (2.13)$$

The two-level model discussed above is adequate for atomic species, and for a few simple diatomics at lower pressures. However, for most radical species of interest, a more detailed model is needed. Figure 2.2 demonstrates the additional complications arising in molecular LIF studies. A detailed analysis of the effects of these complications can be found elsewhere (Reisel et al., 1993). Only a brief description of their impact on LIF measurements will be given here. In particular, the additional complications caused by molecular energy storage can be divided into three categories: vibrational transfer effects, rotational transfer effects, and ionization effects.

All molecules can store energy in their vibrational energy modes. Adding these modes to the two-level model changes the fluorescence scheme by opening up two new pathways for energy transfer. First of all, assuming that only a single transition is being excited, the upper level can now undergo spontaneous emission to multiple vibrational levels in the ground electronic state. Thus, only a portion of the total fluorescence coming from the excited level will occur within any given vibrational transition. This is not necessarily unfortunate, however, since measuring fluorescence from a non-laser-coupled transition avoids interferences owing to scattering effects. For this reason, most LIF studies employ detection at longer (Stokes-shifted) wavelengths than are used for excitation. The second energy pathway caused by the presence of vibrational energy modes is that of vibrational quenching. Within each electronic state, quenching can exist between the various vibrational levels. Moreover, electronic quenching can now occur from the upper electronic state to a variety of vibrational levels in the lower electronic state.

Each vibrational energy level also contains a number of rotational energy levels, which further complicates LIF. As for the vibrational levels, the rotational levels increase
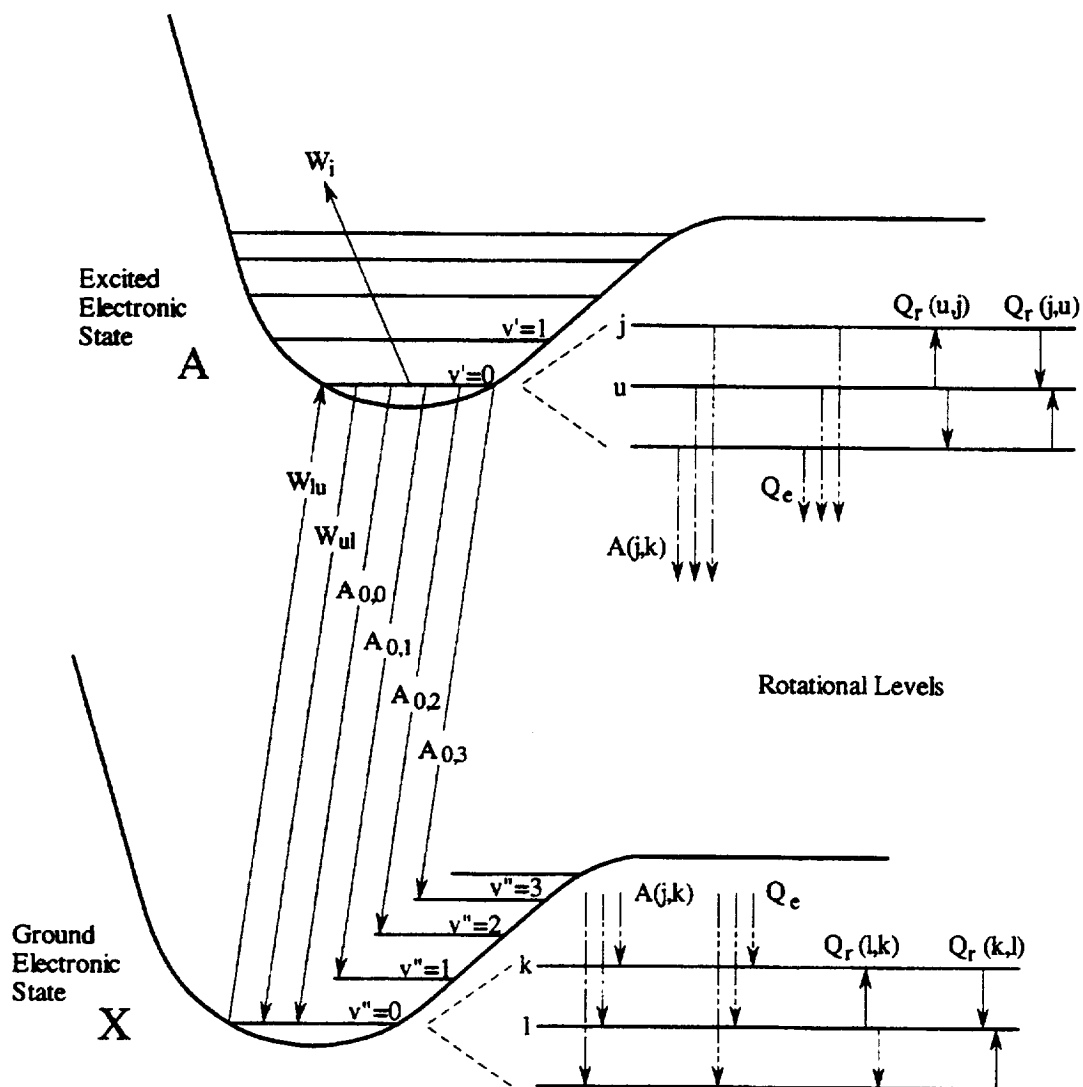
Figure 2.2: Molecular dynamics for LIF studies. The upper and lower laser-coupled rotational levels are labeled $u$ and $l$, respectively. Vibrational quantum numbers in the upper and lower electronic states are indicated as $v'$ and $v''$, respectively. Specific rotational levels in the excited and ground electronic states are indicated by $j$ and $k$, respectively. Shown in the vibrational model are the rate coefficients for absorption ($W_{lu}$), stimulated emission ($W_{ul}$), spontaneous emission ($A_{v',v''}$) and photoionization ($W_i$). Rate coefficients for the rotational model include those for electronic quenching ($Q_e$), rotational relaxation ($Q_r(m,n)$) and spontaneous emission ($A(j,k)$). Vibrational quenching ($Q_v$) in the ground electronic state is not shown for the sake of clarity.

the number of levels available for both emission and quenching. Rotational relaxation is so rapid in both the excited and ground electronic states that it must be accounted for in LIF studies. Typically, two approaches have been used to handle this problem. The first is to model the fraction of molecules that would transfer out of the directly excited rotational level before fluorescing and to develop a new fluorescence equation based on this fraction (Carter *et al.*, 1987). This approach has been used with OH and other species for which sufficient fluorescence exists to continue to detect a single rovibronic transition. The second approach, which is generally used in studies of NO, is to detect not just one transition, but a significant portion of a vibrational band containing many rovibronic transitions (Reisel *et al.*, 1993). The latter technique, called broadband LIF, provides a much larger signal than the former but has the disadvantages of offering a wider detection window in which interferences can occur plus further complicating the fluorescence model.

A final process which must be considered when dealing with some molecules is photoionization. This process will have the net effect of depleting the excited state without emitting a fluorescence signal. For some molecules, photoionization, rather than quenching, can thus be considered the limiting depletion rate in LIF. For NO, this is not the case, although in saturation measurements at atmospheric pressure, Reisel *et al.* (1993) showed that the ionization rate is as significant as that for electronic quenching. However, for high-pressure, linear LIF measurements, the quenching rate will be enhanced by the greater collision rate. Hence, photoionization should not make a significant contribution to the depletion of excited state NO molecules.

By including these three considerations in our simple two-level model, we obtain the excitation scheme shown in Fig. 2.2. There are now seven types of rate processes occurring, each with their corresponding rate coefficient ($s^{-1}$). They are absorption ($W_{lu}$), stimulated emission ($W_{ul}$), spontaneous emission ($A(j,k)$), electronic quenching ($Q_e$), vibrational quenching ($Q_v$), and rotational relaxation ($Q_r(m,n)$). Since the ground vibrational level in the upper electronic state is generally used for excitation, little vibrational quenching will occur in the excited electronic state. Thus, for most

applications, we can neglect this effect when developing rate equations for the upper rovibronic levels. Letting the subscript $j$ represent each rovibronic level in the excited electronic state and $k$ each such level in the ground electronic state, we can write rate equations for each rovibronic level in the excited state. For the directly excited rovibronic levels, this equation is

$$\frac{dN_u}{dt} = N_l W_{lu} - N_u \left\{ W_{ul} + Q_e + W_i \right\} - \sum_{j \neq u} N_u Q_r(u,j)$$
$$- \sum_k N_u A(u,k) + \sum_{j \neq u} N_j Q_r(j,u) .$$

(2.14)

For the remaining levels in the excited state, we have

$$\frac{dN_j}{dt} = \sum_{m \neq j} \left\{ N_m Q_r(m,j) - N_j Q_r(j,m) \right\} - \sum_k N_j A(j,k) - N_j (Q_e + W_i) .$$

(2.15)

Assuming steady state, we can now obtain expressions for the number density of each excited rovibronic level. Specifically, for the directly excited level,

$$N_u = \frac{N_l W_{lu} + \sum_{j \neq u} N_j Q_r(j,u)}{W_{ul} + Q_e + W_i + \sum_{j \neq u} Q_r(u,j) + \sum_k A(u,k)} .$$

(2.16)

For the remaining excited rovibronic levels,

$$N_j = \frac{\sum_{m \neq j} N_m Q_r(m,j)}{Q_e + W_i + \sum_{m \neq j} Q_r(j,m) + \sum_k A(j,k)} .$$

(2.17)

For broadband detection, fluorescence from all of these excited levels can be collected, so that the overall fluorescence signal will be the sum of each of these transitions. Thus, through comparison with Eqs. (2.10) and (2.11), we obtain the following equation for our overall, broadband fluorescence signal,

$$V_{f,b} = \beta h c G V_c \left( \frac{\Omega_c}{4\pi} \right) \left\{ v_f(u,k) A(u,k) N_u + \sum_{j \neq u} v_f(j,k) A(j,k) N_j \right\} .$$

(2.18)

Here $v_f(j,k)$ is the wavenumber of the specific fluorescence transition.

Since the individual rate coefficients for rotational relaxation of each transition are not well known, it would be nearly impossible to use Eqs. (2.16) and (2.17) to determine

directly the number densities of each excited level. However, the above formulation does demonstrate how more signal is available via broadband detection as compared to that for a single transition with narrowband detection.

## 2.3 LIF Measurements of NO at High Pressure

Several laser-induced fluorescence studies have provided semi-quantitative measurements of NO in combustion environments, but very few have done so at the high-pressure conditions found in most modern gas-turbine engines. This section reviews the history of these high-pressure LIF measurements of NO as well as discussing some of the key concerns involved in them.

The first high-pressure LIF study of NO formation in a combustion environment was performed at Purdue University (Reisel *et al.*, 1993; Reisel and Laurendeau 1994a). NO concentrations were measured in the post-flame zone of a series of premixed $C_2H_6/O_2/N_2$ flames stabilized on a water-cooled McKenna burner at pressures ranging from 1 to 14.6 atm, equivalence ratios from 0.6 to 1.6, and a dilution ratio of 3.1. The most important result from this study was simply the demonstration that quantitative high-pressure LIF measurements of NO were possible in combustion environments. Essentially, complete saturation was achieved at atmospheric pressure when using excitation via the $Q_2(26.5)$ transition of NO with a laser power of ~2 mJ/pulse and a spot size of ~250 μm. However, unlike for OH (Carter *et al.*, 1991), saturation of NO could not be maintained at higher pressures, leading to completely linear fluorescence at $P \geq 6.1$ atm. For all of these linear-fluorescence measurements, it was further demonstrated by computer modeling that the variation in quenching rate coefficient should be less than 15% in comparison to that for the calibration condition ($\phi$=0.8) at each pressure. Hence, quenching effects were ignored in these measurements. Detection of the fluorescence signal employed a ½-meter monochromator and an ~3 nm region of the NO spectrum centered on the $\gamma(0,1)$ band of NO. Calibration was obtained by doping known amounts of NO into a reference flame and measuring the resulting fluorescence signals at each

pressure. The slope of the calibration curve was then used to determine the NO number density in the undoped flames at the same pressure. This technique neglects NO destruction in the flamefront (modeling predicts less than 5%), as well as any possible non-NO interferences. The quoted precision and accuracy of these measurements (95% confidence level) were 7.5% and 25%, respectively.

The measurements obtained in the above studies were then compared to modeling predictions using both the Miller-Bowman (1989) and the GMK-DB (Drake and Blint, 1991) reaction mechanisms. While both mechanisms showed good qualitative agreement with NO trends as a function of equivalence ratio and pressure, the GMK-DB mechanism provided much better quantitative predictions of NO concentrations in these flames. These comparisons were later extended to include $C_2H_4/O_2/N_2$ flames for the same pressure and equivalence ratio ranges as for the $C_2H_6/O_2/N_2$ flames (Reisel and Laurendeau, 1995). This follow-up study compared the GMK-DB model with a model comprised of the Miller-Milleus (1992) hydrocarbon kinetics combined with the Drake and Blint (1991) nitrogen kinetics (MIME-DB). Once again, the GMK-DB model proved to be superior in predicting NO concentrations in high-pressure premixed flames, although neither model predicted NO concentrations well at lower pressures (P $\leq$ 6.1 atm). The LIF measurements in this latter study used identical procedures as in the previous two; however, in this case, the quenching coefficient varied by as much as 20% from that in the calibration flame (although this was noted to still fall within the error bars of the experiment). An additional feature of this study was the inclusion of a comparison between LIF measurements of NO using excitation via the $Q_2(26.5)$ and the $R_1(18.5)$ transitions of NO. Good agreement was found between the two sets of measurements, leading to the conclusion that LIF measurements are essentially independent of the chosen excitation line.

To extend these studies to flames exhibiting strong Zeldovich NO production, a further set of measurements was obtained in the post-flame zone of flames stabilized on an uncooled Hencken type burner (Reisel and Laurendeau, 1994b). These $C_2H_6/O_2/N_2$ flames were found to have flame temperatures ranging from 2100 to 2300 K as compared

to the 1600 to 1850 K flames studied previously (Reisel and Laurendeau, 1994a). Excitation scans were used in this study to indicate the absence of $O_2$ interference effects; however, this conclusion was limited to pressures $P \leq 3.05$ atm. A further novelty of this experiment was that temperatures were obtained in the post-flame zone via Rayleigh scattering measurements. An additional study by Reisel et al. (1995) investigated the transportability of an LIF calibration for NO at high pressures. The basic conclusion was that while a calibration at one pressure could be used over a range of conditions at that pressure, such a calibration could not be used at different pressures. It was also recommended that the calibration be performed in a flame with a temperature within 500 K of the flame being studied. More recently, Reisel (1998) found that the above LIF measurements of NO in lean $C_2H_6/O_2/N_2$ and $C_2H_4/O_2/N_2$ flames (Reisel et al., 1993; Reisel and Laurendeau 1994a; 1995) can be collapsed onto a single [NO] vs. $\phi$ curve by normalizing the data from each combination of fuel and pressure by its peak value. In particular, the best equivalence ratio axis for this collapsed profile was found to be $\phi_{82\%}$ $_{Max}$-$\phi$. This work is intriguing because of the excellent collapse of the data over a wide range of pressures and two different fuels. The author suggests that this correlation only works in low-temperature flames for which Zeldovich NO formation in the post-flame zone is not significant.

In consideration of the importance of natural gas as an energy source for gas-turbine engines, the above research was next extended to a study of high-pressure, premixed $CH_4/O_2/N_2$ flames (Klassen et al., 1995). These methane flames were studied first by employing the same pressure and equivalence ratio ranges as for the $C_2H_6/O_2/N_2$ flames. The study was then extended to a series of flames at pressures ranging from 1 to 14.6 atm, equivalence ratios from 0.5 to 0.8, and a dilution ratio of 2.2. These lower dilution ratio flames were chosen to permit further investigation of the chemical kinetics involved in NO formation at higher temperature, leaner conditions than those attainable with a dilution ratio of 3.1. These kinetics are particularly important owing to the prominence of lean premixed combustion as a $NO_x$ reduction strategy for advanced gas-turbine engines. An important discovery of this study was the increasing influence of $O_2$

interferences for LIF measurements of NO in ultra-lean, high-temperature, high-pressure flames. These interferences led to higher uncertainties in the reported concentration measurements for such flames. Another feature of this work was its comparison to modeling using the GMK-DB (Drake and Blint, 1991) reaction mechanism. The mechanism was found to dramatically over-predict the increase in temperature within these flames as a function of pressure, especially at near stoichiometric equivalence ratios. This feature led to a large overprediction of thermal NO production in such flames. In addition to this temperature effect, the mechanism was found to over-predict flamefront NO formation in all but the leanest flames studied, indicating a possible overemphasis on the prompt NO pathway within the GMK-DB mechanism.

Similar research at Stanford University has focused primarily on the application of planar laser-induced fluorescence (PLIF) to NO measurements at high pressures (Battles *et al.*, 1994). In this study, point LIF and PLIF measurements of NO and OH were obtained in lean ($\phi$=0.4), $CH_4/O_2/N_2$ flames at pressures of 1.2 and 10.2 atm. In both cases, the $N_2/O_2$ dilution ratio was modified to attain flame temperatures near 2000 K. Since the focus of this work was on the PLIF technique rather than on measured concentrations, most of the results were presented on a relative basis. This investigation was also one of the first to acknowledge in a clear manner the problem of $O_2$ fluorescence interferences for LIF measurements of NO in lean, high-pressure flames. In addition to fluorescence signal corruption, this $O_2$ fluorescence was found to cause potential beam attenuation effects on the order of 30%/cm at 10 atm.

Battles *et al.* (1994) employed modeling of the $O_2$ spectrum in conjunction with excitation scans of the NO spectrum to locate an NO feature that was relatively free of $O_2$ interferences. Consequently, excitation was performed using a multiple-line feature containing the $Q_1(14.5)$, $Q_2(20.5)$, and $P_1(23.5)$ lines of the $\gamma(0,0)$ band of NO ($\lambda\approx226.034$ nm). It should be noted, however, that compared to the previous studies the $O_2$ interference problem was enhanced in this study by the use of a broadband detection scheme both for the PLIF and LIF point measurements. Without a monochromator to reject most of the $O_2$ interference, the ratio of NO to $O_2$ fluorescence measured in the 10-

atm flame was found to be less than 0.5 at temperatures greater than 1800 K. This $O_2$ interference was removed by making a second fluorescence measurement at each point using off-line excitation ($\lambda \approx 226.015$ nm) and subtracting it from the original measurement. The technique assumes that no NO signal is present in the off-line measurement and that the $O_2$ background is the same at both the on- and off-line locations. A useful experimental comparison is also presented by Battles *et al.* (1994) which shows that the overall NO fluorescence signal varies with both temperature and pressure, and drops by ~50% from 1600 K to 2300 K and by ~55% from 1 to 10 atm.

Partridge *et al.* (1996) responded to the above research by experimentally determining optimal excitation and detection schemes to minimize the effect of non-NO interferences for LIF and PLIF measurements of NO in lean, high-temperature, premixed flames at pressures of 1.0 and 6.1 atm. Their results indicated that this spectral determination is experiment specific; hence, a procedure is presented by which the choice of excitation/detection schemes can be made for any given experiment. A major conclusion of this work is that even with narrow-band detection using a monochromator, $O_2$ interferences could become a problem in ultra-lean, higher-pressure flames (P $\geq$ 6.1 atm). However, atmospheric LIF and PLIF measurements of NO are relatively free from such interferences.

Thomsen *et al.* (1997) further addressed the $O_2$ interference issue by developing a systematic procedure for subtracting $O_2$ interference signals from high-pressure LIF measurements of NO. Their work minimized the amount of $O_2$ fluorescence collected by limiting detection to an ~2.7 nm region of the $\gamma(0,1)$ band of the NO molecule. Unfortunately, as discussed by Sick *et al.* (1996), $O_2$ rotational energy transfer will cause some $O_2$ fluorescence signal to spread into even this smaller detection window. Thus, an on- and off-line excitation technique was employed to determine the remaining $O_2$ contribution and to subtract it from the NO measurement. One feature of this technique was that while it depended on the location of an off-line excitation wavelength with the same $O_2$ signal as the on-line wavelength, it did not assume the absence of NO fluorescence in the off-line signal. Using this technique, Thomsen (1996) repeated the NO

measurements of Klassen et al. (1995) for their lean (0.5 ≤ φ ≤ 0.8), high-pressure, 2.2 dilution ratio, $CH_4/O_2/N_2$ flames, which should provide a worst-case condition for $O_2$ interferences. A careful error analysis demonstrated the ability of this technique to measure an NO concentration of 7.4 ppm with an accuracy of 28.1% (95% confidence level) for a 2.2 dilution ratio, 0.6 equivalence ratio, 14.6 atmosphere $CH_4/O_2/N_2$ flame.

An alternate method for dealing with $O_2$ interferences while still employing broad-band detection was presented by Di Rosa et al. (1996). They used improved modeling of both NO and $O_2$ fluorescence to predict the existence of two separate detection regions, one containing both NO and $O_2$ fluorescence and the other containing only $O_2$ fluorescence. Based on their spectral modeling, they showed that the $O_2$ fluorescence within one region is proportional to that in the other; hence, by using a single excitation wavelength, a correction scheme could be developed to permit PLIF imaging of NO in high-pressure environments despite significant $O_2$ interferences. Another feature of this work was the observation that the NO fluorescence spectrum more closely resembles a fluorescence model that assumes zero rotational energy transfer in the upper electronic state than full rotational energy transfer. This result indicates that the electronic quenching rate for NO is fast compared to rotational energy transfer in the excited electronic state. Note that the big advantage of the proposed technique is its applicability to single-shot measurements in turbulent flowfields for which a two-line excitation technique may be impossible to implement.

A review of the above techniques and their performance at pressures up to 30 atm was presented by Kuligowski and Laurendeau (1998). Among their findings was the increased importance of beam steering when applying laser-based diagnostics to high-pressure flames. For laminar flames, this effect, caused by thermal gradients in optically dense, high-pressure gases, can degrade the spatial resolution and precision of virtually any optical technique. For many turbulent, high-pressure combustion environments, this particular problem could make quantitative laser measurements impossible above 15 atm unless conditional sampling procedures are implemented to correct the problem on a shot-to-shot basis. Another feature of this study was the extension of the two-line $O_2$

correction procedure of Thomsen *et al.* (1997) to excitation utilizing the NO bandhead and a region off the bandhead with no NO fluorescence contribution. This type of excitation scheme may become necessary at pressures above 15 atm, since pressure broadening causes the difference between the on- and off-line NO signals to become too small for effective resolution of the NO signal when using the excitation scheme of Thomsen *et al.* (1997).

A further paper regarding interferences among $O_2$, NO, and O-atom fluorescence was presented by Wysong *et al.* (1989). Although their study did not extend to high-pressure conditions, it did consider in detail the various spectral features surrounding the $Q_2(25.5)$ transition of NO. In this work, the NO fluorescence signal was the interference as they were attempting to measure O-atom concentrations. A novel result of their study was the suggestion that the spectral overlap of the excitation frequencies for these three species could be used as a method for obtaining simultaneous O, $O_2$, and NO concentration measurements by using narrow-band detection to distinguish among the three fluorescence signals.

Following the developmental work described above, the LIF technique is now being employed by several research groups for making high-pressure measurements of NO in combustive environments. Allen *et al.* (1995a) utilized the technique of Battles *et al.* (1994), described above, to obtain PLIF measurements of NO in a spray flame combustor at pressures ranging from 1 to 10 atm. Although they report no quantitative PLIF data, they claim detection limits in the few tens of ppm for NO at 10 atm for single-shot PLIF measurements. Their follow-up work in the same types of flames (Upschulte *et al.*, 1996) demonstrated qualitative NO PLIF images for pressures ranging from 1 to 8 atm. An important feature of this work was the discovery of large interferences other than from $O_2$ in these spray flames which the authors speculated arose from unburned hydrocarbons. In their work, the contribution from these interferences could be determined by simply removing $N_2$ altogether from the flame environment. This tactic was possible because their study involved very low dilution ratio, high-temperature flames for which removal of the $N_2$ should not significantly affect the flame chemistry. Another feature of this work is

the use of atmospheric calibration of the NO image. This strategy was coupled with modeling of temperature and pressure effects on the LIF process to obtain approximate mole fractions of NO in their high-pressure flames. In the end, they reported single-shot NO detection limits of a few hundred ppm.

Vyrodov et al. (1995) were the first investigators to use NO LIF to make temperature measurements in high-pressure, $CH_4$/air flames. They utilized broadband detection to obtain excitation spectra of the $\gamma(0,0)$ band of NO which they then fit to a spectral model to obtain flame temperatures. To avoid the $O_2$ interference problem, they doped additional NO into the flame to make the NO signal dominant. They report that their temperature measurements agree to within 3% of those obtained from independent CARS measurements at pressures up to 30 atm.

Brugman et al. (1997) utilized PLIF measurements to image NO concentrations inside a diesel engine. There were two novel components to this research. The first was the use of an excimer laser to excite the NO D-X(0,1) band at ~193 nm. Because of the lower UV wavelength of this laser, absorption effects were even greater than those for the more traditional A-X(0,0) bamd. The second component was a post-processing procedure developed by the authors to account for attenuation of both the excitation beam and the detected fluorescence. Procedures were also developed to account for window fouling owing to soot formation in this diesel engine.

Finally, Schulz et al. (1997) have recently presented LIF measurements of NO at pressures up to 40 bars. Employing the NO A-X(0,2) system for excitation at 247.95 nm, the authors were able to avoid both beam attenuation and $O_2$ interferences at the expense of using a much weaker NO transition which requires a significantly stronger pump laser for successful measurements. Using this technique, they were able to obtain quantitative measurements of NO, but only in the 300-400 ppm range. In a continuation of this work, Schulz et al. (1999) performed a complete analysis of this A-X(0,2) technique for LIF measurements of NO in high-pressure flames. Among other things, they evaluated the linear range of this techniques as a function of pressure. Additionally, they utilized measured excitation and fluorescence spectra, at a variety of pressures, to examine the

effects of rotational and vibrational energy transfer as well as electronic quenching on the LIF signal. Furthermore, they discussed the applicability of a doping-based calibration procedure for quantifying their NO measurements. In general, this latter publication presents an excellent review of their technique, which, by avoiding interference issues, may be applicable to much higher pressures than the NO A-X(0,0) excitation strategy employed in this work. However, this advantage is gained at the expense of a considerably increased detection limit.

## 2.4 NO Formation Pathways

NO has traditionally been thought to be produced through three main reaction mechanisms (Miller and Bowman, 1989; Drake and Blint, 1991): (1) the Zeldovich, or thermal-NO mechanism, (2) the $N_2O$-intermediate mechanism, and (3) the prompt-NO mechanism. The amount of NO formed through each of these mechanisms depends on the temperature, pressure and equivalence ratio of the flame.

The Zeldovich or thermal NO pathway (Zeldovich, 1946) is the simplest of all the NO formation mechanisms and represents the break-down of atmospheric nitrogen into nitrogen atoms and the subsequent formation of NO. It most commonly includes the following three reactions (R1-R3) (Miller and Bowman, 1989):

$$O+N_2 \Leftrightarrow NO+N \qquad (R1)$$

$$N+O_2 \Leftrightarrow NO+O \qquad (R2)$$

$$N+OH \Leftrightarrow NO+H. \qquad (R3)$$

Nitric oxide formed via the Zeldovich NO pathway can basically be divided into two categories, that generated within the flamefront and that produced in the post-flame zone. Flamefront Zeldovich NO formation is enhanced by super-equilibrium concentrations of atomic oxygen (Drake and Blint, 1991), which leads to a sharp increase in NO over a very short distance within the flame. This sudden increase of NO in the flamefront is part of what early researchers first dubbed "prompt" NO (Fenimore, 1971), although we have now defined this latter term more strictly as referring to NO formed via

nitrogen-carbon chemistry interactions within the flame front. Zeldovich NO production within the post-flame zone is characterized by a high activation temperature (~1800 K) and is the dominant form of post-flame NO production. This thermal NO contribution leads to an almost linear increase of NO with residence time in the post-flame region. For low-temperature flames (T < 1850 K), the amount of NO produced through this mechanism is small. However, for high-temperature flames, the thermal NO mechanism becomes the dominant pathway for NO production (Corr *et al.*, 1992).

The $N_2O$ intermediate pathway, though relatively unimportant in stoichiometric to rich flames, has been found to play a significant role with respect to flamefront NO formation in lean premixed flames (Malte and Pratt, 1974, Corr *et al.*, 1992). This pathway consists of five primary steps:

$$N_2 + O + M \Leftrightarrow N_2O + M \tag{R4}$$

$$N_2O + O \Leftrightarrow NO + NO \tag{R5}$$

$$N_2O + O \Leftrightarrow N_2 + O_2 \tag{R6}$$

$$N_2O + H \Leftrightarrow NO + NH \tag{R7}$$

$$N_2O + H \Leftrightarrow N_2 + OH. \tag{R8}$$

Several additional reactions involving $N_2O$ must be considered when performing detailed kinetics calculations (Nicol *et al.*, 1993). As for the Zeldovich pathway, the $N_2O$-intermediate pathway is enhanced by super-equilibrium concentrations of OH and O in the flame front (Drake *et al.*, 1990).

The prompt NO pathway is the most complicated of the NO formation pathways. As indicated previously, the term "prompt" NO, originally used to account for the seemingly instantaneous formation of NO in the flamefront (Fenimore, 1971), now more specifically refers to NO formed via carbon-nitrogen species interactions within the flame. More importantly, the latter still accounts for the dominant amount of flamefront NO formation in stoichiometric to rich flames (Drake and Blint, 1991). The initiation step for the prompt NO pathway is generally agreed to be

$$CH+N_2 \Leftrightarrow HCN+N, \tag{R9}$$

although other possibilities have been considered for this role (Corr *et al.*, 1992).

The manner by which the prompt mechanism converts the resulting HCN and N radicals into NO is a matter of some debate. Many authors suggest that the N radical is the ultimate intermediate, with NO then being formed via the Zeldovich reactions (R2) and (R3) (Glarborg et al., 1986; Morley, 1981; Bockhorn et al., 1991). Other authors suggest that the NH radical is the controlling intermediate, with NO being formed through relevant amine radical reactions (Bian et al., 1990; Vandooren, 1992; Seery and Zabielski, 1977). A review of this problem as examined in the literature is presented in the next section.

Prompt NO is primarily formed through a reaction sequence that involves the rapid reaction of hydrocarbon radicals with molecular nitrogen (Miller and Bowman, 1989). Thus, this mechanism tends to produce much more NO under moderately fuel-rich conditions than under fuel-lean conditions. However, prompt-NO production is also significantly curtailed for highly fuel-rich combustion. Reisel and Laurendeau (1994a) demonstrated the importance of the rate coefficient for Rxn. (R9) with respect to the overall prediction of NO formation in rich ethane flames. Unfortunately, there is considerable uncertainty in the rate coefficient for this reaction (Drake and Blint, 1991), although more recent work appears to be alleviating this problem (Miller and Walch, 1997).

Miller and Bowman (1989) performed a thorough chemical kinetics modeling study to determine the relative importance of the various reaction paths. They found that, in general, the NO production reactions must be coupled with those reactions involving oxidation of the fuel. This procedure is necessary because of the presence of O and OH radicals in the thermal-NO and $N_2O$ mechanism and of CH in the prompt-NO mechanism. Their work also suggests that the rapid drop-off of prompt-NO production in rich flames correlates with a rapid decrease in HCN concentration.

Corr et al. (1992) recommend that all three mechanisms should be considered for lean, premixed combustion. This recommendation is further substantiated by the work of Drake et al. (1990) who found that for high-pressure, low-temperature, lean, premixed $C_2H_6/O_2/N_2$ flames, all three mechanisms (with the thermal-NO and $N_2O$-intermediate mechanisms enhanced by super-equilibrium O-atom concentrations) contribute

significantly to flamefront NO production. Unlike nonpremixed flames, which appear to be dominated by thermal-NO production at the high-temperature flamefront, the lower temperatures of non-stoichiometric premixed flames tend to enhance the influence of the prompt and $N_2O$ mechanisms. Since advanced gas turbines are expected to closely approximate lean premixed combustion (Correa, 1992), all three reaction mechanisms and their pressure scaling must be investigated for lean premixed flames.

In addition to the three previously discussed NO production mechanisms, Bozelli and Dean (1995) have recently proposed the existence of a new mechanism for NO production involving the reaction

$$O + NNH \Leftrightarrow NH + NO. \tag{R10}$$

For this reaction to be significant, the authors proposed that much more NNH is formed via the reaction

$$H + N_2 \Leftrightarrow NNH \tag{R11}$$

than predicted by the commonly used mechanism of Miller and Bowman (1989). Harrington et al. (1996) attempted to experimentally verify the importance of this mechanism in low-temperature combustion. They studied low-temperature, low-pressure, fuel-rich, premixed hydrogen-air flames and demonstrated the inability of the other three NO production mechanisms to account for formation of the experimentally observed NO. Hence, this new mechanism could become important in determining NO formation for conditions which minimize the other three, more well-known, NO formation mechanisms. Specifically, the NNH pathway could become important for the lean-premixed flames being pursued in advanced gas-turbine engines. On the other hand, Marinov et al. (1998) recently examined premixed hydrogen/air flames in spark-ignition engine conditions (P=40 atm, inlet temperature = 900 K, $\phi$ = 0.4). They found the contribution of this NNH pathway to NO concentration to be on the order of 4 ppm under these conditions, as compared to a total predicted NO concentration of 186 ppm.

## 2.5 NO Formation via the Prompt NO Pathway

While widespread agreement has been reached that Rxn. (R9) is the primary initiating step for the prompt-NO mechanism, equally widespread disagreement exists over which intermediate species forms the final bridge to NO formation for this pathway. The N, NH and $NH_2$ radicals have all been considered for this role, but most of the debate lies between the nitrogen atom and some combination of the two amine radicals as the primary source. Numerous studies have considered the problem of HCN, $NH_3$ or fuel-nitrogen oxidation. This section reviews a number of these studies, the types of flames considered, and the results that can be drawn from these studies.

Haynes (1977) studied the effect of seeding varying amounts of fuel nitrogen sources (ammonia, pyridine, nitric oxide) into a number of fuel-rich ethylene- and acetylene-air flames on NO formation and destruction. Probe measurements were used to determine concentrations of NO, HCN, and $NH_i$ within the flame. By correlating the effect of OH concentration on the formation rate of NO and on the destruction rates of $NH_i$, Haynes (1977) determined that the nitrogen atom is the key intermediate for NO formation. The author does, however, admit that these results may not hold in cooler and leaner flames.

Morley (1981) suggests that the dominant intermediate for NO formation depends on the conditions in the flame, with the nitrogen atom becoming dominant in flames with high radical concentrations. In his experimental study of premixed $H_2/O_2/Ar$ flames doped with $CH_3CN$, he measured OH, NH, CN and NO concentrations using laser-induced fluorescence. The author was interested in determining the primary pathway for the creation of NO from nitrogen compounds contained in the fuel. Since the amount of NO in his flames did not correlate with the measured NH signal, Morley (1981) concluded that NH, or any equilibrated $NH_i$ species, does not react appreciably with NO under these conditions. Additionally, he experimentally determined that NH was largely removed by the reaction

$$NH + H \Leftrightarrow N + H_2, \qquad (R12)$$

thus coming to the conclusion that for his flames, N atoms were the primary intermediate for the formation of NO from fuel-bound nitrogen.

Miller *et al.* (1984) studied the conversion of seeded HCN to NO in $H_2/O_2/Ar$ flames at low pressures for equivalence ratios of 0.5, 1.0 and 1.5. Their probe measurements of a number of flame species and LIF measurements of the CN radical and temperature were compared to a relatively simple kinetic mechanism. Once they were convinced that the model accurately predicted their results, they analyzed their model in detail to determine that nitrogen atoms are the dominant intermediate for NO formation.

Glarborg *et al.* (1986) developed a complex kinetic model which basically implies that prompt NO is formed via the sequence HCN/CN→NCO→NH→N→NO. No experimental work was presented by Glarborg *et al.* (1986) to validate this particular sequence, though the mechanism as a whole was shown to predict overall NO formation well in a few test cases. Miller and Bowman (1989), in the development of their complex chemical kinetics model, performed a detailed sensitivity analysis on the different mechanisms of NO formation. Their conclusion regarding prompt NO was that the primary sequence for NO formation was CH→HCN→NCO→NH→N→NO, similar to that of Glarborg *et al.* (1986). They also studied mechanisms of NO conversion in rich flames, ammonia oxidation, fuel-nitrogen conversion in well-stirred reactors, and the thermal de-$NO_x$ process. Only in the last of these do the authors suggest NH as a primary NO forming radical. While numerous studies have indicated the limitations of the above mechanism, the widespread agreement it finds with many realistic flame conditions has made it, until recently, the yardstick by which other models were assessed for potential improvement.

Bockhorn *et al.* (1991) studied premixed, low-pressure, propane/air flames ($\phi$=0.8, 1.0, 1.2) using resonance absorption techniques to measure NO and OH concentrations, as well as microprobe sampling for major species concentrations. Because of the low temperatures of these flames (T≈1800 K), they assumed that the vast majority of NO was formed via the prompt-NO pathway. They compared their experimental work with a kinetic model containing 604 elementary reactions among 60 chemical species. One

limitation of this study, however, is that it did not include reactions for the creation and destruction of $N_2O$ and $NO_2$. The authors found that with their assumptions and model, 59% of the NO formed in these flames was through nitrogen atoms via the two Zeldovich reactions (R2 and R3) and 30% was through the intermediates NCO and NH. They suggested that since nitrogen atoms are formed mainly via the prompt mechanism, the primary intermediate for prompt NO formation is the N atom. They also acknowledged the extreme sensitivity of their predicted NO concentrations to the reaction rates for Rxn (R9) and to the main oxidizing reaction

$$CH + O_2 \Leftrightarrow CHO + O. \qquad (R13)$$
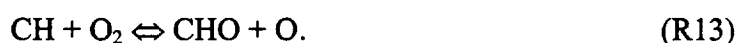
While a large number of studies have agreed on the dominance of the N-atom pathway, as early as 1977 researchers were discovering some flaws with this conclusion. Seery and Zabielski (1977) studied a low-pressure $CO-NH_3-O_2$ flame using probe sampling to measure species concentration profiles above a water-cooled, flat-flame burner. This study, though not determining the intermediate species responsible for NO formation, was one of the first to demonstrate a condition for which the data were not consistent with the N-atom intermediate theory. The authors suggested that perhaps the NH radical was responsible for this behavior.

Bian *et al.* (1990) used modeling and molecular beam sampling measurements to examine the main paths leading to NO and $N_2O$ formation in a series of low-pressure (P=34.5 Torr) $H_2/O_2/Ar$ flames ($\phi$=0.12, 1.00; $T \approx 1100$, 1400 K) seeded with $NH_3$ or $NH_3$ + NO. They studied the addition of ammonia because of recent interest in using seeded ammonia to remove $NO_x$ from practical burners in a process called thermal $deNO_x$. However, their findings relate directly to our study of prompt-NO kinetics. They found that nitric oxide was produced primarily by the reactions

$$NH + O_2 \Leftrightarrow NO + OH \qquad (R14)$$

and

$$NH_2 + O \Leftrightarrow NO + H_2 \qquad (R15)$$
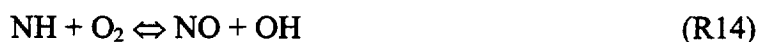
instead of by the N-atom reactions from the Zeldovich mechanism. Nitrous oxide was found to be formed subsequently through Rxn. (R7). The authors suggest that the Miller

and Bowman (1989) mechanism either underpredicts the NO formed from $NH_i$ species or overpredicts the NO destroyed by $NH_i$ species owing to their estimates for unmeasured reaction rate coefficients. Specifically, the experimental results indicated that the rate coefficients used by Miller and Bowman (MB) and others for Rxn. (R14) have generally been underestimated. In subsequent work (Vandooren, 1992), it was suggested that the above problem in the MB mechanism is made even worse by their overprediction of the rate coefficient for Rxn. (R9). This combination may explain why the MB mechanism predicts that the nitrogen atom is the key intermediate for NO formation rather than NH.

Lindstedt *et al.* (1994) attempted to bridge the gap between these seemingly disparate views of the pathway for prompt NO formation. They found that the Miller-Bowman (1989) mechanism did a good job predicting NO formation in high-temperature ammonia flames, while the mechanism proposed by Vandooren (1992) did a much better job predicting NO formation in low-temperature, hydrogen-oxygen flames seeded with $NO/NH_3$. The authors suggest that the differences arise from their treatment of the $NH_2/NH$ destruction paths. By studying a sequence of flames bridging the conditions at which each model works best, the authors attempted to develop a chemical kinetics model which accurately portrays the ammonia oxidation process. A complete sensitivity analysis was employed to determine which reactions dominated under differing flame conditions. It was determined that $NH_2$, NH, and N atoms all played roles for differing stoichiometries and doping levels. For pure ammonia flames and lean doped hydrogen flames, they found NO to be formed mainly from $NH_2$ and NH via the HNO intermediate, whereas in other doped hydrogen flames the N-atom path was dominant for both NO formation and destruction. However, in both cases, they found that the limiting reaction was the formation of HNO via the reaction

$$NH_2 + O \Leftrightarrow HNO + H. \hspace{3cm} (R16)$$

The results of their study were compared to experimental data with fairly good but not perfect agreement. Whether or not this work has all the kinetics correct, it was the first investigation to seriously address the range of conditions for which different pathways become dominant.

More recently, Dupont and Williams (1998) examined both NO formation and destruction reactions in a rich, partially-premixed, $CH_4$/air flame. Based on modeling using the GRI mechanism version 2.11 (Bowman et al., 1995), the authors demonstrated that at different flame locations, different NO production reactions dominated, despite the fact that prompt NO apparently dominated at all locations. In particular, the N-atom route seemed to account for 30-50% of NO production at locations of peak NO formation. The other significant intermediate identified in this work is the HNO molecule which is a significant product of the NO reburn reactions.

## 2.6 NO Formation in Gas Turbine Combustors

In addition to the fundamental LIF and pathway studies mentioned previously, much research has gone into determining methods of reducing $NO_x$ emissions from gas-turbine engines. A large portion of this research has in turn pointed toward the use of lean-premixed combustion. Leonard and Correa (1990), for example, used uncooled quartz probes in conjunction with chemiluminescent detection to measure $NO_x$ concentrations downstream of a preheated, turbulent, lean premixed flame stabilized on a perforated alumina plate. They found that because of the relatively low flame temperatures of lean-premixed flames, low $NO_x$ levels (less than 10 ppm) could be produced, and that these results were basically independent of both pressure and the use of secondary cooling air. The first result demonstrates that the $\sqrt{P}$ dependence, traditionally used for scaling $NO_x$ production with pressure in diffusion flames, does not hold in ultra-lean premixed flames, for which the majority of NO is not produced via the Zeldovich mechanism. The second result suggests that the addition of secondary air can be delayed to provide more time for completion of pyrolysis reactions within the primary reaction zone of the combustor.

Correa (1992) has presented an overall review of recent research on $NO_x$ formation in gas-turbine engines. The major techniques currently being considered for low-$NO_x$ engine design include water injection, ammonia de$NO_x$, staged combustion

(RQL), lean-direct injection, and lean-premixed combustion. The high inlet temperatures associated with lean direct injection create accelerated $NO_x$ formation zones which may eliminate this technique from practical use in advanced gas turbines. Most of the other techniques are similarly restricted by stoichiometric interfaces with high $NO_x$ production rates. The major conclusion of this report was that lean-premixed combustion is probably the only combustion technology which can provide ultra-low $NO_x$ emissions (<10 ppm) in the immediate future. Because current burner exit temperatures are limited by material properties in the turbines, Correa (1992) suggested that lowering the equivalence ratio to decrease $NO_x$ production should not compromise efficiency. In addition, Zeldovich NO formation was found to dominate in diffusion-type flames while the $N_2O$ intermediate pathway became more important in lean-premixed flames (both laminar and turbulent). Thus, NO formation in these lean-premixed flames should be roughly independent of pressure.

Another review of recent advances in low-emission combustors for gas turbines was presented by Lefebvre (1995). His primary emphasis was on fuel preparation and delivery, but some results relating to $NO_x$ formation were also presented. Like Correa (1992), Lefebvre (1995) also concluded that lean, premixed, prevaporized combustion appears to be the only technique capable of achieving ultra-low $NO_x$ emissions from practical combustors. He further notes that reducing $NO_x$ formation in aircraft engines is much more complicated than land-based turbines owing to the liquid fuel used in aircraft propulsion and the accompanying higher peak flame temperatures. In addition, supersonic aircraft being considered for future long-distance markets could dump $NO_x$ directly into the upper atmosphere, leading to possible depletion of the stratospheric ozone layer. Hence, limiting $NO_x$ production in such engines is crucial. Lefebvre (1995) also points out several studies showing that NO formation is independent of pressure in lean-premixed flames, and attributes this result to the dominance of the prompt and $N_2O$ intermediate pathways. He also predicts that engine pressure ratios will continue to rise up to a maximum of around 50 in the immediate future. Thus, the study of pressure effects on NO formation is crucial.

A more recent effort to study NO formation in realistic gas turbine conditions was performed by Bengtsson *et al.* (1998). The authors constructed a high-pressure, jet-stirred reactor and compared probe measurements of $NO_x$, $N_2O$ and CO to predictions using a variety of chemical kinetic mechanisms. They found that the GRI mechanism (Bowman *et al.*, 1995) as well as two other hybrid mechanisms used in their work successfully predicted the negative pressure trend of $NO_x$ in this flame configuration, while the earlier Miller-Bowman (1989) mechanism did not. In each case, however, all measured concentrations were lower than the predictions from the mechanisms.

In summary, these general studies have shown that the pressure dependence of NO is heavily influenced by flame geometry. In the perforated plate flames of Leonard and Correa (1990), $NO_x$ concentrations were found to be independent of pressure for lean flames. Meanwhile, the jet-stirred reactor flames of Bengtsson *et al.* (1998) demonstrated a negative pressure dependence. Both of these findings, in turn, contradict the positive pressure dependence found in the flat, laminar flames of Klassen *et al.* (1995). Each configuration results in a different combination of species, temperature and residence time within the flame front, thus altering the dominant NO chemistry. This complication helps explain why, despite continued optimization of reaction mechanisms to specific data sets, no single complex mechanism has yet emerged that accurately predicts NO formation for all conditions.

## 2.7 Counterflow Premixed Flame Studies

Many of the NO measurements and modeling discussed in this chapter employed flat laminar flames stabilized on a water-cooled burner. This geometry has traditionally been used because it produces one-dimensional flames that are easy to model, extremely stable, and simple to use. One problem with this configuration is that the flamefront sits extremely close to the burner, especially at high pressures. This fact makes it impossible to obtain experimental profiles of temperature and species concentration through the flamefront or even to experimentally validate the concentrations and temperatures

upstream of the flame. An alternate configuration that promises to provide this capability while retaining a one-dimensional structure for ease of modeling is that of counterflow premixed flames. Because the flames are stabilized by curvature effects rather than by heat loss to the burner, significant separations can exist between the flamefront and the burner surface in these flames. In addition, because there is less heat loss to the burner in such flames, near adiabatic conditions may be obtained which allow for the study of much leaner flames than can be stabilized on traditional flat-flame burners. This feature is advantageous for the study of lean premixed combustion which is being pursued for $NO_x$ abatement in advanced gas turbines. In this section, we review recent work that has been performed using these burners and identify areas where contributions can still be made.

Much of the work performed to date in counterflow premixed flames has to do with one of two topics: extinction or flame speed. Giovangigli and Smooke (1987) were among the first to use modeling based on the counterflow geometry to predict extinction limits as a function of strain rate. Their study included both $H_2$/air and $CH_4$/air flames. They compared their predictions to the experimental work of Sato (1982) who determined cold-flow-rate extinction limits for counterflow premixed flames at different Lewis numbers. A recent work in this area is that of Konnov et al. (1996) who experimentally studied the effect of cold-flow velocities and nonadiabaticity on extinction limits in laminar methane-air flames. Because of the increasing effect of heat loss to the burner at lower flow rates, they found that the velocity and extinction distance between the two burners were not proportional, as might be expected if strain rate were the only consideration. Another important aspect of this work is that it was apparently the first to use LIF to measure OH concentrations in this type of configuration. All of the flames studied were at the low pressure of 4.2 kPa. From their OH and temperature measurements, Konnov et al. (1996) were able to conclude that while the peak temperature was affected by heat losses and changes in the strain rate, neither were the temperature or OH concentration gradients in the region of maximum heat release.

Another study concerned with the effects of nonadiabaticity on extinction in counterflow premixed flames was performed by Guo et al. (1997). Here, modeling was

employed to predict the existence of a low-strain rate extinction limit for ultra-lean premixed methane-air flames that arises from radiation heat loss. They found that for $\phi \leq$ 0.48, such a low-strain rate limit does exist, as well as the standard high-strain rate limit examined by previous investigators (Giovangigli and Smooke, 1987; Konnov et al., 1996). A later work by these authors (Guo et al., 1998) extended this study to look at the effects of radiative reabsorption on extinction limits. In this study, they confirmed that reabsorption has little effect on the extinction curves predicted for $CH_4$/air flames. However, they found that reabsorption had a strong effect on the temperatures and extinction limits of $CH_4/CO_2/O_2$ premixed flames, extending the minimum strain rate at which such flames may be stabilized. A final study in this area was that of Im et al. (1996) who considered the effect of oscillating strain rates on the structure and extinction of counterflow premixed flames. This study was primarily concerned with the behavior of oscillating premixed flames because of the application of laminar flamelet theory to turbulent combustion modeling. They found that extinction could be delayed when the strain rate oscillates about the static extinction point, which suggests that the laminar flamelet regime may be wider than that predicted solely from studies of steady flames.

An example of the use of counterflow premixed flames for flame speed measurements is the work of Egolfopoulus et al. (1990). In this study, the investigators employed kinetic modeling to predict laminar flame speeds and compared their predictions to measurements taken in counterflow premixed flames at pressures from 0.25 to 3 atm. A robust examination of the accuracy of the counterflow premixed flame technique for making such flame-speed measurements was later presented by Chao et al. (1997). Many of the details required to obtain accurate computer modeling of this flow geometry are also given by Chao et al. (1997); further references for earlier flame-speed studies are provided as well.

Recently, Raman scattering techniques have been used to obtain temperature and concentration profiles in counterflow premixed flames. Law et al. (1994) studied the sensitivity of these profiles to variations in the strain rate for a series of atmospheric methane/air flames. An LDV system was used to obtain velocity profiles throughout the

flames and Raman scattering was used to measure temperature as well as concentrations of $N_2$, $O_2$, CO, $CO_2$, $H_2O$, and $CH_4$ in these flames. Modeling predictions were shown to agree quite well with the experimental results and were then used to show that the flame structure and thickness of these flames are insensitive to strain rate variations for near adiabatic conditions. This is primarily due to the ability of this flame configuration to adjust its location to offset changes in the cold flow strain rate. This behavior is in contrast to counterflow diffusion flames, which have been shown computationally to become thinner with increasing strain rate (Dixon-Lewis, 1990).

A follow-up investigation (Sun *et al.*, 1996) extended the previous study to different pressures, ranging from 0.6 to 5 atm. In addition to strain rate variations, the effect of pressure fluctuations on the structure of these counterflow premixed flames as well as on counterflow diffusion flames was studied. The insensitivity of the premixed flame structure to strain rate variations was again demonstrated while the flame thickness was shown to decrease with increasing pressure. In general, this work, which again utilized Raman scattering to determine major species concentration profiles, represents one of the first uses of laser diagnostics to obtain concentration information in high-pressure counterflow premixed flames. A final study by this group (Sung *et al.*, 1996) extended the atmospheric study to different fuels, propane and hydrogen, so as to investigate the effect of non-equidiffusivity on the above results. As might be expected, they found that the structure of non-equidiffusive flames are still mostly insensitive to any changes in strain rate.

There are a few additional studies worth noting here because of their examination of NO formation in counterflow flames. The first of these was a theoretical analysis of the effect of radiative heat loss on the formation of NO in high-pressure counterflow diffusion flames (Vranos and Hall, 1993). Although this study was for diffusion rather than premixed flames and contained no experimental data, it is worth mentioning here because it discusses strain rates and temperatures ($\sim 200$ s$^{-1}$ and 2400 K at 10.5 bar, respectively) at which radiative heat loss becomes important in modeling counterflow flames. This concept may need to be considered in opposed premixed flames as well. In another

study, Nishioka *et al.* (1996) used counterflow premixed flames as one of three geometries in their study of the behavior of three key elementary reactions controlling the formation of NO in methane-air flames. The primary thrust of their work was to demonstrate how emission characteristics are affected by flame geometry. The study further illustrates how a mechanism which works well for predicting NO formation in one configuration may not work well for another owing to changes in the importance of each of the NO formation pathways as a function of flame structure.

Finally, two more recent investigations deserve mention here for presenting the first experimental measurements of NO in flames with the counterflow geometry. Ravikrishna *et al.* (1998) used saturated LIF to measure NO concentrations in a series of atmospheric pressure, $C_2H_6/O_2/N_2$ counterflow diffusion flames. Though only a short communication, this work presented the first LIF measurements of NO in flames using the counterflow geometry. A similar work by Sick *et al.* (1998) presented planar LIF measurements of NO concentration in atmospheric $CH_4$/air counterflow diffusion flames. The main contribution of this work was a review of several key reactions for NO formation and destruction via prompt NO chemistry and a discussion of their relative uncertainties.

## 2.8 Summary

Laser-induced fluorescence has been proven to be an accurate, non-intrusive tool for measuring NO concentrations in high-pressure flame environments. However, as flame studies progress toward high-pressure, ultra-lean, premixed conditions found to be necessary for modern ultra-low $NO_x$ combustors, the problem of $O_2$ interferences for LIF measurements of NO becomes more pronounced. Fortunately, correction techniques have been developed which permit quantitative NO measurements in combustive environments at pressures up to 14.6 atm. Nevertheless, relatively few studies have measured ambient NO concentrations in the 10 ppm range within high-pressure combustors.

Basic LIF theory has been summarized as well as the basic kinetics important for NO formation in lean premixed flames. All three traditional NO-forming pathways, (Zeldovich, prompt, and $N_2O$ intermediate) were found to be important for lean premixed combustion. Some disagreement was found to exist in the exact mechanism responsible for prompt NO formation. In addition, a fourth NO pathway involving the NNH radical could prove to be important in predicting NO concentrations in low-$NO_x$ advanced gas turbines.

Finally, the utility of counterflow premixed flames was examined for combustion studies. It was found that this configuration has gained much attention for determining laminar flame speeds and extinction limits of premixed mixtures. In addition, the structure of these flames and their response to variations in strain rate have been studied. However, to date, there have been no high-pressure measurements of minor species concentrations within these types of flames.

# 3. EXPERIMENTAL APPARATUS AND COMPUTER MODELING

## 3.1 Introduction

The goal of reducing $NO_x$ production in advanced gas turbine engines requires the formulation of an accurate, simplified modeling scheme for predicting NO formation in realistic flame environments. The development of such a scheme, in turn, depends on an accurate basis for comparison. This basis can be provided either by a more complex modeling scheme or by in-situ measurements of NO in realistic flame conditions. In reality, both of these are needed owing to the complexity of the physical process.

In this study, laser-induced fluorescence (LIF) is used to measure NO concentrations in high-pressure, premixed $CH_4/O_2/N_2$ flames. Previous work by Reisel and Laurendeau (1994a; 1995) and Thomsen (1996) demonstrated the ability of this technique to produce accurate ($\pm25\%$) NO concentration measurements in $C_2H_6/O_2/N_2$, $C_2H_4/O_2/N_2$, and $CH_4/O_2/N_2$ premixed flames at pressures from 1 to 14.6 atm. The current work not only compares some of these earlier measurements with newer modeling schemes, but also applies the LIF technique to measure NO concentration profiles in a series of counterflow, premixed $CH_4/O_2/N_2$ flames.

This chapter describes the experimental apparatus used for performing the above LIF measurements of NO. Descriptions are included of several improvements which have been made to the overall apparatus since the work of Thomsen (1996). The procedures and assumptions used in making the subsequent theoretical predictions of NO formation are also discussed.

## 3.2 Experimental Apparatus

For the present LIF measurements of NO, excitation is achieved through use of the $Q_2(26.5)$ line in the $\gamma(0,0)$ band ($\lambda \approx 225.6$ nm). Reasons for the selection of this transition are discussed elsewhere (Thomsen, 1996). The excitation wavelength is generated by employing the second harmonic ($\lambda = 532$ nm) of a Quanta-Ray DCR-3G Nd:YAG laser to pump a mixture of rhodamine 590 perchlorate and rhodamine 610 perchlorate dyes in a PDL-2 dye laser, producing laser radiation at ~572 nm. The output of the dye laser is frequency doubled ($\lambda \approx 286$ nm) in a Quanta-Ray Wavelength Extender (WEX -1), and the doubled-dye beam is mixed with the first harmonic of the Nd:YAG laser ($\lambda = 1064$ nm), producing radiation at $\lambda \approx 225.6$ nm. The various collinear beams (with wavelengths of 1064, 572, 532, 286, and 225.6 nm) are then dispersed using a Pellin-Broca prism. The desired beam ($\lambda \approx 225.6$ nm) is subsequently raised with a prism assembly and directed out of the WEX. The maximum mixed beam energy at this point is ~3 mJ/pulse.

A diagram of the experimental apparatus is shown in Figure 3.1. One improvement to the current facility involves the incorporation of a wavelength locking system utilizing the approach reported by Cooper and Laurendeau (1997). Before being dumped into the side of the WEX, a portion of the residual dye beam ($\lambda \approx 572$ nm) is split and reflected into an optical chain near the laser system. A focussing lens is used to provide a converging beam which is passed through an air-spaced Fabry-Perot etalon (FSR, 1 cm$^{-1}$; finesse, 20). The etalon has the net effect of creating a ring pattern which changes diameter as a function of wavelength. This ring pattern is then imaged onto a Hamamatsu linear image sensor (N-MOS Model S3903-1024Q) containing 1024 photodiodes, each with an area of 25 $\mu$m $\times$ 0.5 mm. As described by Cooper and Laurendeau (1997), "the sensor is mounted on a Hamamatsu C4070 driver-amplifier circuit with master clock pulses supplied by a C4091 pulse generator and master start pulses supplied by a synchronized output from the Nd:YAG laser. The master start pulse interval corresponds to the signal exposure time, whereas the master clock pulse determines the rate at which the linear array is scanned. The accumulated electrical charge is stored by the capacitance of the photodiode junction and read out sequentially through
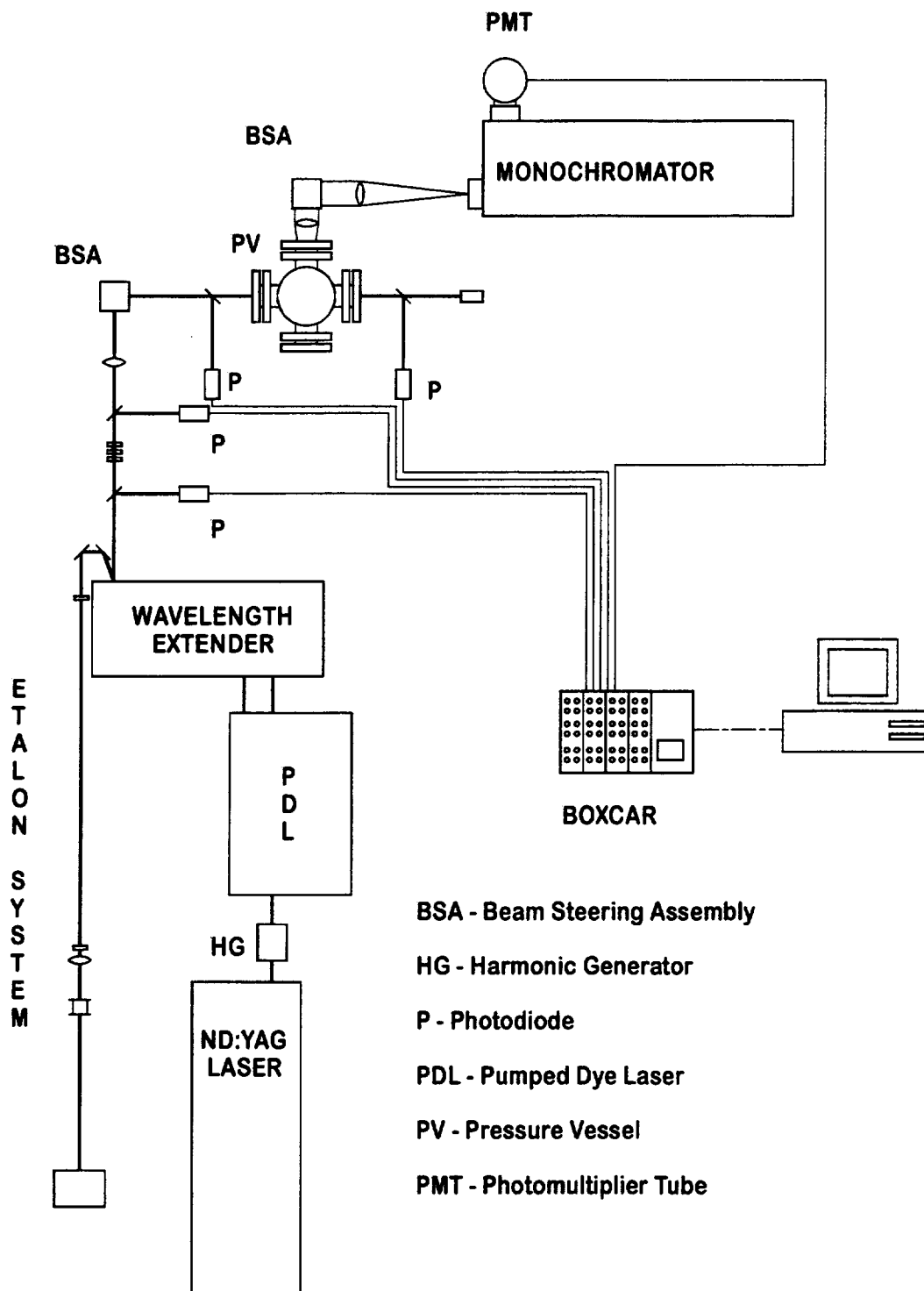
Figure 3.1: Schematic diagram of experimental apparatus.

an N-MOS field-effect transistor to an external circuit. Hence each image recorded by the linear image sensor represents only one pulse from the laser system. The electronic components are all housed and mounted on an X-Z translation stage to permit alignment of the linear sensor with a major diameter of the circular fringe patterns produced by the Fabry-Perot etalon." Compared to the seeded Nd:YAG laser of Cooper and Laurendeau (1997), our unseeded laser produces a less distinct fringe pattern with wider peaks and higher background. The resulting ring pattern is analyzed using Labview software and facilitates the implementation of a wavelength locking system that can effectively lock the excitation wavelength to within .0002 nm of the NO peak for the duration of the experiment. This system also allows for similar resolution in wavelength determination for application to excitation scans.

After leaving the WEX, the UV beam passes through the first of four fused silica plates which split portions of the beam onto UV-sensitive photodiodes (Thor Labs DET200 photodetector). The first of these photodiodes is used to provide a triggering pulse for the electronic equipment. The beam next passes through a series of neutral density filters which allow for attenuation of the laser beam as necessary to achieve linear excitation of the NO transition. Alternately, the laser power could be reduced by lowering the Nd:YAG power settings. However, because of thermal lensing effects in the YAG rod, a reduction in the laser power at this point can alter the focal point location and size of the optical system. Another technique is to slightly defocus the WEX mixing crystals. This would indeed provide a sensitive method of reducing laser power; however, thermal shifts during the course of the experiment can cause the effective mixing efficiency of the WEX crystals to change, thus requiring frequent repeaking. Utilizing an off-peak crystal angle accentuates this problem and causes much greater fluctuations of laser power during the course of an experiment. The linear range of these LIF measurements was determined experimentally and for the optical setup used in this thesis was found to be: 0.4 mW at 1.00 atm, 0.7 mW at 2.02 atm, 1.0 mW at 3.04 atm, 1.3 mW at 4.06 atm, and 1.6 mW at 5.08 atm.

Following the neutral density filters, a second beam-splitter/photodiode assembly is employed to monitor the beam energy, which is required for normalization of the fluorescence signal. The beam is then focused with a 600-mm focal length lens (CVI Laser Corporation, PLCX-25.4-309.1-UV), resulting in an ~250 μm spot size over the burner. Another improvement to the current system is provided by the third beam-splitter/photodiode assembly. A 50-μm pinhole is positioned at the entrance of the photodiode assembly and located at the same optical distance along the UV beam as the probe volume within the high-pressure assembly. The resulting photodiode voltage has been found to be much more sensitive to laser position than the actual LIF signal and provides for a convenient and reliable method of ensuring, throughout the experiment, that the excitation beam is precisely located in the center of the probe volume.

The burner is located inside the high-pressure combustion facility described by Carter *et al.* (1989). The pressure vessel has four optical ports, two of which provide the optical access for the laser beam through the combustion facility. A two-mirror beam steering assembly is used to raise and direct the main beam through the center of the optical ports and thus over the burner. After leaving the vessel, the fourth beam-splitter/photodiode assembly is employed to monitor the power of the laser for purposes of zeroing the burner position relative to the laser beam. The remainder of the beam is then directed to a beam dump.

For fluorescence detection, we make use of an optical port perpendicular to the laser entrance and exit ports. A 254-mm focal-length fused silica lens (CVI Laser Corporation PLCX-50.8-130.8-UV) is used to collimate the fluorescence. A mirror assembly then raises and rotates the fluorescence by 90°. The fluorescence is next focused by a 400-mm focal-length fused silica lens (CVI Laser Corporation PLCX-50.8-206.0-UV) onto the entrance slit of a 1-m monochromator (SPEX 1000M). The detector is a Hamamatsu R106UHHA photomultiplier tube specially wired for temporal resolution of the fluorescence signal (Harris et al., 1976).

For these linear LIF measurements, the entrance slit width of the 1-m monochromator is set at 1 mm and the entrance slit height is set at 2.0 mm. With a

magnification of 1.6 in the collection optics, the image of the entrance slit over the burner is thus 0.625 mm × 1.25 mm. Hence, the image of the entrance slit is much larger than the width of the beam (250 μm) and the beam width thus defines the actual probe-volume dimensions of 0.25 mm × 1.25 mm.

The exit slit on the 1-m monochromator is set at 3 mm. Thus, the broadband fluorescence signal encompasses a spectral width of ~2.4 nm detected over a spectral region centered at ~236.8 nm. This location and spectral width correspond to the $\gamma(0,1)$ band of NO. Reasons for the selection of this band are discussed in detail by Thomsen (1996). Three SR250 gated integrators are used to capture the signals from the photomultiplier tube, the laser-power photodiode and the pinhole photodiode. In each case, the signal is averaged over a 20-ns gate. The output voltages from these gated integrators are digitized and stored with the SR245 computer interface module and a Labview software package, respectively. Each data point is averaged over 600 laser shots.

Two different burners are utilized in this study. The first burner is a 2.5-cm diameter, water-cooled, sintered-bronze McKenna flat-flame burner. This burner produces laminar, one-dimensional, premixed, flat, burner-stabilized flames over a wide range of equivalence ratios and pressures. Unfortunately, the flames produced by this burner are limited, by its relatively cool boundary condition, to equivalence ratios higher than those found in the typically preheated, high-pressure combustors used in gas turbines. Moreover, from an experimental standpoint, it is impossible to obtain measurements through the flamefront using this burner owing to the close proximity of the flame to the burner's surface. In an attempt to circumvent these limitations, a 1-cm diameter, counterflow burner has been designed, built, tested and used for the remainder of the work in this report. Descriptions of the burner's design, performance characteristics and limitations are included in Chapters 5 and 6.

Mass flow controllers are used for gas delivery to both burners. Calibration of these mass flow controllers was performed using a dry-test volumetric flowmeter and a bubble meter. A closed-loop water cooling system was used for both burners as well.

This system allowed variation of the cooling water temperature and inlet pressure as well as providing for automatic fuel-delivery shut down in case of coolant failure.

Temperature measurements were obtained through the use of an uncoated Pt-Pt/10%Rh thermocouple (bead diameter ~0.2 mm, wire diameter ~.08 mm). The measurements were corrected for radiative heat loss by using the procedures found in Bradley and Matthews (1968). The calculated precision and accuracy (95% confidence level) for these measurements at typical flame temperatures are ±30 K and ±75 K, respectively.

## 3.3 Chemical Kinetic Modeling

The majority of the experimental flames in this study were investigated through computer modeling. The modeling of the chemical kinetics for the McKenna-burner flames was performed using the Sandia, steady, laminar, one-dimensional, premixed flame code (Kee et al., 1985). Similarly, modeling for the counterflow-burner flames was performed using the Sandia, opposed-flow, diffusion flame code (OPPDIF) (Lutz et al., 1996). Both of these fortran programs solve the species conservation equations, thus providing the concentration of each species under consideration, as well as the density of the combustion products and the flow velocity, as a function of height above the burner. Solutions can be obtained either with a user-specified temperature profile or with a temperature profile generated by solution of the energy equation, considering conductive heat loss to the burner but not radiative heat loss. The programs use Newton's method and time-stepping procedures to solve the boundary value problem. In addition, the CHEMKIN-II computer program library (Kee et al., 1989) was used to process the reaction mechanism into a form that is appropriate for use by the Sandia flame code. A burner surface temperature of 300 K was used for all the modeling in this study.

An important limitation of OPPDIF is that it does not consider the effects of radiation heat loss. To account for such effects on the temperature and NO predictive capabilities of the code, a radiation subroutine developed by Gore and coworkers (1999)

was incorporated into the energy equation within the OPPDIF code. This routine, which assumes optically thin radiation originating from the major species within the flame, has previously been shown to have a significant impact on NO concentration predictions in lower strain rate counterflow diffusion flames (Gore *et al.*, 1999; Ravikrishna and Laurendeau, 1999).

The first mechanism used as the chemical kinetics input into the computer model is based on the comprehensive reaction mechanism assembled by Glarborg et al. (1986), as modified by Drake and Blint (1991). For simplicity, this kinetic mechanism will be referenced as GMK-DB in the remainder of this report. The GMK-DB mechanism considers 49 species and over 200 chemical reactions. Drake and Blint (1991) adopted most of the reaction mechanism from Glarborg et al. (1986); however, they made a few modifications. These include the introduction of pressure dependency into four unimolecular reactions, the addition of a $C_3H_8$ reaction mechanism, and the introduction of rate parameters for $CH + N_2 \Leftrightarrow HCN + N$ based on measurements in a high temperature shock tube (Dean et al., 1988). The rate parameters for the unimolecular reactions at pressures of 3.05, 6.1, and 9.15 atm are given by Drake et al. (1990). The rate parameters at 11.9 atm and 14.6 atm were obtained from Drake and Blint (1992). A table of these modified rate parameters for the pressures modeled in this study can be found in Reisel (1994). This reference also includes a thorough discussion of the procedures required to obtain modeling solutions with the Sandia, laminar, one-dimensional flame code. The complete GMK-DB mechanism is included in Appendix A. The thermodynamic and transport properties, required by the Sandia flame code for calculation of the species concentration profiles, were provided by a thermodynamic property data base (Kee et al., 1987) and a transport property data base (Kee et al., 1986).

The second mechanism used as the chemical kinetics input into the computer model is the Gas Research Institute's comprehensive reaction mechanism, version 2.11, as assembled by Bowman et al. (1995). This kinetic mechanism will be referenced as GRI in the remainder of this report. The GRI mechanism considers 49 species and 277 chemical reactions and was optimized for natural gas combustion. A complete listing of these

reactions is included in Appendix B. The thermodynamic and transport properties, required by the Sandia flame code for calculation of the species concentration profiles, were provided with the mechanism and used without modification.

Various Sun, HP, and IBM workstations as well as Pentium-based personal computers were used in this modeling study. Test cases demonstrated that these machines provided nearly identical results. Hence, the type of platform used for each prediction will not be explicitly stated within this report.

## 3.4 Summary

In this chapter, the experimental apparatus used for obtaining high-pressure LIF measurements of NO has been described. In addition, the chemical kinetic mechanisms and the NO modeling procedures used in this study have been discussed. The modeling and experimental measurements provide a useful combination for evaluating the accuracy of current chemical kinetic models for the prediction of NO in flat, laminar, high-pressure, premixed $CH_4/O_2/N_2$ flames.

## 4. KINETIC MODELING OF HIGH-PRESSURE FLAT FLAMES

### 4.1 Introduction

Nitric oxide (NO) is an atmospheric pollutant that has been tied to both the destruction of the ozone layer and to the creation of photochemical smog. Because of these effects, current government emission standards have mandated that advanced gas turbines produce low $NO_x$ levels (<10 ppm @ 15% $O_2$, as corrected through the addition of dilution air). Since $NO_x$ production by nonpremixed combustion generates $\geq 100$ ppm (@ 15% $O_2$) for non-nitrogen bound fuels (Correa, 1992), the goal of lower $NO_x$ emissions will require partially or fully premixed combustion. Lean, premixed combustion reduces thermal $NO_x$ by preventing the creation of high-temperature stoichiometric interfaces. However, $NO_x$ emissions are also intimately and inversely coupled to those of CO and unburned hydrocarbons (UHC). These restrictions result in a set of competing goals: the increase in pressure and temperature required to improve efficiency results in more $NO_x$, while leaning the mixture to reduce $NO_x$ results in operation nearer the weak limit with a corresponding increase in CO. Hence, a more thorough understanding is needed of the chemical kinetics of pollutant formation in lean, premixed combustion. Of particular interest is the development of a simplified, high-pressure $NO_x$ model capable of predicting NO formation for practical gas turbine conditions. To achieve this goal, a complete understanding is needed of the chemical kinetics involved in the production of NO at high pressure. This knowledge, in turn, requires accurate *in situ* measurements of NO concentration to verify any proposed kinetic modeling scheme.

As indicated above, the goal of reducing nitric oxide production in advanced gas-turbine engines depends on the development of a kinetic model to accurately predict the formation of NO and other pollutants in lean, high-pressure premixed flames. Many

detailed kinetic schemes have been proposed (Glarborg *et al.*, 1986; Miller and Bowman, 1989; Drake and Blint, 1991; Bowman *et al.* 1995). Unfortunately, the overall accuracy of these complex reaction mechanisms with respect to predicting NO formation in high-pressure, high-temperature flames is still uncertain. Most of the relevant chemical kinetics models have been developed using low-pressure measurements and thus their applicability to high-pressure flames remains unclear. Previous work by Reisel and Laurendeau (1994a;1995) has shown that modeling using the Sandia, steady, laminar, one-dimensional, premixed flame code (Kee *et al.*, 1985), in conjunction with the Glarborg-Miller-Kee reaction mechanism (1986) as modified by Drake and Blint (1991) (GMK-DB), predicts at least qualitative trends of NO formation in high-pressure flames fairly well for $C_2H_6/O_2/N_2$ and $C_2H_4/O_2/N_2$ premixed flames at pressures up to 14.6 atm. Klassen *et al.* (1995) extended the above work to high-pressure premixed $CH_4/O_2/N_2$ flames. They found that the GMK-DB model produced similar trends to the experimental data but greatly overpredicted temperatures and NO concentrations at higher pressures. In addition, this model tended to underpredict NO formation under the ultra-lean conditions ($0.5 \leq \phi \leq 0.8$) of most practical interest.

In response to the obvious limitations of the GMK-DB and other early comprehensive mechanisms, an elementary reaction mechanism is being developed for methane-air combustion calculations by the Gas Research Institute (Bowman *et al.*, 1995). The purpose of this chapter is to analyze the ability of the current version of this mechanism (GRI Mech vs 2.11) to predict NO formation in high-pressure $CH_4/O_2/N_2$ flames. Modeling using the Sandia premixed flame code (Kee *et al.*, 1985) is compared to LIF measurements of NO in the post-flame zone of a variety of lean, premixed, high-pressure $CH_4/O_2/N_2$ flames. The performance of this new mechanism is then analyzed and compared to the older GMK-DB mechanism. The strengths of the new mechanism are then discussed, as well as areas for future improvements.

FROM LASER
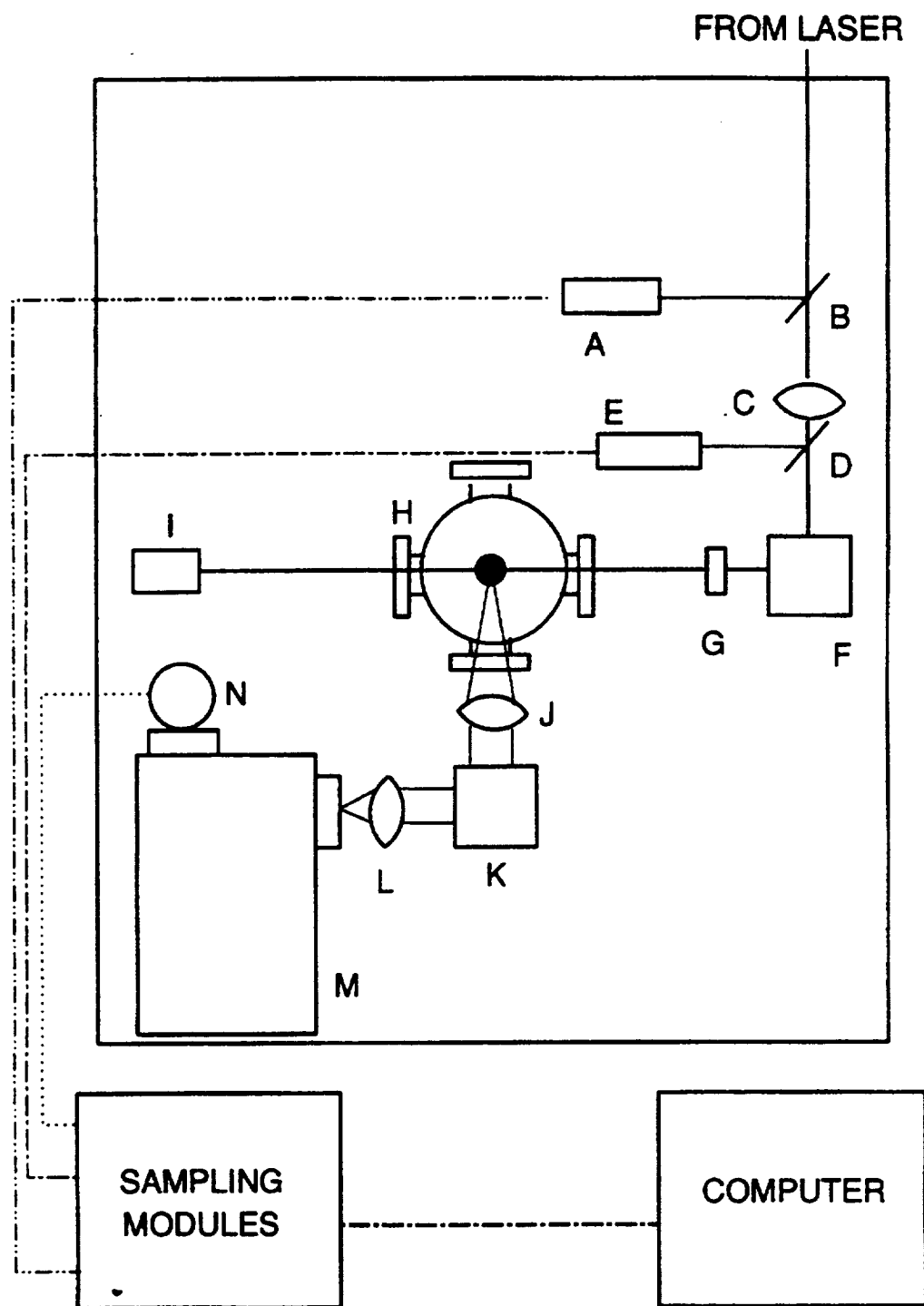


Figure 4.1: Schematic diagram of experimental apparatus: A- trigger photodiode; B,D- beam-splitter; C- 1000-mm focal-length lens; E- power-monitoring photodiode; F,K- beam steering assembly; G- aperture; H- pressure vessel; I- beam dump; J- 200-mm focal length lens; L- 300-mm focal-length lens; M- 1/2 m monochromator; N- PMT.

## 4.2 Experimental Techniques

The laser system and optical layout used in performing the LIF measurements of NO (Fig. 4.1) are described elsewhere (Reisel *et al.*, 1993); however, the most relevant points are repeated here. Excitation of NO is achieved through use of the $Q_2(26.5)$ line in the $\gamma(0,0)$ band. The $Q_2(26.5)$ line was chosen because (1) its Boltzmann fraction is insensitive to temperature variations over the range of temperatures of our flames, and (2) interferences from other species, such as $O_2$, are minimized (Partridge *et al.*, 1996). The excitation wavelength is generated by employing the second harmonic ($\lambda = 532$ nm) of a Quanta-Ray DCR-3G Nd:YAG laser to pump a PDL-2 dye laser, which produces laser radiation at ~572 nm. The output of the dye laser is frequency doubled in a Quanta-Ray Wavelength Extender (WEX -1), and the doubled-dye beam is mixed with the first harmonic of the Nd:YAG laser, producing ~1 mJ/pulse at 225.5 nm. The resulting minimum NO detectability limit is estimated to be ~1 ppm.

After leaving the laser system, the beam is directed over a 2.5-cm diameter, water-cooled, sintered-bronze McKenna flat-flame burner. The burner is located inside the high-pressure combustion facility described by Carter *et al.* (1989). The pressure vessel has four optical ports, two of which provide optical access for the laser beam through the combustion facility. The spot size produced by the optical arrangement is ~250 μm. Before entering the vessel, the beam passes through a fused silica plate which directs a portion of the beam toward a UV-sensitive photodiode. This photodiode is employed to monitor the beam energy, which is required for normalization of the fluorescence signal.

For fluorescence detection, we make use of an optical port perpendicular to the laser entrance and exit ports. The fluorescence is focused on the entrance slit of a ½-m monochromator. The detector is an RCA 1P28B photomultiplier tube specially wired for temporal resolution of the fluorescence signal (Harris *et al.*, 1976). The broadband fluorescence signal encompasses a spectral width of ~3 nm and is detected over a spectral region centered at ~236 nm. This location and spectral width correspond to the $\gamma(0,1)$ band of NO. Excitation and fluorescence scans verify that this spectral region is free of major interferences from species other than NO. To account for pressure shifting of the

$Q_2(26.5)$ absorption line, the laser and collection optics are tuned for the maximum NO fluorescence signal at each pressure. A 500-ps window at the peak of the fluorescence pulse is sampled using a Stanford Research Systems SR255 fast sampler. The image of the entrance slit over the burner is 80 $\mu$m $\times$ 6.67 mm. Each data point is averaged over 600 laser shots.

When performing linear LIF measurements, one must be concerned with the effects of both laser power fluctuations and quenching variations on the fluorescence signal. Corrections for laser power fluctuations can be made by normalizing the fluorescence signal using the measured laser power. Quenching variations could be handled in a similar manner; however, measurement of the quenching rate coefficient is not a trivial task. Comparisons of measurements obtained using both LIF and laser-saturated fluorescence (LSF) in the present $CH_4/O_2/N_2$ flames at atmospheric pressure demonstrate that quenching variations for our flame conditions are not significant at constant pressure. In addition, Klassen et al. (1995) modeled the NO quenching rate coefficient and found that it varied by less than 15% over the range of equivalence ratios of interest in this study.

Since the quenching environment is fairly insensitive to changes in stoichiometry at a given pressure, the ratio of linear fluorescence signals for any two flames at the same pressure should give approximately the ratio of NO number densities. On this basis, the fluorescence signals at a given pressure were calibrated by doping different levels of NO in a $\phi = 0.8$ flame and measuring the fluorescence voltage produced in the burnt-gas region (Reisel and Laurendeau, 1994a). The data from the various doping conditions were used to obtain a linear calibration plot which could then be applied to the calibration ($\phi = 0.8$) flame. The fluorescence signal for other flames at a given pressure could subsequently be compared to that of the calibration flame to obtain quantitative NO number densities. We assumed that the doped NO does not react as it passes through the flame; this assumption is supported both by computer modeling and by the linearity of the calibration plots.

The influence of non-NO interferences must also be accounted for in LIF measurements of NO. Although the selection of the $Q_2(26.5)$ transition minimizes these

interferences (Partridge *et al.*, 1996), they remain significant at high pressure. A technique developed in our laboratory (Thomsen *et al.*, 1997) was used to calculate and correct for these interferences for all of the LIF measurements presented in this chapter. A more careful application of this correction technique accounts for the small differences between the data presented here and those reported by Klassen *et al.* (1995).

## 4.3 Modeling Methodology

The modeling of the chemical kinetics was performed using the Sandia, steady, laminar, one-dimensional, premixed flame code (Kee *et al.*, 1985). In addition, the CHEMKIN-II computer program library (Kee *et al.*, 1989) was used to process the reaction mechanism into a form which is appropriate for use by the Sandia flame code. A burner surface temperature of 300 K was used as a boundary condition for the modeling. Well-resolved, experimentally measured temperature profiles are not easily obtained at high pressures owing to the close proximity of the flame front to the burner surface. Thus, a temperature profile generated via solution of the energy equation was used for the modeling cases presented in this study.

The first mechanism used as the chemical kinetics input into the computer model is based on the comprehensive mechanism assembled by Glarborg *et al.* (1986) as modified by Drake and Blint (1991). For simplicity, this mechanism will be referenced as GMK-DB. This elementary reaction mechanism considers 49 species and over 200 chemical reactions. Drake and Blint (1991) adopted most of the reaction mechanism from Glarborg *et al.* (1986); however, they made a few modifications. These include the introduction of pressure dependency into four unimolecular reactions, the addition of a $C_3H_8$ reaction mechanism, and the introduction of rate parameters for the reaction
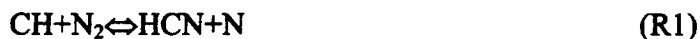
$$CH+N_2 \Leftrightarrow HCN+N \tag{R1}$$

based on measurements in a high temperature shock tube (Dean *et al.*, 1988). The rate parameters for the unimolecular reactions at pressures of 3.05, 6.1, and 9.15 atm are given by Drake *et al.* (1990). The rate parameters at 11.9 atm and 14.6 atm were obtained from

Drake and Blint (1992). For this mechanism, the thermodynamic and transport properties, required by the Sandia flame code for calculation of the species concentration profiles, were provided by a thermodynamic property data base (Kee *et al.*, 1987) and a transport property data base (Kee *et al.*, 1986).

The second comprehensive mechanism used in the modeling is the GRI mechanism, version 2.11 (Bowman *et al*, 1995). This mechanism considers 49 species and 277 reactions and was used without modification. For this elementary mechanism, we employed the thermodynamic and transport property files provided with the mechanism.

## 4.4 Results And Discussion

Using the experimental techniques discussed above, quantitative LIF measurements of NO were obtained in flat, laminar $CH_4/O_2/N_2$ flames at pressures ranging from 1 to 14.6 atm. Flames with a $N_2/O_2$ dilution ratio (D.R.) of 2.2 were investigated so as to obtain stable flames at $\phi < 0.6$. The total flow rates were held constant at each pressure and dilution ratio, and were as follows: 3.50 slpm (1 atm), 6.20 slpm (3.05 atm), 9.1 slpm (6.1 atm), 10.95 slpm (9.15 atm), 12.75 slpm (11.9 atm), 14.5 slpm (14.6 atm). The temperatures in the post-flame region of these flames, as measured with radiation-corrected Pt-Pt/10%Rh thermocouples, ranged from 1710 to 1880 K. Table 4.1 presents these measured temperatures for selected flames with a dilution ratio of 2.2.

Modeling predictions for temperature in these same flames were obtained via solution of the energy equation within the Sandia, steady, laminar, one-dimensional, premixed flame code (Kee *et al.*, 1985) in conjunction with the GRI mechanism, version 2.11. The results, presented in Table 4.2, show remarkable agreement with the measured temperatures of Table 4.1. This agreement can be seen more clearly in a plot of the results shown in Figure 4.2. As Fig. 4.2 demonstrates, the predicted post-flame zone temperature is within 40 K of the corresponding thermocouple measurement for all of the flames studied, which is clearly within the accuracy of the thermocouple measurements. Since it is impossible to obtain accurate, spatially resolved temperature measurements through the

Table 4.1: Radiation-corrected thermocouple measurements (K) in the post-flame zone of selected $CH_4/O_2/N_2$ flames with a dilution ratio of 2.2. The precision is $\pm 30$ K and the accuracy is $\pm 75$ K (95% confidence level). All high-pressure measurements were taken 3 mm above the burner surface; atmospheric measurements were taken 7 mm above the burner surface.

| $\phi$ | P | | | (atm) | | |
|---|---|---|---|---|---|---|
| | 1.00 | 3.05 | 6.10 | 9.15 | 11.9 | 14.6 |
| 0.50 | 1710 | 1760 | 1780 | 1790 | 1800 | 1800 |
| 0.55 | 1730 | 1770 | 1800 | 1810 | 1820 | 1830 |
| 0.60 | 1750 | 1790 | 1810 | 1820 | 1830 | 1840 |
| 0.65 | 1770 | 1810 | 1820 | 1830 | 1840 | 1850 |
| 0.70 | 1790 | 1820 | 1840 | 1840 | 1850 | 1850 |
| 0.75 | 1810 | 1840 | 1860 | 1850 | 1860 | 1860 |
| 0.80 | 1840 | 1860 | 1880 | 1870 | 1870 | 1880 |

Table 4.2:   Predicted post-flame zone temperatures of selected $CH_4/O_2/N_2$ flames with a dilution ratio of 2.2. Modeling employed the GRI mechanism (version 2.11) and the energy equation of the Sandia laminar, premixed flame code. All high-pressure predictions are for 3 mm above the burner surface; atmospheric predictions are for 7 mm above the burner surface.

| $\phi$ | P | (atm) | | | | |
|---|---|---|---|---|---|---|
| | 1.00 | 3.05 | 6.10 | 9.15 | 11.9 | 14.6 |
| 0.50 | 1712 | 1725 | 1749 | 1757 | 1768 | 1774 |
| 0.55 | 1733 | 1742 | 1765 | 1774 | 1786 | 1792 |
| 0.60 | 1751 | 1760 | 1783 | 1792 | 1805 | 1811 |
| 0.65 | 1773 | 1778 | 1800 | 1810 | 1824 | 1830 |
| 0.70 | 1796 | 1798 | 1819 | 1829 | 1843 | 1850 |
| 0.75 | 1822 | 1821 | 1840 | 1850 | 1865 | 1872 |
| 0.80 | 1851 | 1848 | 1867 | 1876 | 1889 | 1898 |
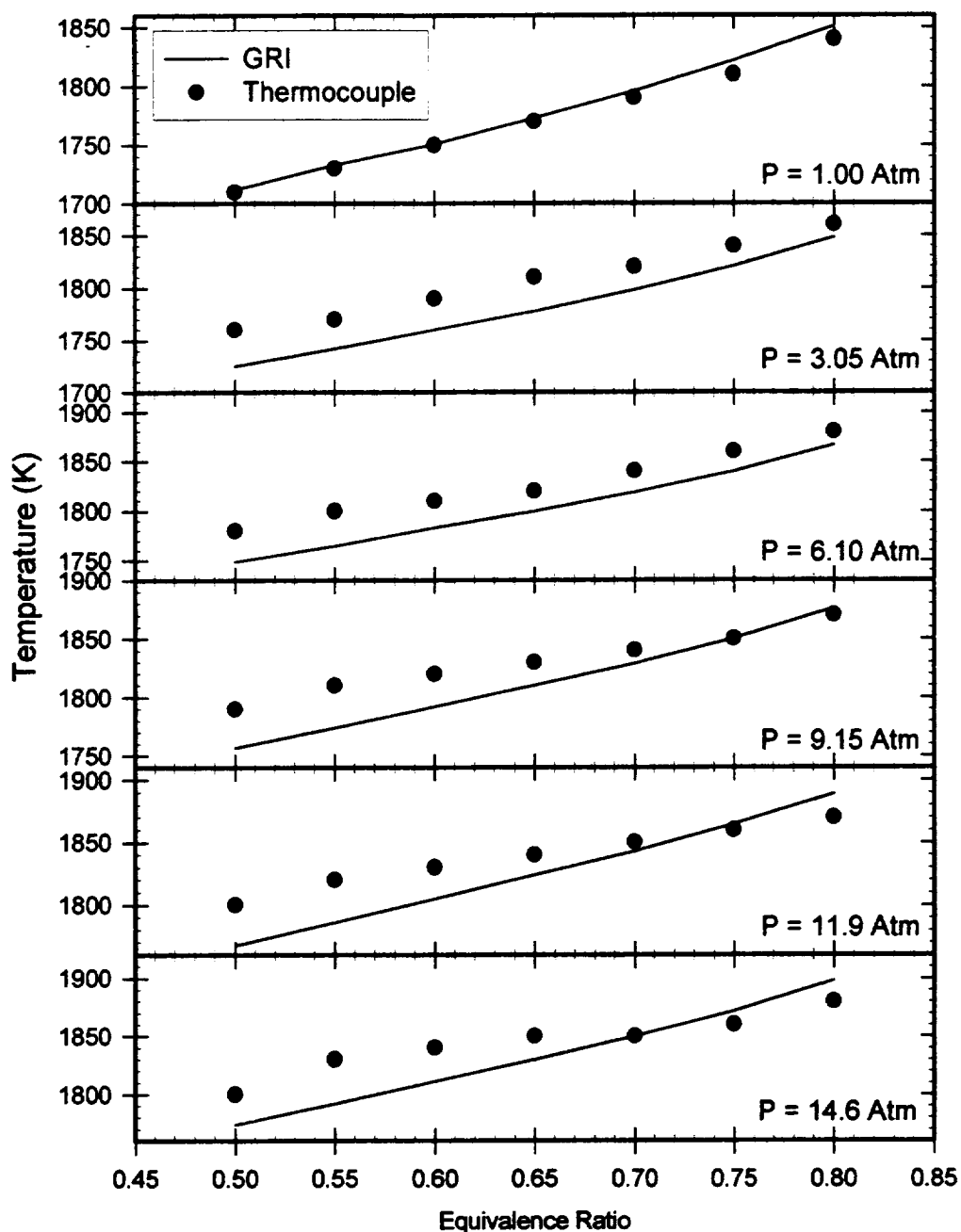
Figure 4.2: Comparison of temperature measurements using radiation-corrected thermocouples and temperatures predicted by solving the coupled species-energy equations using the GRI reaction mechanism (version 2.11) in the post-flame zone of selected $CH_4/O_2/N_2$ flames with a dilution ratio of 2.2. The precision is $\pm 30$ K and the accuracy is $\pm 75$ K (95% confidence level). All high-pressure measurements are taken 3 mm above the burner surface; atmospheric measurements are taken 7 mm above the burner surface.

flamefront of the high-pressure flames and because of the good post-flame zone agreement between the measured and predicted temperatures, it was decided that the energy-solution temperature profile provides the best possible condition for modeling the formation of NO in these flames.

This good temperature agreement is in stark contrast to the findings of Klassen *et al.* (1995), who discovered that the use of the energy solution in conjunction with the GMK-DB mechanism greatly overpredicted the increase in temperature with pressure in these same flames. This temperature overprediction by an average of approximately 85 K in these high-pressure flames led to a corresponding overprediction of thermal NO, which impeded the ability of their study to fully analyze the capability of the GMK-DB mechanism with respect to NO predictions in these flames. Thus, to eliminate the effect of temperature overprediction for comparisons of the nitrogen kinetics of the two mechanisms, the GRI temperature profiles were used for all modeling cases in this study, including those using the GMK-DB mechanism.

Although good agreement has been shown between the post-flame zone temperature predictions and measurements, there is some concern that the slope of the temperature profile through the flame front could still affect the production of NO in this region. Reisel and Laurendeau (1994b) examined the effect of changing the burner surface temperature on modeling when using the GMK-DB mechanism and found that both the post-flame zone temperatures and NO concentrations were relatively unaffected by changes in surface temperature of up to 700 K. This result indicates that small variations in the flame location or temperature-profile slope should not drastically affect the ability of the code to predict NO formation in these water-cooled flames. Hence, we can proceed with some confidence in our comparison of the mechanism's performance using the predicted temperature profile.

Figures 4.3 and 4.4 present measurements of NO concentration in the post-flame region of the selected premixed flames as a function of equivalence ratio. Also shown on these plots are the NO concentrations predicted by both the GRI mechanism and the GMK-DB mechanism when using temperature profiles generated by the GRI mechanism.
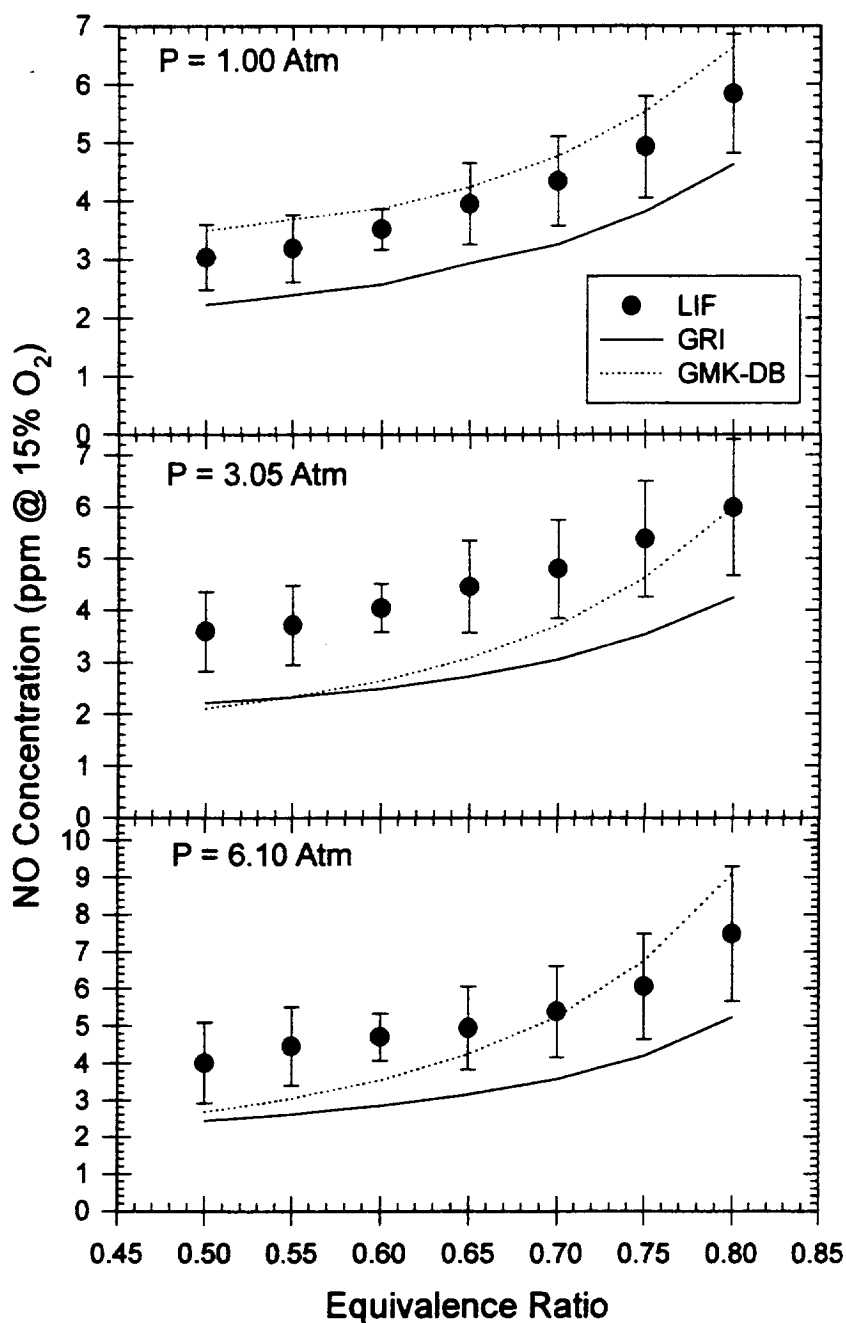
Figure 4.3: LIF-measured and predicted NO concentrations in 2.2 dilution ratio
CH₄/O₂/N₂ flames at 1.00-6.10 atm. The high-pressure measurements were
taken at 3 mm above the burner surface, whereas the atmospheric
measurements were taken at 7 mm above the burner surface. Error bars are
shown for a 95% confidence level. Predictions were found using
temperatures predicted by the coupled species and energy equations using
the GRI mechanism in conjunction with both the GRI and GMK-DB kinetics.
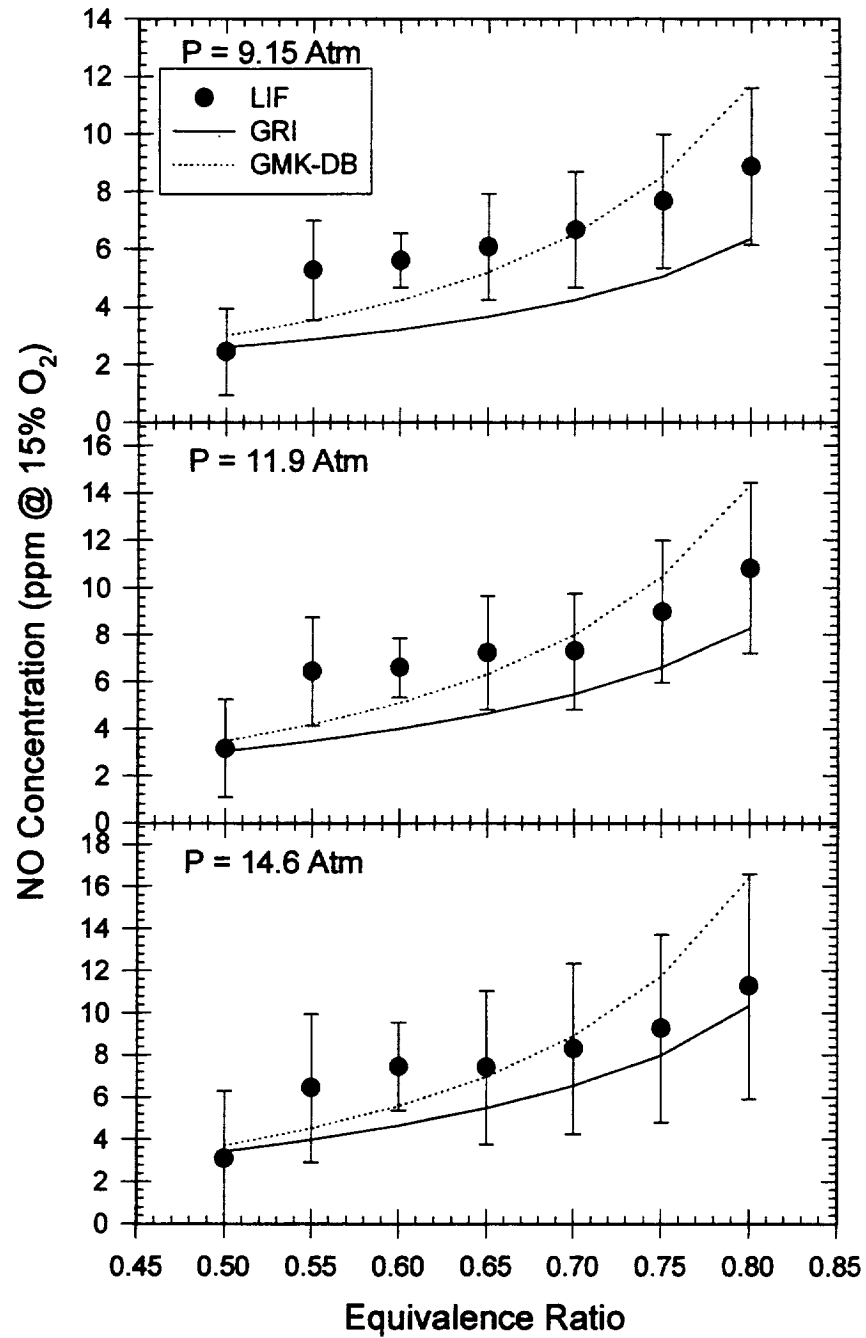
Figure 4.4: LIF-measured and predicted NO concentrations in 2.2 dilution ratio $CH_4/O_2/N_2$ flames at 9.15-14.6 atm. These measurements were taken at 3 mm above the burner surface. Error bars are shown for a 95% confidence level. Predictions were found using temperatures predicted by the coupled species and energy equations using the GRI mechanism in conjunction with both the GRI and GMK-DB kinetics.

Table 4.3:  Measured NO concentrations (ppm @ 15% $O_2$ wet) in the lean $CH_4/O_2/N_2$ flames with a dilution ratio of 2.2.

| φ | P (atm) | | | | | |
|---|---|---|---|---|---|---|
| | 1.00 | 3.05 | 6.10 | 9.15 | 11.9 | 14.6 |
| 0.50 | 3.0 | 3.6 | 4.0 | 2.4 | 3.1 | 3.1 |
| 0.55 | 3.2 | 3.7 | 4.5 | 5.3 | 6.4 | 6.4 |
| 0.60 | 3.5 | 4.0 | 4.7 | 5.6 | 6.6 | 7.4 |
| 0.65 | 3.9 | 4.5 | 4.9 | 6.1 | 7.2 | 7.4 |
| 0.70 | 4.3 | 4.8 | 5.4 | 6.7 | 7.3 | 8.3 |
| 0.75 | 4.9 | 5.4 | 6.1 | 7.7 | 9.0 | 9.2 |
| 0.80 | 5.8 | 6.0 | 7.5 | 8.9 | 10.8 | 11.3 |

The LIF measured NO concentrations are also listed in Table 4.3. To facilitate better comparison between the NO concentrations in these flames, the data have been converted to parts per million (ppm) at a constant product $O_2$ concentration of 15% (wet). This correction technique follows that suggested by Turns (1996). The uncorrected concentration in ppm is multiplied by a ratio of the total number of moles in the products divided by the total number of moles that would be present in the products given sufficient oxidizer, at the $N_2/O_2$ dilution ratio used in the experiments, to produce the desired $O_2$ concentration in the products assuming complete combustion.

One feature observable from Figures 4.3 and 4.4 is that the NO concentration increases with equivalence ratio in these lean flames. Both of the models capture this effect; however, the GMK-DB model seems to overpredict the magnitude of this increase at pressures greater than 1 atm. Thus, although the GMK-DB mechanism offers better quantitative predictions of NO formation over most of our conditions, there are obviously some problems with its NO formation chemistry in addition to its previously mentioned problems with respect to temperature predictions. By comparison, the GRI mechanism seems to capture the equivalence ratio trend well, but uniformly underpredicts the amount of NO formed by 30-50% in the majority of the flames studied.

The abrupt increase in NO formation from an equivalence ratio of $\phi$=0.50 to $\phi$=0.55 for the highest pressure flames (P ≥ 9.15 atm) is most likely due to the fact that the former flames are approaching their extinction limit and becoming less stable. This development causes the flat-flame assumption to no longer be valid and thus this behavior may be due to changes in flame configuration and temperature rather than to a legitimate drop in NO formation owing to stoichiometry alone. One final observation on Figures 4.3 and 4.4 is that while both models seem to accurately predict a small increase in NO concentration with pressure from 3.05 to 14.6 atm, they both predict a decrease in NO formation from 1.00 to 3.05 atm that is not observed in the experimental data although this decrease is not nearly as pronounced using the GRI mechanism as it is using the GMK-DB mechanism.
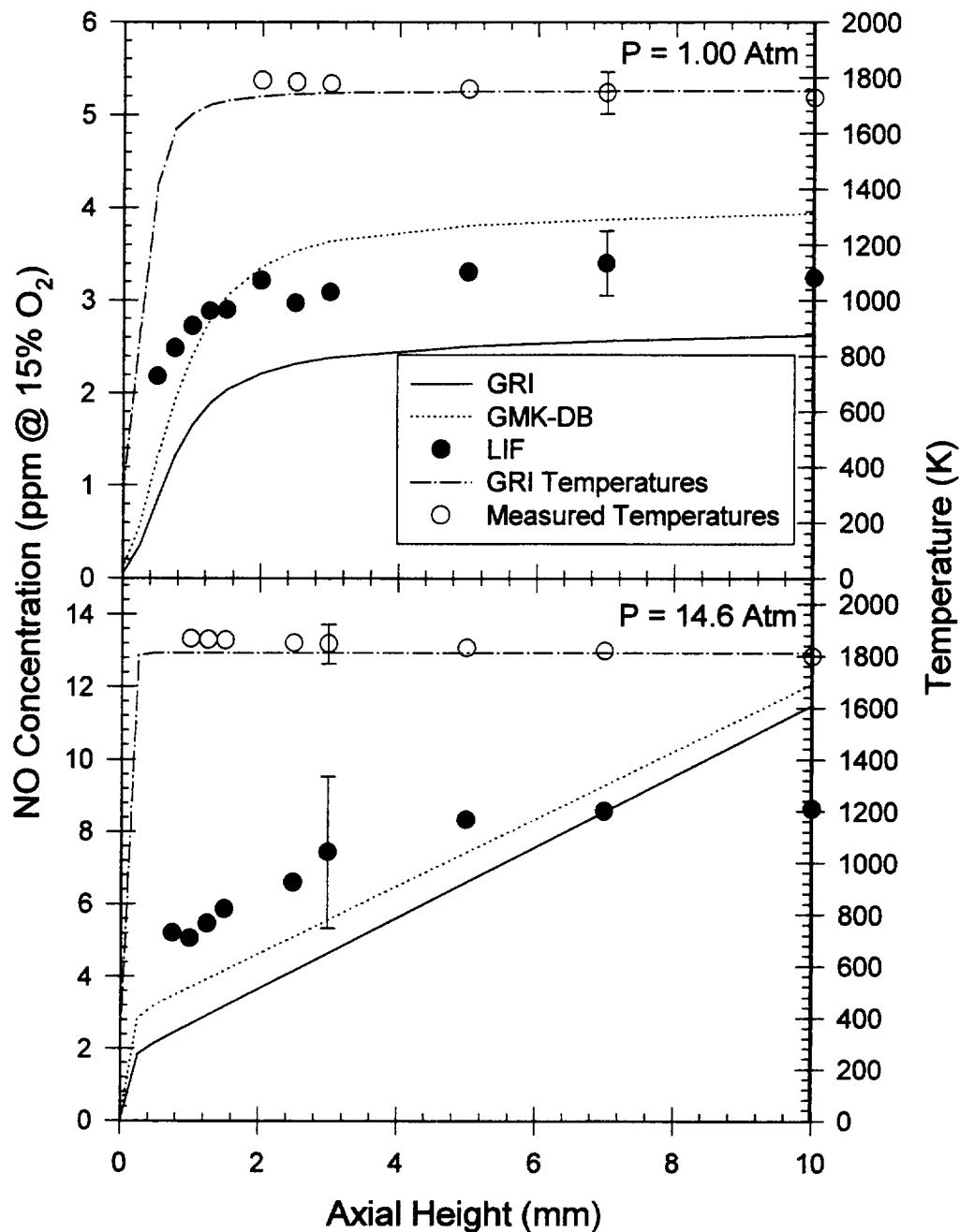
Figure 4.5: Axial profiles of NO concentration and temperature in premixed $CH_4/O_2/N_2$ flames ($\phi$=0.60) at pressures of 1.00 and 14.6 atm. The dilution ratio for both flames was 2.2. NO concentrations presented include both LIF-measured concentrations and predictions using the GRI and GMK-DB reaction mechanisms. Measured temperatures were obtained using radiation-corrected thermocouples. Modeled temperatures come from solution of the joint species and energy equations of the Sandia laminar, premixed flame code in conjunction with the GRI mechanism, version 2.11.

Further information about the modeling capabilities of the two mechanisms can be obtained by examining axial profiles of NO concentration and temperature in these flames. Figure 4.5 shows two such profiles for the $\phi$=0.60 flames at pressures of 1.00 and 14.6 atm. We first note that there is relatively little temperature drop in these flames as a function of height above the burner, which tends to validate our use of the energy-solution temperature profile and its corresponding neglection of radiation heat losses. Secondly, we note that in both the 1.00 and 14.6 atm cases, the slopes of the experimental axial profiles of NO very nearly match those of both the GRI and GMK-DB modeling predictions. This result indicates that the Zeldovich NO production rates, which are perhaps the most well-known kinetic rates in the NO formation process, are indeed correct for both of these mechanisms. This feature also underscores the validity of our temperature modeling scheme. By examining this slope we can also see that changes in the profile owing to radiation heat loss and/or diffusion of species from the guard flow do not become significant until beyond the region in the post-flame zone used for our equivalence ratio profile measurements (7 mm above the burner at 1 atm and 3 mm above the burner at higher pressures). This conclusion was also confirmed via radial profiles, which showed a flat temperature and concentration region in the center of these flames at all of the pressures studied.

Finally, we note that at both pressures the GRI mechanism underpredicts flamefront NO formation. This result is true not only for these two cases but for almost all of the cases studied. There are many possible explanations for this behavior. NO formation via the thermal and $N_2O$ intermediate routes enhanced by super-equilibrium concentrations of O and OH radicals play an important role in flamefront NO formation in lean flames (Drake et al., 1990; Corr et al., 1992), while the breakup of diatomic nitrogen by CH and other hydrocarbons contributes in lean and even more significantly in moderately rich flames (Drake et al., 1990). In addition, it has been proposed that another possible pathway involving the NNH radical could be responsible for flamefront NO formation (Bozzelli and Dean, 1995). Thus, it is not a trivial task to determine what changes need to be made to the GRI mechanism to account for this discrepancy. The

GMK-DB mechanism, on the other hand, seems to overpredict flamefront NO at 1 atm while underpredicting it at 14.6 atm. Returning to Figures 4.3 and 4.4, we again note the high-pressure behavior of the GMK-DB model; i.e., underpredicting NO formation in the leanest flames and then overpredicting the increase of NO formation with equivalence ratio. Since, as we have shown, Zeldovich post-flame NO formation appears to be accurately modeled in these flames, it is thus the behavior of flamefront NO formation that is responsible for these trends.

To further explore the possible reasons for this behavior by both mechanisms, we applied our same modeling procedure to predict NO concentrations in a variety of 3.1 dilution ratio ($N_2/O_2$), premixed, laminar, $CH_4/O_2/N_2$ flames with equivalence ratios ranging from 0.6 to 1.6. The results of this study are shown in Figure 4.6, where the experimental data are taken from Klassen $et\ al.$ (1995). This figure shows that the GMK-DB mechanism does a good job qualitatively of predicting the peak location of NO formation in these flames, but greatly overpredicts this peak value, whereas the GRI mechanism does a bad job qualitatively of predicting the peak location of NO formation in these flames and also underpredicts the peak value.

In measurements and modeling of a similar series of premixed $C_2H_6/O_2/N_2$ flames, Reisel and Laurendeau (1994a) found that the equivalence ratios corresponding to peak NO formation in moderately rich flames coincided with those displaying the highest amount of CH. This led them to the conclusion that NO formation via CH attack on $N_2$ dominated in these flames. The fact that the GMK-DB mechanism accurately predicts this qualitative behavior but overpredicts the magnitude of the effect suggests that perhaps the rate coefficient for Reaction (R1) is too high in this mechanism, but that this route should still dominate NO formation in these flames. Similarly, the failure of the GRI mechanism to capture this qualitative behavior indicates that perhaps its coefficient for this reaction is too low. Both may be the case since at reasonable flame temperatures the rate coefficients used for this reaction differ between the two mechanisms by almost a factor of 10. Recent work by Berg $et\ al.$ (1998) concludes that the rate coefficient for Reaction (R1) used in the GRI mechanism must be increased by a factor of between 2.1 and 2.8 in order to
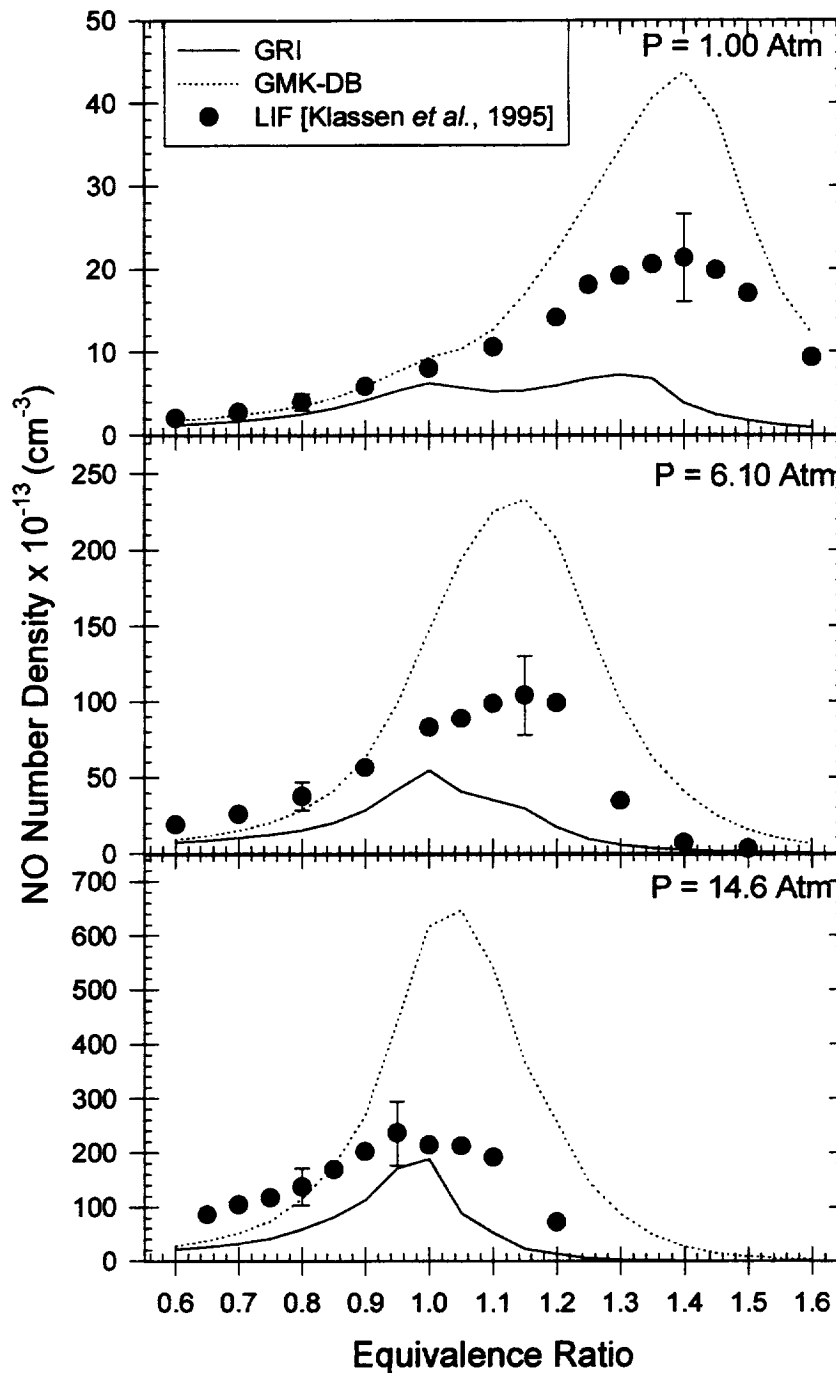
Figure 4.6: Comparison of LIF measurements of NO (Klassen *et al.*, 1995) and predicted NO concentrations in 3.1 dilution ratio $CH_4/O_2/N_2$ flames. The high-pressure measurements were taken at 3 mm above the burner surface while the atmospheric measurements were taken 7 mm above the burner surface. Predictions were found using temperatures predicted by the coupled species and energy equations using the GRI mechanism in conjunction with both the GRI and GMK-DB kinetics.

match their measurements in a series of low-pressure methane flames. This degree of change, however, would be insufficient to account for the factor of five underprediction of NO found in the $\phi = 1.4$, atmospheric flame of Fig. 4.6.

Another possibility for the apparent underprediction of prompt NO formation in the GRI mechanism is inaccuracies in its CH production and destruction kinetics. In a recent study, Woiki *et al.* (1998) found that one of the rate coefficients in the GRI mechanism, involving the CH and $O_2$ molecules, is low by a factor of three, which had the effect of causing their CH predictions to be high by a factor of 1.8 in a series of $CH_4/O_2/Ar$ flames. Correcting this problem, however, would tend to further reduce the CH concentration and thus NO formation in these flames. Another recent study by Sick *et al.* (1998) suggests that the large value of the rate coefficient for the CH destruction reaction, CH + $H_2O$, in addition to the low value of the rate coefficient for Reaction (R1), could be responsible for the GRI mechanism's underprediction of NO concentration in a series of methane/air counterflow diffusion flames. Hence, a combination of problems in the CH chemistry as well as deficiencies in the rate coefficient for Reaction (R1) are probably responsible for the underprediction of prompt NO in rich flames, as shown in Fig. 4.6. These problems with the prompt NO kinetics of the GRI mechanism could also be partly responsible for the underprediction of flamefront NO, as observed in the lean flames of this investigation.

To better understand the behavior of the GRI mechanism in its prediction of NO formation in lean premixed flames, we sought to determine the relative predicted contribution of each of the four major NO formation pathways (Zeldovich, $N_2O$ intermediate, prompt, and NNH) to the overall NO concentrations predicted by both the GRI and GMK-DB models. In this type of analysis, the contribution of each mechanism is determined by either removing an initiation reaction for a pathway (subtraction technique) or including only the relevant kinetics for a given pathway (addition technique) and determining the effect on the predicted NO contribution for the full kinetic model. The accuracy of such a modeling technique only holds to the extent that the species concentrations modified by the changes in the overall chemical kinetic mechanism do not

significantly inhibit or accelerate the kinetics of the other pathways. For the cases presented in this chapter, such inter-pathway dependencies have been found to be minimal, although similar effects could limit the applicability of this technique for other flame conditions.

For this work, the various NO pathway contributions were determined in the following manner. The prompt NO contribution was determined simply by the removal of Rxn. (R1) from the overall chemical kinetic mechanism. The Zeldovich, or thermal NO, contribution was determined by removing all three principal reactions of this pathway, Rxns. (R2)-(R4) below, from the overall kinetic scheme.

$$N+NO \Leftrightarrow N_2+O \qquad (R2)$$

$$N+O_2 \Leftrightarrow NO+O \qquad (R3)$$

$$N+OH \Leftrightarrow NO+H \qquad (R4)$$

The $N_2O$ intermediate contribution was determined simply by removing all reactions involving the $N_2O$ molecule from the overall kinetic scheme. Finally, the contribution of the NNH pathway could have been determined by simply subtracting the sum of the NO contributions of the other three pathways from the total predicted NO concentration. However, this would then attribute to the NNH pathway any discrepancy caused by interpathway dependencies. Alternately, it was found that the NNH pathway could be better calculated by removing from the GRI mechanism all reactions involving $N_2O$, the three Zeldovich reactions and all reactions involving species containing the carbon atom such as HCN or NCO, leaving only those reactions relevant to the NNH pathway. Using the above technique, it was found that the sum of the individual contributions agreed with the total NO concentration calculated by the full GRI or GMK-DB mechanisms to within 10% in the rich flames and within 5% in the lean flames for all the cases studied. A more thorough discussion of the benefits and limitations of this type of analysis can be found in the work by Thomsen (1996).

Employing the above technique, the contributions of each of the NO formation pathways, as predicted by the two models studied in this investigation, were calculated for the $CH_4/O_2/N_2$ flames at $\phi=0.6$, D.R.=2.2, and pressures of 1.00 and 14.6 atm. The

results of this study are shown in Figure 4.7. First of all, we note that the two mechanisms predict almost identical contributions for the Zeldovich NO formation pathway at each pressure, both in the flame front and in the post-flame zone. This is not surprising since the Zeldovich pathway is the simplest and most well known of the NO formation pathways. Second, we find that the $N_2O$ intermediate pathway is predicted to be the most important pathway for flamefront NO production in these lean flames, although the two mechanisms do not agree on either the magnitude of this contribution or on its pressure dependence. Third, we note that the GRI mechanism predicts almost no contribution from the prompt NO pathway in these flames, while the GMK-DB mechanism predicts prompt NO to be an important part of flamefront NO, especially at high pressure. Finally, we see that the GRI mechanism predicts a strong NNH pathway contribution at atmospheric conditions but virtually none at high pressure.

We recall from Fig. 4.6 that the worst agreement between the GRI mechanism and the LIF measurements of NO was found in moderately rich flames, for which the GRI mechanism was not able to qualitatively predict even the stoichiometry of peak NO production and the shift of this peak with pressure. Figure 4.8 shows predicted NO pathway contributions using the GRI mechanism for the equivalence ratio corresponding to peak measured NO concentration at pressures of 1.00, 6.10 and 14.6 atm. We observe that for both of the lower pressures, prompt NO dominates at these stoichiometries and the GRI mechanism does a very poor job of predicting NO concentrations. At 14.6 atm, the NO peak is at stoichiometric conditions where Zeldovich NO dominates; thus, we find from Fig. 4.6 that the GRI predictions and the LIF measurements of NO concentration at this flame condition agree very well.

The above findings bolster the supposition that the prompt NO kinetics within the GRI mechanism need improvement so as to accurately predict NO formation over a wide range of flame conditions. However, we also suggest that changes in the prompt mechanism alone are unlikely to account for the 30-50% difference between NO predictions and LIF measurements of NO concentration for lean, premixed $CH_4/O_2/N_2$ flames. Since both temperature and thermal NO seem to be accurately measured, the
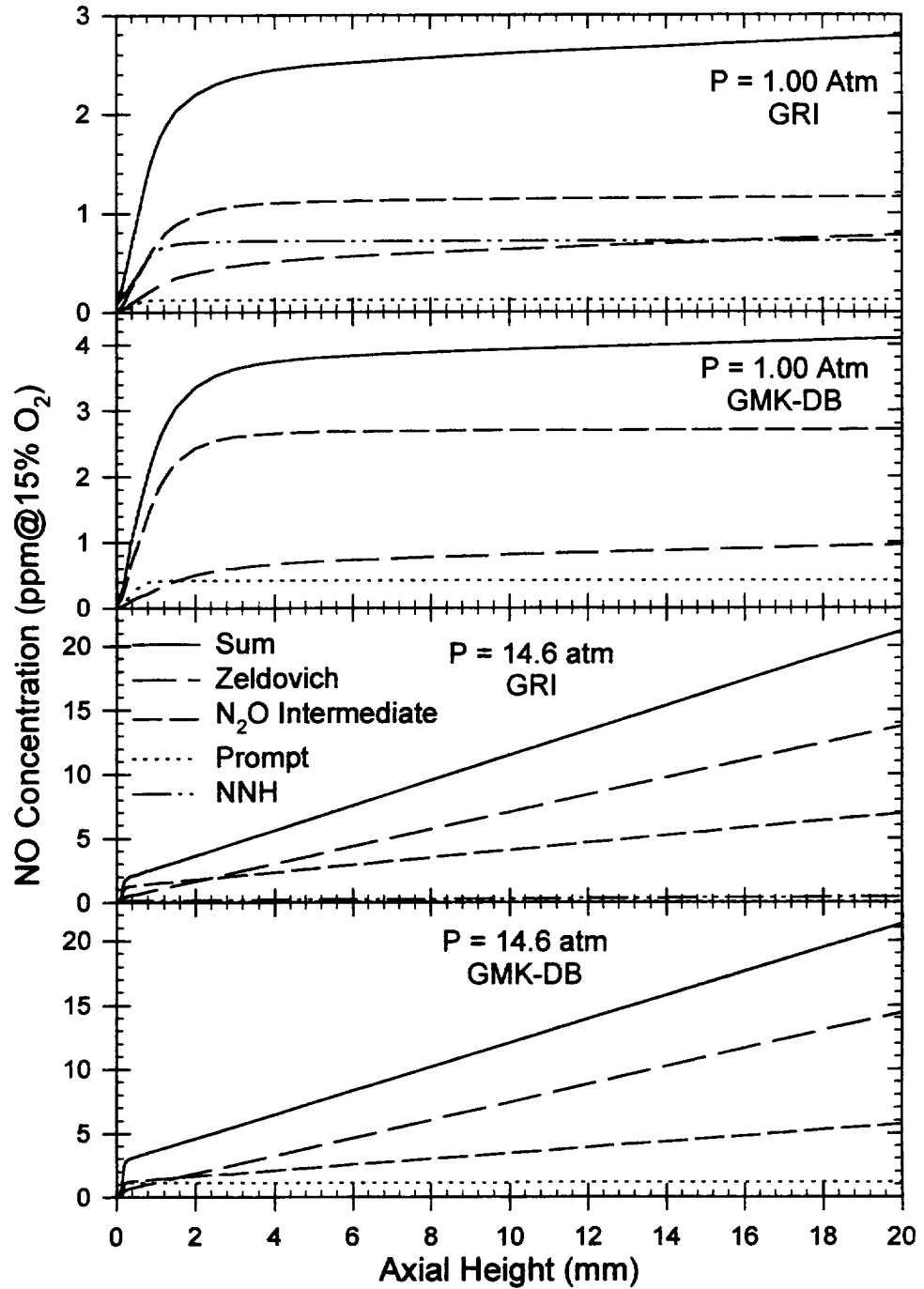
Figure 4.7: Predicted pathway contributions for modeling of NO formation in $\phi$=0.6, D.R.=2.2, $CH_4/O_2/N_2$ premixed flames. Predictions were found using temperatures predicted by the coupled species and energy equations using the GRI mechanism in conjunction with both the GRI and GMK-DB kinetics.
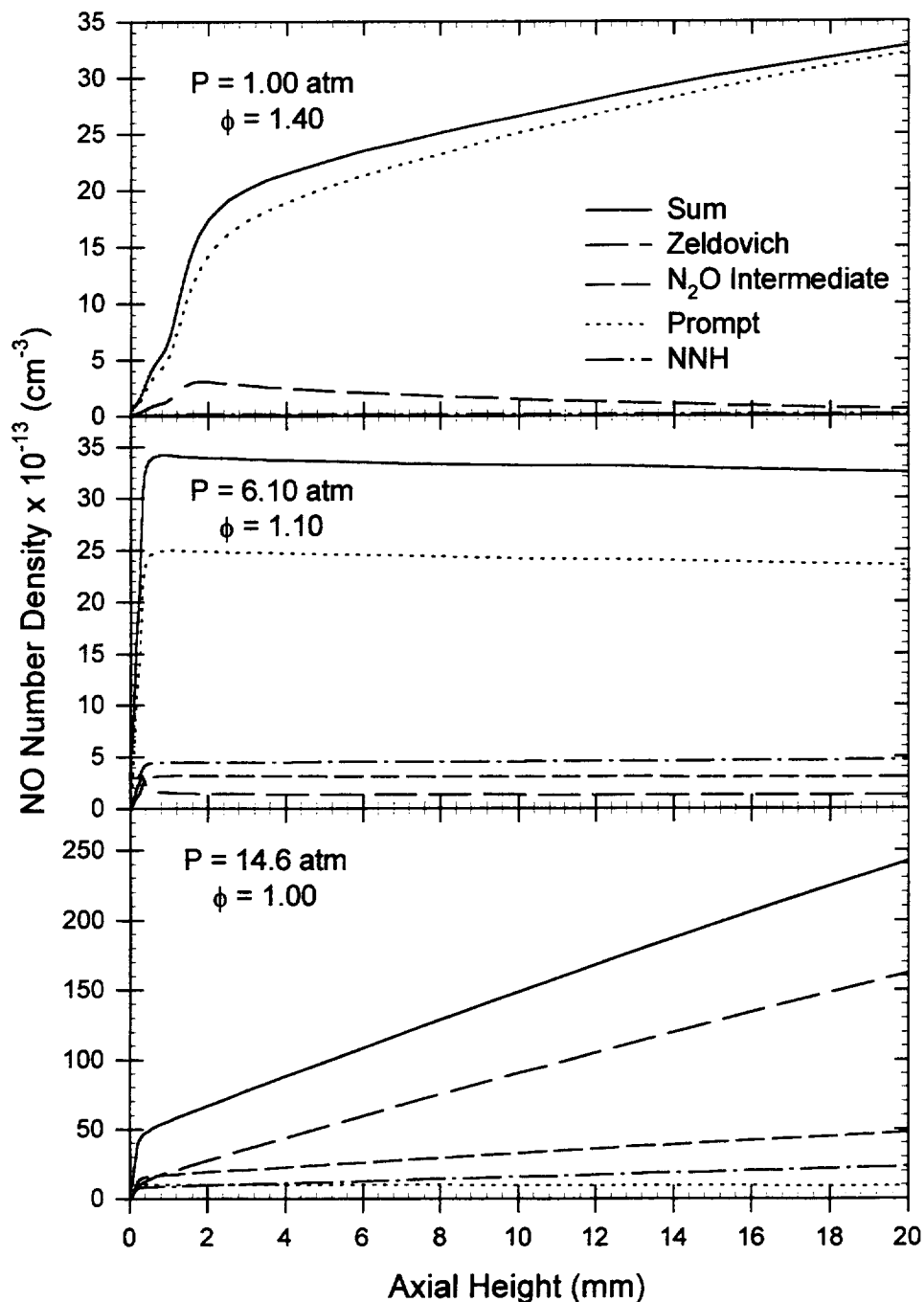
Figure 4.8: Predicted pathway contributions for modeling of NO formation at stoichiometries corresponding to peak NO concentrations in D.R.=3.1, $CH_4/O_2/N_2$ premixed flames. Predictions were found using temperatures predicted by the coupled species and energy equations using the GRI mechanism in conjunction with both the GRI and GMK-DB kinetics.

remainder of this discrepancy may indicate the need for small modifications in the $N_2O$ intermediate or NNH pathways within the GRI mechanism.

## 4.5 Conclusions

Quantitative LIF measurements of NO were obtained in flat, laminar, premixed $CH_4/O_2/N_2$ flames at pressures ranging from 1 to 14.6 atm. Radiation-corrected thermocouple measurements were also obtained in the post-flame region of these same flames. Modeling using the Sandia flat flame code and the GRI mechanism accurately predicted the post-flame zone temperature in all of the lean flames studied. This result is in direct contrast to earlier work which showed a large over-prediction of temperature in high-pressure flames when using the GMK-DB mechanism. Employing the temperature profiles obtained with the GRI model, predictions of NO concentration were also obtained using both the GRI and GMK-DB mechanisms. These results indicate that the GRI mechanism underpredicts flamefront NO production over the entire range of cases studied and does not predict qualitatively the location of peak NO formation in moderately rich flames. By comparison, the GMK-DB mechanism underpredicts NO concentrations in ultra-lean flames and overpredicts NO concentrations in moderately rich flames, while qualitatively capturing the equivalence ratio for peak NO formation. These results seem to suggest too large of an emphasis on the breakup of molecular nitrogen by hydrocarbon species in the GMK-DB model and too small of an emphasis on this NO formation pathway in the GRI model.

# 5. COUNTERFLOW BURNER DESIGN

## 5.1 Introduction

The NO measurements and modeling discussed in Chapter 4 pertained to the post-flame zone of flat laminar flames stabilized on a water-cooled burner. This geometry has traditionally been used because it produces one-dimensional flames that are easy to model, extremely stable, and simple to use. One problem with this configuration is that the flamefront sits extremely close to the burner, especially at high pressures. This feature makes it impossible to obtain experimental profiles of temperature and species concentrations through the flamefront or even to experimentally validate the concentrations and temperatures upstream of the flame. An alternate configuration that promises to provide this capability while retaining a one-dimensional structure for ease of modeling is that of counterflow premixed flames.

As mentioned in Chapter 2, there are several key advantages to the counterflow configuration for studies of lean premixed flames. First of all, the nearly adiabatic nature of these flames permits the study of much leaner conditions than could be achieved on a water-cooled flat flame burner. This is important since most proposed low-$NO_x$ burners designed for advanced gas-turbine engines utilize lean, premixed combustion. The second advantage of this configuration is that it allows for the probing of species concentrations and temperatures upstream, within, and downstream of the reaction zone of the flame. Even if the flame zone at higher pressures becomes so thin that resolving measurements within it becomes impossible, having reliable measurements of the pre-flame zone temperature and NO concentration will help in analyzing the accuracy of our modeling schemes. The final advantage of this configuration is that, as for the flat, burner-stabilized

flames studied previously, it can be simulated by a simple one-dimensional model along its centerline.

Because of the above advantages, we decided to develop a counterflow premixed burner for use in our high-pressure facility. This chapter describes the design of just such a burner. Starting with the design criteria, we examine in detail the design process used in manufacturing this burner. We also present the final design, discuss the operating characteristics of the resulting burner, and suggest improvements or modifications that may be implemented in future designs.

## 5.2 Design Criteria

Several key design constraints became important for this task. The first set of constraints had to do with burner size. The burner had to be small enough, including all of its support structure, to fit inside our high pressure facility (Carter *et al.*, 1989). It also had to be light enough to be translated using the existing vertical and horizontal translation stages. Furthermore, the diameters of the flow passages had to be small enough to ensure that the existing mass flow control system could provide sufficient flow to achieve velocities greater than the laminar flame speeds of these mixtures, even at high pressure. In competition with the above requirements was the desire to have a sufficiently large burner diameter to ensure a flat flame whose centerline is undisturbed by diffusion from the surrounding guard flow.

In addition to size constraints, several operating criteria were established based on previous experience with a large scale counterflow burner designed by Kuhl (1996). First of all, it was desired that both the top and bottom burners should have water cooling and guard flow capabilities. Water flow was necessary for both burners because of the higher heat output of high-pressure flames as well as the confined space within the high-pressure facility. Furthermore, cooling both burners provides some control of inlet gas temperature. A dual guard flow configuration was desired for several reasons. First, it protects both burners from direct contact with the undiluted product stream. Second, it

prevents entrainment of combustion products and limits the shear experienced by the reactant flow exiting the burner. Furthermore, having a guard flow on only one side tends to cause a greater coupling between guard flow velocity and flame position than a dual-guard flow configuration. Since no preheating was desired for these experiments, an elaborate system to remove the products was unnecessary; instead, the products were simply allowed to flow up around the top burner and exhaust at the top of the vessel. For this reason, heat resistance of the top burner assembly became an important design criterion as well.

Additional operating criteria for this burner were established as follows. Most importantly, flat velocity profiles were required at the burner exit for a wide range of flow conditions. The separation distance between the top and bottom burner needed to be adjustable and well known; also, there had to be an easy way to properly orient the two burners relative to each other. A technique was needed to prevent condensation from forming on the top burner and dripping into the flame zone. Moreover, the burner had to be able to survive long periods of use enclosed within a pressure vessel. Lastly, the burner needed to be easily opened for cleaning and maintenance.

## 5.3 Counterflow Burner Design

The first decision made for this burner design was which basic type of burner construction to use. For this type of burner, two basic strategies have been utilized by other researchers to ensure flat, laminar profiles at the burner exit. The first of these consists of contouring the burner nozzle such that a flat exit profile is achieved (e.g., Sung *et al.*, 1996). The advantage of this method is that there is nothing to trip the flow at the exit plane, thus providing perhaps the highest quality laminar flow at the exit plane of the burner. Furthermore, this open design lends itself to applications requiring particle seeding, such as LDV. A contoured design also tolerates preheating well and allows the use of physical probes to determine temperature and species concentrations at the exit plane. The major disadvantage of this approach is that, in general, perfectly flat profiles

are only obtained for a limited range of flow conditions; in addition, it is susceptible to flashback and tends to be very large and cumbersome which rules out applications within our high-pressure facility. The second type of burner uses flow straightening devices such as glass beads, screens, sintered metal plugs and/or honeycomb materials to flatten the flow profile and to prevent the onset of turbulence (Kuhl, 1996). The advantages of this type of burner include design simplicity, compactness, some flashback protection, and performance characteristics more independent of flow rate than those of the nozzle-type burners. The disadvantages include possible nonuniformities in the velocity profile at the exit plane owing to irregularities in the flow-straightening materials, higher frictional losses through the burner, and obstructions of the flow passage which essentially prevents particle seeding experiments unless the burner is specially designed with such applications in mind. Based primarily upon our size constraints, this latter type of counterflow burner was chosen for this application.

The second design decision which had to be made was that of exit diameter. Our existing mass flow controllers are capable of delivering 2.0 SLPM of $CH_4$, 5.0 SLPM of $O_2$ and 20.0 SLPM of $N_2$ to each burner. From these constraints, we determined that for lean equivalence ratios ($0.5 \leq \phi \leq 1.0$), a 20 SLPM maximum flow rate was an acceptible design limit. While additional mass-flow controllers could be purchased to extend this range, a maximum fuel flow rate of 2.0 SLPM through each burner also corresponds to about the maximum heat release rate that can be handled safely in our high-pressure facility. Now, to avoid flashback, it is also necessary to exceed the laminar flame speed at each operating condition to be studied. An approximation for the pressure and temperature dependence of the laminar flame speed is given by Turns (1996). Considering only the pressure dependence, we have

$$S_L = S_L^0 \left( \frac{P}{P^0} \right)^\beta \tag{5.1}$$

where

$$\beta = -0.16 + 0.22(\phi - 1). \tag{5.2}$$

Here, $S_L$ is the laminar flame speed, $S_L^0$ is the laminar flame speed at a reference pressure

Table 5.1: Estimated laminar flame speeds and maximum burner diameters for counterflow premixed flames at 1.0 and 15.0 atm.

| | $S_L$ (cm/s) | | $D_{max}$ (cm) | |
|---|---|---|---|---|
| $\phi$ | P=1.0 atm | P=15.0 atm | P=1.0 atm | P=15.0 atm |
| 0.6 | 18 | 9.20 | 4.86 | 1.75 |
| 0.8 | 33 | 19.0 | 3.59 | 1.22 |
| 1.0 | 40 | 25.9 | 3.26 | 1.04 |

(1 atm) and temperature (300 K), $\phi$ is the equivalence ratio, $P^0$ is the reference pressure and $P$ is the actual pressure. For methane, atmospheric laminar flame speeds at $0.6 \leq \phi \leq 1.0$ range from 18 to 40 cm/s (Avallone and Baumeister, 1987). Combining Eqs. (5.1) and (5.2) with the previously defined maximum flow rate of 20 SLPM, we may estimate maximum burner diameters for which the flame speed would be exceeded as a function of pressure. The results of this study for our low- and high-pressure limits are presented in Table 5.1. Based on these results and a desire to maintain as large a burner diameter as possible to limit the effect of guard-flow diffusion into the reactant stream, a burner diameter of 1.00 cm was chosen. Even with a 2.0 factor of safety, this diameter should provide adequate flow velocities for lean flame studies ($\phi \leq 0.8$) up to pressures of at least 10 atm. The tube diameter for the guard flow was then chosen such that the area of the annulus carrying the guard flow was approximately equal to that of the reactant tube. Once again, this choice was made based on the mass-flow controller range and the desire to have equal exit velocities for the guard and reactant streams.

Using these tube diameters, two identical burners were designed to meet the previously discussed design criteria. An assembled view of this counterflow burner is illustrated in Figure 5.1. A few of the key features of this design are as follows. Starting at the fuel inlet, 3/8" NPT threading allows for attachment of a swagelock fitting directly in line with the 1-cm diameter, inner tube. The fitting presses into three sintered stainless plugs which both remove the boundary layer and nonuniformities of the fuel stream and act as flame arrestors to prevent flashback of the premixed gases. A hastalloy honeycomb plug is used to further flatten the velocity profile and ensure laminar flow at the exit plane. This type of exit plug has been used successfully for several existing laminar burners within our laboratory. It can handle higher temperatures and is less susceptible to plugging by soot or other fine particles than sintered materials.

Immediately next to the central fuel tube is an annulus for the passage of a protective guard flow. As mentioned previously, this passage has the same exit area as the central tube. However, because of space constraints, it was necessary to bring the guard flow in from the sides of the base. To equally distribute the guard flow and ensure a flat
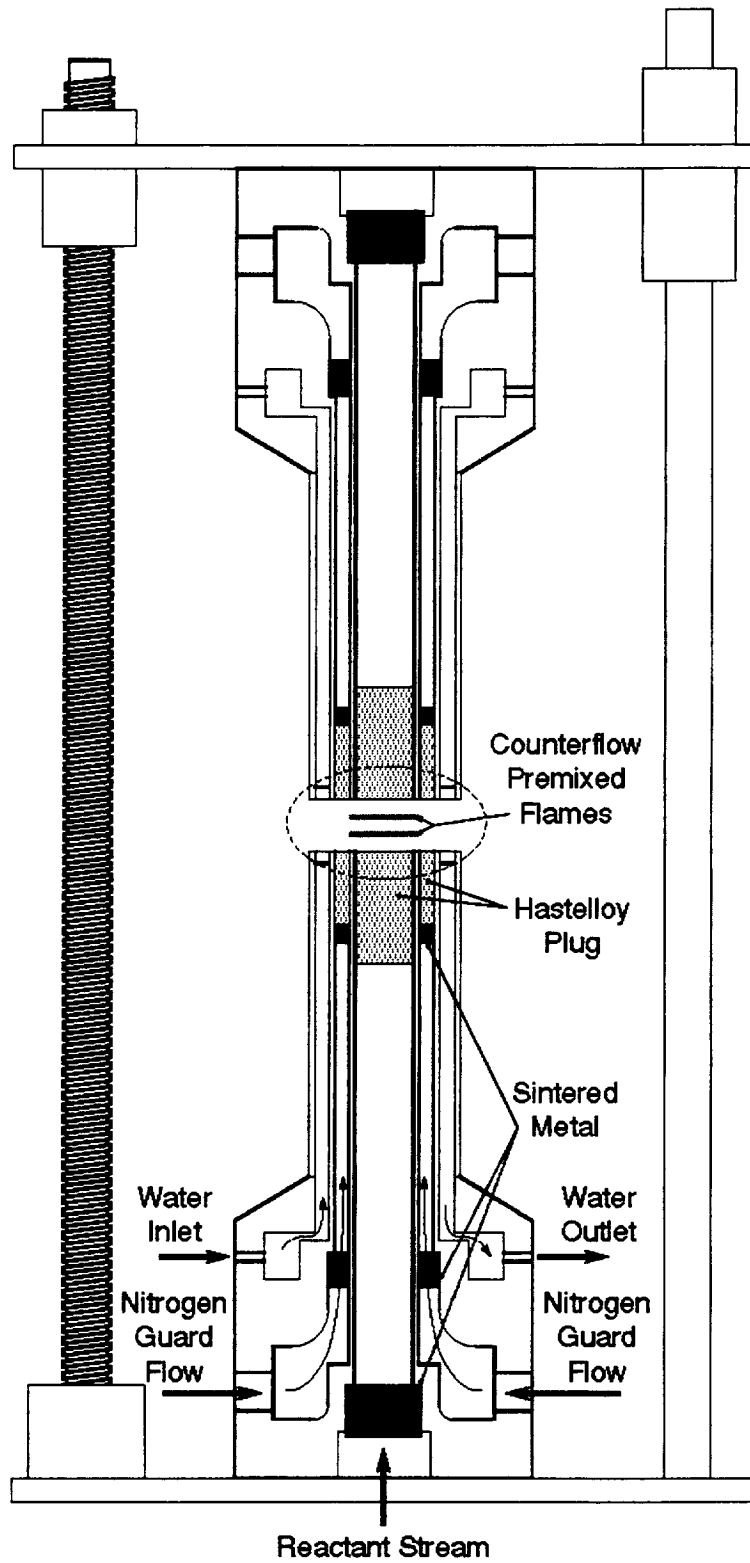
Figure 5.1: Assembled view of single counterflow burner.

profile at the exit plane, the incoming guard flow is first passed through a bed of loosely packed glass beads. The flow must then pass through two layers of sintered stainless material, which help flatten the velocity profile, act as spacers when reassembling the burner, and keep the beads from pouring into the annulus. After flowing down the passage, another stainless plug is used to break up the pipe-flow contour which may develop before the exit plane and a hastalloy honeycomb exit plug is used to deliver the laminar flow to the burner surface. The existence of a protective guard flow at both the top and bottom burner offers additional protection for the inner flat flame with respect to flow disturbances within the pressure vessel.

Because of the small size and intricate nature of the components, it was necessary to solder rather than weld the individual pieces together. Hence, continued and effective cooling of each burner is absolutely imperative for their survival during normal use. To address these needs, an outer passage designed for water cooling of the burner surface is positioned around the guard flow annulus. This cooled surface is especially important for the top burner since the hot combustion products will impinge upon it as they flow up to the exhaust. Water enters through a soldered tube fitting on one side of the burner, passes through a series of winding passages designed to cause impingement of the water upon the burner cap, and passes out a tube fitting on the opposite side. The flow passages are constructed via the insertion of six guide vanes between the guard flow tube and the outer burner wall. To prevent condensation from building up on the top burner and dripping into the flame zone, the cooling water for this system must be preheated. For our work, a closed loop cooling system was designed that allowed variation of both coolant temperature and inlet pressure. Furthermore, a solenoid valve was installed in each fuel line and tied to a flow switch in the coolant system; hence any loss of coolant results in the immediate termination of fuel delivery, thus further protecting the burner system. Details of the burner design can be found in the design schematics presented in Appendix C.

The next step in the design process was to manufacture a mounting assembly to reliably position the two burners in an opposed configuration, permit a variable separation distance, and survive in a harsh environment. Since all the components on the top mount

are exposed to high-temperature exhaust gases during normal operation, the more sensitive positioning components were all placed on the lower mount. Specifically, an X-Y translation stage (Thor labs model #ST1XY-A) was used to exactly position the lower burner under its top counterpart. This translation stage, in turn, was mounted to an aluminum base plate along with a three-post support system for the top platform. The three posts consisted of two ½" diameter stainless steel shafts and a ball screw mounted on a quick-mount block (Thomson-Saginaw #7824154).

The top burner was mounted to a skeletonized, stainless-steel base plate designed to minimize resistance to the exhaust flow. Because of the high temperatures and corrosive environment, all stainless steel components were used to connect this base plate to the three-post support. The ball nut used was a Thomson-Saginaw model #5707645, which allows separation distances up to about 4 cm. To maintain a strict vertical mount for the top burner, twin stainless steel bearings (Thomson model #A-81420-SS) were mounted in specially designed holders for mating with each stainless steel shaft. Design schematics for both the top and bottom bases are included in Appendix C. Finally, stainless steel swagelock components were used to attach tubing to both burners.

## 5.4 Operating Characteristics of Counterflow Burner

In its ideal form, the flowfield and flame configuration of this type of counterflow burner should closely resemble that illustrated in Figure 5.2. The central stagnation plane should clearly separate the two flamefronts and significant separation should exist between each flamefront and its corresponding burner. For comparison with this ideal behavior, a picture of the resulting burner configuration as installed in the high-pressure facility's translation system is shown in Figure 5.3. Here the tight fit of the burner inside the assembly becomes apparent. In this picture, the separation distance has been approximately set to 1 cm. Figure 5.3 displays the nice flat profile of the resulting premixed flames ($\phi \approx 0.65$). In fact, for all of our atmospheric pressure, premixed, $CH_4/O_2/N_2$ cases ($0.65 \leq \phi \leq 1.5$), we were able, by varying the flow rates, to obtain steady,
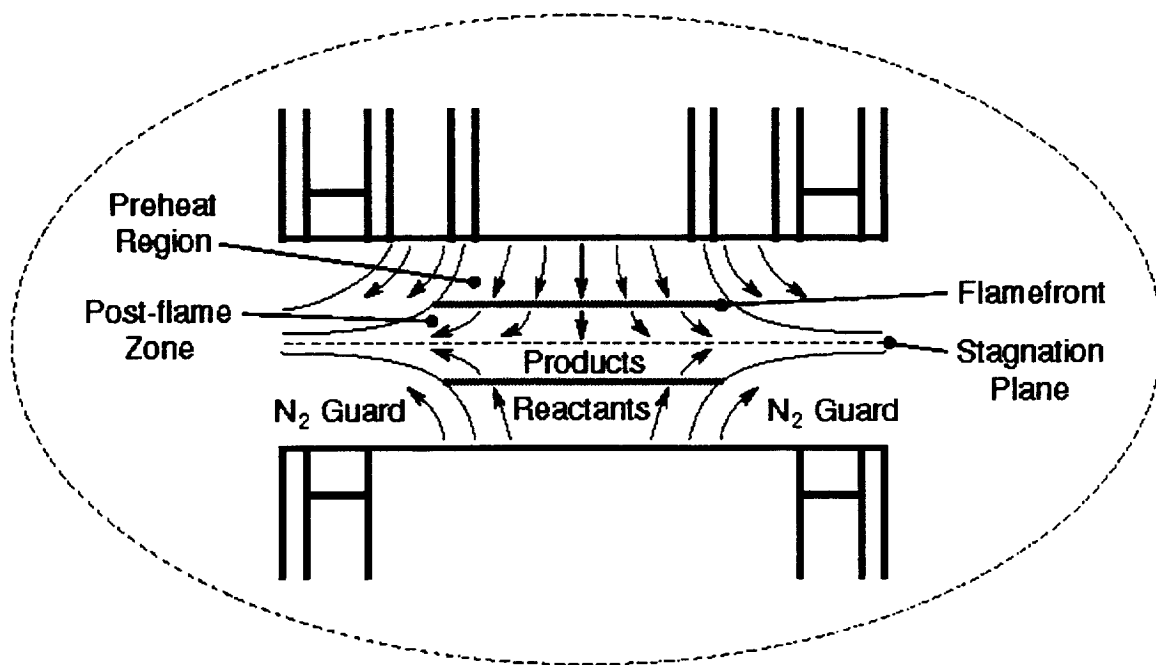
Figure 5.2: Idealized flame configuration for counterflow premixed flames.
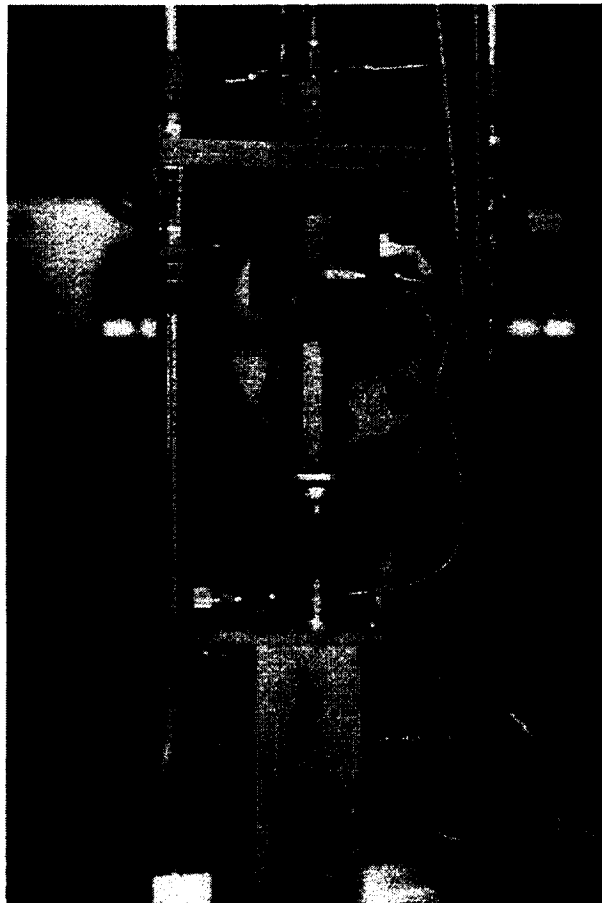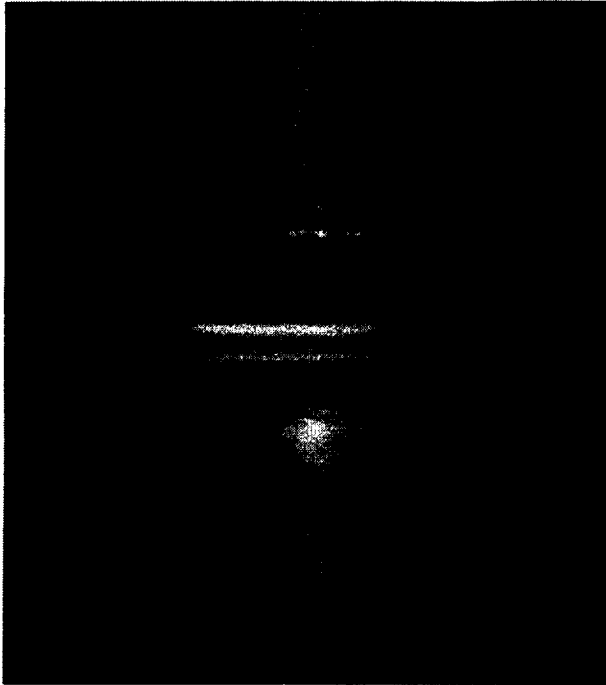
Figure 5.3: Premixed counterflow $CH_4/O_2/N_2$ flame.

flat, reproducable twin flames with separation distances of ~3 mm. This system was also tested for counterflow diffusion flames with great success. Figure 5.3 clearly shows the beginnings of condensation on the top burner. These pictures were taken during testing prior to the installation of our coolant preheat system, thus demonstrating the need for preheat.

As the pressure rose, the flamefronts became thinner and buoyancy became increasingly dominant, especially for the leanest flames considered. The buoyancy effect is twofold, shifting both flamefronts upward and compressing them closer together. The result of this limitation is that by approximately 6 atm, it becomes impossible to stabilize ultra-lean flames ($\phi \leq 0.65$) with separation distances greater than 2 mm. Furthermore, at pressures of about 5 atm and greater, a small amount of buoyant bounce begins to cause unsteadiness, especially in the lower flamefront. These limitations restricted the range of lean, high-pressure flames that could be studied in this investigation.

One way around the buoyancy problem is to study hotter, higher-velocity flames such as those closer to stoichiometric conditions. Unfortunately, at pressures of 3.0 atm and greater, a second difficulty begins to emerge in these hotter flames; specifically, they begin to exhibit a distinct multi-dimensional topography. These flame fronts no longer look flat, but display hills and valleys possibly caused by differences in frictional losses within the separate passages of the hastalloy honeycomb used in this design. Although the flames are still steady, the local strain rate at the flamefront is altered by this behavior and the flames are no longer flat. While further revision of the design could help alleviate this problem, the buoyancy issue would still limit the effective study of the ultra-lean premixed flames desired in the current work. Consequently, the limited set of high-pressure flames studied here represents almost the entire useful range of conditions accessible with this burner system. The performance of the burners for counterflow-diffusion flames, on the other hand, has been demonstrated to be excellent, at reasonable strain rates, for pressures in excess of 10 atm.

## 5.5 Recommendations For Future Burner Design

The major conclusion from the above discussion is that this burner provides excellent results at atmospheric pressure for all of the flames of interest, both premixed and nonpremixed. However, as pressure is increased, the useful range of premixed conditions available for study becomes limited by both buoyancy and frictional effects. Because of these effects, measurements of NO in premixed flames at pressures of 6 atm and greater were not attainable with this configuration. On the other hand, high quality, nonpremixed flames were attainable at pressures up to 10 atm. While the buoyancy problem cannot be solved without the use of microgravity research, a contoured nozzle could be used to avoid the topography effect. However, this would require a much bigger system than would fit in our existing high-pressure facility.

For counterflow burners of this type, but without the severe size constraints of the present work, several recommendations can be made based on experiences with the current system. First, using fewer, larger components that can be welded rather than soldered together would be much better. Considerable time and energy were spent on this burner attempting to get all of the solder joints properly sealed; moreover, the burner is still susceptible to damage in the case of coolant failure. Second, the ball-screw assembly, while allowing for great flexibility in separation distance, is unnecessary. In reality, the separation distance is kept constant for most studies. In place of the ball-screws and linear bearings, three threaded posts with nuts and washers would be sufficient. Another option would be to simply have clamps on the three posts and some sort of fine adjustment to vertically orient the top burner. Third, a larger design could use threaded fittings for all gas and water ports, which would make replacement easier and provide greater flexibility in connection type.

In conclusion, a design has been presented for a counterflow burner system for use within our high-pressure facility. It is compact, flexible, and produces beautiful flames at atmospheric pressure. While the high-pressure capabilities of this burner are not as great as we had hoped, it still provides some interesting and unique flames for our studies of NO formation.

# 6. LIF MEASUREMENTS AND MODELING OF NITRIC OXIDE CONCENTRATION IN ATMOSPHERIC COUNTERFLOW PREMIXED FLAMES

## 6.1 Introduction

Nitric oxide (NO) is an atmospheric pollutant that has been tied to both the destruction of the ozone layer and the creation of photochemical smog. Because of these effects, current government emission standards have mandated that advanced gas turbines produce low $NO_x$ levels (<10 ppm @ 15% $O_2$ as corrected through the addition of dilution air). Since $NO_x$ production by nonpremixed combustion generates $\geq 100$ ppm (@ 15% $O_2$) for non-nitrogen bound fuels (Correa, 1992), the goal of lower $NO_x$ emissions will require partially or fully premixed combustion. Hence, a more thorough understanding is needed of the chemical kinetics of pollutant formation in lean, premixed combustion. Of particular interest is the development of a simplified, high-pressure $NO_x$ model capable of predicting NO formation for practical gas turbine conditions. To achieve this goal, a complete understanding is needed of the chemical kinetics involved in the production of NO at high pressure. This knowledge, in turn, requires accurate *in situ* measurements of NO concentration to verify any proposed kinetic modeling scheme.

In pursuit of this goal, laser-induced fluorescence (LIF) has recently been used (Reisel and Laurendeau, 1994a; Klassen *et al.*, 1995; Thomsen, 1996) to obtain quantitative measurements of NO concentration in laminar premixed flames stabilized upon a water-cooled McKenna burner at 1-14.6 atm. This geometry has traditionally been used because it produces one-dimensional flames that are easy to model, extremely stable, and simple to use. One problem with this configuration is that the flamefront sits extremely close to the burner, especially at high pressures. Consequently, it becomes impossible to obtain experimental profiles of temperature and species concentrations

through the flamefront or even to experimentally validate concentrations and temperatures upstream of the flame. An alternate configuration that promises to provide this capability while retaining a one-dimensional structure for ease of modeling is that of counterflow premixed flames. Because the flames are stabilized by curvature effects rather than by heat loss to the burner, significant separations can exist between the flamefront and the burner surface. In addition, because less heat loss occurs to the burner in such flames, near adiabatic conditions may be obtained which allow for the study of leaner flames than can be stabilized on traditional flat-flame burners. This approach is particularly advantageous for the study of lean premixed combustion which is being pursued for $NO_x$ abatement in advanced gas turbines.

In this chapter, LIF measurements of NO concentration are presented for a series of flat, laminar, counterflow premixed $CH_4/O_2/N_2$ flames at atmospheric pressure. Scientific issues regarding the application of LIF to this flame configuration are discussed as well as the utility of the counterflow configuration for chemical kinetic comparisons. The measurements are then compared to modeling predictions by using the GRI mechanism, version 2.11 (Bowman *et al.*, 1995). Finally, pathway, sensitivity, and quantitative reaction path analyses are used to pursue in more detail the kinetic implications of the above comparisons.

## 6.2 Experimental and Modeling Techniques

The laser system and optical layout used in performing the LIF measurements of NO are described completely in Chapter 3; however, the most relevant points are repeated here. Excitation of NO is achieved through use of the $Q_2(26.5)$ line in the $\gamma(0,0)$ band (~225.5 nm). An etalon-based feedback system is used to provide a stable laser excitation wavelength (Cooper and Laurendeau, 1997). After leaving the laser system, the beam is directed over a 1-cm diameter, counterflow flat-flame burner designed for use in the high-pressure combustion facility described by Carter *et al.* (1989). Figure 6.1 provides a schematic of this counterflow burner arrangement, which is described in detail in Chapter
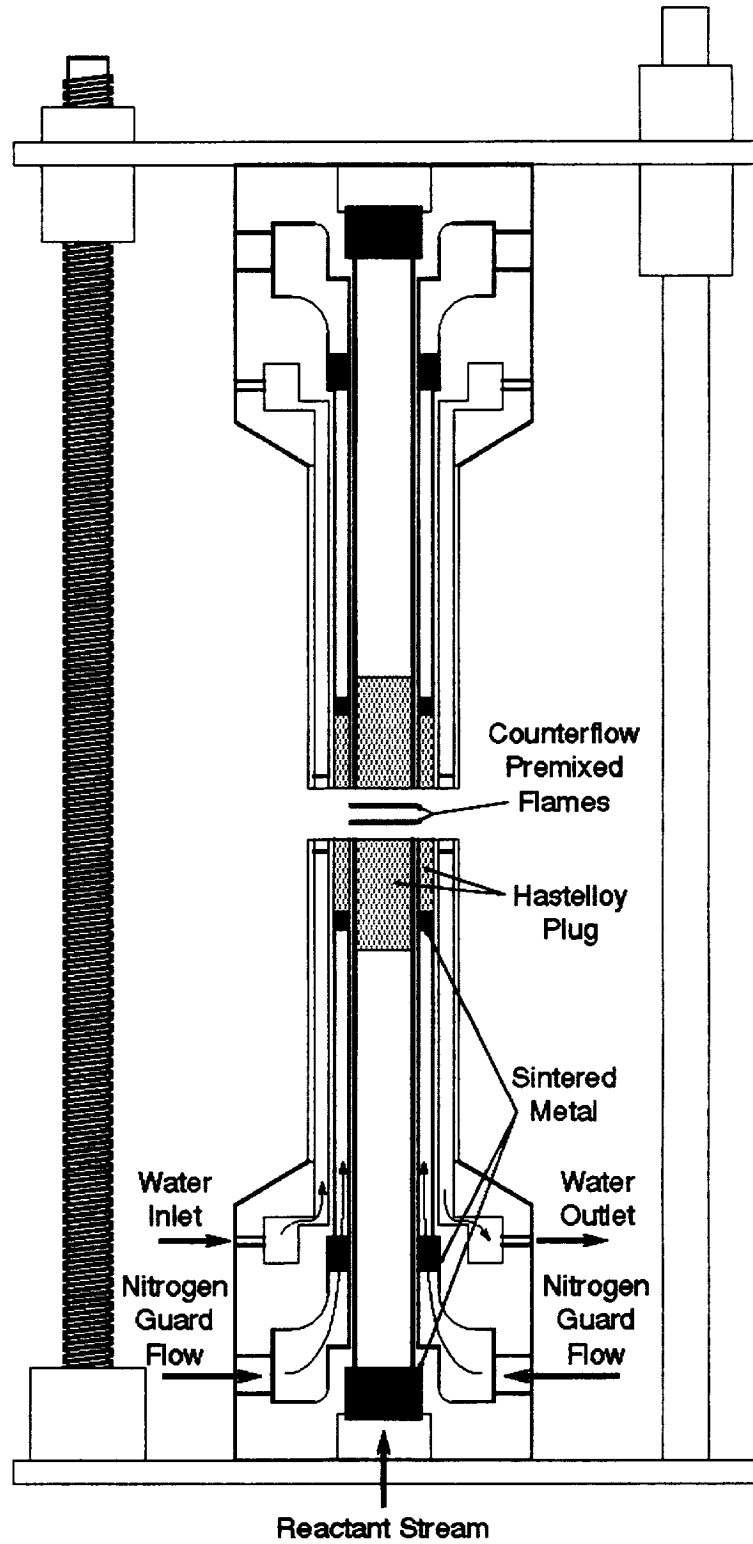
Figure 6.1: Schematic diagram of counterflow burner.

5. The pressure vessel has four optical ports, two of which provide optical access for the laser beam through the combustion facility. The spot size produced by the optical arrangement is ~250 μm. Before entering the vessel, the beam passes through a fused silica plate which directs a portion of the beam toward a UV-sensitive photodiode. This photodiode is employed to monitor the beam energy, which is required for normalization of the fluorescence signal.

For fluorescence detection, we make use of an optical port perpendicular to the laser entrance and exit ports. The fluorescence is focused on the entrance slit of a 1-m monochromator. The detector is an Hammamatsu R106UHHA photomultiplier tube (PMT) specially wired for temporal resolution of the fluorescence signal (Harris *et al.*, 1976). The broadband fluorescence signal encompasses a spectral width of ~3 nm and is detected over a spectral region centered at ~236 nm. This location and spectral width correspond to the $\gamma(0,1)$ band of NO. Each data point is averaged over 600 laser shots. A diagram of the experimental apparatus is shown in Figure 6.2.

A new procedure, based on a previous calibration technique developed in our laboratory for flat burner-stabilized flames (Thomsen *et al.*, 1997), was developed for calibrating the fluorescence signals. This technique involved doping different levels of NO, first into one and then into the other premixed stream of a $\phi = 0.7$ counterflow premixed flame, and measuring the fluorescence voltage produced in the burnt-gas region. The data from the various doping conditions were used to obtain a linear calibration plot which could then be applied to the calibration flame ($\phi = 0.7$). The fluorescence signal for other flames could subsequently be compared to that of the calibration flame and corrected for changes in both the absorption efficiency and the electronic quenching rate coefficient so as to obtain quantitative NO number densities. We assumed both that the doped NO does not react as it passes through the flame and that summing the signals obtained from doping into each side individually contributed the same amount of signal as doping into both sides simultaneously. To confirm these assumptions, computer modeling was used to predict the effect of independently doping a known concentration of NO into each stream of the counterflow calibration flames. The results of this study are shown in
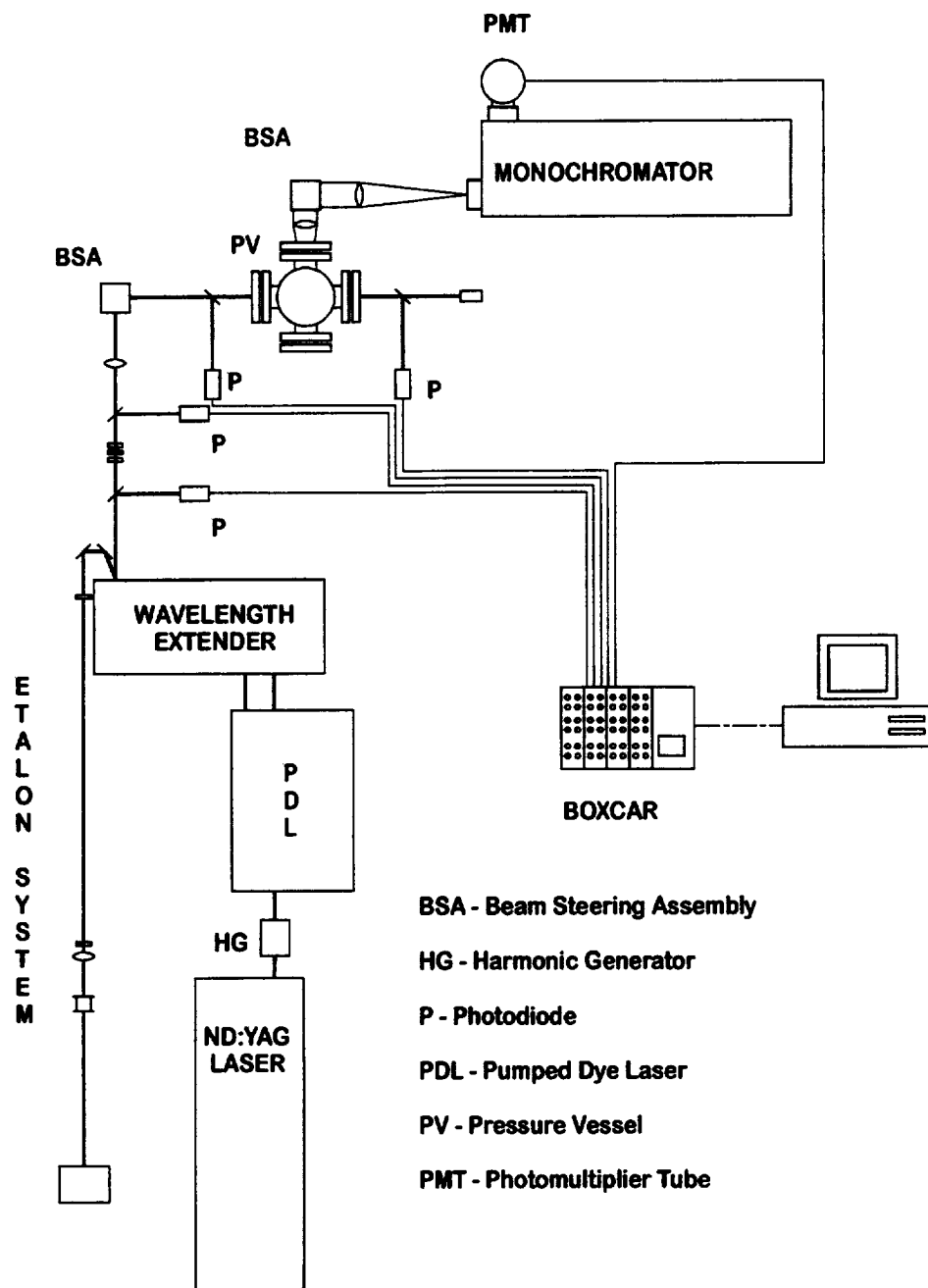
Figure 6.2: Schematic diagram of experimental apparatus.

Figure 6.3(a). We find that the "calibration" profile obtained by summing the NO profiles of the two doped cases and subtracting twice the ambient NO profile produces a constant region near the centerline with an NO concentration equal to the total amount of NO doped into each stream independently. The utility of this approach is further supported by the linearity of the resulting experimental calibration plot shown in Figure 6.3(b). Finally, measurement of the fluorescence signal by using an off-line excitation wavelength confirmed that the contribution to the signal from non-NO interferences was negligible in these flames (<1%).

The modeling of the chemical kinetics was performed using the Sandia, steady, laminar, opposed diffusion flame code (Lutz *et al.*, 1996). A burner surface temperature of 300 K was used as the boundary condition for the modeling. The applicability of this boundary condition was verified by thermocouple measurements of the reactant stream in the cold-gas regions of these flames which yielded temperatures ranging from 303 to 310 K. Furthermore, computations indicated that a 10 K rise in the boundary condition is insignificant in terms of the code predictions. Temperatures through the remainder of the flame were obtained through joint solution of the energy and species equations within the OPPDIF code. The comprehensive mechanism used in the modeling is the GRI mechanism, version 2.11 (Bowman *et al.*, 1995). This reaction mechanism, which can be found in Appendix B, considers 49 species and 277 reactions and was used without modification. In addition, we employed the thermodynamic and transport property files provided with the mechanism.

Finally, OPPDIF allows for calculation of species diffusion using either mixture averaged or multi-component diffusivities. Thermal diffusion of species can also be considered as an additional option. Mixture averaged diffusivities were employed for all the modeling presented in this chapter. Comparisons between calculations employing mixture averaged and multi-component diffusivities demonstrated negligible effects (<1%) on either the postflame zone temperature or NO concentration. Inclusion of the thermal diffusivity option in the OPPDIF code (which seems to be applicable only in concert with
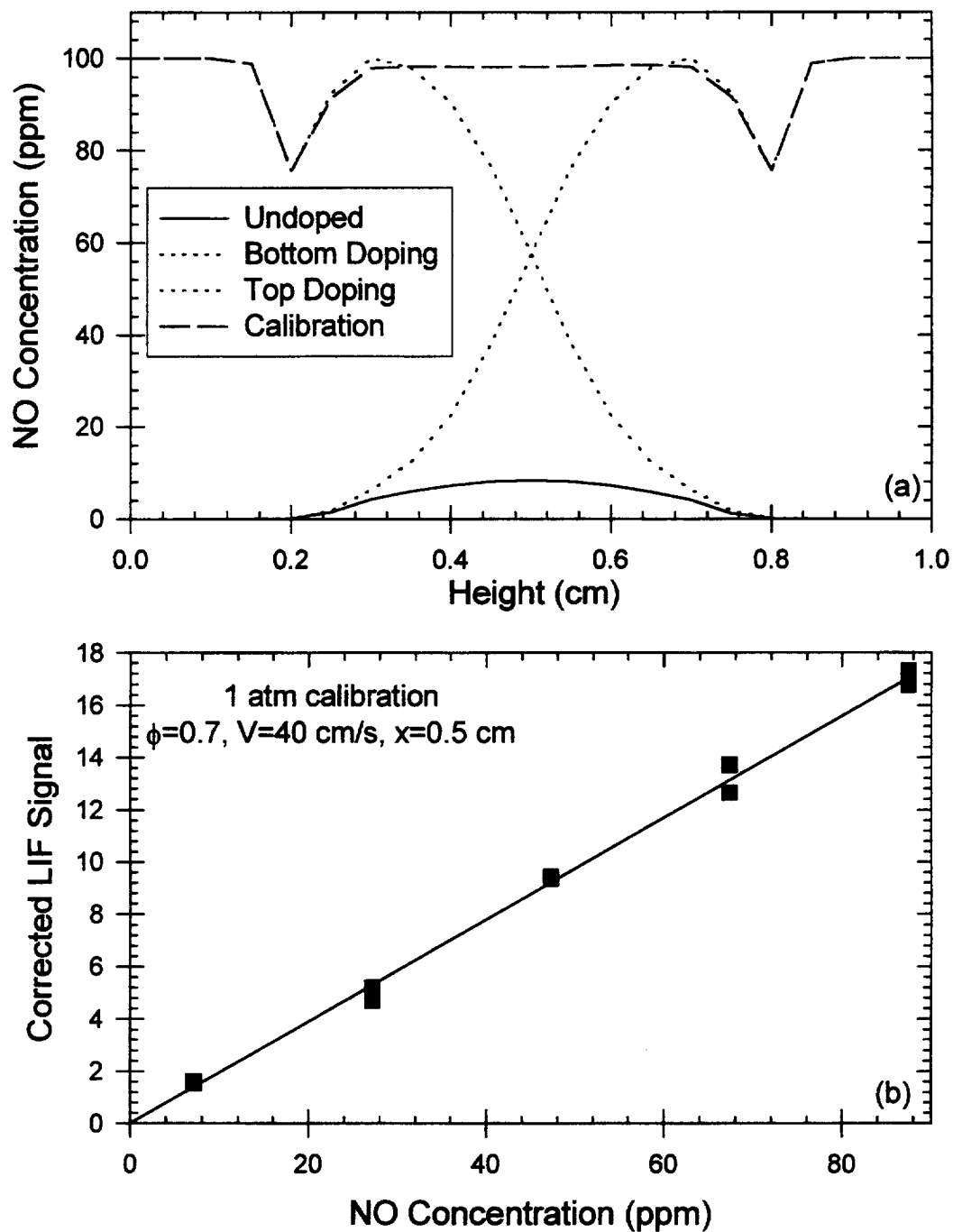
Figure 6.3:  LIF calibration technique for counterflow flames:  (a) modeling of NO destruction through premixed flames and (b) calibration in $\phi$=0.7, $CH_4/O_2/N_2$ flames at 1.0 atm.

the multi-component option) did have some impact on the NO and temperature predictions. As an example, the inclusion of thermal diffusivity reduced the predicted peak NO concentration from ~33.4 ppm to ~31.7 ppm in a $\phi$=1.20, V=125 cm/s, counterflow premixed flame. However, this ~5% change is not sufficient to alter any of the conclusions made in this chapter.

An important limitation of the Sandia opposed diffusion flame code is that it does not consider the effects of radiation heat loss. To account for such effects on the temperature and NO predictive capabilities of the code, a radiation subroutine developed by Gore and coworkers (1999) was incorporated into the energy equation within the OPPDIF code. This routine, which assumes optically thin radiation originating from the major species within the flame, has previously been shown to have a significant impact on NO predictions in lower strain rate counterflow diffusion flames (Gore *et al.*, 1999; Ravikrishna and Laurendeau, 1999).

When performing linear LIF measurements, one must be concerned with the effects of laser power fluctuations as well as absorption and quenching variations as a function of temperature and species composition. Corrections for laser power fluctuations can be made by normalizing the fluorescence signal using the measured laser power. Quenching variations could be handled in a similar manner; however, measurement of the quenching rate coefficient is not a trivial task. Furthermore, the large variations in temperature and composition across the flame front make both quenching and absorption corrections significant in these flames.

In general, the quenching rate coefficient and absorption efficiency are functions of temperature and major species concentrations. For linear LIF measurements, the fluorescence equation reduces to the form

$$S_f = \frac{V_f}{I_L} \propto \frac{\alpha N_T}{Q_{ul}}, \tag{6.1}$$

where $S_f$ is the laser-power corrected fluorescence signal, $V_f$ is the integrated PMT voltage, and $I_L$ is the laser irradiance (W/cm$^2$). The parameter $\alpha$ is the absorption coefficient per unit NO number density (cm$^{-1}$/(molecules/cm$^3$)), which includes the effects

of Boltzmann fraction, line strength and overlap fraction, as described in Chapter 2. The final two terms, $Q_{ul}$ and $N_T$, refer to the quenching rate coefficient ($s^{-1}$) and the NO number density (molecules/$cm^3$), respectively. The proportionality constant implied by Eq. (6.1) can be determined by using the calibration technique described previously. However, since measurements are being taken across the flamefront, the quenching and absorption terms can vary significantly in these flames.

Unfortunately, without measurements of temperature and major species concentrations, it is essentially impossible to predict $Q_{ul}$ and $\alpha$ so as to correct the LIF measurements. On the other hand, major species and temperature information are available from the predictions. Thus, the modeling can be "uncorrected" for quenching and absorption effects to produce an uncorrected number density which can be directly compared to the LIF measurements. This calculation was accomplished by first multiplying the predicted number density at each location by the ratio of the quenching rate coefficient predicted for that location over that predicted for the calibration flame. This revised number density was then divided by a similar ratio of actual to calibration absorption coefficients. The above technique was used for the majority of the comparisons in this chapter.

To obtain the absorption coefficient $\alpha$ from the predicted major species concentrations and temperatures, we utilized an absorption code developed by Seitzmann (1991). This code accounts for changes both in the ground state Boltzmann distribution and the overlap fraction between the laser linewidth and the collisionally broadened NO spectrum. Comparisons between NO absorption spectra generated by this code and excitation scans performed in our laboratory yielded excellent agreement both at 1.00 and 14.6 atm. The atmospheric agreement, which is most pertinent to the current work, is shown in Fig. 6.4. Several non-NO features appear in the experimental spectra, as described by Thomsen (1996). Nevertheless, the shape, magnitude and position of the NO features are well predicted by the model. This agreement gave us confidence that the absorption code is suitable for correcting our LIF measurements of NO.
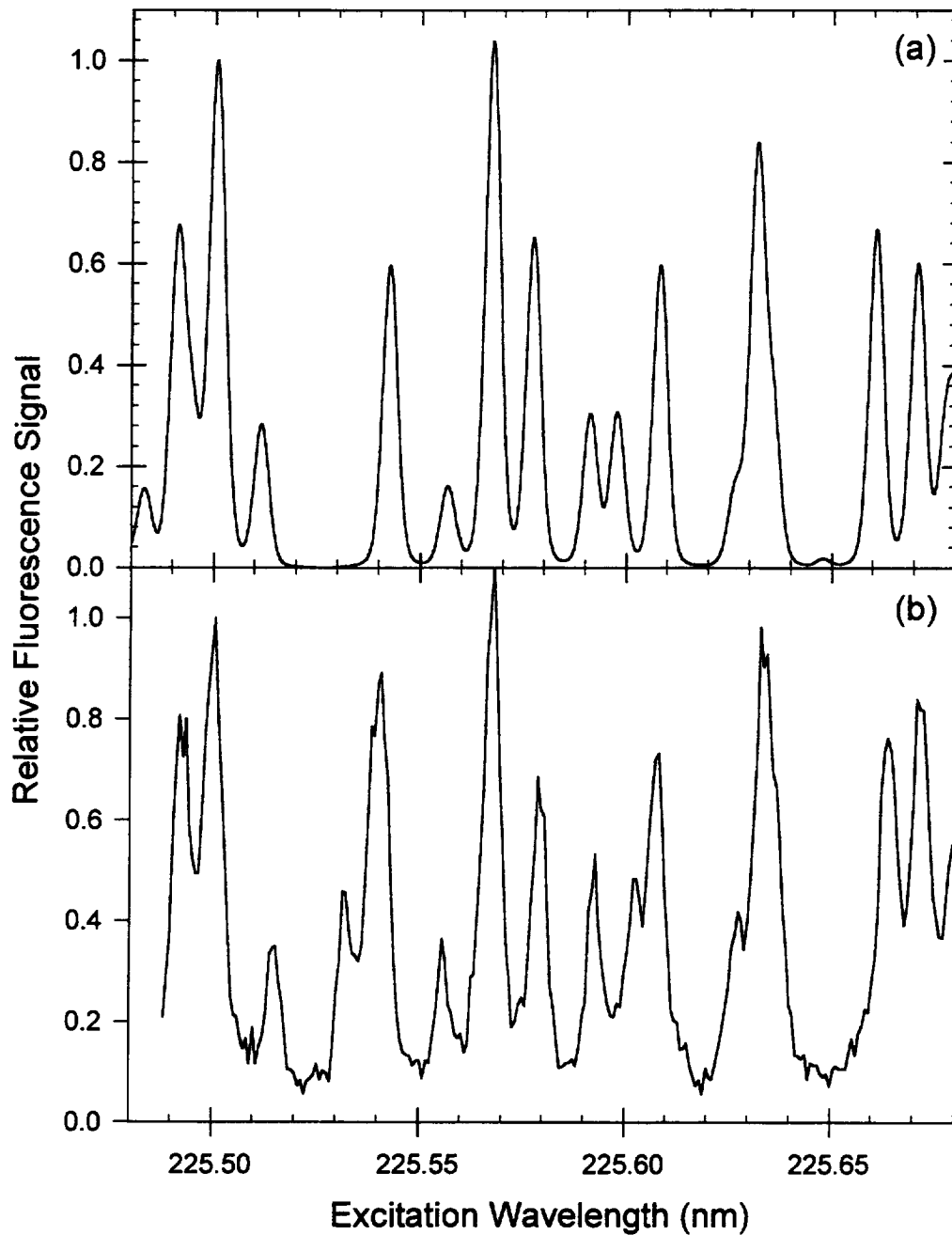
Figure 6.4: Comparison of experimental and predicted NO excitation spectra at atmospheric pressure. The predicted spectrum (a) assumes a temperature of 1800 K. The experimental spectrum (b) was taken in a $\phi$=0.60, $N_2/O_2$=3.10, $CH_4/O_2/N_2$ flame stabilized on a water cooled McKenna burner (Thomsen *et al.*, 1997) and includes interfering spectral features from other species, such as $O_2$.

To account for quenching variations, quenching cross-sections were calculated using the correlations of Paul *et al.* (1995) and combined in a computer code developed in our laboratory to calculate the quenching rate coefficients needed for correction of the fluorescence signal. Though earlier modeling using these correlations had predicted less than a 10% variation in the quenching rate within the post-flame zone of a series of lean, premixed flames (Klassen *et al.*, 1995), significant differences were found between the quenching environments of the post-flame and preheat zones of the current flames.

For some counterflow flames, the LIF data were corrected directly for variations in the quenching and absorption coefficients based on the major species concentrations and temperature predictions from the GRI modeling. Previous comparisons between GRI predictions and experimental measurements of temperature in the post-flame zone of a series of lean, premixed, burner-stabilized $CH_4/O_2/N_2$ flames, as shown in Chapter 4, demonstrated that this mechanism accurately predicts post-flame zone temperatures (within 40 K) in such flames. Hence, the temperature profiles predicted with this mechanism should be sufficient for correcting the quantitative LIF measurements. As will be shown later, this assumption is further supported in lean counterflow flames by the fact that the predicted and measured NO profiles have similar widths, which implies a good estimation of flame speed by the code. However, in rich flames, this is not the case, and thus no attempt was made to correct the LIF measurements of NO by using this technique in rich flames.

Another concern in applying such corrections to lean flames is buoyancy, which is not modeled in the Sandia flame code and which requires the axial coordinate of the experimental measurements to be adjusted slightly so as to match the positions of the predicted flamefronts. This was accomplished by matching the location of the one-half maximum fluorescence signal at each flame front with that predicted from the GRI modeling. These corrected coordinates were then used with the modeling to determine major species concentrations and temperatures for each experimental measurement.

<u>6.3 Results and Discussion</u>

Using the above techniques, LIF measurements of NO concentration were obtained in a series of premixed, counterflow, $CH_4/O_2/N_2$ flames. The separation distance of the two 1-cm diameter burners was chosen to be 1.0 cm. In the first group of flames, the $N_2/O_2$ dilution ratio was maintained at 3.76 to simulate air. The next two groups of flames varied the $N_2/O_2$ dilution ratio so as to maintain a constant reactant velocity, 35 cm/s and 40 cm/s, respectively, with changes in stoichiometry. In all cases, the top and bottom streams were identical and the velocity of the reactants was chosen to place the visible flamefront approximately 3 mm from the bottom burner surface. A summary of the flame conditions studied is provided in Table 6.1; the listed flow rates are the same for each of the opposed reactant streams.

Figure 6.5 shows the results of these measurements for the leanest flames studied at a dilution ratio of 3.76: $\phi=0.65$, V=35 cm/s; $\phi=0.70$, V=40 cm/s; and $\phi=0.75$, V=50 cm/s where V is the cold-flow velocity at the burner exit. As described above, all of the the modeling predictions have been uncorrected to facilitate direct comparison with the LIF data. The outstanding feature of these three plots is the excellent agreement between the LIF measurements and the GRI modeling. This agreement is far superior to that previously found in the burner-stabilized, lean-premixed flames of Chapter 4, indicating that either the dominant NO formation mechanism in these flames is better known than for those stabilized on a water-cooled burner or some fortuitous combination of inaccuracies leads to better agreement for this configuration.

Another feature of Fig. 6.5 is the effect of buoyancy, as indicated by the slight difference in the location of each flamefront between the experimental and modeling results. Buoyancy has the net effect of shifting the flamefronts toward the top burner and slightly compressing the distance between the top and bottom flamefronts. Thus, buoyancy causes the greatest discrepancy in each case for the location of the bottom flamefront. We further note that the leaner, lower velocity flames are affected by this tendency to a greater extent than their richer, higher velocity counterparts. For all of these

Table 6.1: Flame conditions, predicted peak temperatures and flow rates for atmospheric pressure, counterflow, premixed $CH_4/O_2/N_2$ flames. OPPDIF predicted temperatures were calculated via the coupled species and energy equations without the inclusion of a radiation source term in conjunction with the GRI reaction mechanism.

| Dilution Ratio | Equiv. Ratio | Exit Vel. (cm/s) | Predicted Temp. (K) | Component Flow Rates (SLPM) | | |
|---|---|---|---|---|---|---|
| | | | | $CH_4$ | $O_2$ | $N_2$ |
| 3.76 | 0.65 | 35 | 1750 | 0.105 | 0.324 | 1.22 |
| 3.76 | 0.70 | 40 | 1830 | 0.129 | 0.369 | 1.39 |
| 3.76 | 0.75 | 50 | 1900 | 0.172 | 0.459 | 1.73 |
| 3.76 | 0.80 | 65 | 1970 | 0.237 | 0.594 | 2.23 |
| 3.76 | 0.90 | 120 | 2040 | 0.488 | 1.085 | 4.08 |
| 3.76 | 1.00 | 150 | 2070 | 0.672 | 1.344 | 5.05 |
| 3.76 | 1.10 | 150 | 2080 | 0.732 | 1.331 | 5.01 |
| 3.76 | 1.20 | 125 | 2040 | 0.659 | 1.099 | 4.13 |
| 3.76 | 1.30 | 100 | 1950 | 0.566 | 0.871 | 3.28 |
| 3.76 | 1.40 | 65 | | 0.393 | 0.561 | 2.11 |
| 3.76 | 1.50 | 50 | | 0.321 | 0.428 | 1.61 |
| Constant velocity flames based on $\phi$=0.65 nominal condition. | | | | | | |
| 4.13 | 0.70 | 35 | 1750 | 0.105 | 0.301 | 1.24 |
| 4.86 | 0.80 | 35 | 1740 | 0.105 | 0.264 | 1.28 |
| 5.59 | 0.90 | 35 | 1700 | 0.105 | 0.234 | 1.31 |
| Constant velocity flames based on $\phi$=0.7 nominal condition. | | | | | | |
| 4.44 | 0.80 | 40 | 1830 | 0.129 | 0.323 | 1.43 |
| 5.12 | 0.90 | 40 | 1790 | 0.129 | 0.287 | 1.47 |
| 5.80 | 1.00 | 40 | 1700 | 0.129 | 0.258 | 1.50 |
| 5.75 | 1.10 | 40 | 1680 | 0.142 | 0.258 | 1.48 |
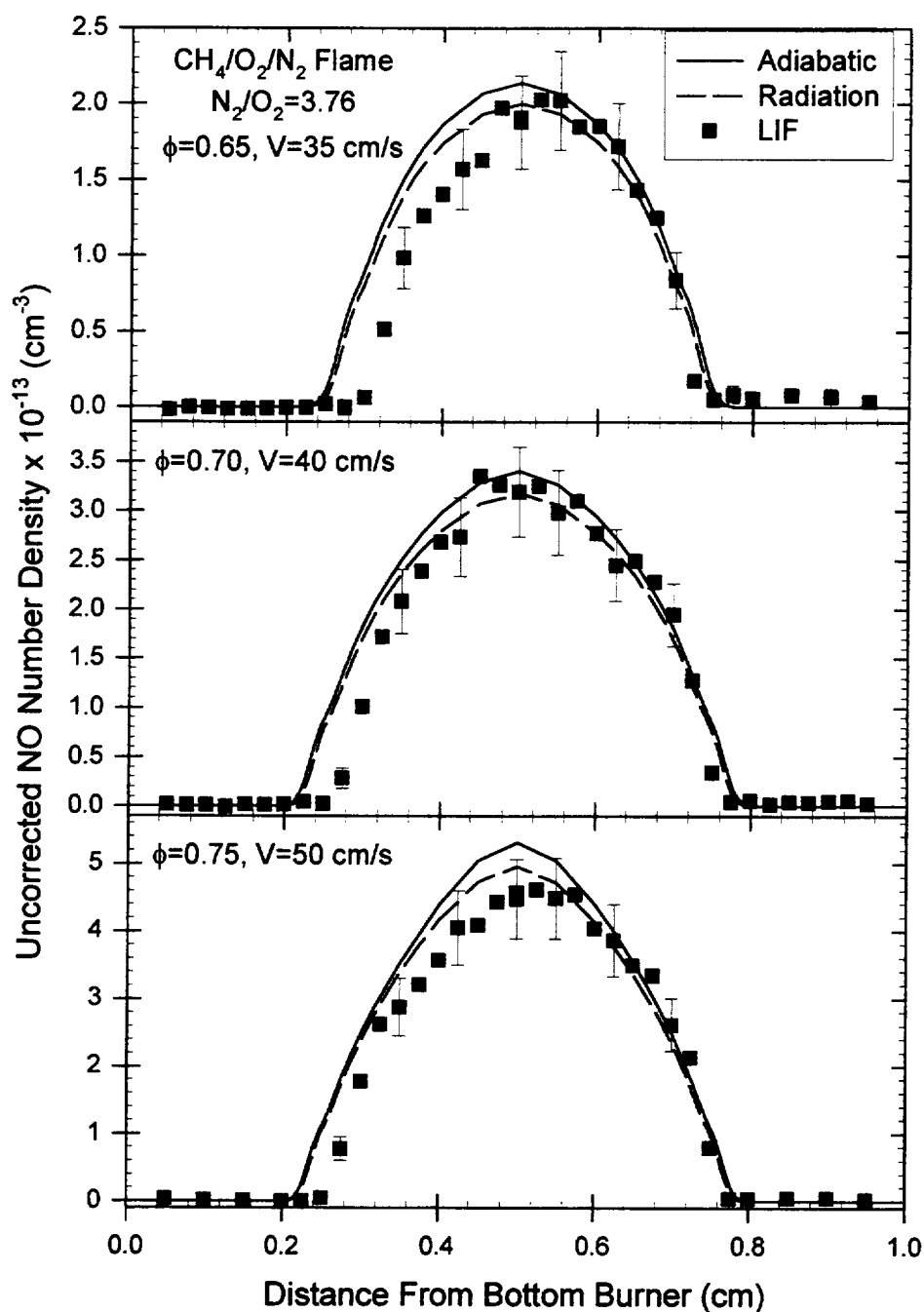
Figure 6.5: LIF-measured and predicted NO concentrations (uncorrected) in lean premixed, atmospheric pressure, $CH_4/O_2/N_2$ flames $(0.65 \leq \phi \leq 0.75)$. Predictions were obtained using temperatures found via the coupled species and energy equations with and without the inclusion of a radiation source term in conjunction with the GRI reaction mechanism.

flames, however, the effect is minimal and thus the comparison between predictions and measurements can proceed with confidence.

The flames in Fig. 6.5 also show only a modest 5-10% sensitivity in peak NO concentration to the inclusion of radiation in the OPPDIF code. Furthermore, this sensitivity does not seem to increase with flame temperature as might be expected. The explanation for this behavior is most likely the presence of higher velocities and lower residence times in the higher temperature flames, which restricts both the time for heat transfer to occur and the time over which the temperature-sensitive thermal NO pathway can form NO in the post-flame zone.

Figure 6.6 considers similar measurements for slightly lean to stoichiometric flames: $\phi$=0.80, V=65 cm/s; $\phi$=0.90, V=120 cm/s; and $\phi$=1.00, V= 150cm/s. The results for these three flames are not as well predicted as those shown in Figure 6.5. However, in each case, the predicted peak NO concentration still falls within the error bars of the experimental measurements. This agreement is still considerably better than that found in the burner-stabilized flames of Chapter 4. Two further observations can be made about the flames of Fig. 6.6. First, we note that the radiation correction becomes insignificant closer to stoichiometric conditions. This observation is somewhat counterintuitive because of the higher temperatures of near stoichiometric flames, as well as the greater dependence of NO concentration on the highly temperature-sensitive, thermal NO pathway. However, as mentioned previously, this unexpected behavior results from the decreased residence time of these high-velocity flames.

The second observation from Fig. 6.6 is that the experimental profile becomes increasingly wide relative to the modeling predictions at higher equivalence ratios. In fact, in the stoichiometric case, the full-width at half-maximum of the experimental NO concentration profile is nearly twice that predicted by the modeling. This behavior indicates some disturbing discrepancies between the predicted and actual flame speeds for these flame conditions, as probe volume effects with the 250-$\mu$m laser beam cannot explain the 0.5 to 1.0 mm discrepancy in the position of each profile. Furthermore, model predictions show no significant separation between the flame front and the predicted NO
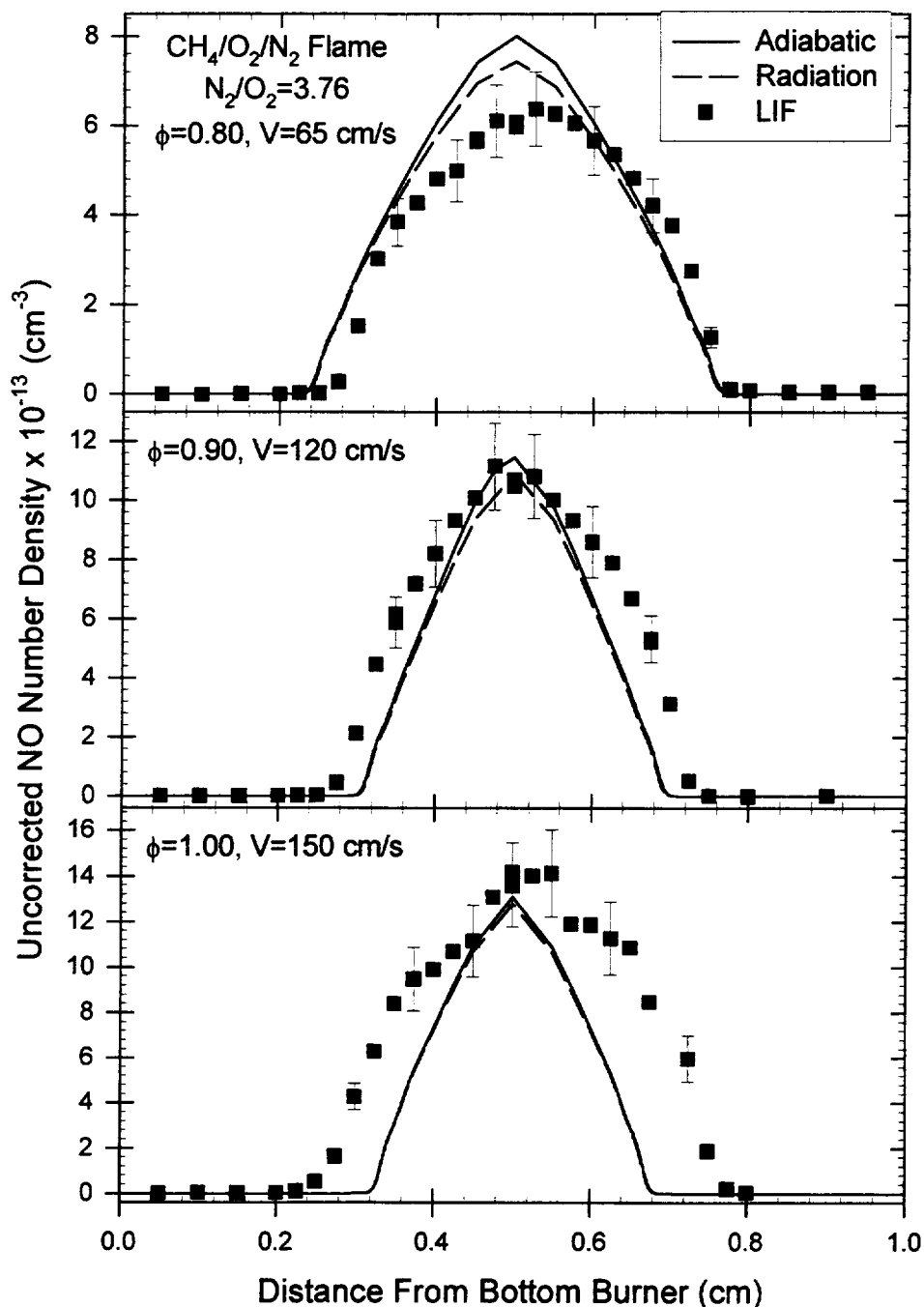
Figure 6.6:  LIF-measured and predicted NO concentrations (uncorrected) in slightly-lean, premixed, atmospheric pressure, $CH_4/O_2/N_2$ flames ($0.80 \leq \phi \leq 1.00$). Predictions were obtained using temperatures found via the coupled species and energy equations with and without the inclusion of a radiation source term in conjunction with the GRI reaction mechanism.

profile, which could indicate an overprediction of NO destruction on the reactant side of the flame. The conclusion seems to be that there is some real discrepancy in flame location between experiments and measurements, which may indicate the need for some modification in the hydrocarbon chemistry of the current GRI reaction mechanism (version 2.11), although clearly it is beyond the scope of the current investigation to suggest exactly what changes need to be made in this area.

This unfortunate trend of wider experimental profiles continues under moderately rich conditions as shown in Fig. 6.7, which extends the measurements to the following flames: $\phi$=1.10, V=150 cm/s; $\phi$=1.20, V=125 cm/s; and $\phi$=1.30, V= 100cm/s. We note that despite the continuing discrepancy in profile width, the modeling does predict the shift from peaked NO profiles near stoichiometric conditions to relatively flat profiles in rich flames. However, under these moderately rich conditions, we begin to observe the first significant deviation between peak NO concentrations as predicted by the GRI reaction mechanism and those measured experimentally. Specifically, the code begins to dramatically underpredict NO concentrations as the stoichiometry shifts toward moderately rich conditions. Furthermore, it becomes impossible to obtain code solutions for stoichiometries beyond those shown in Fig. 6.7, possible owing to continued flame-speed problems and thus premature predictions of flame extinction.

The peak NO concentrations in these flames, as measured using LIF as well as predicted with the GRI reaction mechanism, display trends that are quite similar to those found in Chapter 4 for the post-flame zone of flat, laminar, premixed, burner-stabilized flames. To compare the two cases, Figure 6.8 displays the measured and modeled peak NO concentrations from the counterflow flames of this chapter beneath a similar profile of measured and modeled NO concentrations for the atmospheric flames of Chapter 4. The first observation from this figure is that the NO concentrations are considerably higher in the counterflow flames. This behavior is consistent with the higher flame temperatures found in these nearly adiabatic flames as compared to the highly-nonadiabatic, burner-stabilized flames. Second, the underprediction (by 30-50%) of NO concentration in lean, premixed, burner-stabilized flames is not duplicated in the counterflow flames. This
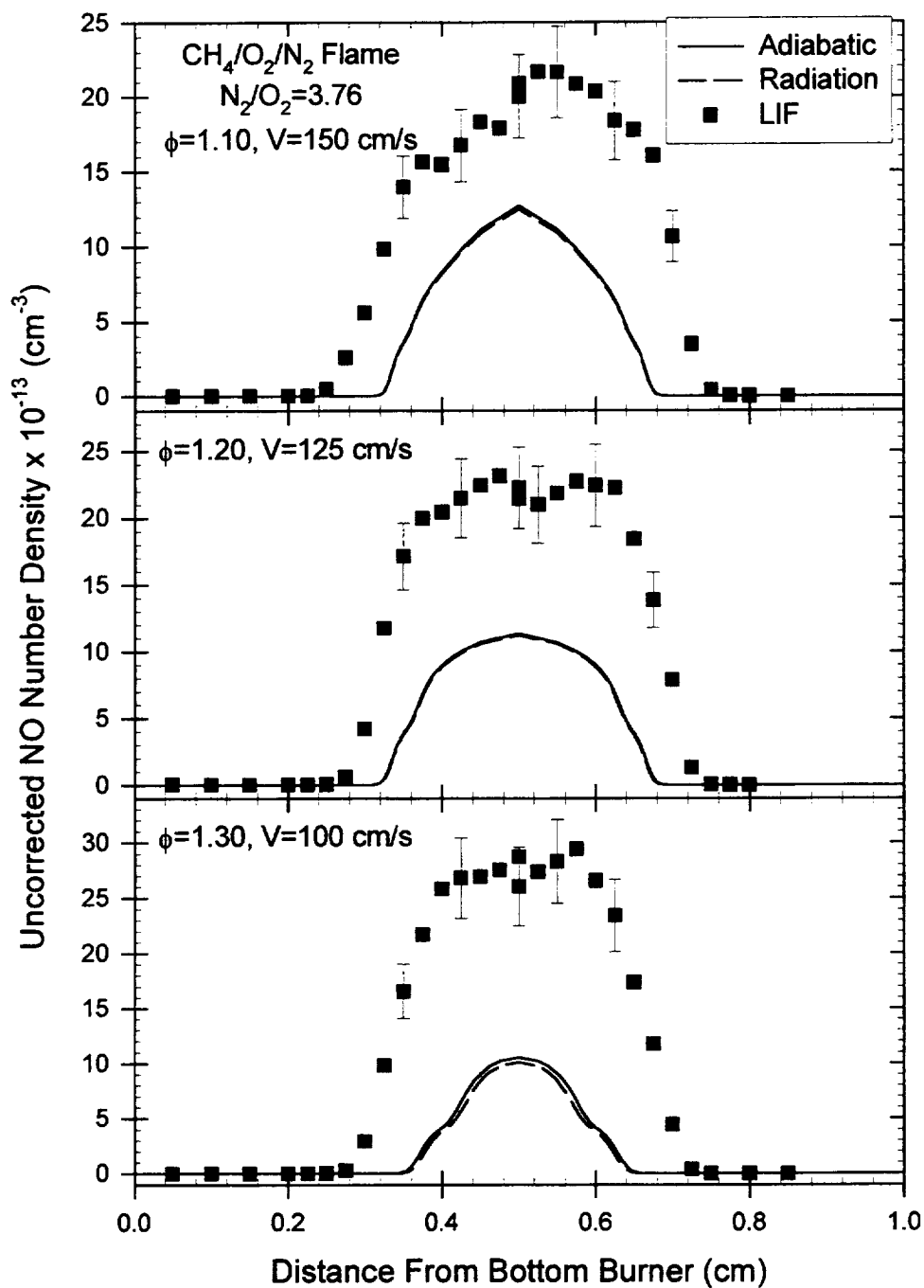
Figure 6.7: LIF-measured and predicted NO concentrations (uncorrected) in slightly-rich, premixed, atmospheric pressure, $CH_4/O_2/N_2$ flames ($1.10 \leq \phi \leq 1.30$). Predictions were obtained using temperatures found via the coupled species and energy equations with and without the inclusion of a radiation source term in conjunction with the GRI reaction mechanism.
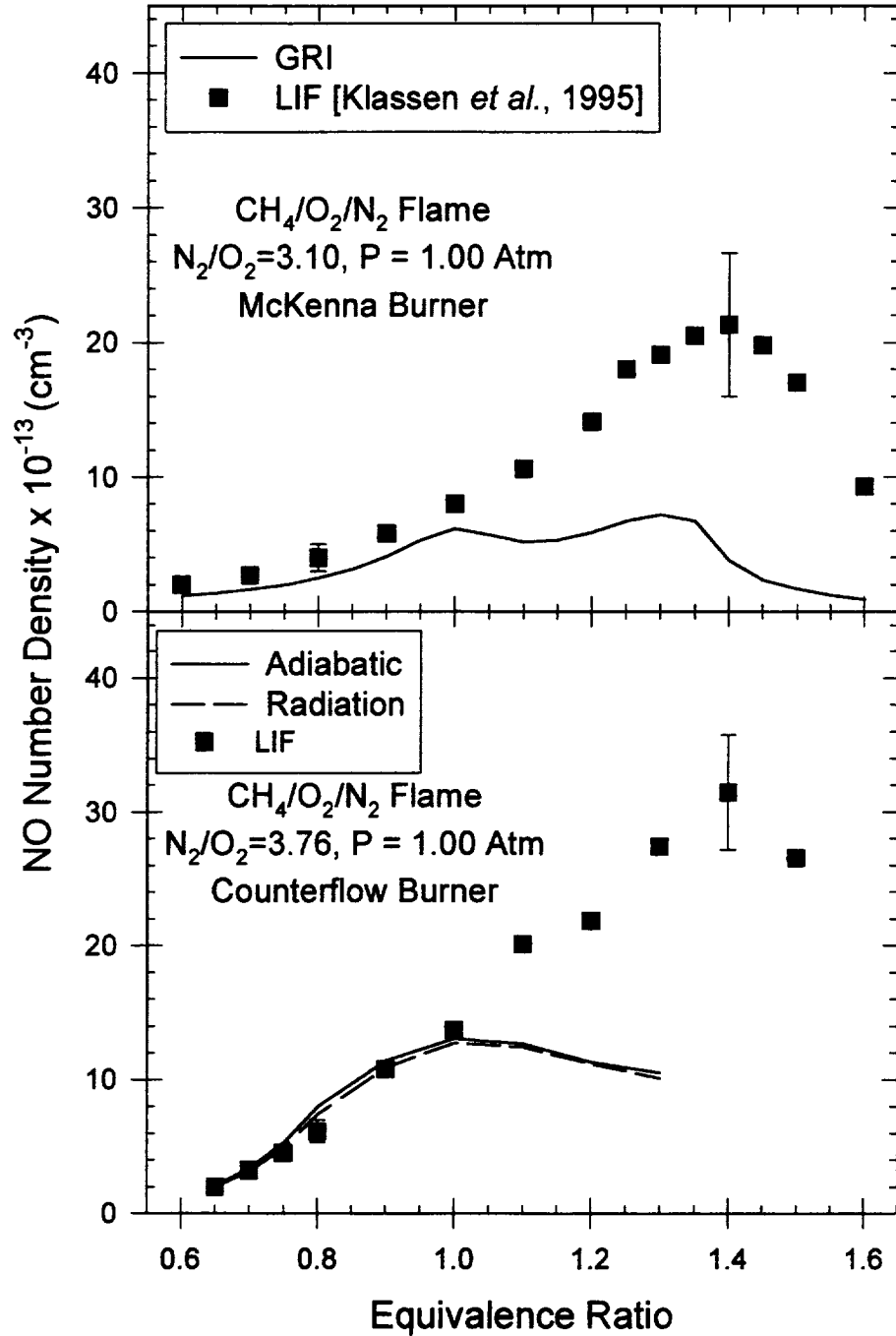
Figure 6.8: Peak LIF-measured and predicted NO concentrations in burner stabilized (top) and counterflow (bottom) premixed, atmospheric pressure, $CH_4/O_2/N_2$ flames. Predictions were obtained using temperatures predicted via the coupled species and energy equations with and without the inclusion of a radiation source term in conjunction with the GRI reaction mechanism.

feature could indicate either a shift in key reaction pathways, such as an increased importance of Zeldovich NO formation in the higher-temperature counterflow flames, or an incorrect temperature dependence for some of the NO formation reactions.

A third observation from Figure 6.8 is that the rich-side behavior of both the experiments and predictions is nearly identical for the two flame configurations. In both cases, the peak NO concentration is found at the moderately rich stoichiometry of $\phi$=1.40. Moreover, for both configurations, the GRI reaction mechanism completely fails to capture even the qualitative behavior of NO formation in rich flames, leading to substantial underprediction of the peak NO concentrations.

As mentioned in Chapter 4, the failure of the GRI mechanism to capture this qualitative behavior under rich conditions indicates that perhaps the rate coefficient for the prompt initiation reaction,

$$CH+N_2 \Leftrightarrow HCN+N, \qquad (R1)$$
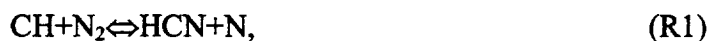
is too low. Recent work by Berg $et$ $al.$ (1998) concludes that the rate coefficient for Reaction (R1), as used in the GRI mechanism, must be increased by a factor of between 2.1 and 2.8 to match their measurements in a series of low-pressure methane flames. However, such a modification would still be inadequate to explain the large underprediction of NO observed in the ultra-rich flames ($\phi \geq 1.30$) of Fig. 6.8. Another possibility for the apparent underprediction of prompt NO formation in the GRI mechanism is inaccuracies in its CH production and destruction kinetics.

Because of the excellent agreement between the shape and magnitude of the experimental and predicted NO profiles for the leanest flames of Figures 6.5 and 6.6, we would expect similarly good predictions of the major species concentrations and temperatures via the GRI reaction mechanism for these lean flames. Based on this presumption, we may employ predicted profiles to correct the NO measurements directly for quenching and absorption so as to obtain absolute NO concentration profiles. To correct for any shift of the flamefronts owing to buoyancy effects, the half-maximum LIF signal was matched with the half-maximum "uncorrected" concentration predictions of Figures 6.5 and 6.6. This procedure provided an adjusted coordinate scheme which
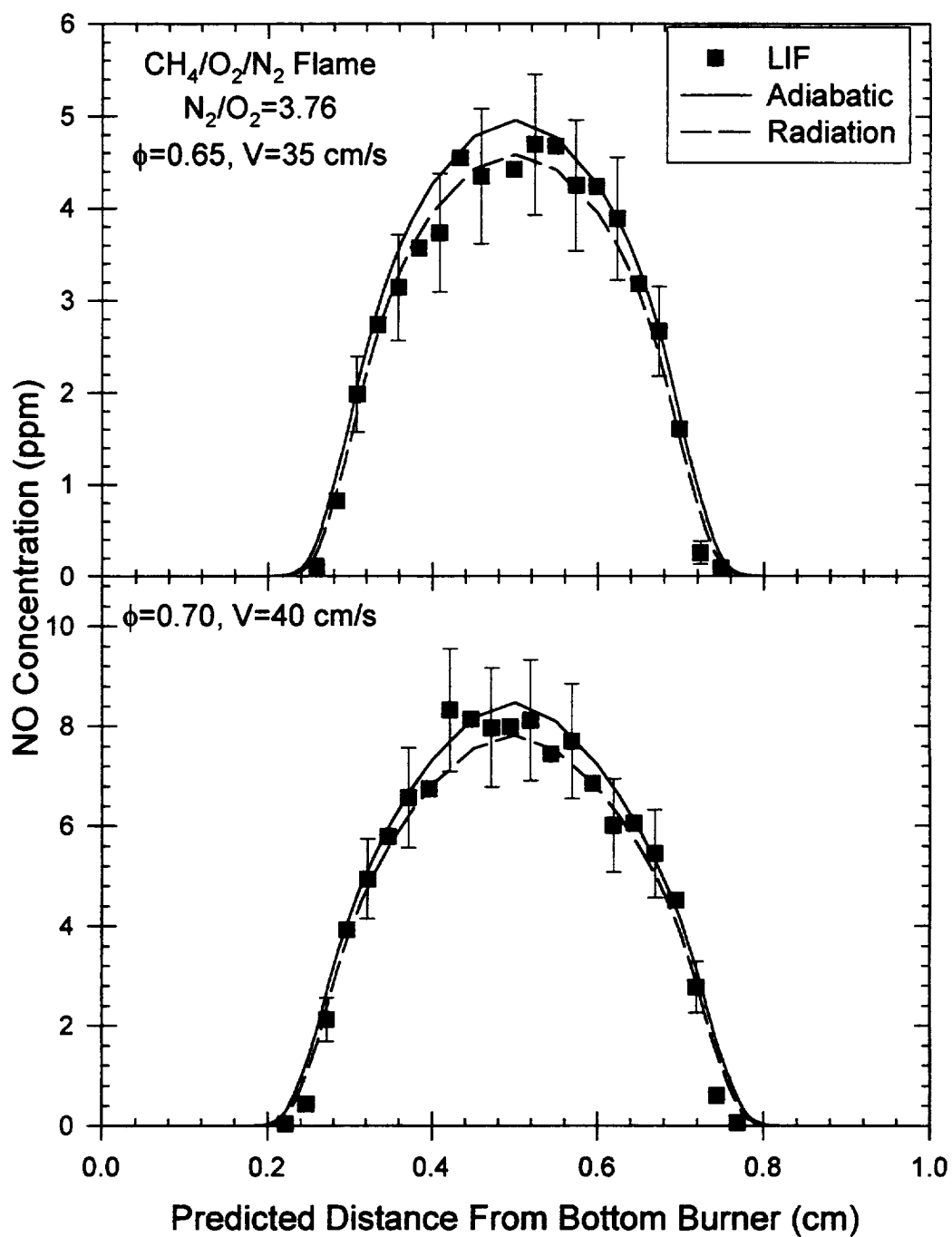
Figure 6.9: Corrected LIF-measured and predicted NO concentrations in lean premixed, atmospheric pressure, $CH_4/O_2/N_2$ flames at $\phi=0.65$ and $\phi=0.70$. Predictions were obtained using temperatures found via the coupled species and energy equations with and without the inclusion of a radiation source term in conjunction with the GRI reaction mechanism.
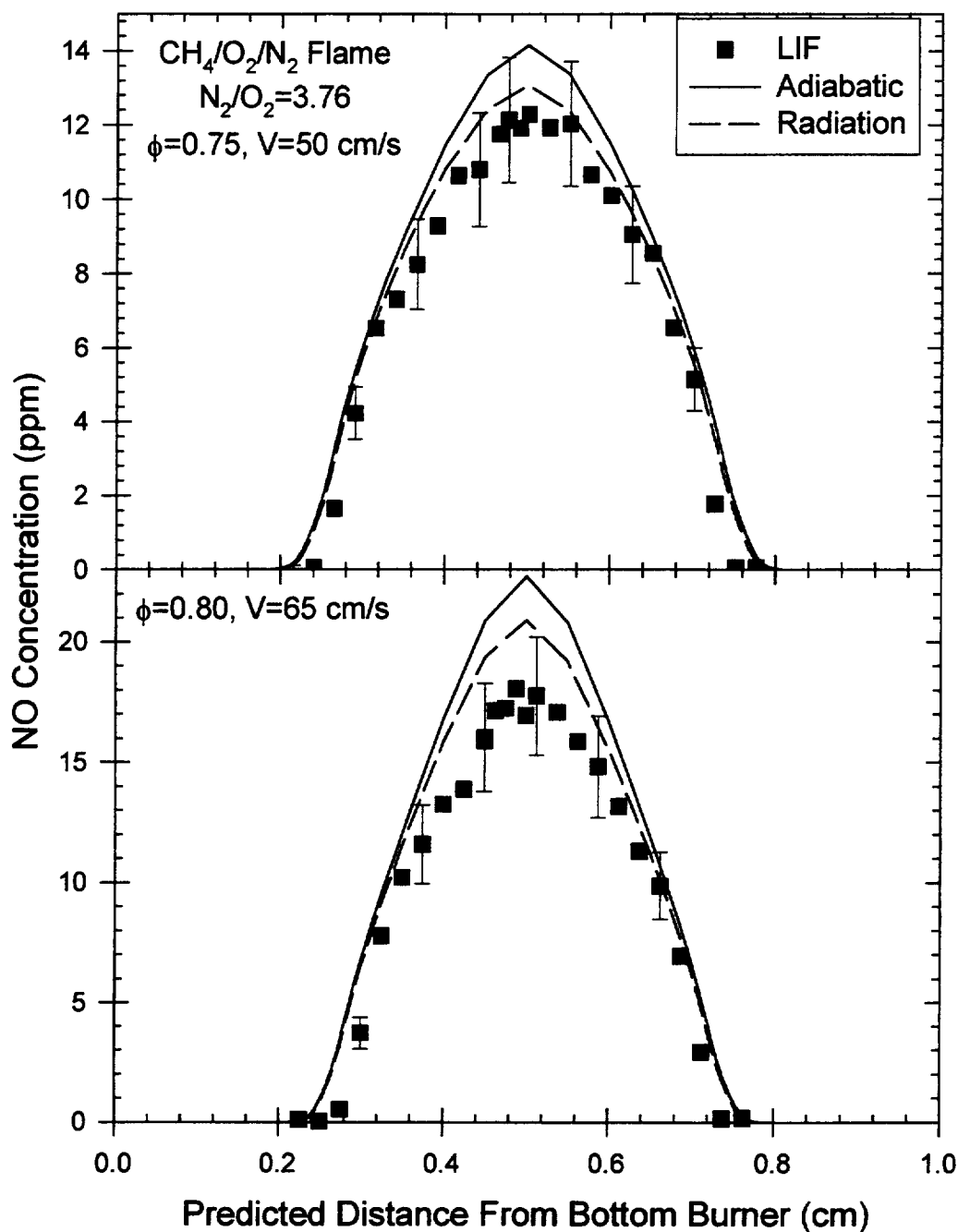
Figure 6.10: Corrected LIF-measured and predicted NO concentrations in lean premixed, atmospheric pressure, $CH_4/O_2/N_2$ flames at $\phi=0.75$ and $\phi=0.80$. Predictions were obtained using temperatures found via the coupled species and energy equations with and without the inclusion of a radiation source term in conjunction with the GRI reaction mechanism.

permitted the association of predicted major species concentrations and temperatures to each experimental data point. The results of this analysis are shown in Figs. 6.9 and 6.10. These figures further emphasize the excellent agreement displayed between the experimental and predicted NO profiles in these lean counterflow premixed flames and demonstrate the ability of the LIF technique to provide quantitative NO measurements for this flame configuration.

For the above NO concentration profiles, the stoichiometry was altered while the dilution ratio and relative flame positions were kept constant. This experimental procedure results in large variations in flame temperature which could have a profound impact on the underlying NO kinetics. Therefore, an apparent change in the predictive capability of the model from one flame condition to another could just as easily be due to improper activation energies and temperature exponential factors for some key reactions as to shifts between well- and poorly-known NO formation pathways owing to changes in the stoichiometry. To separate some of these effects, we have also investigated a range of flames at relatively constant temperature but varying stoichiometry. Consequently, two new series of flames were identified in which the $N_2/O_2$ dilution ratio was varied to compensate for the oxygen removed when proceeding to the next richer condition. The flow rates, dilution ratios, stoichiometries and predicted temperatures of these flames are summarized in Table 1. The resulting lean flames now exhibit a slight decrease in temperature with increases in stoichiometry instead of the strong increase in temperature observed for the constant dilution ratio cases.

The first series of such diluted flames was based on the standard case of a $\phi$=0.65, V=35 cm/s, $CH_4/O_2/N_2$ flame. As oxygen was removed to increase the stoichiometry to equivalence ratios of $\phi$=0.7, 0.8, and 0.9, additional nitrogen was added to keep the flame velocity and temperature nearly constant. The results of this study are shown in Fig. 6.11. One observation from Fig. 6.11 is that the NO concentrations in these flames are all lower than their undiluted counterparts, with the largest decrease (~50%) occurring in the $\phi$=0.90 flame. This result underscores the importance of temperature in NO formation chemistry. Another observation is that as $\phi$ increases, the diluted flames do not exhibit the
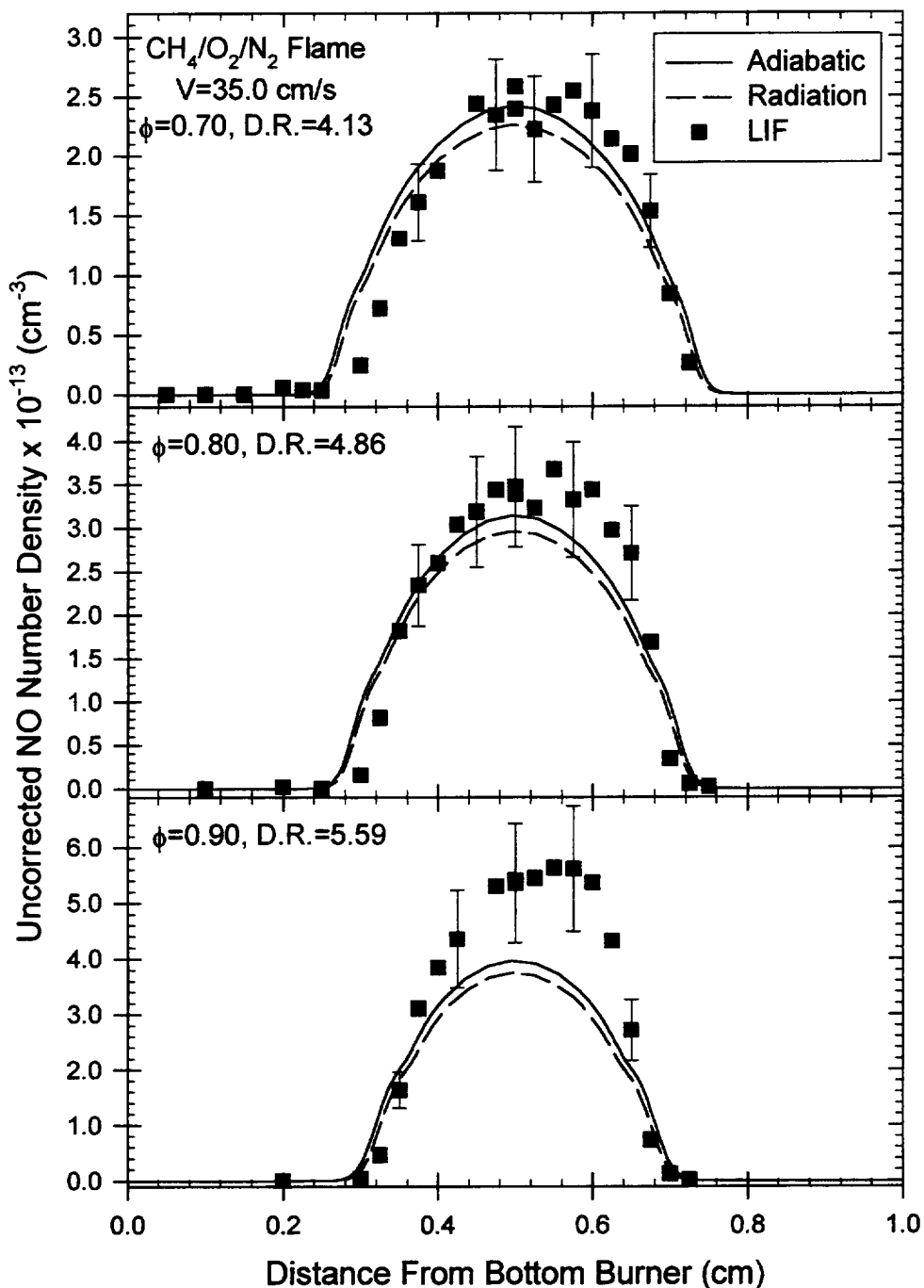
Figure 6.11: LIF-measured and predicted NO concentrations (uncorrected) in nitrogen-diluted, premixed, atmospheric pressure, $CH_4/O_2/N_2$ flames (V=35.0 cm/s). Predictions were obtained using temperatures found via the coupled species and energy equations with and without the inclusion of a radiation source term in conjunction with the GRI reaction mechanism.
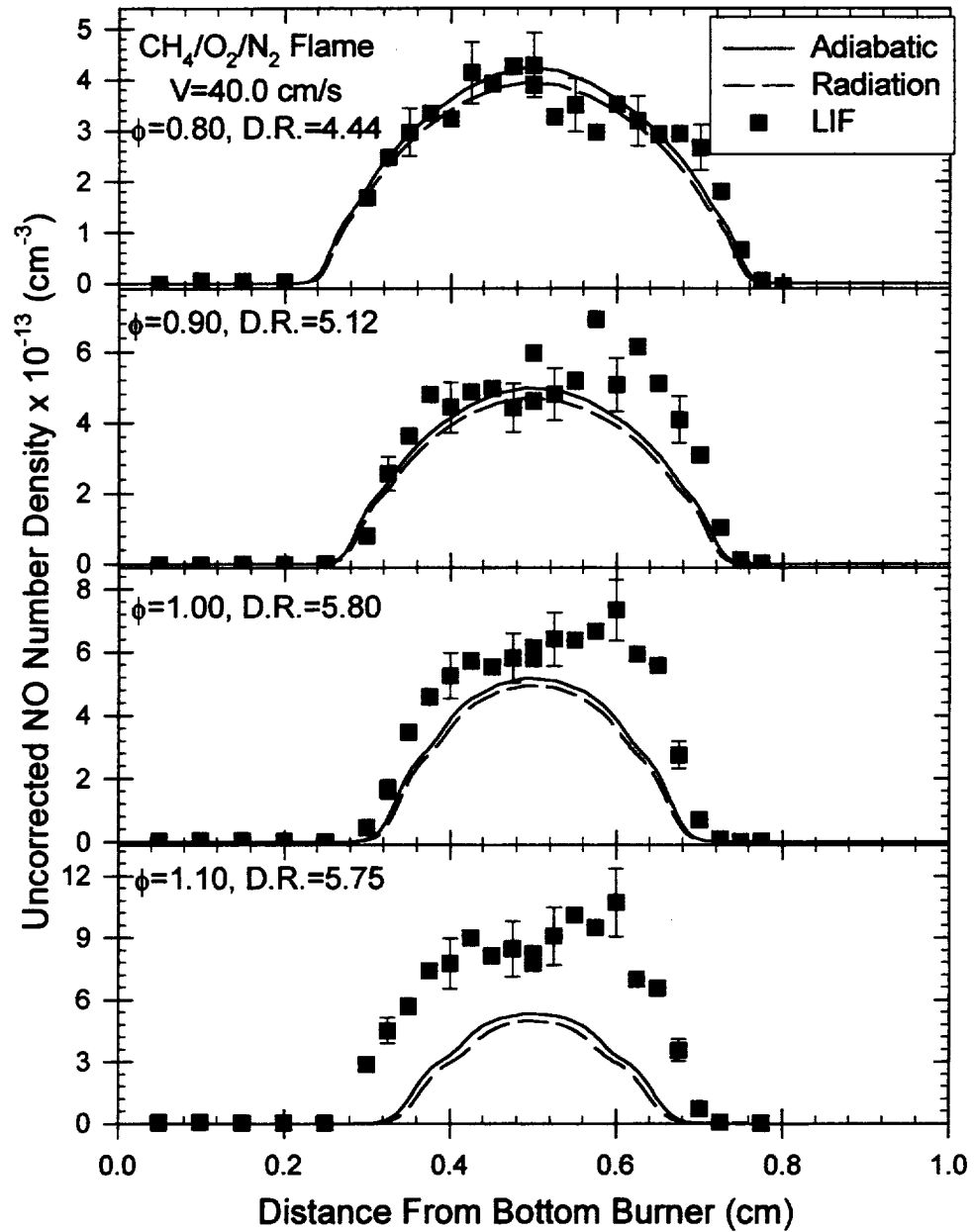
Figure 6.12: LIF-measured and predicted NO concentrations (uncorrected) in nitrogen-diluted, premixed, atmospheric pressure, $CH_4/O_2/N_2$ flames. Predictions were obtained using temperatures found via the coupled species and energy equations with and without the inclusion of a radiation source term in conjunction with the GRI reaction mechanism.

increasingly pointed profile observed in the undiluted flames. This feature is also expected since a pointed profile is indicative of a strong thermal NO contribution in the post-flame zone, which would not be present in these cooler flames.

Two more observations can be made about these diluted flames. First of all, the widening of the experimental NO profile, with increases in stoichiometry, relative to that predicted by the GRI mechanism seems to be delayed in these flames. This widening was clearly visible in the undiluted, $\phi=0.9$ flame of Fig. 6.6; however, no such widening occurs in the diluted $\phi=0.9$ flame of Fig. 6.11. This result could indicate that incorrect predictions of either strain rate or temperature effects on the predicted flame speed are responsible for the widening behavior. The second observation from Fig. 6.11 is that peak NO concentrations are being underpredicted at leaner stoichiometries in these diluted flames as compared to the undiluted flames. This observation is consistent with the underprediction of NO concentrations in the rich flames of Fig. 6.7. In particular, for the undiluted flames, the dominance of the relatively well-known thermal NO mechanism near $\phi=1$ apparently delays any underprediction to richer stoichiometries, possibly owing to inaccuracies in the prompt NO kinetics.

To extend this study to higher temperatures as well as to slightly richer stoichiometries, a second series of nitrogen diluted flames was studied based on the reference condition for a $\phi=0.70$, V=40 cm/s, $CH_4/O_2/N_2$ flame. The results of this investigation are shown in Fig. 6.12. As for the previous series of diluted flames, these flames do not exhibit the pointed profiles observed for the near stoichiometric undiluted flames. A similar delay also exists in the widening of the experimental profile, although significant widening is observed for the $\phi=1.10$ flame of Fig. 6.12. Unlike the previous series, however, no distinct overprediction of NO occurs in the $\phi=0.90$ flame. This behavior, as well as the generally higher concentrations of NO in these flames, may be due to a moderate increase in peak temperature (from ~1720 K to ~1800 K) between these two series of flames.

## 6.4 Analysis of Chemical Kinetic Behavior

To better understand the behavior of the GRI mechanism with respect to its prediction of NO formation in premixed counterflow flames, we sought to determine the relative contribution to the overall NO concentration from each of the four major NO formation pathways (Zeldovich, $N_2O$ intermediate, prompt, and NNH). In this type of analysis, the contribution of each mechanism is determined by either removing an initiation reaction for a pathway (subtraction technique) or including only the relevant kinetics for a given pathway (addition technique) and determining the effect on the predicted NO contribution for the full kinetic model. The accuracy of such a modeling technique only holds to the extent that the species concentrations modified by the changes in the overall chemical kinetic mechanism do not significantly inhibit or accelerate the kinetics of the other pathways. For the cases presented in this chapter, such inter-pathway dependencies have been found to be minimal, although such effects could limit the applicability of this technique for other flame conditions.

For this study, the various NO pathway contributions were determined in the following manner. The prompt NO contribution was determined simply by the removal of Reaction (R1) from the overall chemical kinetic mechanism. Unlike the similar analysis performed in Chapter 4, the thermal NO contribution was determined by removing only the initiation reaction of this pathway, i.e.,

$$N+NO \Leftrightarrow N_2+O, \tag{R2}$$

from the overall kinetic scheme. It was found in the current study that removal of the other two Zeldovich reactions, while having no effect on the predicted peak NO concentration, did perturb the NO profiles through the flamefront.

The $N_2O$ intermediate contribution was determined simply by removing all reactions involving the $N_2O$ molecule from the overall kinetic scheme. Finally, the contribution of the NNH pathway could have been determined by simply subtracting the sum of the NO contributions of the other three pathways from the total predicted NO concentration. However, this would then attribute to the NNH pathway any discrepancy caused by interpathway dependencies. Furthermore, the addition technique utilized in

Chapter 4 displayed some minor discrepancies for the rich flames of the current study. Alternately, it was found that the NNH pathway could best be calculated by removing only its initiation reaction from the GRI mechanism, i.e.,

$$NNH + O \Leftrightarrow NH + NO. \qquad (R3)$$

Using this procedure, it was found that the sum of the individual contributions agreed with the total NO concentration calculated by the full GRI mechanism to within 5% for all of the cases studied in this investigation. A more thorough discussion of the benefits and limitations of this type of analysis can be found in the work by Thomsen (1996).

Employing the above methodology, the contributions of each of the NO formation pathways were calculated for a sampling of the counterflow $CH_4/O_2/N_2$ flames investigated in this chapter. Figure 6.13(a) demonstrates the results of this analysis for the leanest flame of the current study ($\phi$=0.65, V=35 cm/s). For lean premixed flames, it has long been suggested that the $N_2O$-intermediate pathway dominates NO formation (Malte and Pratt, 1974; Nicol et al. 1993). However, as indicated by Fig. 6.13(a), the GRI mechanism predicts an equal or greater contribution from the relatively unknown NNH pathway (Bozzelli and Dean, 1995) for the $\phi$=0.65 counterflow premixed flame. The question as to whether such a large contribution from a mechanism not even included in most previous NO kinetic schemes (Glarborg et al, 1986; Miller and Bowman, 1989) is justified remains open to debate; however, as mentioned in Chapter 4, the NNH contribution should become less pronounced at higher pressures.

We further note that the predicted contribution from the prompt NO mechanism is relatively small in this flame. Recalling the results of Fig. 6.5, the experimental and predicted NO concentration profiles for this flame demonstrate remarkable agreement. However, as we can see from Fig. 6.13(a), the fact that several different pathways are prominent in this flame indicates that this good agreement could just as easily be produced by conflicting inaccuracies in multiple pathways as by an overall accurate kinetic mechanism. In fact, the poor performance of the GRI mechanism in rich flames indicates that the former may indeed be the case.
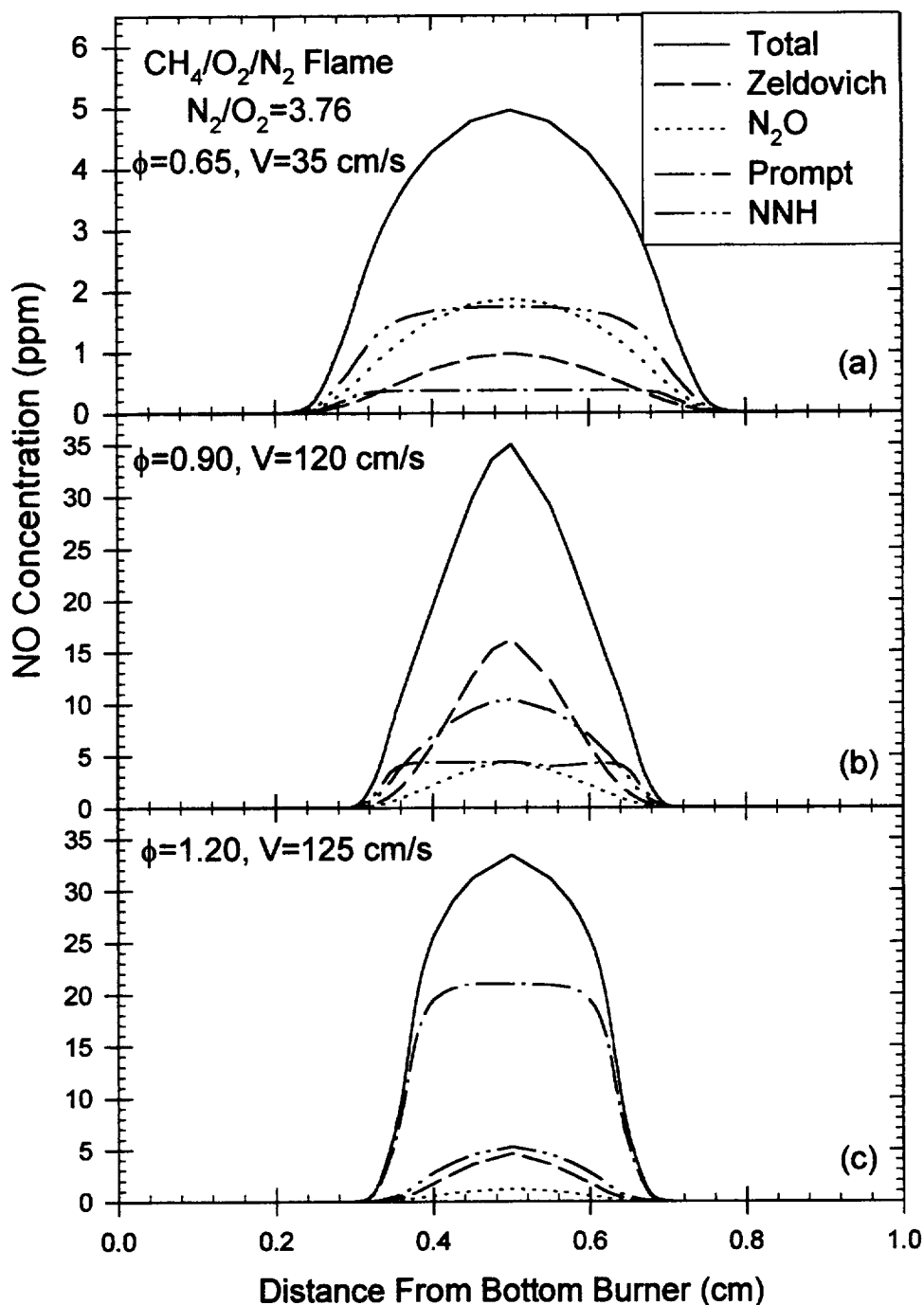
Figure 6.13: Predicted pathway contributions for modeling of NO formation in $CH_4/O_2/N_2$ counterflow premixed flames at $\phi$=0.65, $\phi$=0.90 and $\phi$=1.20. Predictions were obtained using the GRI mechanism and temperatures predicted by the coupled species and energy equations without the radiation source term.

The pathway analysis was extended next to near stoichiometric and slightly rich flames, $\phi$=0.90, V=120 cm/s and $\phi$=1.20, V=125 cm/s, respectively. Figures 6.13(b) and (c) demonstrate the results of this analysis. For the $\phi$=0.90 case, Zeldovich NO formation is the largest single contributor as might be expected for this high-temperature flame. However, a surprisingly large contribution remains from the NNH pathway. As expected, the $N_2O$ intermediate pathway begins to drop off in importance at richer stoichiometries and the prompt NO kinetics become more important. For the $\phi$=1.20 flame, prompt NO clearly dominates as a result of the higher CH concentrations under rich conditions. As shown by Fig. 6.7, NO concentrations in rich flames are substantially underpredicted by the GRI mechanism, perhaps indicating inaccuracies in the prompt NO kinetics.

To better understand which reactions play key roles for each of the NO pathways, quantitative reaction path diagrams (QRPDs) were produced for each of the above three cases using techniques similar to those employed by Lim (1998). For a QRPD, the net specific rate at which a particular elementary reaction is occurring (reactions/(cm$^3$·s)) is calculated at each grid point using a chemkin post-processing package. These rates are then numerically integrated along the central axis of the flame to obtain a total net specific reaction rate throughout the flame (reactions/(cm$^2$·s)). These integrated rates are then scaled to a maximum value and those reactions with integrated rates above some threshold percentage (1% for the current work) are shown graphically on a reaction path diagram. The thickness of the arrow representing each reaction is chosen to be proportional to its integrated net specific reaction rate, thus providing a pictorial representation of the flow of molecules within a given combustion system. For the current work, we considered only the nitrogen kinetics. Furthermore, because of the high forward and backward rates of the reactions controlling the concentrations of $N_2O$ and NNH, these reactions were lumped together and represented simply by a net reaction arrow on the respective diagrams.

Figure 6.14 shows the results of this type of analysis for the leanest flame studied ($\phi$=0.65). The relative importance of the $N_2O$ and NNH pathways clearly stands out in this diagram. For the NNH pathway, Reaction (R3) seems to be the rate-limiting step. The $N_2O$ pathway isn't quite as simple since both the $N_2O+O \Leftrightarrow 2NO$ and

116
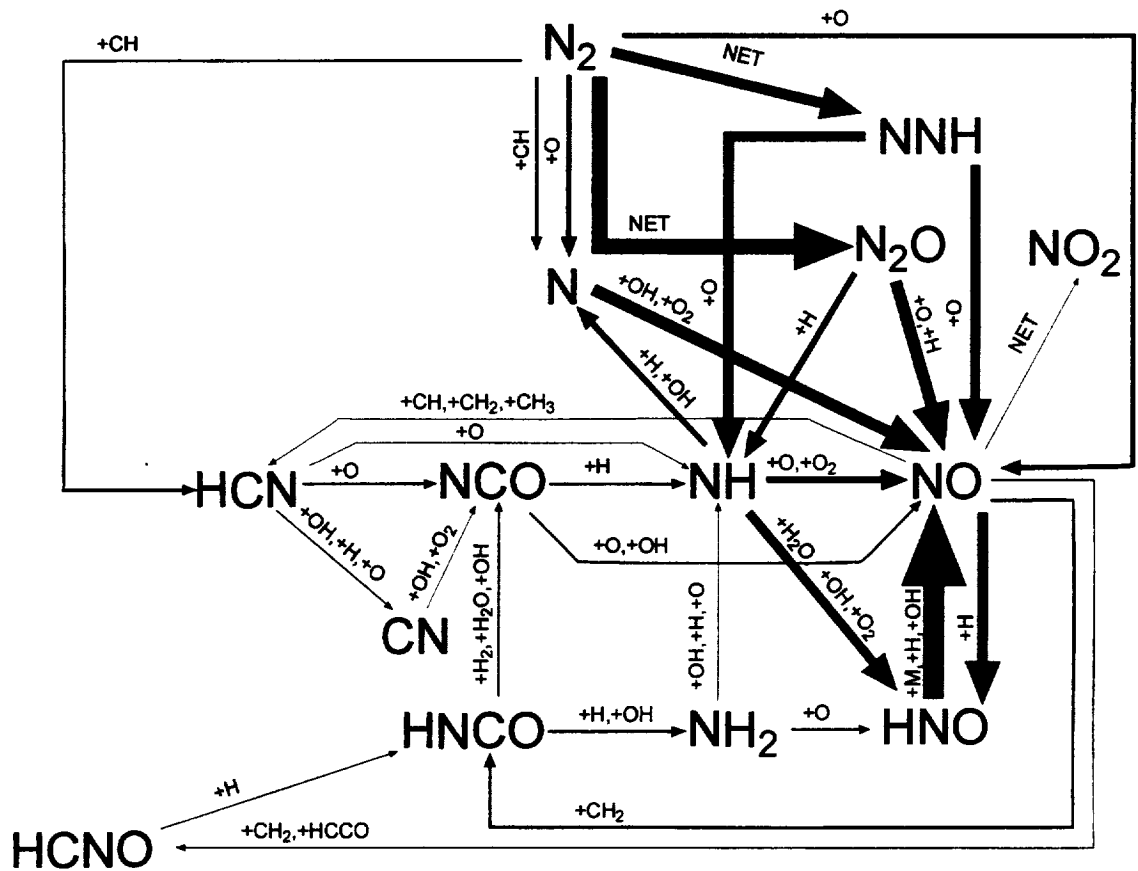


Figure 6.14: Quantitative reaction path diagram for OPPDIF predictions of NO formation in a $\phi=0.65$, $CH_4/O_2/N_2$ counterflow premixed flame at atmospheric pressure. Predictions were obtained using the GRI mechanism and temperatures found via the coupled species and energy equations without the radiation source term.

$N_2O+H\Leftrightarrow NO+NH$ reactions contribute significantly to NO formation. Furthermore, we note that the NH and HNO radicals as well as the N atom play important roles as intermediates in the NO formation chain.

For the $\phi=0.90$ flame, the $N_2O$ pathway becomes less important while the Zeldovich and prompt mechanisms become more important, as shown in Figure 6.15. The roles of atomic nitrogen and HNO as flame intermediates consequently become even more significant. Furthermore, in both lean flames, very little NO reburn is predicted by the GRI reaction mechanism. In comparison, for the flame at $\phi=1.20$, the GRI mechanism predicts a dominant contribution from the prompt NO pathway, as shown in Fig. 6.16. The activation of this pathway leads to a much larger number of intermediate species playing major roles in the NO chemistry. Furthermore, substantial NO reburn begins to show up, converting NO into such molecules as HCNO and HNCO. However, no significant pathway was found which converted NO back into $N_2$. This result seems to indicate that once $N_2$ is converted into HCN, NH, N or NO, reconversion to $N_2$ in any significant quantity will not occur under any flame conditions studied in this chapter. Finally, for richer flames, intermediate molecules such as HCN begin to become products of combustion as well. In any real combustion system, these molecules would eventually need to be burned out in a stoichiometric to lean flame which would result in their reconversion to NO. However, in this case, they exist as products and uncertainty in their final concentrations will directly impact predicted NO emissions. This issue could represent another factor leading to the large underprediction of NO concentration in these flames, as observed in Figure 6.7.

The above pathway and QRPD analyses have allowed us to identify first in a broad sense, and then in more detail, which pathways, species and individual reactions play the most important roles in forming NO for these counterflow, premixed flames. However, the magnitude of a specific reaction rate is not sufficient to determine the sensitivity of the overall NO concentration to its existence. For some reactions, alternate pathways exist which could become dominant should such reactions be removed. For example, in the prompt mechanism, removing the paths from NH to HNO would appear from Figure 6.13
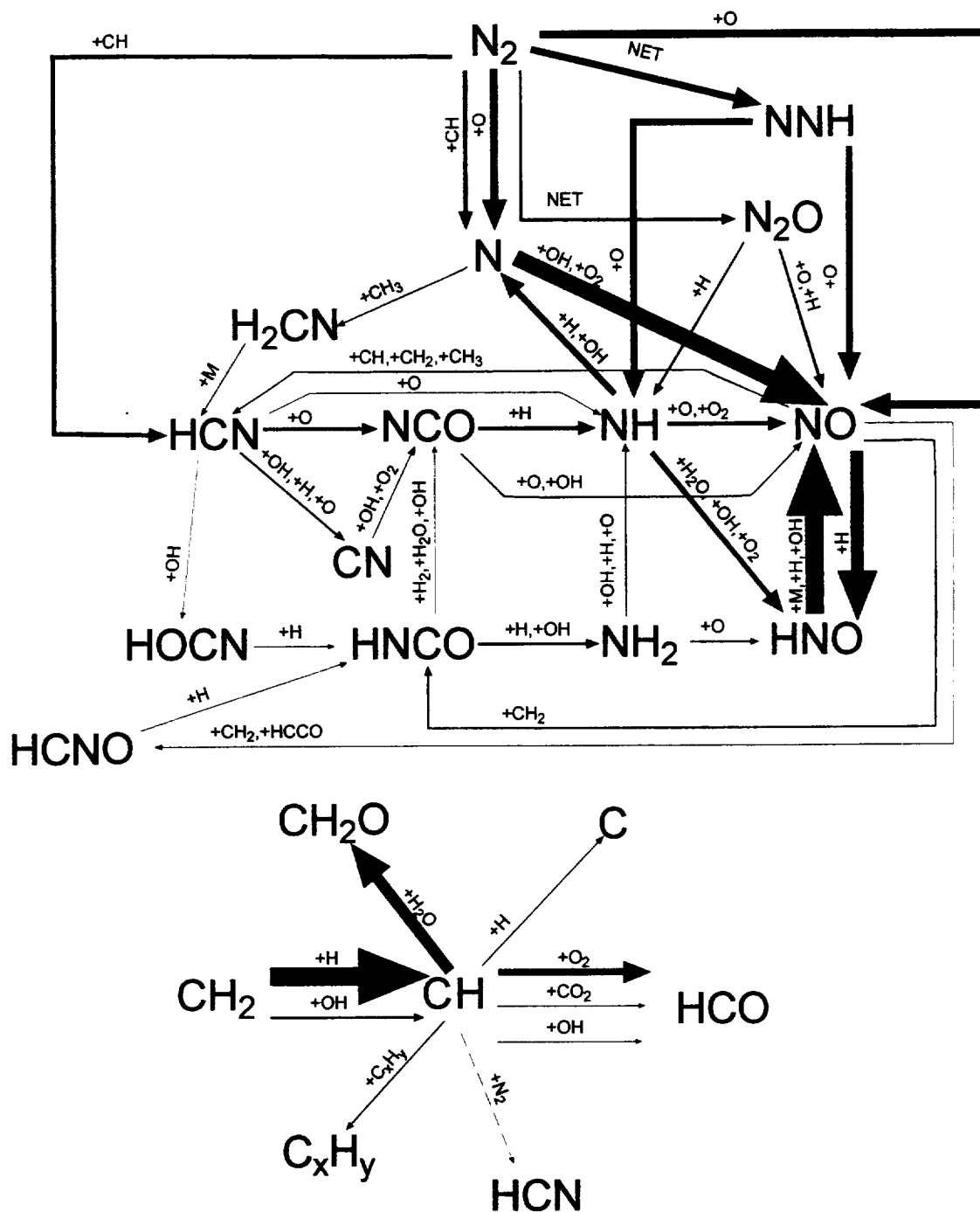
Figure 6.15: Quantitative reaction path diagram for OPPDIF predictions of NO formation in a φ=0.90, CH₄/O₂/N₂ counterflow premixed flame at atmospheric pressure. Predictions were obtained using the GRI mechanism and temperatures found via the coupled species and energy equations without the radiation source term.

Figure 6.16: Quantitative reaction path diagram for OPPDIF predictions of NO formation in a φ=1.20, CH₄/O₂/N₂ counterflow premixed flame at atmospheric pressure. Predictions were obtained using the GRI mechanism and temperatures found via the coupled species and energy equations without the radiation source term.

to effectively block the majority of NO formation. However, if reactions from NH to N and NO are fast compared to the prompt initiation step, it is possible that no net change in NO concentration would be noticed by this removal although the resulting QRPD would look different.

Fortunately, an option in the OPPDIF code permits the calculation of sensitivity coefficients, which describe the impact of small changes in individual reaction rate coefficients on the overall concentration of various flame species. With appropriate extraction and post-processing routines, these coefficients can be reduced to the form

$$S_{X_j,i} = \frac{A_i}{X_{j,\max}} \cdot \frac{dX_j}{dA_i}.$$  (6.2)

Here, $X_j$ is the mole fraction of species $j$ and $A_i$ is the pre-exponential factor of the modified Arrhenius rate expression for the $i^{th}$ elementary reaction. Since the forward and reverse reaction rate coefficients for a given elementary reaction are related by the expression

$$\frac{k_f}{k_r} = K_c,$$  (6.3)

the sensitivity coefficient represents the impact of increasing both the forward and backward rate coefficients of a specific reaction rather than changing the relative magnitude of each direction. Applying this technique, the sensitivity of the peak NO concentration to each of the reactions within the GRI reaction mechanism was calculated for the same flame conditions studied in the pathway and QRPD analyses. The results of this analysis are shown in Table 6.2. Here, the reactions have been divided into those which are primarily responsible for determining the general radical pool concentrations and flame speed, those related directly to CH concentration and/or prompt NO chemistry, and those associated directly with either the Zeldovich, $N_2O$ intermediate or NNH pathways of NO formation. The reactions shown in Table 6.2 include all those which have a sensitivity of 0.1 or greater in any of the three flames studied.

The first thing that becomes apparent when studying Table 6.2 is that many reactions having a strong NO sensitivity are not directly related to the NO chemistry. For

Table 6.2: Peak NO concentration sensitivity coefficients for counterflow, premixed $CH_4/O_2/N_2$ flames at atmospheric pressure.

| Rxn # | Reaction Description | Sensitivity Coefficients | | |
|-------|----------------------|------------|------------|------------|
| | | $\phi=0.65$ | $\phi=0.90$ | $\phi=1.20$ |
| **Radical Chemistry** | | | | |
| 38 | $H+O_2 \Leftrightarrow O+OH$ | -0.37 | -0.39 | -0.48 |
| 35 | $H+O_2+H_2O \Leftrightarrow HO_2+H_2O$ | -0.41 | -0.09 | -0.00 |
| 10 | $O+CH_3 \Leftrightarrow H+CH_2O$ | -0.01 | -0.06 | -0.29 |
| 52 | $H+CH_3(+M) \Leftrightarrow CH_4(+M)$ | 0.06 | 0.07 | 0.19 |
| 99 | $OH+CO \Leftrightarrow H+CO_2$ | -0.12 | -0.04 | 0.04 |
| 36 | $H+O_2+N_2 \Leftrightarrow HO_2+N_2$ | -0.08 | -0.01 | -0.00 |
| **Prompt Chemistry** | | | | |
| 240 | $CH+N_2 \Leftrightarrow HCN+N$ | 0.08 | 0.12 | 0.63 |
| 127 | $CH+H_2O \Leftrightarrow H+CH_2O$ | -0.03 | -0.06 | -0.40 |
| 126 | $CH+H_2 \Leftrightarrow H+CH_2$ | 0.07 | 0.08 | 0.19 |
| 135 | $CH_2+O_2 \Leftrightarrow OH+HCO$ | -0.07 | -0.07 | -0.13 |
| 125 | $CH+O_2 \Leftrightarrow O+HCO$ | -0.04 | -0.04 | -0.08 |
| **Zeldovich Chemistry** | | | | |
| 178 | $N+NO \Leftrightarrow N_2+O$ | 0.20 | 0.46 | 0.14 |
| **NNH Chemistry** | | | | |
| 208 | $NNH+O \Leftrightarrow NH+NO$ | 0.37 | 0.28 | 0.16 |
| **$N_2O$ Chemistry** | | | | |
| 185 | $N_2O(+M) \Leftrightarrow N_2+O(+M)$ | 0.35 | 0.11 | 0.03 |
| 183 | $N_2O+H \Leftrightarrow N_2+OH$ | -0.25 | -0.09 | -0.03 |
| 199 | $NH+NO \Leftrightarrow N_2O+H$ | 0.23 | 0.10 | 0.03 |
| 182 | $N_2O+O \Leftrightarrow 2NO$ | 0.12 | 0.01 | 0.00 |

example, reactions such as H+O$_2$⇔O+OH have a strong influence on the concentrations of O, OH, and H within the flame front, and these radicals in turn are critical for all of the NO formation pathways. However, the systematic optimization of such reaction rate coefficients would require a study of flame speeds, direct measurements of relative radical concentrations, as well as shock tube studies of individual reaction rates. This process has been ongoing as part of the development of the GRI reaction mechanism and it is beyond the scope of this work to suggest changes in the hydrocarbon chemistry. However, the good temperature agreement found for the flames of Chapter 4 in conjunction with the good target agreements shown on the GRI website (Bowman *et al.*, 1995) seem to suggest that at least over a limited set of conditions, the hydrocarbon chemistry is reasonably well defined in the GRI mechanism. But having said that, problems in the prediction of flamefront location for the rich opposed flames of Figure 6.7 seem to suggest that considerable room exists for improvement in this area.

The second group of reactions shown in Table 6.2 directly impacts the prompt NO chemistry. As shown both in the flames of this chapter and in the burner-stabilized flames of Chapter 4, strong evidence exists that this mechanism is under-emphasized in the GRI mechanism (version 2.11). As suggested previously, the prompt NO initiation step, CH+N$_2$⇔HCN+N, is the most sensitive reaction for prompt NO chemistry. However, several reactions involving CH concentration have sensitivity coefficients of a similar magnitude for NO formation. Specifically, in the $\phi$=1.20 flame, GRI reactions 125 and 127 are principally responsible for CH destruction and GRI reaction 126 is principally responsible for CH formation. GRI reaction 135 on the other hand is an alternate pathway for the destruction of CH$_2$ which avoids the formation of CH. It is the balance of these four reactions which determines CH concentration and thus heavily influences prompt NO formation. The strong sensitivity of prompt NO formation to CH concentration suggests that improvements to the prompt NO pathway will be more complicated than simply varying the rate coefficient of one reaction, as has been implied by some authors (Berg *et al.*, 1998; Ravikrishna and Laurendeau, 1999). One further comment on the prompt chemistry is the surprising lack of any sensitivity to the large number of reactions which

process the HCN and N radicals into NO. As indicated in the QRPD analysis of Fig. 6.16, although several reactions involving these species are very active in rich flames, in every case there are other reactions which could provide the same functionality, converting N atoms and HCN into NO. Thus, from the current analysis we can conclude that in the absence of any one of these reactions, the peak NO concentration would remain relatively unchanged.

Unlike the prompt chemistry, both the Zeldovich and NNH pathways seem to be primarily sensitive only to their respective initiation reactions. While the rate coefficient for the Zeldovich reaction is perhaps the best known and most widely studied, the NNH initiation reaction has only recently been discovered (Bozzelli and Dean, 1995) and is relatively poorly known. Thus, the NNH+O⇔NH+NO reaction could represent a substantial uncertainty in the NO predicting capabilities of the GRI reaction mechanism. Furthermore, we note that both the Zeldovich and NNH initiation reactions have greater than 0.1 sensitivity coefficients for all three of the cases studied; thus, the uncertainties in the NNH initiation reaction could have an impact on all of the NO predictions in this study.

As far as the $N_2O$ intermediate mechanism is concerned, there are four reactions which have nearly equal impact on NO concentration. For the NNH pathway, the NNH concentration is insensitive to any single reaction rate because of the many fast reactions which work together to determine its concentration. However, for the $N_2O$ intermediate pathway, the $N_2O$ concentration is determined by a fewer number of competing reactions whose individual rate coefficients exhibit substantial sensitivities with respect to $N_2O$ and thus NO concentration. Additionally, some of the reactions which break down $N_2O$ to form NO have high sensitivities for NO formation. Note that the most sensitive $N_2O$ formation reaction involves collisions with O atoms (GRI reaction 185) while the most sensitive $N_2O$ destruction reaction involves collisions with H atoms (GRI reaction 183). This combination insures that the $N_2O$ concentration, and thus the importance of this pathway, depends strongly on the equivalence ratio. Finally, as mentioned by Dryer *et al.* (1998), considerable uncertainty exists for several of these $N_2O$ reactions; hence, they

represent yet another area which could be optimized within the NO formation kinetics of the GRI mechanism.

## 6.5 Conclusions

Quantitative LIF measurements of NO were obtained in flat, laminar, premixed counterflow $CH_4/O_2/N_2$ flames at atmospheric pressure. This flame configuration permits the measurement of NO concentration profiles in the preheat zone, through the flamefront and into the postflame zone of premixed flames. NO predictions using the Sandia opposed diffusion flame code in conjunction with the GRI reaction mechanism (version 2.11) were compared to the measured NO concentrations. Under lean conditions, remarkable agreement was found between predictions and measurements; however, this agreement was found to break down in moderately rich flames both with respect to the peak NO concentration and to the relative shape of the NO profiles. Pathway, quantitative reaction path, and sensitivity analyses were used to identify the important paths and reactions for NO formation in lean, near stoichiometric and rich counterflow premixed flames. Key reactions were identified for each NO formation pathway and those most likely to contribute to the inaccuracies of the current GRI mechanism were identified and discussed in the context of future improvements to the NO kinetics scheme.

Specifically, it was determined that NO formation by each of the four pathways is intricately tied to radical chemistry that influences concentrations of O and OH in the flamefront. However, assuming this chemistry to be correct, key reactions were identified which have strong sensitivities for NO formation without seriously affecting this radical pool. For NO formation via the Zeldovich and NNH pathways, significant NO sensitivity was found only for their initiation reactions, GRI reactions 178 and 208, respectively. $N_2O$ intermediate kinetics were slightly more complex with a total of four reactions showing significant sensitivities. These reactions involved two which determined the $N_2O$ concentration (GRI reactions 185 and 183) and two which determined the rate of NO production from $N_2O$ (199 and 182). Finally, prompt NO formation in these atmospheric

pressure flames was found to have significant sensitivity to a variety of reactions influencing the CH radical concentration (125, 126, 127, and 135) as well as the prompt initiation reaction (240).

# 7. LIF MEASUREMENTS AND MODELING OF NITRIC OXIDE CONCENTRATION IN HIGH-PRESSURE COUNTERFLOW PREMIXED FLAMES

## 7.1 Introduction

Nitric oxide formation in high-pressure flames is a research area of great practical interest owing to the presence of high pressures in all practical power-generation and propulsion engines combined with the relative paucity of experimental data available for such devices. Because of this lack of data, most chemical kinetic codes available for the prediction of NO formation in combustion systems have been developed via comparisons with atmospheric and sub-atmospheric pressure target flames with little or no comparisons to high-pressure conditions (Bowman *et al.*, 1995; Miller and Bowman, 1989; Glarborg *et al.*, 1986). Consequently, those high-pressure flame conditions that industry is most interested in studying may not be well modeled by the mechanisms available to study them.

To help bridge the current gap between low-pressure kinetics and high-pressure applications, laser-induced fluorescence (LIF) has recently been used (Reisel and Laurendeau, 1994a; Klassen *et al.*, 1995; Thomsen, 1996) to obtain quantitative measurements of NO formation in laminar premixed flames stabilized upon a water-cooled McKenna burner at 1.0 to 14.6 atm. Great strides have been made in both increasing the accuracy of these measurements (Thomsen *et al.*, 1997) and in broadening the conditions studied to different fuels and ever increasing pressures (Reisel and Laurendeau, 1994a; Reisel and Laurendeau, 1995; Klassen *et al.*, 1995; Kuligowski, 1998; Charlston-Goch, 1999). However, the flame geometry used in these studies is not without its limitations, both for experimental application and ease of modeling.

An important experimental problem with using a McKenna burner is that the flamefront sits extremely close to the burner surface, especially at high pressures.

Consequently, it becomes impossible to obtain experimental profiles of temperature and species concentrations through the flamefront or even to experimentally validate concentrations and temperatures upstream of the flame. Furthermore, the high degree of heat loss in these flames results in narrowing the flammability limits to a smaller range of stoichiometries at each pressure. Because of this limitation, for the study of ultra-lean or moderately rich flames, researchers have typically been forced to vary the dilution ratio ($N_2/O_2$) of the oxidizer to obtain higher-temperature, stable, premixed flames over a wider range of conditions (Klassen et al., 1995).

Recently, Dong and coworkers (1999) presented a study showing the sensitivity of predicted NO concentrations to a variety of non-kinetic factors in this type of flame configuration. Their study revealed several difficulties associated with this burner type, as well as some relevant to any flame configuration. Specifically worth mentioning in the current context is the sensitivity of such predictions to temperature and velocity profiles. For a water-cooled flame, flame temperature is a function of the rate of heat loss to the burner surface. This rate of heat loss is determined by a balance between thermal diffusion and flow velocity. In a real burner-stabilized flame, buoyancy has the effect of increasing the axial velocity of the reactant stream and also narrowing its radial extent. Thus, the corresponding temperature predictions of the Sandia premixed flame code (Kee et al., 1985) may be considerably in error if this profile effect is neglected. As shown in Chapter 4, radiation-corrected thermocouple measurements of temperature in the post-flame zone of a series of $CH_4/O_2/N_2$ flames show remarkable agreement with modeling predictions when using the GRI reaction mechanism (version 2.11). This agreement would seem to indicate that this effect is minimal for our range of flame conditions. However, owing to the strong temperature sensitivity of NO kinetics, even a relatively modest temperature effect could have a strong influence on the predictive capabilities of the code. Furthermore, the accuracy of such temperature measurements may not be sufficient to guarantee the validity of the modeled temperatures.

In addition to these concerns associated with temperature predictions, another concern with modeling NO formation in this type of burner-stabilized flame is the

possibility of catalytic effects caused by the burner surface. Radical recombination may be significantly enhanced by the close proximity of the burner to the flamefront. This effect could impact both the radical pool of the flame as well as providing another source of heat loss to the burner surface. Finally, having the burner surface so close to the flamefront brings into question the choice of surface temperature used in the modeling. If the conduction rate to the cooling water is insufficient, hot spots could develop on the surface of the sintered plug used in these burners, especially at the higher heat release rates found in high-pressure flames. While Reisel and Laurendeau (1994b) demonstrated that fairly large changes in this temperature boundary condition are required to have any impact on post-flame zone temperatures and subsequent NO predictions, this problem does add another small uncertainty with respect to the modeling of such flames.

In summary, the difficulties associated with the use of a water-cooled McKenna burner for high-pressure flame studies of NO kinetics can be divided into two categories: those associated with the flamefront being too close to the burner surface and those associated with a reliable prediction of the temperature profile. In the previous several chapters, an alternate flame configuration has been proposed that promises to avoid many of these difficulties while retaining a one-dimensional structure for ease of modeling. This configuration is that of counterflow premixed flames. Because the flame is stabilized by curvature effects rather than by heat loss to the burner, significant separations can exist between the flamefront and the burner surface in these flames. In addition, because less heat loss occurs to the burner in such flames, near adiabatic conditions may be obtained which allow for the study of leaner flames than can be stabilized on traditional flat-flame burners. This is advantageous for the study of lean premixed combustion which is being pursued for $NO_x$ abatement in advanced gas turbines. Furthermore, the stabilizing counterflow geometry may generate flames for which the flow-field shape is not affected by buoyancy, thus removing uncertainties in modeling based on the cross-sectional area of the flame. The removal of surface heat losses also makes the temperature profiles in counterflow flames less sensitive to flow-field uncertainties even if they exist.

The purpose of this chapter is to examine the utility of the counterflow premixed flame geometry for use in kinetic studies of NO formation at high pressure. Issues impacting the accuracy of laser-induced fluorescence measurements of NO will be addressed as well as non-kinetic issues impacting our ability to accurately model NO formation in these flames. Through the course of this discussion, LIF measurements of NO will be presented under a variety of high-pressure conditions and compared to predictions using the GRI reaction mechanism (version 2.11). Those conclusions which can be drawn from these comparisons will be discussed and also compared to similar measurements in McKenna burner flames, as detailed in Chapter 4.

## 7.2 Experimental and Modeling Techniques

The laser system and optical layout used in performing the LIF measurements of NO are described completely in Chapter 3; however, the most relevant points are repeated here. Excitation of NO is achieved through use of the $Q_2(26.5)$ line in the $\gamma(0,0)$ band ($\sim$225.5 nm). An etalon-based feedback system is used to provide a stable laser excitation wavelength (Cooper and Laurendeau, 1999). After leaving the laser system, the beam is directed over a 1-cm diameter, counterflow flat-flame burner designed for use in the high-pressure combustion facility described by Carter et al. (1989). Figure 7.1 provides a schematic of this counterflow burner which is described in detail in Chapter 5. The pressure vessel has four optical ports, two of which provide optical access for the laser beam through the combustion facility. The spot size produced by the optical arrangement is $\sim$250 µm. Before entering the vessel, the beam passes through a fused silica plate which directs a portion of the beam toward a UV-sensitive photodiode. This photodiode is employed to monitor the beam energy, which is required for normalization of the fluorescence signal.

For fluorescence detection, we make use of an optical port perpendicular to the laser entrance and exit ports. The fluorescence is focused on the entrance slit of a 1-m monochromator. The detector is an Hammamatsu R106UHHA photomultiplier tube

Figure 7.1:    Schematic diagram of counterflow burner.

(PMT) specially wired for temporal resolution of the fluorescence signal (Harris *et al.*, 1976). The broadband fluorescence signal encompasses a spectral width of ~3 nm and is detected over a spectral region centered at ~236 nm. This location and spectral width correspond to the $\gamma(0,1)$ band of NO. Each data point is averaged over 600 laser shots. A diagram of the experimental apparatus is shown in Figure 7.2.

A new procedure, based on a previous calibration technique developed in our laboratory for flat burner-stabilized flames (Thomsen *et al.*, 1997), has been developed for calibrating the fluorescence signals. This technique involved doping different levels of NO, first into one and then into the other premixed stream of a $\phi = 0.7$ counterflow premixed flame system, and measuring the fluorescence voltage produced in the burnt-gas region. The data from the various doping conditions were used to obtain a linear calibration plot which could then be applied to the calibration flame ($\phi = 0.7$). The fluorescence signal for other flames could subsequently be compared to that of the calibration flame and corrected for changes in both the absorption efficiency and the electronic quenching rate coefficient so as to obtain quantitative NO number densities. We assumed both that the doped NO does not react as it passes through the flame and that summing the signals obtained from doping into each side individually contributed the same amount of signal as doping into both sides simultaneously. To confirm these assumptions, computer modeling was used to predict the effect of independently doping a known concentration of NO into each stream of the counterflow, premixed calibration flames. As demonstrated in Chapter 6, the "calibration" profile obtained by summing the NO profiles of the two doped cases and subtracting twice the ambient NO profile produces a constant region near the centerline with an NO concentration equal to the total amount of NO doped into each stream independently.

As discussed by Thomsen *et al.* (1997), $O_2$ fluorescence and other interference signals can become significant for LIF measurements of NO in high-pressure flames. To assess the contribution of these interferences to the overall fluorescence signal at each pressure, it was necessary to include an off-line curve in each calibration. Calibration results for pressures ranging from 2.02 to 5.08 atm are presented in Fig.

PMT

BSA

MONOCHROMATOR

BSA  PV

P          P

P

P

WAVELENGTH
EXTENDER

E
T
A
L
O
N

S
Y
S
T
E
M

P
D
L

BOXCAR

HG

ND:YAG
LASER

BSA - Beam Steering Assembly

HG - Harmonic Generator

P - Photodiode

PDL - Pumped Dye Laser

PV - Pressure Vessel

PMT - Photomultiplier Tube
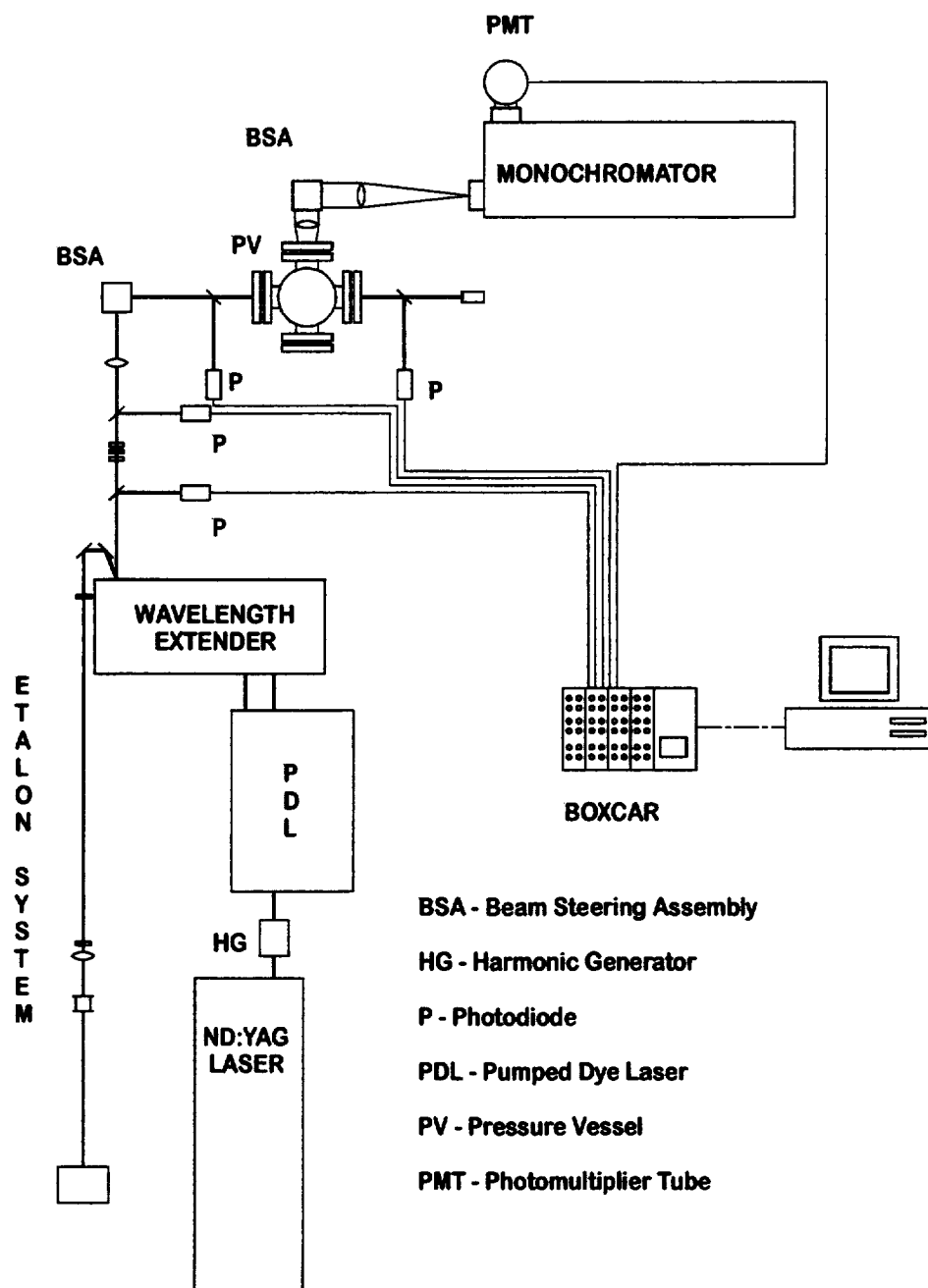
Figure 7.2: Schematic diagram of experimental apparatus.

7.3. The calibration plots exhibit an extremely tight linearity both for on- and off-line excitation. This result is consistent with that found by Thomsen *et al.* (1997) in their calibrations of NO LIF signals in McKenna burner flames up to 14.6 atm. The strong linearity further supports the utility of the proposed calibration technique. Furthermore, it is worth noting that each doping condition plotted in Fig. 7.3 was repeated and thus there are two data points plotted for each case. The fact that, for most of these conditions, the two points overlap so tightly that they appear to be the same further demonstrates the strong repeatability of this calibration procedure.

As expected, the relative magnitude of the background signal for each case of Fig. 7.3 increases steadily with pressure. At 2.02 atm, the background contribution accounts for about 1.8% of the NO signal in the undoped flames, which when applying the calibration would be equivalent to an additional NO concentration of 0.15 ppm. At 3.04 atm, this contribution increases to an equivalent NO concentration of 0.24 ppm, with an increase to 0.3 ppm at 4.06 atm and finally 0.5 ppm at 5.08 atm. At the highest pressure, for reasons which will be discussed later in this chapter, it was necessary to utilize a leaner stoichiometry with a corresponding lower NO concentration for the calibration flame. The result is that the background corresponds to nearly 11% of the overall fluorescence signal under this condition. Thomsen *et al.* (1997) discovered that these background signals in the post-flame zone were relatively constant with respect to equivalence ratio at a given pressure and thus could be subtracted from each corresponding LIF measurement. However, the extension of this technique to LIF studies of counterflow premixed flames is unclear owing to the fact that the LIF measurements take place not only in the post-flame zone but also in the flamefront as well as the preheat region of these flames. Consequently, the background contribution may not be constant over the resulting range of species concentrations and temperatures. In high-temperature regions, $O_2$ fluorescence will become stronger and most likely will be the dominant source of interference. However, in low-temperature regions, Rayleigh scattering and other interferences may become dominant. Fortunately, we find that the background in cold-gas regions is never as high as that determined in the post-flame zone; however, the background can become
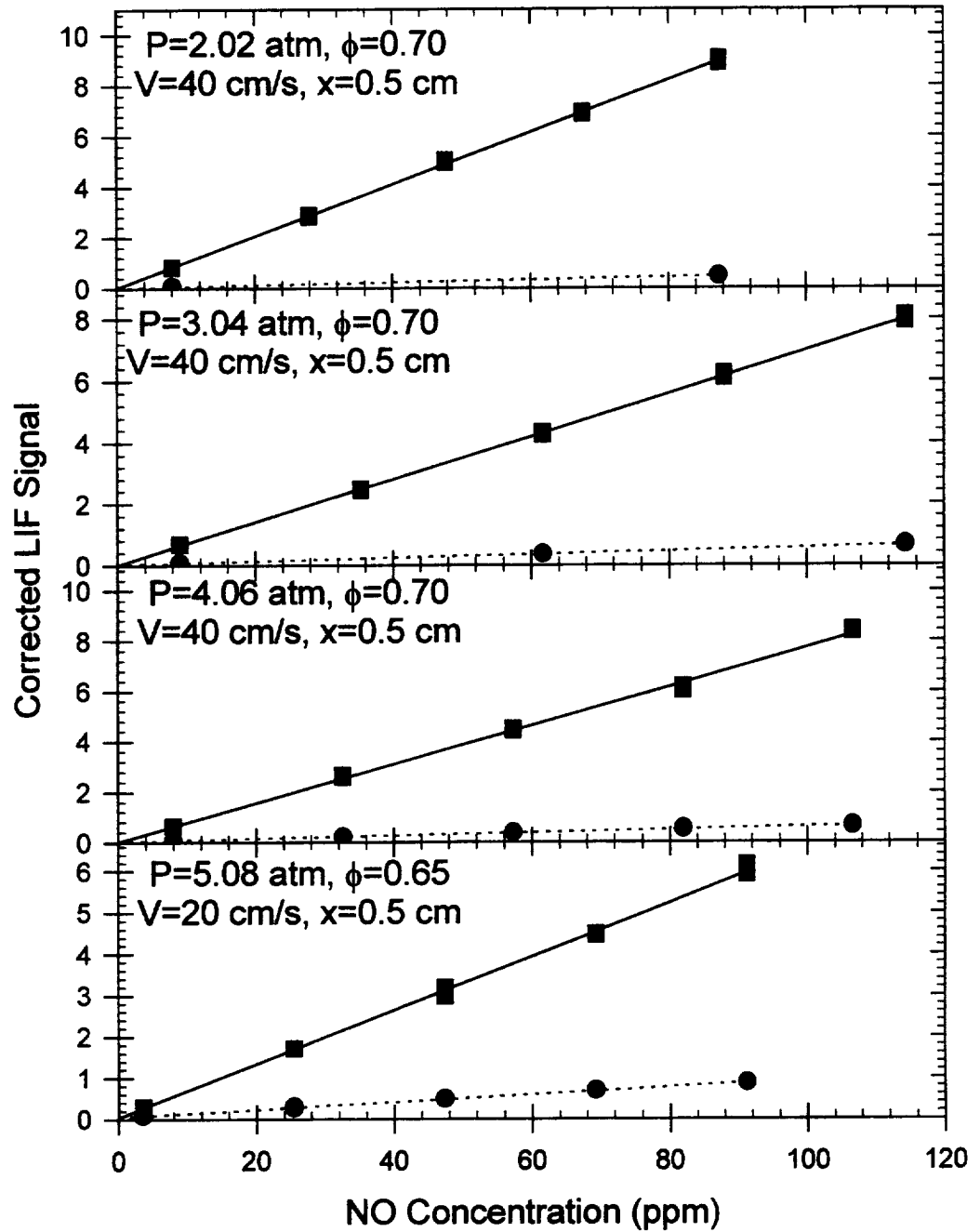
Figure 7.3:  Calibration curves for laser-induced fluorescence measurements of NO in high-pressure counterflow $CH_4/O_2/N_2$ premixed flames.

significant, especially on a relative scale, in flames at higher pressures. Based on these uncertainties and on the relatively low background contributions in these flames, no corrections were made here for interferences in the LIF measurements. The resulting uncertainties in the measured NO concentrations are discussed in Appendix D and are included in the error bars displayed for these experiments.

The modeling of the chemical kinetics was performed using the Sandia, steady, laminar, opposed diffusion flame code (Lutz *et al.*, 1996). For the sake of uniformity, a constant burner surface temperature of 300 K was used as a boundary condition for all of the NO predictions. In reality, for these flames, it became necessary at higher pressures to increase the temperature of the water flow used to cool the burners so as to prevent condensation from forming on the burner surface during the course of the experiments. These elevated cooling temperatures resulted in slightly increased reactant temperatures as well. Thermocouple measurements of the reactant stream in the cold-gas regions of these flames yielded temperatures ranging from 303 to 316 K. Fortunately, computations indicate that this relatively modest rise in the thermal boundary condition is insignificant in terms of the code predictions. Temperatures through the remainder of the flame were obtained through joint solution of the energy and species equations within the OPPDIF code. The comprehensive mechanism used in the modeling is the GRI mechanism, version 2.11 (Bowman *et al.*, 1995). This reaction mechanism, which can be found in Appendix B, considers 49 species and 277 reactions and was used without modification. In addition, we employed the thermodynamic and transport property files provided with the mechanism. Finally, OPPDIF allows for calculation of species diffusion using either mixture-averaged or multi-component diffusivities, with an additional option of considering thermal diffusion of species. Mixture-averaged diffusivities were employed for all the modeling presented in this chapter.

An important limitation of the Sandia opposed diffusion flame code is that it does not consider the effects of radiative heat loss. To account for such effects on the temperature and NO predictive capabilities of the code, a radiation subroutine developed by Gore and coworkers (1999) was incorporated into the energy equation within the

OPPDIF code. This routine, which assumes optically thin radiation originating from the major species within the flame, has previously been shown to have a significant impact on NO concentration predictions in lower strain rate counterflow diffusion flames (Gore *et al.*, 1999; Ravikrishna and Laurendeau, 1999).

When performing linear LIF measurements, one must be concerned with the effects of laser power fluctuations as well as absorption and quenching variations as a function of temperature and species composition. Corrections for laser power fluctuations can be made by normalizing the fluorescence signal using the measured laser power. Quenching variations could be handled in a similar manner; however, measurement of the quenching rate coefficient is not a trivial task. Furthermore, the large variations in temperature and composition across the flame front make both quenching and absorption corrections significant in these flames.

To assess the capability of the GRI mechanism to accurately predict NO concentrations in counterflow premixed flames, it was necessary to compare the modeling results to the LIF measurements. Unfortunately, as mentioned above, the LIF measurements depend on two parameters, the quenching rate coefficient and the absorption coefficient, which in turn are functions of temperature and major species concentrations. For linear LIF measurements, the fluorescence equation reduces to the form

$$S_f = \frac{V_f}{I_L} \propto \frac{\alpha N_T}{Q_{ul}}, \tag{7.1}$$

where $S_f$ is the laser-power corrected fluorescence signal, $V_f$ is the integrated photomultiplier tube voltage, and $I_L$ is the laser irradiance (W/cm$^2$). The parameter $\alpha$ is the absorption coefficient per unit NO number density (cm$^{-1}$/(molecules/cm$^3$)), which includes the effects of Boltzmann fraction, line strength and overlap fraction, as described in Chapter 2. The final two terms, $Q_{ul}$ and $N_T$, refer to the quenching rate coefficient (s$^{-1}$) and the NO number density (molecules/cm$^3$), respectively. The proportionality constant in Eq. (7.1) can be determined by using the calibration technique described previously. However, since measurements are being taken across the flamefront, the quenching and

absorption terms vary significantly in these flames. Unfortunately, without measurements of temperature and major species concentrations, it is essentially impossible to predict these terms so as to correct the LIF measurements. On the other hand, major species and temperature information are available from the predictions. Thus, the modeling can be "uncorrected" for quenching and absorption effects to produce an uncorrected number density which can be directly compared to the LIF measurements. This calculation was accomplished by first multiplying the predicted number density at each location by the ratio of the quenching rate coefficient predicted for that location over that predicted for the calibration flame. This revised number density was then divided by a similar ratio of actual to calibration absorption coefficients.

To obtain the absorption rate coefficient $\alpha$ from the predicted major species concentrations and temperatures, we utilized an absorption code developed by Seitzmann (1991). This code accounts for changes both in the ground state Boltzmann distribution and the overlap fraction between the laser linewidth and the collisionally broadened NO spectrum. Comparisons between NO absorption spectra generated by this code and excitation scans, performed in the post-flame zone of lean, premixed, $CH_4/O_2/N_2$ flames at pressures of 1.0 and 14.6 atm, yielded excellent agreement, which gives us confidence that the absorption code is suitable for correcting our LIF measurements of NO. For the moderate pressures of the current study, the NO excitation spectra are more similar to the atmospheric pressure scan shown in Fig. 6.4 than the 14.6 atm scan of Thomsen (1997).

To account for quenching variations, quenching cross-sections were calculated using the correlations of Paul et al. (1995) and combined in a computer code developed in our laboratory to calculate the quenching rate coefficients needed for correction of the fluorescence signal. Though earlier modeling using these correlations had predicted less than a 10% variation in the quenching rate within the post-flame zone of a series of lean, premixed flames (Klassen et al., 1995), significant differences were found between the quenching environments of the post-flame and preheat zones of the current flames.

## 7.3 Results and Discussion

Using the above techniques, LIF measurements of NO concentration were obtained in a series of premixed, counterflow, $CH_4/O_2/N_2$ flames at 1.00 to 5.08 atm. The separation distance of the two 1-cm diameter burners was chosen to be 1.0 cm. In all cases the $N_2/O_2$ dilution ratio was maintained at 3.76 to simulate air and the top and bottom streams were identical while the velocity of the reactants was chosen to place both visible flamefronts approximately 3 mm from their respective burners. A summary of the flame conditions studied is provided in Table 7.1.

Starting with the leanest conditions studied, the results of these LIF measurements of NO in a series of $\phi=0.60$ counterflow premixed flames are presented in Fig. 7.4. The effect of buoyancy is immediately evident in these ultra-lean flames. In particular, buoyancy in such flames acts to first narrow the separation distance between the two premixed flamefronts and then to shift both flamefronts toward the top burner. As mentioned previously, two of the difficulties associated with studies utilizing water-cooled McKenna burners were that the heat loss restricted the equivalence ratios that could be studied and buoyancy brought into question the validity of the modeling strategy. Hence, it was hoped that the counterflow geometry would both allow for leaner flame studies and provide flowfields that were dominated by factors other than buoyancy. Figure 7.4 demonstrates the limitations of this strategy.

While leaner flames can be stabilized under the nearly adiabatic conditions of counterflow premixed flames, achieving significant separation distances between the flamefronts of ultra-lean flames is nearly impossible without reducing flow rates to the point where buoyancy forces significantly alter the flowfield at high pressure. However, even acknowledging this limitation, we note that the GRI mechanism does an excellent job of predicting post-flame zone NO concentrations in these flames. Owing to the low flame temperatures, nearly all the NO is formed in the flamefront and thus the narrower separation distance in the experimental flames should have a negligible effect on the peak NO concentration. Furthermore, since convective heat loss is negligible in these flames, perturbation of the velocity profile via buoyancy has a much smaller effect on flame

Table 7.1: Flame conditions, predicted peak temperatures and flow rates for high-pressure counterflow, premixed $CH_4/O_2/N_2$ flames. OPPDIF predicted temperatures were calculated via the coupled species and energy equations without the inclusion of a radiation source term in conjunction with the GRI reaction mechanism.

| Pressure | Equiv. Ratio | Exit Vel. (cm/s) | Predicted Temp. (K) | Component Flow Rates (SLPM) | | |
|---|---|---|---|---|---|---|
| | | | | $CH_4$ | $O_2$ | $N_2$ |
| 1.00 | 0.65 | 35.0 | 1750 | 0.105 | 0.324 | 1.22 |
| 1.00 | 0.70 | 40.0 | 1830 | 0.129 | 0.369 | 1.39 |
| 1.00 | 0.75 | 50.0 | 1900 | 0.172 | 0.459 | 1.73 |
| 2.02 | 0.60 | 17.5 | 1670 | 0.099 | 0.329 | 1.24 |
| 2.02 | 0.65 | 30.0 | 1760 | 0.183 | 0.562 | 2.11 |
| 2.02 | 0.70 | 40.0 | 1840 | 0.261 | 0.745 | 2.80 |
| 2.02 | 0.75 | 50.0 | 1920 | 0.348 | 0.927 | 3.49 |
| 3.04 | 0.60 | 12.0 | 1670 | 0.102 | 0.340 | 1.28 |
| 3.04 | 0.65 | 25.0 | 1760 | 0.229 | 0.704 | 2.65 |
| 3.04 | 0.70 | 40.0 | 1840 | 0.392 | 1.121 | 4.22 |
| 3.04 | 0.75 | 52.0 | 1920 | 0.544 | 1.451 | 5.45 |
| 3.04 | 1.40 | 37.5 | 1950 | 0.689 | 0.984 | 3.70 |
| 4.06 | 0.60 | 8.0 | 1660 | 0.091 | 0.302 | 1.14 |
| 4.06 | 0.65 | 20.0 | 1760 | 0.245 | 0.752 | 2.83 |
| 4.06 | 0.70 | 40.0 | 1840 | 0.524 | 1.498 | 5.63 |
| 5.08 | 0.65 | 18.0 | 1760 | 0.275 | 0.847 | 3.19 |
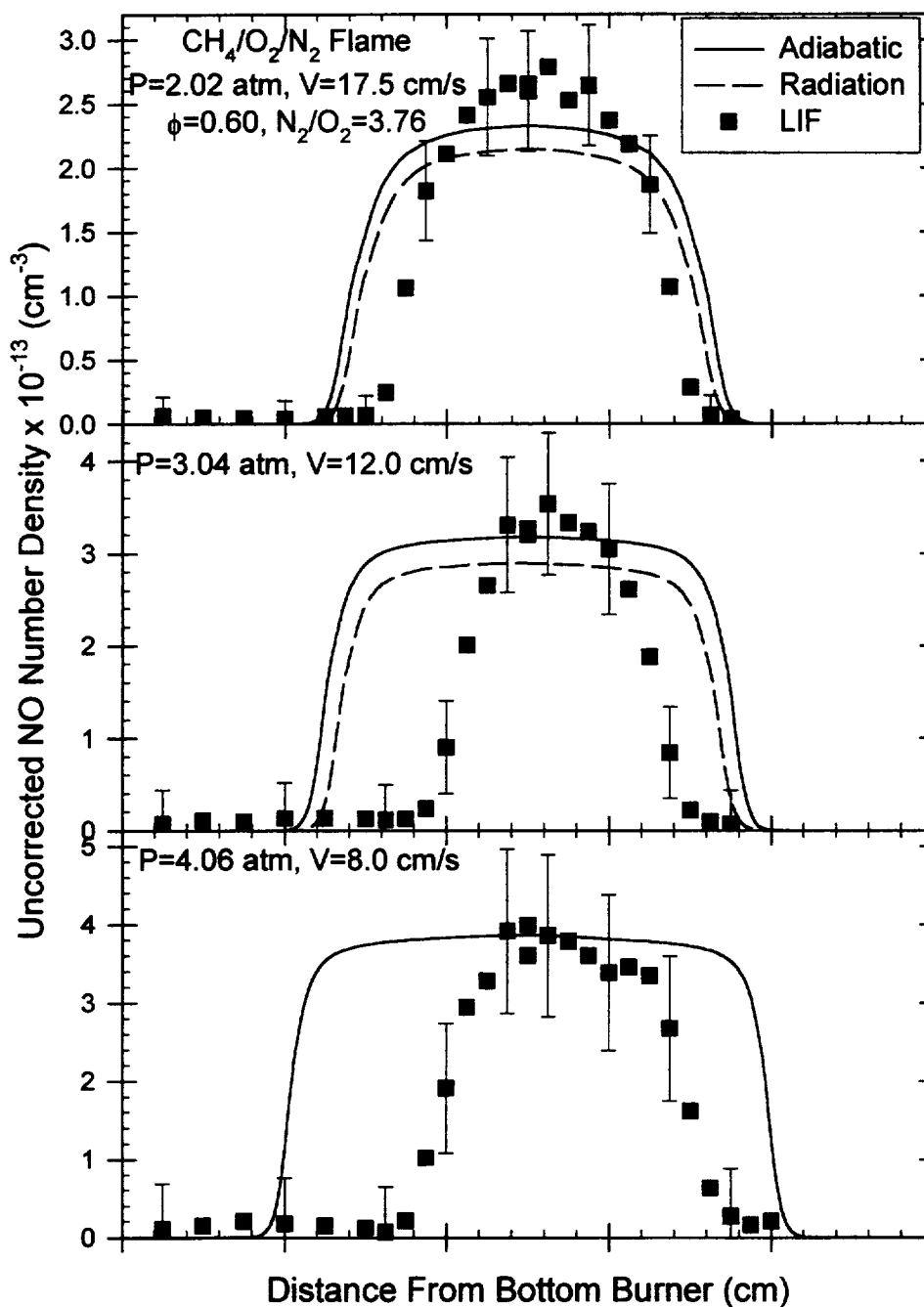
Figure 7.4: LIF-measured and predicted NO concentrations (uncorrected) in $\phi$=0.60, premixed, $CH_4/O_2/N_2$ flames at 2.02-4.06 atm. Predictions were obtained using temperatures found via the coupled species and energy equations with and without the inclusion of a radiation source term in conjunction with the GRI reaction mechanism. No solution could be obtained for the radiation case at 4.06 atm.

temperature and chemistry than in the McKenna burner flames. In fact, the magnitude of this impact can be estimated by the difference between the NO concentrations formed through each of the two flamefronts, which will be perturbed in opposite ways with respect to a non-buoyant flame. Based on the small difference in these measured NO concentrations, we find that evaluation of the GRI mechanism for ultra-lean flames can still be made using these counterflow studies. Unfortunately, at pressures greater than 4.06 atm, it becomes nearly impossible to stabilize a $\phi$=0.60 counterflow premixed flame having significant separation between the two flamefronts without bringing the top flame too close to the top burner to assume adiabatic conditions. Finally, we note that the radiation correction in the ultra-lean flames of Fig. 7.4 is relatively small (<10%), although the radiation case did not solve for the 4.06 atm flame.

The stoichiometry for which the greatest range of pressures (1.00 atm $\leq$ P $\leq$ 5.08 atm) could be examined with the current experimental setup was $\phi$=0.65. LIF measurements of NO concentration for the resulting flames are presented in Fig. 7.5. These flames, with peak temperatures around 1630 K, have high enough flame speeds to at least postpone the onset of the buoyancy-induced problems observed in Fig. 7.4, while being cool enough to avoid significant post-flame zone NO formation as well as several additional problems, mentioned later in this chapter, which plague the near stoichiometric flames.

Several interesting behaviors can be observed for the flames of Fig. 7.5. First of all, this sequence clearly shows the impact of pressure on buoyancy effects in such flames. As pressure increases, the flamefronts slowly move closer to each other and toward the top burner. As in the case of the $\phi$=0.60 flames of Fig. 7.4, at higher pressures, it eventually becomes impossible to obtain a satisfactory $\phi$=0.65 flame with separated flamefronts that are clear of interactions with the burner surfaces. However, in the current case, this limitation is delayed to pressures of 6.10 atm and above.

Another behavior apparent in Fig. 6.5 is the narrowing of the flamefront with increasing pressure. At atmospheric pressure, the NO profiles exhibit a gradual, parabolic profile indicative of relatively wide flamefronts. At higher pressures, however, this profile
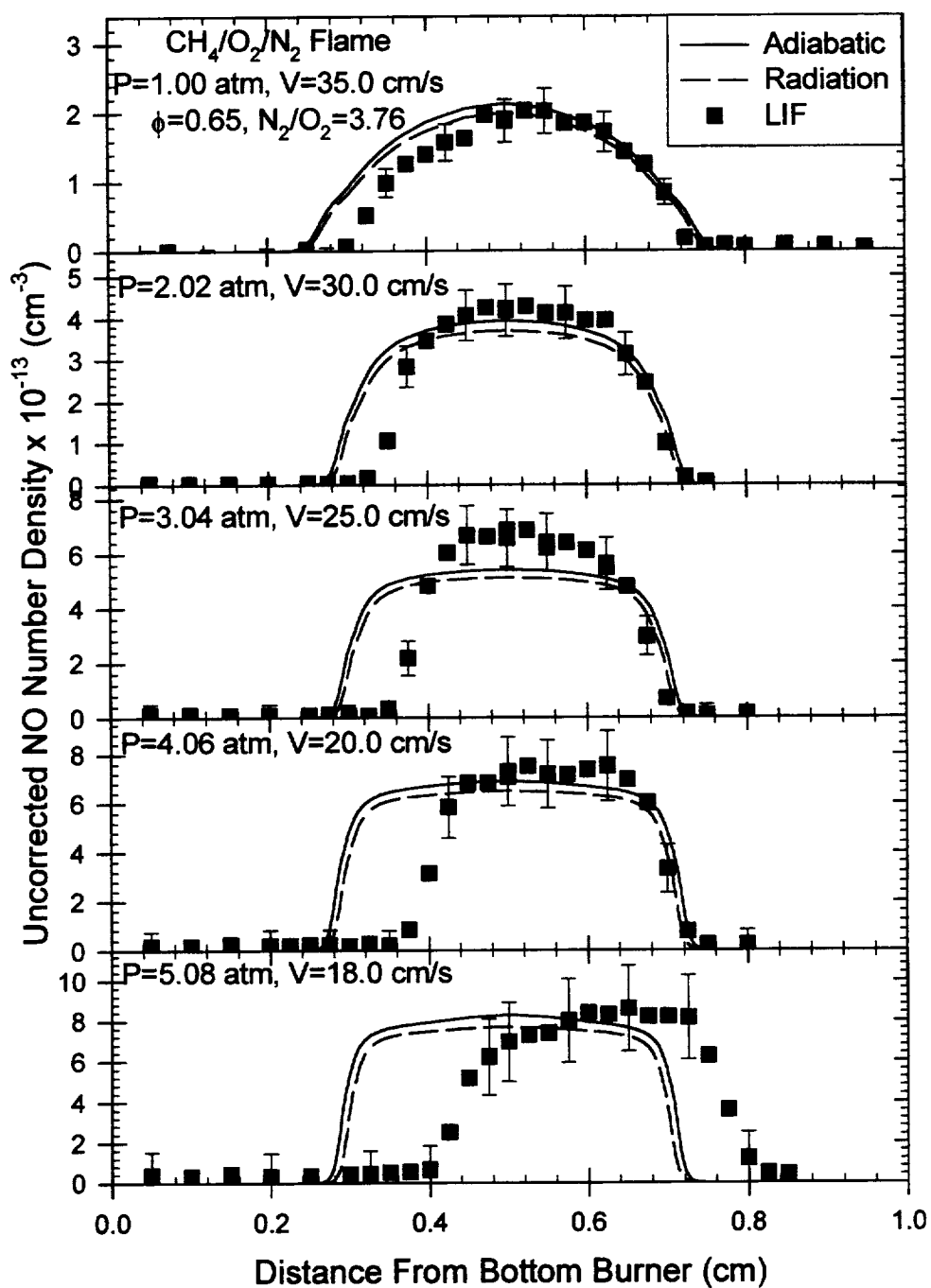
Figure 7.5: LIF-measured and predicted NO concentrations (uncorrected) in $\phi$=0.65, premixed, $CH_4/O_2/N_2$ flames at 1.00-5.08 atm. Predictions were obtained using temperatures found via the coupled species and energy equations with and without the inclusion of a radiation source term in conjunction with the GRI reaction mechanism.

becomes more top-hat in nature, with the flamefronts becoming sharp and well defined. This observation demonstrates one of the advantages of this configuration over the McKenna burner flames. In the McKenna burner, no conclusions could be made about flame width owing to the close proximity of the flame to the burner surface. In this case, the NO profiles clearly portray flames dominated by flamefront rather than post-flame zone NO formation.

Despite the limitations of the flame code with respect to buoyancy, the agreement between predicted and measured post-flame NO concentrations is remarkable. Once again, the relatively low temperatures of these flames, and the resulting dominance of flamefront NO formation, results in peak NO predictions that are relatively insensitive to the effect of buoyancy. Hence, based on these measurements, the GRI reaction mechanism seems to do an excellent job of predicting NO formation for counterflow premixed conditions. We further note that the radiation effect becomes nearly negligible under these conditions.

The next series of flames which we examine are those used for calibration at pressures ranging from 1.00 to 4.06 atm; specifically, those with an equivalence ratio of $\phi=0.7$ (Fig. 7.6). The first observation regarding these flames is that buoyancy no longer seems to be a problem over the range of pressures studied here. Specifically, the experimental profiles do not experience enhanced narrowing relative to the modeling profiles with increases in pressure. Furthermore, Fig. 7.6 displays the same narrowing of flamefronts with an increase in pressure as found in Fig. 7.5 for pressures up to 3.04 atm. In the last flame of Fig. 7.6 (P=4.06 atm), the flamefront seems to broaden out; the cause of this behavior is another of the limitations of the current burner system. At high pressure and velocity conditions, the premixed flamefronts begin to become wrinkled, owing most likely to non-uniformities in the hastalloy honeycomb at the exit of the burner. While these flames are still extremely steady, demonstrating no fluctuations or bounce, the one-dimensional nature of the flamefronts begins to break down at higher pressures. Measurements across these flamefronts are averaged across the wrinkles, resulting in a wider and more gradual increase in NO formation as demonstrated in Fig. 7.6.
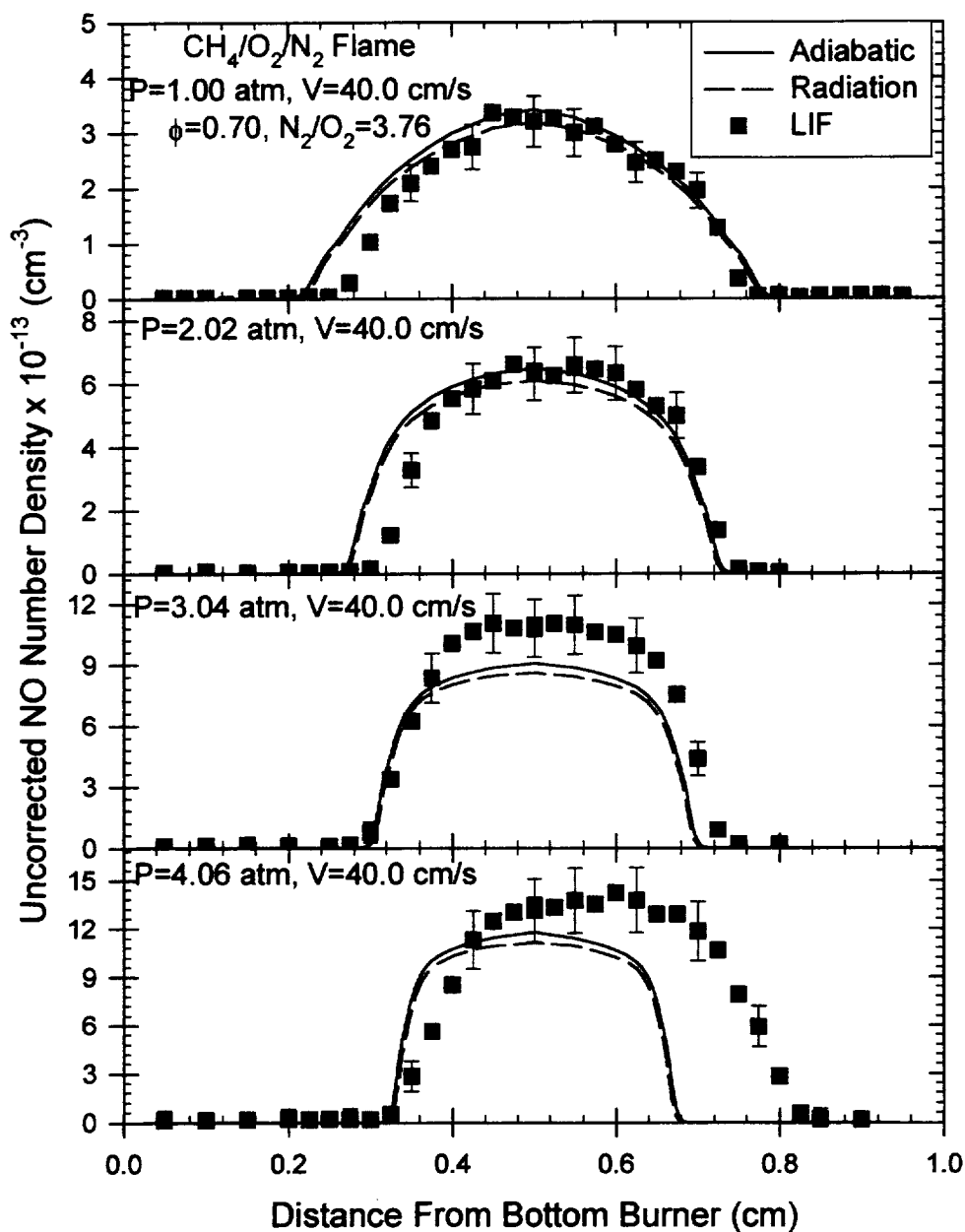
Figure 7.6: LIF-measured and predicted NO concentrations (uncorrected) in $\phi$=0.70, premixed, $CH_4/O_2/N_2$ flames at 1.00-4.06 atm. Predictions were obtained using temperatures found via the coupled species and energy equations with and without the inclusion of a radiation source term in conjunction with the GRI reaction mechanism.

Fortunately, the majority of NO in such flames is still formed in the flamefront and is thus less affected by this behavior than it would be nearer to stoichiometric conditions; however, any serious study of kinetics under these conditions would require a burner capable of obtaining truly flat velocity profiles.

The contoured burners utilized by Law and coworkers (1994) may be more ideally suited for this type of study; however, because of their larger size and weight, it would be impossible to incorporate them into our existing high-pressure facility. Furthermore, these contoured burners would not remove the buoyancy problems arising in our leaner flames and thus would not be helpful in the study of ultra-lean premixed combustion at high pressure, which is of most practical interest for $NO_x$ abatement in advanced turbine combustion.

Fortunately, whether or not this wrinkling effect influences NO formation in premixed counterflow flames, it does not appear to degrade the utility of the counterflow geometry as a calibration source for other flame configurations. Even the 4.06-atm case plotted in Fig. 7.6 demonstrates a flat post-flame zone region, and thus one would not expect significant NO destruction through the wrinkled flamefront any more than for its flat counterpart. As shown in Fig. 7.3, calibration plots obtained in these flames display remarkable linearity and precision. Hence, the current burner system can be used in conjunction with these flames to provide accurate calibrations for LIF measurements of NO in other flames which do not display flame wrinkling. Indeed, Ravikrishna (1999) has applied this technique in his study of counterflow diffusion and partially premixed flames at high pressure with good success.

Finally, we note from Fig. 7.6 that once again the GRI mechanism (version 2.11) does a good job of predicting NO formation in these high-pressure, lean, premixed flames. The ability of this mechanism to correctly model the relative increase of NO concentration with pressure in lean flames confirms similar findings found for the McKenna burner flames of Chapter 4. However, the current measurements lack the uniform 30-50% underprediction of NO observed under those conditions. This improvement in predictive capability for the current study may be due to either a shift in the importance of different

NO pathways to those more correctly predicted by the GRI mechanism, or perhaps to non-kinetic effects which impact on the burner-stabilized flame predictions. We also note that the radiation correction has become negligible in these higher velocity flames.

Results for flames at higher equivalence ratios are limited to the four cases shown in Figure 7.7. The first three of these cases portray flames with a stoichiometry of $\phi$=0.75. The higher temperatures present under these conditions clearly contribute to the importance of thermal NO in the post-flame zone. As can be seen in the 1.00 and 2.02 atm flames of Fig. 7.7, a peaked, rather than top-hat, profile occurs for these flames. However, the agreement with modeling is still superb. Unfortunately, for these richer flames, wrinkling occurs even at 3.04 atm, as indicated by the sudden widening of the experimental NO profile. An additional drawback of this wrinkling effect is that it becomes impossible to determine whether or not these flames exhibit the same type of kinetic-based broadening in comparison to the GRI predictions as found in the atmospheric flames of Chapter 6. Furthermore, for the current flames, post-flame zone NO formation is significant. Hence, this wrinkle-based broadening effect, which creates regions in the post-flame zone with higher residence times, must be considered in comparisons with modeling predictions.

Based on the wrinkling effect alone, it appears that near stoichiometric to moderately rich conditions could be studied at 2.02 atm; however, the heat release rate of these flames becomes too great for the current experimental apparatus. Nevertheless, it was desired to gain some indication as to whether the poor predictive capability of the GRI mechanism exhibited in the rich flames of Chapters 4 and 6 was also present in these high-pressure counterflow premixed flames. Hence, the study was extended to include a $\phi$=1.40 flame at a pressure of 3.04 atm. The resulting profile is shown at the bottom of Fig. 7.7. A simple glance at this profile emphasizes the severity of the problems associated with rich-flame NO predictions when using the GRI reaction mechanism. In this case, an order of magnitude underprediction of NO results from employing the GRI mechanism. This underprediction cannot be explained by a simple underprediction of the prompt initiation reaction (Berg et al., 1998; Ravikrishna and Laurendeau, 1999), but indicates the
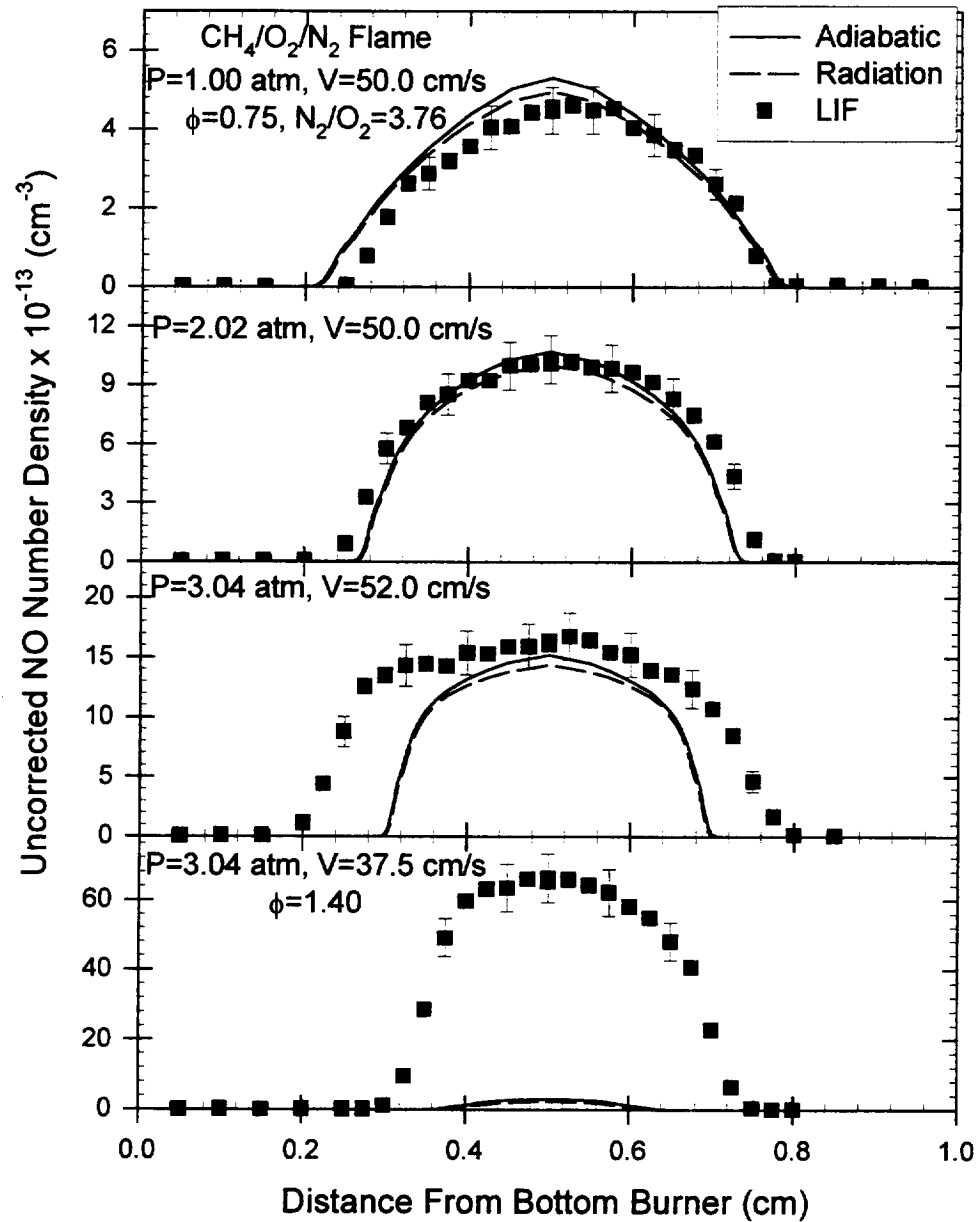
Figure 7.7: LIF-measured and predicted NO concentrations (uncorrected) in $\phi$=0.75 and 1.40, premixed, $CH_4/O_2/N_2$ flames at 1.00-3.04 atm. Predictions were obtained using temperatures found via the coupled species and energy equations with and without the inclusion of a radiation source term in conjunction with the GRI reaction mechanism.

need for substantial modification of the CH chemistry within the GRI mechanism, as discussed in Chapters 4 and 6.

A summary of the high-pressure NO measurements in lean flames is provided by Fig. 7.8, which plots measured and modeled peak NO concentrations as a function of pressure for each equivalence ratio. To facilitate this comparison, the NO concentrations have been converted to ppm values, which do not exhibit the additional pressure sensitivity, owing to density effects, included in the previous figures. The temperatures used for the conversion of LIF number densities to ppm values are those given in Table 7.1 and were obtained via joint solution of the species and energy equations within the OPPDIF code without the inclusion of a radiation source term. Inclusion of the radiation source term would not significantly alter the results shown here. Finally, it was necessary here to assume negligible variations in quenching and absorption coefficients between peak measurement locations and the calibration location at each pressure. These assumptions are the same as those used by Klassen et al. (1995) in their study of premixed, high-pressure $CH_4/O_2/N_2$ flames. The associated uncertainties, based on modeling of absorption and quenching variations, have been included in the error bars of Fig. 7.8.

An additional insight that can be gained from the pressure plots of Fig. 7.8 is that NO formation in these lean flames is not strongly influenced by pressure. For all of these cases, the total spread in the data is less than 30% of the peak value. The strongest pressure sensitivity seems to occur in the $\phi=0.75$ flames, which could be indicative of the influence of Zeldovich NO formation with its known $P^{0.5}$ pressure dependence. In the leanest flames, where the $N_2O$ intermediate mechanism should dominate, a negative pressure dependence appears to hold both in the measurements and the predictions. However, for all these cases, an insufficient change in NO concentration occurs with pressure, relative to the measurement uncertainty, to make any firm conclusions about the pressure sensitivity of NO formation under these conditions. Finally, Fig. 7.8
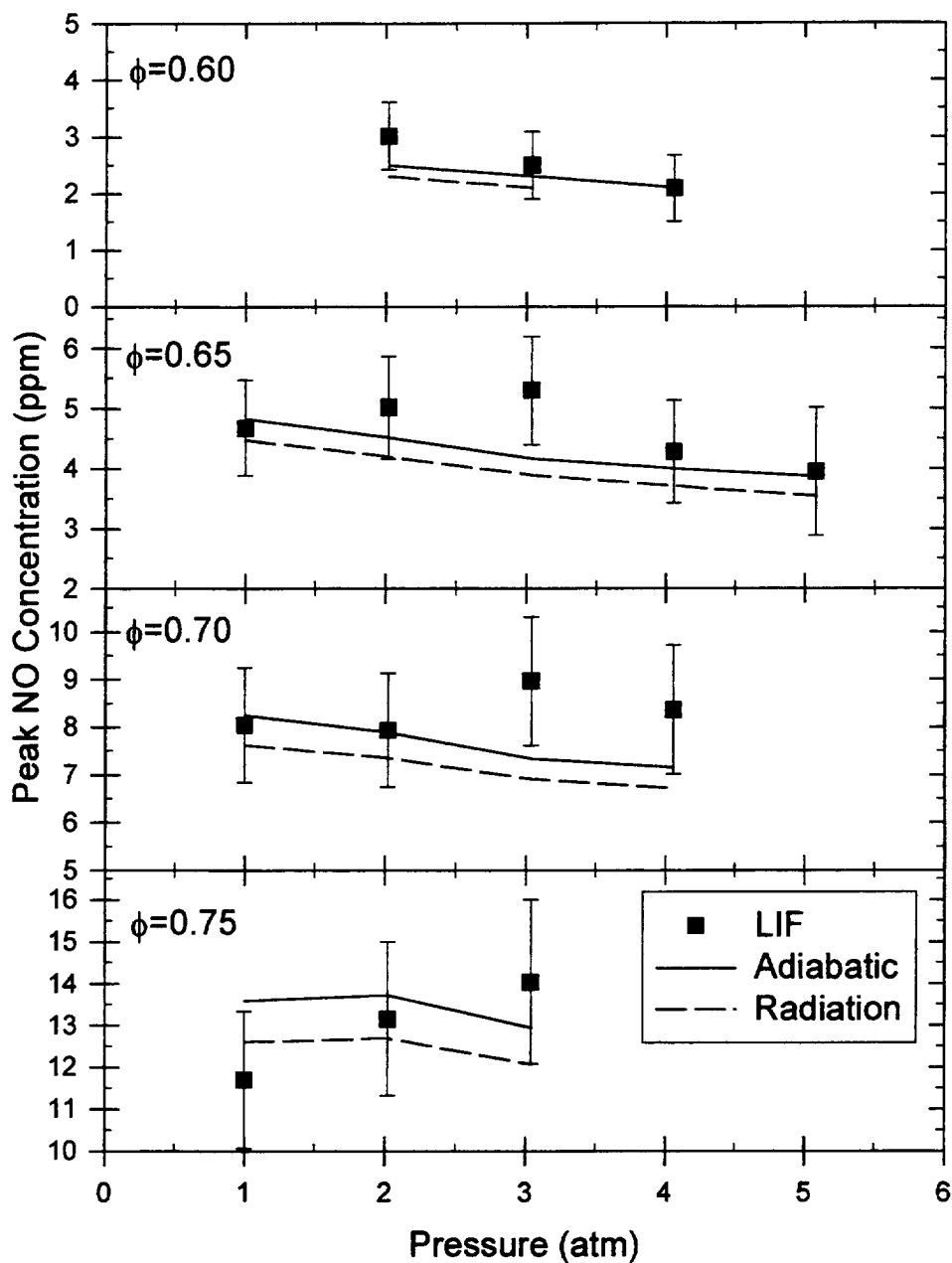
Figure 7.8:  Peak LIF-measured and predicted NO concentrations as a function of pressure in lean, premixed, counterflow $CH_4/O_2/N_2$ flames. Predictions were obtained using temperatures found via the coupled species and energy equations with and without the inclusion of a radiation source term in conjunction with the GRI reaction mechanism.

reemphasizes the relatively strong NO predictive capability of the GRI reaction mechanism in lean, premixed, counterflow flames.

## 7.4 Conclusions

Based on several limitations in the application of burner-stabilized flames, such as those produced on water-cooled McKenna burners, we decided to investigate the advantages and disadvantages of a counterflow flame geometry for the study of NO formation in high-pressure premixed flames. Using the burner discussed in Chapter 5, LIF profiles of NO concentration were obtained in a series of high-pressure, counterflow premixed flames. These measurements represent the first application of the LIF technique to high-pressure NO concentration measurements for this flame configuration. Unfortunately, the utility of this counterflow system is not without its limitations.

The effect of buoyancy was found to limit the applicability of the counterflow configuration when studying ultra-lean flames. While nearly adiabatic flames could be achieved, buoyancy effects strongly reduced the flame separation distance and eventually drove the flames into contact with the upper burner surface. A horizontally oriented burner system could limit this effect; however, the result of buoyancy in this configuration would be the creation of a highly non-one-dimensional flowfield with flames curling upward near the stagnation region.

Limitations on the heat release rate combined with the development of a wrinkling effect on the burner surface also prevent the application of this configuration to studies of near-stoichiometric flames. While the wrinkling effect could be minimized through careful design of a contoured nozzle, counterflow burner, such a design would be too large and heavy for use in the current high-pressure facility at Purdue University. Furthermore, these higher temperature flames are of little practical interest in NO formation studies since the amount of NO formed is much higher than current regulations.

On the positive side, the counterflow configuration can provide a valuable calibration source for LIF measurements of NO in a variety of counterflow diffusion and

partially premixed flames up to pressures of 5.08 atm. Comparisons between measurements and predictions of NO in high-pressure, lean premixed flames demonstrate remarkable agreement when utilizing the GRI reaction mechanism (version 2.11), thus showing that both the pressure and equivalence ratio trends of this mechanism are apparently sufficient for lean, adiabatic flames. However, the GRI mechanism again dramatically underpredicts NO formation in rich premixed flames. This behavior indicates the need for additional refinement of the CH chemistry within this mechanism, a subject pursued in greater detail in Chapter 8.

# 8. CHEMICAL KINETIC ANALYSIS OF NO FORMATION IN METHANE FLAMES

## 8.1 Introduction

As mentioned in previous chapters, the majority of chemical kinetic codes available for prediction of NO formation in combustion systems were developed via comparisons with target flames at atmospheric and sub-atmospheric pressures and with little or no comparisons to high-pressure conditions (Bowman et al., 1995; Miller and Bowman, 1989; Glarborg et al., 1986). Historically, the primary reason for this lack of high-pressure targets has been that few quantitative measurements of NO concentration were available over a sufficiently broad range of atmospheric and high-pressure conditions. The goal of the majority of this thesis has been to meet this need through the development and application of the laser-induced fluorescence (LIF) technique. The resulting measurements have been compared to chemical kinetic modeling utilizing the GRI reaction mechanism, version 2.11 (Bowman et al., 1995), and preliminary conclusions have been drawn about the strengths and weaknesses of this comprehensive reaction scheme.

Concurrent to this investigation, we have worked with other researchers to apply our LIF technique to an even wider range of flame conditions. The result of these collaborations has been the development of a truly unique database of nitric oxide measurements in a wide variety of methane/air flames. These flames include the counterflow premixed flames of the current work ($1.00$ atm $\leq P \leq 5.08$ atm, $0.6 \leq \phi \leq 1.50$, $3.76 \leq N_2/O_2 \leq 5.80$), burner-stabilized premixed flames (Thomsen, 1996) ($1.00$ atm $\leq P \leq 14.6$ atm, $0.5 \leq \phi \leq 1.60$, $2.20 \leq N_2/O_2 \leq 3.10$), counterflow diffusion and partially-premixed flames (Ravikrishna, 1999 ) ($1.00$ atm $\leq P \leq 5.08$ atm), and low specific-energy

gas premixed flames (Charlston-Goch, 1999) ($CH_4/H_2/CO/N_2/CO_2$ fuel mixture, 1.00 atm $\leq P \leq 14.6$ atm).

The purpose of this chapter is to employ this database of NO concentration measurements to re-examine the performance of the GRI mechanism over a broad range of conditions. The hope is that specific suggestions can then be made toward the improvement of this mechanism as well as toward further illumination of what problems remain to be solved and what steps should be taken to resolve them.

## 8.2 Modeling Methodology

The modeling of the chemical kinetics in this chapter was performed using two different flame codes developed by Sandia National Laboratories. For the burner-stabilized flames, we utilized the steady, laminar, one-dimensional, premixed flame code, PREMIX (Kee *et al.*, 1985); for the counterflow flames, both premixed and diffusion, we employed an opposed diffusion flame code, OPPDIF (Lutz *et al.*, 1996). In both cases, the CHEMKIN-II computer program library (Kee *et al.*, 1989) was used to process the reaction mechanism into a form which is appropriate for use by the Sandia flame codes. A burner surface temperature of 300 K was used as a boundary condition for the modeling. Well-resolved, experimentally measured temperature profiles are not easily obtained at high pressures, particularly in the burner-stabilized flames, owing to the close proximity of the flame front to the burner surface. Thus, a temperature profile generated via solution of the energy equation was used for all flame scenarios considered in this study. The applicability of the 300-K boundary condition for the counterflow flames was verified by thermocouple measurements of the reactant stream in the cold-gas regions of these flames, which yielded temperatures ranging from 303 to 310 K. Moreover, computations indicated that a 10 K rise in the boundary condition used in the model is insignificant in terms of the code predictions. For the burner-stabilized flames, it was impossible to verify this chosen upstream temperature. However, radiation-corrected thermocouple measurements of the temperature in the post-flame zone of these flames demonstrated

excellent agreement (as discussed in Chapter 4) with those predicted by the modeling. Specifically, the predicted post-flame zone temperature was found to be within 40 K of the corresponding thermocouple measurement for all of the flames studied, which is clearly within the accuracy of the thermocouple measurements. This excellent agreement increases our confidence in this modeling strategy.

The comprehensive mechanism used in the modeling is the GRI mechanism, version 2.11 (Bowman et al., 1995). This reaction mechanism, which can be found in Appendix B, considers 49 species and 277 reactions and was used initially without modification. In addition, we employed the thermodynamic and transport property files provided with the mechanism. Finally, these codes allow for calculation of species diffusion using either mixture averaged or multi-component diffusivities, with an additional option of considering the thermal diffusion of species. Mixture averaged diffusivities were employed for all the modeling presented in this chapter. Comparisons made between calculations employing mixture averaged and multi-component diffusivities demonstrated negligible effects (<1%) on either postflame zone temperature or NO concentration for all the premixed flames of this study. Inclusion of the thermal diffusivity option in the OPPDIF code (which seems to be applicable only in concert with the multi-component option) did have some impact on NO and temperature predictions. As an example, the inclusion of thermal diffusivity reduced the predicted peak NO concentration from ~33.4 ppm to ~31.7 ppm in a $\phi$=1.20, V=125 cm/s, counterflow premixed flame. However, this change is not sufficient to alter any of the conclusions made in this chapter.

An important limitation of the Sandia flame codes is that they do not consider the effects of radiation heat loss. To account for such effects on the temperature and NO predictive capabilities of the OPPDIF code, a radiation subroutine developed by Gore and coworkers (1999) was incorporated into the energy equation. This routine, which assumes optically thin radiation originating from the major species within the flame, has previously been shown to have a significant impact on NO concentration predictions in lower strain-rate, counterflow diffusion flames (Gore et al., 1999; Ravikrishna and Laurendeau, 1999). The excellent agreement found between predicted and measured

temperatures in the post-flame zone of the burner-stabilized flames, combined with the lower temperatures and residence times of these non-adiabatic flows, indicates that such a correction is unimportant in these flames. Hence, the radiation routine was only employed for our modeling of counterflow premixed and diffusion flames.

## 8.3 Chemical Kinetic Study of NO Formation in Methane Flames

### 8.3.1 Selection of Test Cases

As mentioned previously, the current study, in conjunction with several others performed at Purdue's Flame Diagnostics Laboratory, has produced a large database of NO concentration measurements in a wide variety of methane flames. Manipulation of this entire database for the optimization of chemical kinetic models would be cumbersome at best and most likely impossible. Thus it becomes necessary to extract from this database a subset of cases which represent, as well as possible, the range of conditions studied while reducing the number of flame targets to a manageable level. Hence, we now discuss the studies which have been done and list reasons for the selection of specific cases for further analysis.

We first discuss a group of measurements that are not included directly in the current study, but which impact our modeling corrections. The work in question was funded by the Australian government, which wished to study the formation of nitric oxide during premixed combustion of low specific-energy gas (LSEG) produced from the processing of low-grade coal in fluidized-bed gasification plants (Charlston-Goch, 1999). The gas consists of a mixture of $CH_4$, $H_2$, $CO$, $N_2$, and $CO_2$ with and without the addition of $NH_3$. The parameters varied in this work, in addition to equivalence ratio and pressure, included the amount of $NH_3$ doped into the flames and the amount of $CH_4$ added to the fuel stream.

There are two features of this work which are significantly different from the remaining flames of this investigation. First of all, in the undoped flames of the LSEG study, the temperatures were relatively low. This factor, combined with the low concentrations of $CH_4$, resulted in flames for which the GRI mechanism predicted domination of NO formation by the NNH pathway (Charlston-Goch, 1999). This result permitted an analysis of the NNH pathway in a fairly direct manner. The results of this analysis are included in the current modeling effort. The second unique feature of this work was the inclusion of ammonia destruction kinetics in the doped flames. Since $NH_3$ levels in the other flames of this study, as well as in typical gas-turbine combustors which are of most practical interest for the current work, are fairly low, these $NH_3$-doped flames were not included in the present analysis.

The second group of flames consists of the counterflow premixed flames investigated in Chapters 6 and 7. These flames were generated on the 1-cm diameter, counterflow burner described in Chapter 5 using a separation distance of 1 cm. Starting with the atmospheric flames of Chapter 6, the first flame chosen for this study was the leanest case, $\phi=0.65$. The reason for this choice is clear as ultra-lean premixed flames are the emphasis of most $NO_x$ reduction strategies for advanced gas-turbine engines. Because of the obvious shortfalls of the GRI mechanism in rich flames, this regime deserved strong attention as well. Consequently, the $\phi=1.20$ flame was also chosen. While richer flames might be preferable, modeling difficulties limited their usefulness to the current study, as discussed in Chapter 6. Finally, the $\phi=0.90$ case was chosen, which (it was hoped) would contain strong NO production from several different NO formation pathways. Three different dilution ratios were also considered at this equivalence ratio so as to study the effect of temperature on the NO kinetics.

Of the high-pressure counterflow premixed flames of Chapter 7, the only case included in the current study is that corresponding to the $\phi=1.40$ flame at 3.04 atm. This flame produces the largest discrepancy between measurement and modeling of any of the premixed counterflow flames studied and thus provides a good selection for probing the weaknesses of the GRI mechanism. While a high-pressure lean case could have been

chosen, the behavior of these flames was similar enough to those at atmospheric pressure that, when combined with the limitations of the high-pressure study discussed in Chapter 7, it was decided not to include them in the current work. The flow conditions for all of the counterflow premixed flames studied in this chapter are provided in Table 8.1.

The next group of flames to be considered for this analysis consists of the burner-stabilized, premixed, $CH_4/O_2/N_2$ flames investigated by Thomsen (1996), as analyzed via the GRI mechanism (version 2.11) in Chapter 4 of this study. These flames were stabilized on a 2.54-cm diameter, water-cooled McKenna burner. At the outset, it was decided to study two of the six pressures presented in this work. Atmospheric pressure was chosen as well as the 9.15-atm case. The reason for the latter is that this pressure is representative of the high-pressure work yet suffers from considerably less interference problems as compared to the 11.9-atm and 14.6-atm cases. At both pressures, the calibration flames for each of the two dilution ratios studied were chosen ($\phi$=0.60, $N_2/O_2$=2.2; $\phi$=0.80, $N_2/O_2$=3.10). These choices reflect the fact that the LIF measurements of NO concentration display their highest accuracy under calibration conditions; moreover, the two stoichiometries represent an ultra-lean case and a case for which multiple pathways should contribute at both pressures.

The final two burner-stabilized flames chosen for the present study represent those stoichiometries producing the highest NO concentration at each pressure ($\phi$=1.40 at P=1.00 atm; $\phi$=1.10 at P=9.15 atm). Since the results of Chapter 4 demonstrated the inability of the GRI mechanism to predict even qualitatively the shift in peak NO concentration to leaner stoichiometries with increase in pressure, we decided to study NO formation under these peak conditions at two different pressures in hopes of illuminating the cause of this misprediction. The flow conditions for all of the burner-stabilized premixed flames are also included in Table 8.1.

The last group of flames considered for this study is the counterflow diffusion flames of Ravikrishna (1999). The atmospheric pressure flames of this study were obtained on a 2.54-cm diameter counterflow burner with a separation distance of 2.00 cm, while the high-pressure flames were obtained on the 1-cm diameter counterflow burner

Table 8.1: Flame conditions and flow rates for chemical kinetic study of NO formation in $CH_4/O_2/N_2$ flames.

| Counterflow Premixed Flames | | | | | | |
|---|---|---|---|---|---|---|
| # | P (atm) | Dilution Ratio | Equiv. Ratio | Velocity (cm/s) | Component Flow Rates (SLPM) $CH_4$ | $O_2$ | $N_2$ |
| 1 | 1.00 | 3.76 | 0.65 | 35 | 0.105 | 0.324 | 1.22 |
| 2 | 1.00 | 3.76 | 0.90 | 120 | 0.488 | 1.085 | 4.08 |
| 3 | 1.00 | 3.76 | 1.20 | 125 | 0.659 | 1.099 | 4.13 |
| 4 | 1.00 | 4.44 | 0.90 | 35 | 0.105 | 0.234 | 1.31 |
| 5 | 1.00 | 5.25 | 0.90 | 40 | 0.129 | 0.287 | 1.47 |
| 6 | 3.04 | 3.76 | 1.40 | 37.5 | 0.689 | 0.984 | 3.70 |

| Burner-Stabilized Premixed Flames | | | | | | |
|---|---|---|---|---|---|---|
| # | P (atm) | Dilution Ratio | Equiv. Ratio | Flow Rate (SLPM) | Component Flow Rates (SLPM) $CH_4$ | $O_2$ | $N_2$ |
| 7 | 1.00 | 2.20 | 0.60 | 3.50 | 0.300 | 1.000 | 2.20 |
| 8 | 1.00 | 3.10 | 0.80 | 3.50 | 0.311 | 0.778 | 2.41 |
| 9 | 1.00 | 3.10 | 1.40 | 3.50 | 0.510 | 0.729 | 2.26 |
| 10 | 9.15 | 2.20 | 0.60 | 10.95 | 0.939 | 3.129 | 6.88 |
| 11 | 9.15 | 3.10 | 0.80 | 10.95 | 0.973 | 2.433 | 7.54 |
| 12 | 9.15 | 3.10 | 1.10 | 10.95 | 1.295 | 2.355 | 7.30 |

| Counterflow Diffusion Flames | | | | | | |
|---|---|---|---|---|---|---|
| | | Fuel Stream Parameters | | | Oxidizer Stream Parameters | | |
| # | P (atm) | Velocity (cm/s) | Flow Rates (SLPM) $CH_4$ | $N_2$ | Velocity (cm/s) | Flow Rates (SLPM) $O_2$ | $N_2$ |
| 13 | 1.00 | 37.7 | 5.791 | 17.37 | 34.7 | 4.476 | 16.83 |
| 14 | 2.02 | 20 | 0.476 | 1.43 | 20 | 0.400 | 1.50 |
| 15 | 4.06 | 20 | 0.957 | 2.87 | 20 | 0.804 | 3.02 |
| 16 | 5.08 | 20 | 1.197 | 3.59 | 20 | 1.006 | 3.78 |

described in Chapter 5 with a 1-cm separation distance. Ravikrishna (1999) found that for most of the atmospheric-pressure flames, a simple modification to the pre-exponential factor of the rate coefficient for the prompt initiation reaction resulted in excellent agreement between experiments and modeling. However, at higher pressures, the agreement broke down, indicating that the pressure trends for NO formation were not being modeled correctly by the GRI mechanism for this flame configuration.

To study this behavior, four diffusion flames were chosen at pressures of 1.00, 2.02, 4.06, and 5.08 atm. All of these flames had fuel streams consisting of 25% $CH_4$ and 75% $N_2$ by volume at similar cold-flow strain rates. The exact flow conditions for these flames are provided in Table 8.1. Ravikrishna (1999) also measured NO concentrations in partially premixed flames; however, these flames are not included in the current study.

## 8.3.2 Pathway Analysis

The first stage of our chemical kinetic analysis of the GRI reaction mechanism was to determine the relative contribution from each of the four major NO formation pathways (Zeldovich, $N_2O$ intermediate, prompt, and NNH) to the total NO concentration predicted for each of the 16 flame conditions of Table 8.1. In this type of analysis, the contribution of each mechanism is determined by either removing an initiation reaction for a pathway (subtraction technique) or including only the relevant kinetics for a given pathway (addition technique) and determining the effect on the predicted NO concentration. The accuracy of such a modeling technique only holds to the extent that the species concentrations modified by the changes in the chemical kinetic mechanism do not significantly inhibit or accelerate the kinetics of the other pathways. For the cases presented in this chapter, such inter-pathway dependencies were found to be minimal, although similar effects could limit the applicability of this technique for other flame conditions.

For this study, the various NO pathway contributions were determined in the following manner. The prompt NO contribution was determined simply by the removal of its initiation reaction,

$$CH+N_2 \Leftrightarrow HCN+N, \hspace{3cm} (R240)$$

from the comprehensive chemical kinetic mechanism (note that the elementary reaction numbers in this chapter correspond to the reaction numbers in the GRI reaction mechanism, version 2.11). Likewise, the Zeldovich, or thermal NO, contribution was determined by removing only the initiation reaction for this pathway, i.e.,

$$N+NO \Leftrightarrow N_2+O, \hspace{3cm} (R178)$$

from the overall kinetic scheme. The $N_2O$ intermediate contribution was determined by simply removing all reactions involving the $N_2O$ molecule from the comprehensive kinetic scheme. Finally, the contribution of the NNH pathway could have been determined by simply subtracting the sum of the NO contributions of the other three pathways from the total predicted NO concentration. However, this would then attribute to the NNH pathway any discrepancy caused by interpathway dependencies. Thus, the NNH pathway was determined independently by removing its initiation reaction from the GRI mechanism, i.e.,

$$NNH+O \Leftrightarrow NH+NO. \hspace{2.5cm} (R208)$$

Using the above technique, it was found that the sum of the individual contributions agreed with the total NO concentration calculated by the full GRI mechanism to within 5% in all cases. A more thorough discussion of the benefits and limitations of this type of analysis can be found in the work by Thomsen (1996).

Employing the above technique, the contributions of each of the NO formation pathways, as predicted by the GRI Mechanism (version 2.11), were calculated for each of the flames studied in this chapter. Table 8.2 summarizes the results of this pathway analysis, including a comparison between the experimental and predicted peak NO concentrations. Table 8.2 also includes the predicted temperatures at the location of peak NO concentration for each of these flames. These predictions were obtained via solution of the joint energy and species conservation equations within the flame codes. For the

Table 8.2: Predicted temperatures and pathway contributions to peak NO concentration in $CH_4/O_2/N_2$ flames. Modeling employed the GRI reaction mechanism, version 2.11.

| # | T (K) | NO Concentration (ppm) | | Pathway Contributions (%) | | | |
|---|---|---|---|---|---|---|---|
| | | LIF | Model | Zeldovich | $N_2O$ | Prompt | NNH |
| 1 | 1750 | 4.6 | 5.0 | 20 | 38 | 7 | 35 |
| 2 | 2040 | 30 | 35.0 | 46 | 12 | 12 | 30 |
| 3 | 2040 | 60 | 33.4 | 15 | 4 | 65 | 16 |
| 4 | 1700 | 12 | 7.7 | 7 | 17 | 23 | 53 |
| 5 | 1790 | 12 | 10.7 | 14 | 20 | 20 | 46 |
| 6 | 1960 | 57 | 2.5 | 0 | 2 | 97 | 1 |
| 7 | 1750 | 4.3 | 3.1 | 23 | 44 | 5 | 28 |
| 8 | 1790 | 9.8 | 6.1 | 23 | 31 | 12 | 34 |
| 9 | 1950 | 57 | 10.2 | 0 | 0 | 100 | 0 |
| 10 | 1790 | 6.8 | 3.9 | 39 | 53 | 2 | 6 |
| 11 | 1830 | 17 | 6.9 | 35 | 46 | 8 | 11 |
| 12 | 1960 | 37 | 13.0 | 4 | 10 | 76 | 10 |
| 13 | 1640 | 22 | 11.6 | 0 | 5 | 72 | 23 |
| 14 | 1680 | 56 | 12.4 | 1 | 12 | 66 | 21 |
| 15 | 1720 | 44 | 12.6 | 2 | 22 | 57 | 19 |
| 16 | 1730 | 34 | 12.1 | 3 | 25 | 53 | 19 |

counterflow diffusion flames, radiation effects were considered by inclusion of a radiation subroutine, as described previously, since the impact of this heat loss term had previously been found to be significant in such flames (Ravikrishna, 1999). However, the premixed flames were modeled without radiative heat loss for this pathway analysis as well as for the quantitative reaction path and sensitivity analyses to be presented later in this chapter.

The utility of the pathway analysis for the current work lies in its division of the test cases into groups which can be used for studying the kinetics of different NO formation pathways and in its provision of an overall understanding of the influence of stoichiometry, temperature, and flame structure on NO formation. Starting with the counterflow premixed flames of Chapters 6 and 7, we note that the leanest case (#1) has nearly equal predicted contributions from the NNH and $N_2O$ intermediate pathways. While it has long been suggested that the $N_2O$-intermediate pathway dominates NO formation in lean-premixed flames (Malte and Pratt, 1974; Nicol *et al.*, 1993), the relatively unknown NNH pathway (Bozzelli and Dean, 1995) is predicted to have a large contribution in these flames. The question as to whether such a large contribution from a mechanism not even included in most previous NO kinetic schemes (Glarborg *et al.*, 1986; Miller and Bowman, 1989) is justified remains open to debate; however, as mentioned in Chapter 4, the NNH contribution becomes less pronounced at higher pressures.

This strong NNH pathway contribution continues in all of the atmospheric pressure, counterflow premixed flames of this study. However, the contribution of the $N_2O$ pathway diminishes with increases in equivalence ratio (#2-5). The $\phi=0.9$ cases (#2,4,5) demonstrate substantial contributions from all of the NO formation pathways with the largest difference being a sharp reduction in Zeldovich NO with increased dilution owing to the simultaneous drop in flame temperature. Finally, as expected, both of the rich flames (#3,6) are dominated by prompt NO. Moreover, this dominance is more pronounced at higher pressure (#6). Finally, we note that the worst agreement between the laser-induced fluorescence measurements of NO concentration and the predictions occurs in the rich, prompt-dominated flames.

The burner-stabilized premixed flames of Klassen *et al.* (1995) and Thomsen (1996) display similar trends to the counterflow premixed flames. The two leanest flames (#7,10), with an equivalence ratio of $\phi$=0.6, are dominated by the $N_2O$ intermediate pathway. We note that while the NNH pathway still contributes significantly at atmospheric pressure (#7), this contribution is lower relative to the $N_2O$ contribution as compared to the leanest counterflow flame (#1). The $\phi$=0.8 flames (#8,11) exhibit strong contributions from several different pathways with a shift of dominance from NNH to $N_2O$ intermediate at higher pressure. For all of these lean, burner-stabilized flames, we note an underprediction of NO concentration by 30-50%, a behavior not observed in the counterflow premixed flames. Finally, as expected, both of the rich, burner-stabilized flames (#9,12) are dominated by prompt NO, and in both cases the overall NO concentration is severely underpredicted by the GRI mechanism.

The last group of flames consists of the counterflow diffusion flames (#13-16) studied by Ravikrishna (1999). In all four of these cases, prompt NO is predicted to contribute over half of the total NO concentration with the remainder being provided by the NNH pathway and, in the high-pressure cases, by the $N_2O$ intermediate pathway. In the high-pressure cases (#14-16), we note that the measured NO concentrations drop off more quickly with rising pressure than the predictions. Furthermore, the peak NO concentrations are once again severely underpredicted for these prompt-NO dominated flames.

In summary, the pathway analysis has allowed us to clearly identify several cases, with varying flow geometries and pressures, that are dominated by prompt NO formation and for which the NO concentration is, to a greater or lesser extent, underpredicted by the GRI reaction mechanism (version 2.11). Furthermore, a few lean premixed flames have been identified for which the NNH or $N_2O$ intermediate paths are dominant, but in general, multiple NO formation pathways are important in lean flames.

The observations made from this analysis will structure the remainder of our study. We will start by discussing the results of Charlston-Goch (1999), who studied a series of flames nearly completely dominated by NNH chemistry. After discussing her conclusions

and how they apply to the current work, we will next analyze those cases found above to be dominated by prompt NO formation. Next, we will turn our attention to the leanest flames, for which the $N_2O$ intermediate pathway ultimately dominates. Finally, we will study the moderately lean flames for which several pathways provide nearly equal contributions.

### 8.3.3 Kinetic Analysis of NNH-Dominated Flames

As mentioned previously, concurrent to this study, the Australian government funded a study on the formation of nitric oxide during premixed combustion of low specific-energy gas (LSEG) (Charlston-Goch, 1999). For these flames, the temperatures were relatively low (1530 K $\leq$ T $\leq$ 1800 K). This factor combined with the low concentrations of $CH_4$ in the LSEG fuel resulted in flames for which the GRI mechanism predicted domination of NO formation by the NNH pathway (Charlston-Goch, 1999). This result allowed for the analysis of this pathway's kinetics in a fairly direct manner.

A sensitivity analysis, based on the GRI reaction mechanism (version 2.11) indicated that the principal reaction responsible for NO production in these flames was the NNH initiation reaction (R208). The study proceeded to vary the preexponential factor of the Arrhenious rate coefficient for this reaction until a value was found which best fit the accumulated data. This value, 1.00E+12, is over an order of magnitude lower than the value of 7.00E+13 used in the original GRI mechanism. On the other hand, the rate coefficients for the majority of reactions in the NNH pathway are poorly known and virtually none of them include non-zero activation energies or temperature exponent terms. Therefore, it is quite possible that the behavior of this pathway upon changes in temperature or pressure is poorly predicted by the GRI mechanism. In the current study, we will eventually examine the impact of this alternate rate coefficient on the predictive capability of the GRI mechanism for the flame targets presented in Table 8.1.

8.3.4 QRPD and Sensitivity Analyses of Prompt-Dominated Flames

As indicated previously, the prompt-NO dominated flames are those for which the GRI mechanism does the worst job of predicting peak NO concentrations. Furthermore, as shown by the pathway analysis, several flame cases exist for which NO formation is clearly dominated by the prompt route. Thus, this pathway will be the first to be fully analyzed in the current work.

To better understand how the GRI mechanism models NO formation via the prompt pathway, it is informative to look at quantitative reaction path diagrams (QRPDs) associated with several of the prompt-dominated flames from this study. In a QRPD, the net specific rate at which a particular elementary reaction is occurring (reactions/(cm$^3$·s)) is calculated at each grid point using a chemkin post-processing package (Kee $et$ $al.$, 1989). These rates are then numerically integrated along the central axis of the flame to obtain a total net specific reaction rate throughout the flame (reactions/(cm$^2$·s)). These integrated rates are then scaled to a maximum value and those reactions with integrated rates above some threshold percentage are shown graphically on a reaction path diagram. In the current work, all reactions with values greater than 10% of the maximum rate are shown as well as the majority of those with values greater than 1%, although some of the latter are removed to improve the clarity of the diagram. The thickness of the arrow representing each reaction is chosen to be proportional to its integrated net specific reaction rate, thus providing a pictorial representation of the flow of molecules within a given combustion system. In some cases, multiple reactions proceed between two molecules. Since the primary purpose of these diagrams is to indicate the important intermediates and reaction paths for these flames, such multiple reactions were typically combined into one arrow for the sake of clarity. For the current work, we considered only the nitrogen kinetics. Furthermore, because of the high backward and forward rates of the reactions controlling the concentrations of $N_2O$ and NNH, these reactions were lumped together and represented by a single net reaction arrow on the respective diagrams.

Our pathway analysis identified eight flame cases which were dominated by prompt NO formation (#3,6,9,12-16). By employing QRPD analysis, we find that these eight

Figure 8.1: Quantitative reaction path diagram for OPPDIF predictions of NO formation in a $\phi$=1.20, $CH_4/O_2/N_2$ counterflow premixed flame at atmospheric pressure (case #3). Predictions were obtained by using temperatures found via the coupled species and energy equations for the GRI mechanism without the radiation source term.

cases can be divided into three distinct categories which share certain kinetic similarities. The first of these three categories is that of near-stoichiometric, rich, premixed flames, as exemplified by cases #3 and #12 of the current analysis. These two cases, with equivalence ratios of $\phi=1.20$ and $\phi=1.10$ respectively, are different from the richer premixed flames in that significant concentrations of O, OH and $O_2$ molecules are still available to participate in the nitrogen chemistry. How this difference affects the kinetic behavior of these types of flames is summarized by the QRPD for case #3, as shown in Fig. 8.1.

The first observation from Fig. 8.1 is that the NNH and Zeldovich pathways do contribute a small percentage of the NO produced in these flames. This observation supports the findings of the pathway analysis summarized in Table 8.2. However, as noted previously, NO is underpredicted in all of the rich flames, most likely owing to an underprediction of prompt NO. Hence, the contribution from the remaining pathways is likely to be even smaller relative to the prompt kinetics than currently predicted by the GRI reaction mechanism. The second observation from Fig. 8.1 is that through most of the HCN oxidation channel, multiple reactions of nearly equal weight are involved leading to different intermediates. This behavior is intimately tied to our earlier observation concerning the availability of oxidizing intermediates in these flames. Since HCN is one of the major products of the prompt initiation reaction (#240), the significance of this observation is the possible reduction of the sensitivity of the final NO concentration to any single reaction associated with this channel. Whether or not this is indeed the case will be examined via a sensitivity analysis later in this chapter.

The third observation about this flame is that the most favored HCN oxidation path seems to proceed along the intermediate sequence HCN$\rightarrow$NCO$\rightarrow$NH$\rightarrow$N$\rightarrow$NO. In fact, this sequence was suggested by Miller and Bowman (1989) for the formation of NO via the prompt pathway. For this sequence, the nitrogen atom becomes the key radical, particularly since the prompt initiation reaction produces one N atom for every HCN radical formed, and the N-atom kinetics typically associated with the Zeldovich mechanism become key for the eventual formation of NO. However, the presence of other routes for

NO formation from these radicals makes these reactions less important than might otherwise be expected. In fact, as discussed by Thomsen (1996), removal of the complete Zeldovich mechanism appears to have no impact on NO formation via the prompt mechanism.

The fourth observation from Fig. 8.1 is that reburn reactions remain relatively unimportant in slightly rich flames as their net reaction rates are small compared to those for NO formation. One exception is the fast, nearly equilibrated, reactions between NO and HNO. However, this exception appears to have little impact on the remainder of the kinetics for this flame. Figure 8.1 includes a smaller QRPD diagram which shows the reactions involved directly in CH formation and destruction for slightly rich premixed flames. From this diagram, it becomes clear that CH is primarily formed from $CH_2$ and primarily destroyed by reaction with $H_2O$ to form $CH_2O$. This behavior is nearly identical for all of the prompt-dominated flames of this study. However, in lean flames, the principal CH destruction reaction shifts to $CH+O_2 \Leftrightarrow HCO+O$, thus making this reaction important for prompt NO formation under leaner conditions.

The second group of prompt-dominated flames is that involving moderately- to highly-rich premixed flames. In the current study, cases #6 and #9 fit into this category. Both have an equivalence ratio of $\phi=1.40$, but the first is a 3.04-atm counterflow, premixed flame while the latter is an atmospheric burner-stabilized, premixed flame. A QRPD for case #9 is shown in Fig. 8.2, which is representative of the chemistry that dominates in highly-rich, premixed flames. Through this diagram, as well as the results of our earlier pathway analysis, it becomes clear that prompt NO formation is completely dominant in these flames. Figure 8.2 also shows that the oxidation of HCN and N atoms is significantly different for these conditions as compared to the near-stoichiometric conditions of Fig. 8.1. The principal difference is the relative paucity of the major oxidizing species $(O,OH,O_2)$ in these flames. This lack of oxidizing partners restricts the flow of N atoms to NO via the Zeldovich route. The drop in atomic oxygen also reduces the significance of the HCN→NCO path which dominated HCN oxidation in Fig. 8.1.
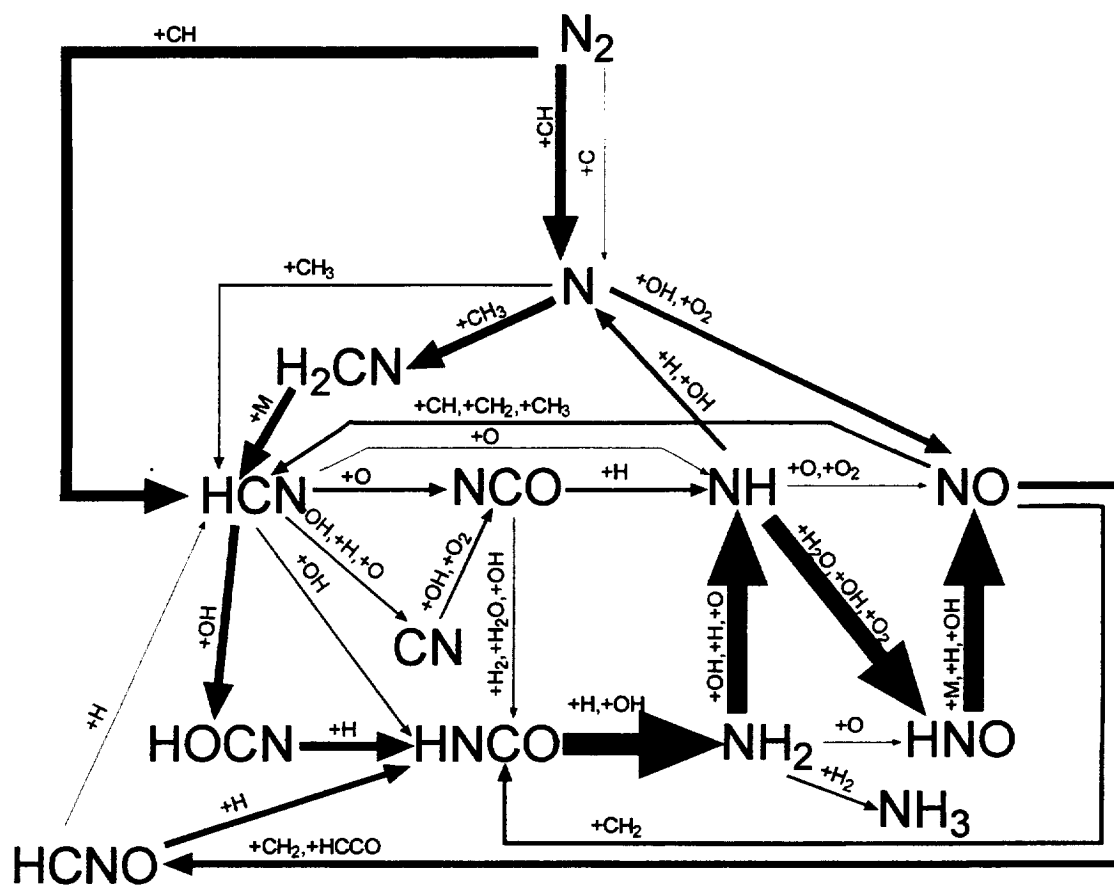
Figure 8.2: Quantitative reaction path diagram for PREMIX predictions of NO formation in a $\phi$=1.40, $N_2/O_2$=3.1, $CH_4/O_2/N_2$ flat, laminar, premixed flame at atmospheric pressure (case #9). Predictions were obtained by using temperatures found via the coupled species and energy equations for the GRI mechanism.

In the absence of these key oxidation pathways, other pathways become dominant in these richer flames. Figure 8.2 demonstrates that instead of N atom production through the HCN radical, the majority of N atoms in these flames actually form HCN by way of an $H_2CN$ intermediate. An important factor in the emergence of the $H_2CN$ channel is the much higher concentration of hydrocarbon radicals, such as $CH_3$. These radicals also contribute to a much higher rate of NO reburn in these flames, which has the net effect of recycling NO back into the HCN, HCNO, and HNCO radical pools. Hence, ever-increasing demands are placed upon the oxidation pathways involving these radicals.

The principal HCN oxidation pathway in these highly rich flames seems to follow the sequence $HCN \rightarrow HOCN \rightarrow HNCO \rightarrow NH_2 \rightarrow NH \rightarrow HNO \rightarrow NO$. Furthermore, other possible sequences for HCN oxidation are significantly restricted in these flames. This feature results in possible kinetic bottlenecks for each step of the above sequence and therefore increases the number of reactions which could influence the predicted concentrations of NO. Because of these bottlenecks as well as the increased amount of HCN production, both by way of the prompt initiation reaction and NO reburn, significant amounts of HCN can exist into the post-flame zone. $NH_3$ can also be formed as a product of these rich premixed flames. The addition of these two products into the chemistry can dramatically influence NO concentrations while simultaneously increasing the complexity of NO predictions for highly-rich flames.

The third and final group of prompt-dominated flames is represented by counterflow diffusion flames. In the current study, cases #13-16 fit into this category. These flames have a fundamentally different structure than the previous premixed flames, which affects both the content and interpretation of their associated QRPD diagrams. One such diagram, for the atmospheric-pressure case #13, is shown in Fig. 8.3. Because of the diffusive structure of such flames, certain reactions will dominate on the fuel side of the flame while others will dominate on the air side. For example, NO diffusing back into the fuel side will likely be strongly affected by reburn chemistry owing to the large concentrations of hydrocarbon radicals found there. This portrayal is clearly evident in Fig. 8.3. However, the radicals produced by the reburn process will most likely be

Figure 8.3:  Quantitative reaction path diagram for OPPDIF predictions of NO formation in a $CH_4/O_2/N_2$ counterflow diffusion flame at atmospheric pressure (case #13).  Predictions were obtained by using temperatures found via the coupled species and energy equations for the GRI mechanism in conjunction with a radiation source term.

transported back into the flamefront where they will be reconverted to NO. Therefore, the strong influence of these reburn reactions may have little effect on peak NO concentrations in nonpremixed flames, while having a significant impact on NO concentrations in rich premixed flames (see Fig. 8.2). Furthermore, the stagnation plane in these flames falls slightly on the fuel side of the flamefront, and thus this region will be the site of greatest mass loss in these counterflow flames. Hence, we would expect the QRPD to show a net production of those radicals present in this portion of the fuel stream. However, this net production will not necessarily impact the concentrations of those radicals at the location of peak NO.

With these considerations in mind, one point Figure 8.3 demonstrates is that both the NNH and $N_2O$ pathways contribute to NO formation in these flames. In fact, as shown in Table 8.2, this contribution shifts from NNH to $N_2O$ with increases in pressure. Furthermore, HCN oxidation seems to proceed according to the same sequence found for the near-stoichiometric, rich flames of Fig. 8.1. However, the sequence passing through the $NH_2$ molecule is also important with respect to the reburn chemistry. Because of the dualistic, fuel-side/air-side chemistry of these flames, it is more difficult to make firm conclusions from QRPD analysis as to what possible bottlenecks or reaction sequences might be critical for determining peak NO concentrations.

An issue that has been mentioned previously is the impact of the final HCN and $NH_3$ concentrations on the total NO concentration. As we have seen in the QRPDs of Figs. 8.1-8.3, once $N_2$, NNH, or $N_2O$ react to form any species containing only a single nitrogen atom, there is no significant pathway to return this nitrogen back to $N_2$. Basically, this nitrogen must proceed to some other product. For these conditions, the result is that NO, HCN, or $NH_3$ will be formed, and the formation of HCN and $NH_3$ as products necessarily detracts from the net amount of NO production. To examine this issue with respect to these prompt-dominated flames, Table 8.3 lists the concentrations of these molecules at the location of peak NO concentration for each condition. Clearly, only the richest premixed cases (#6 and #9) have sufficient predicted concentrations of HCN and $NH_3$ to significantly alter any predictions of peak NO concentration.

Table 8.3: Predicted NO, HCN and NH₃ concentrations in prompt-dominated CH₄/O₂/N₂ flames. Modeling employed the GRI reaction mechanism, version 2.11.

| # | Concentrations (ppm) | | |
|---|---|---|---|
|  | NO | HCN | NH₃ |
| 3 | 33.4 | 0.04 | 0.00 |
| 6 | 2.53 | 6.19 | 2.47 |
| 9 | 10.2 | 7.52 | 2.15 |
| 12 | 13.0 | 0.01 | 0.27 |
| 13 | 11.6 | 0.78 | 0.02 |
| 14 | 12.4 | 0.75 | 0.03 |
| 15 | 12.6 | 0.48 | 0.03 |
| 16 | 12.1 | 0.42 | 0.03 |

In summary, through the application of QRPD analysis, we have separated the prompt-dominated cases of the current study into three groups displaying unique characteristics. Furthermore, this analysis has allowed us to better understand the intermediate species involved in prompt NO formation and to isolate reactions which may be important in determining NO concentrations within prompt-dominated flames. However, QRPD analysis alone is not sufficient to determine which of these individual reactions control peak NO concentrations. To accomplish this task, it is necessary to perform a sensitivity analysis on each of these prompt-dominated flames.

Fortunately, an option is available within both the OPPDIF and PREMIX codes which permits the calculation of sensitivity coefficients. These coefficients describe the influence of small changes in individual reaction rate coefficients on the overall concentrations of various flame species. With appropriate extraction and post-processing routines, these coefficients can be reduced to the form

$$S_{X_j,i} = \frac{A_i}{X_{j,\max}} \cdot \frac{dX_j}{dA_i}.$$

(8.1)

Here, $X_j$ is the mole fraction of species $j$ and $A_i$ is the pre-exponential factor of the modified Arrhenius rate expression for the $i^{th}$ elementary reaction. Since the forward and reverse reaction rate coefficients for a given elementary reaction are related by the expression

$$\frac{k_f}{k_r} = K_c,$$

(8.2)

the sensitivity coefficient represents the impact of increasing both the forward and backward rate coefficients of a specific reaction rather than changing the relative magnitude of each direction.

Applying this technique, the sensitivity of the peak NO concentration to each of the reactions within the GRI reaction mechanism was calculated for each of the prompt-dominated flames of this study. The results of this analysis are presented in Table 8.4. Here, all of the reactions are listed for which the NO sensitivity coefficient exceeds 0.09.

The most apparent observation when studying Table 8.4 is that many reactions with a strong NO sensitivity are not directly related to the NO chemistry. For example, reactions such as $H+O_2 \Leftrightarrow O+OH$ have a strong influence on the concentrations of O, OH, and H within the flame front, and these radicals in turn are critical for all of the NO formation pathways. However, the systematic optimization of such reaction rate coefficients would require a study of flame speeds, direct measurements of relative radical concentrations, as well as shock tube studies of individual reaction rate coefficients. This process has been ongoing as part of the development of the GRI reaction mechanism and it is beyond the scope of this work to suggest changes in such chemistry. However, the good temperature agreement found for the flames of Chapter 4, in conjunction with the good target agreements shown on the GRI website (Bowman *et al.*, 1995), seem to suggest that at least over a limited set of conditions, this hydrocarbon chemistry is reasonably well defined in the GRI mechanism. But having said that, problems in the prediction of flamefront locations in the rich opposed flames of Chapter 6 seem to suggest that considerable room exists for improvement in this area. Table 8.4 also includes the initiation reactions for the NNH, $N_2O$ and Zeldovich pathways. While these reactions have a secondary impact on NO formation, if the prompt NO contribution is indeed being underpredicted by the GRI reaction mechanism, their contributions may actually be even smaller than predicted by Table 8.4.

Therefore, based on the previous discussion, it is important to somehow process the list of reactions in Table 8.4 to identify those which need to be optimized for the prediction of NO formation via the prompt NO pathway. The first step is to remove those reactions which are primarily associated with the other NO formation pathways, specifically, GRI reactions R208, R185, R183, R199, and R178. The remaining reactions can be divided into three groups. The first group contains those reactions whose dominant contribution is to alter O, OH and other radical concentrations, thus affecting flame temperature, flame speed and ultimately NO formation. Reactions whose primary impact on NO formation is through variations in this radical pool will exhibit similar sensitivities to both NO and OH. Thus, these reactions were identified in the current study

Table 8.4: Peak NO concentration sensitivity coefficents for prompt-dominated flames.

| Rxn | Description | Sensitivity Coefficients | | | | | | | |
|---|---|---|---|---|---|---|---|---|---|
| | Case # | 3 | 6 | 9 | 12 | 13 | 14 | 15 | 16 |
| 38 | $H+O_2 \Leftrightarrow O+OH$ | -0.48 | -1.79 | -2.75 | -1.08 | 0.55 | 0.64 | 0.73 | 0.78 |
| 240 | $CH+N_2 \Leftrightarrow HCN+N$ | 0.63 | 0.95 | 0.94 | 0.70 | 0.85 | 0.60 | 0.55 | 0.52 |
| 53 | $H+CH_4 \Leftrightarrow CH_3+H_2$ | 0.01 | 0.40 | 0.68 | 0.16 | 0.03 | -0.03 | -0.02 | -0.02 |
| 127 | $CH+H_2O \Leftrightarrow H+CH_2O$ | -0.40 | -0.55 | -0.50 | -0.56 | -0.59 | -0.44 | -0.42 | -0.39 |
| 52 | $H+CH_3(+M) \Leftrightarrow CH_4(+M)$ | 0.19 | -0.39 | -0.01 | 0.22 | -0.57 | -0.34 | -0.37 | -0.38 |
| 35 | $H+O_2+H_2O \Leftrightarrow HO_2+H_2O$ | 0.00 | -0.11 | -0.09 | -0.06 | -0.54 | -0.32 | -0.42 | -0.45 |
| 126 | $CH+H_2 \Leftrightarrow H+CH_2$ | 0.19 | 0.50 | 0.48 | 0.40 | 0.45 | 0.32 | 0.32 | 0.30 |
| 3 | $O+H_2 \Leftrightarrow H+OH$ | 0.07 | -0.11 | -0.32 | -0.03 | 0.04 | 0.04 | 0.03 | 0.02 |
| 98 | $OH+CH_4 \Leftrightarrow CH_3+H_2O$ | 0.02 | 0.27 | 0.32 | 0.17 | -0.04 | -0.05 | -0.05 | -0.05 |
| 158 | $2CH_3(+M) \Leftrightarrow C_2H_6(+M)$ | 0.02 | 0.30 | 0.10 | 0.07 | -0.05 | -0.02 | -0.01 | -0.01 |
| 10 | $O+CH_3 \Leftrightarrow H+CH_2O$ | -0.29 | 0.10 | 0.30 | -0.07 | -0.13 | -0.12 | -0.11 | -0.11 |
| 119 | $HO_2+CH_3 \Leftrightarrow OH+CH_3O$ | -0.05 | -0.16 | -0.13 | -0.28 | 0.02 | 0.01 | 0.02 | 0.02 |
| 208 | $NNH+O \Leftrightarrow NH+NO$ | 0.16 | 0.01 | 0.00 | 0.09 | 0.28 | 0.18 | 0.17 | 0.17 |
| 99 | $OH+CO \Leftrightarrow H+CO_2$ | 0.04 | -0.22 | -0.23 | -0.09 | 0.25 | 0.16 | 0.16 | 0.15 |
| 97 | $OH+CH_3 \Leftrightarrow CH_2(S)+H_2O$ | 0.04 | 0.02 | 0.06 | 0.04 | 0.24 | 0.15 | 0.14 | 0.14 |
| 135 | $CH_2+O_2 \Leftrightarrow OH+HCO$ | -0.13 | -0.20 | -0.23 | -0.18 | -0.12 | -0.06 | -0.05 | -0.04 |
| 185 | $N_2O(+M) \Leftrightarrow N_2+O(+M)$ | 0.03 | 0.01 | 0.00 | 0.05 | 0.07 | 0.10 | 0.19 | 0.21 |
| 202 | $NH_2+H \Leftrightarrow NH+H_2$ | 0.00 | 0.20 | 0.06 | 0.00 | 0.00 | 0.00 | 0.00 | 0.00 |
| 255 | $CH_3+NO \Leftrightarrow HCN+H_2O$ | 0.00 | -0.19 | -0.06 | 0.00 | 0.00 | -0.01 | -0.01 | -0.01 |
| 166 | $HCO+H_2O \Leftrightarrow H+CO+H_2O$ | -0.07 | 0.03 | 0.06 | -0.01 | 0.19 | 0.08 | 0.06 | 0.06 |
| 84 | $OH+H_2 \Leftrightarrow H+H_2O$ | 0.01 | -0.16 | -0.18 | -0.07 | 0.03 | 0.03 | 0.03 | 0.03 |
| 234 | $HCN+OH \Leftrightarrow HOCN+H$ | 0.00 | 0.14 | 0.17 | 0.00 | 0.00 | 0.00 | 0.00 | 0.00 |
| 183 | $N_2O+H \Leftrightarrow N_2+OH$ | -0.03 | -0.01 | 0.00 | -0.07 | -0.06 | -0.08 | -0.15 | -0.17 |
| 199 | $NH+NO \Leftrightarrow N_2O+H$ | 0.03 | 0.01 | 0.00 | 0.08 | 0.05 | 0.07 | 0.14 | 0.17 |
| 274 | $HCCO+NO \Leftrightarrow HCNO+CO$ | 0.00 | -0.17 | -0.03 | 0.00 | -0.02 | -0.02 | -0.02 | -0.03 |
| 21 | $O+C_2H_2 \Leftrightarrow H+HCCO$ | -0.01 | -0.15 | -0.02 | -0.02 | -0.02 | -0.02 | -0.02 | -0.01 |
| 36 | $H+O_2+N_2 \Leftrightarrow HO_2+N_2$ | 0.00 | -0.02 | -0.01 | -0.01 | -0.14 | -0.07 | -0.09 | -0.09 |
| 178 | $N+NO \Leftrightarrow N_2+O$ | 0.14 | 0.01 | 0.00 | 0.03 | 0.00 | 0.01 | 0.03 | 0.03 |
| 275 | $CH_3+N \Leftrightarrow H_2CN+H$ | 0.00 | -0.13 | -0.07 | 0.00 | -0.01 | 0.00 | 0.00 | 0.00 |
| 43 | $H+OH+M \Leftrightarrow H_2O+M$ | -0.06 | -0.01 | -0.02 | -0.12 | -0.09 | -0.07 | -0.09 | -0.09 |
| 167 | $HCO+M \Leftrightarrow H+CO+M$ | -0.04 | 0.02 | 0.03 | 0.00 | 0.12 | 0.05 | 0.04 | 0.04 |
| 197 | $NH+H_2O \Leftrightarrow HNO+H_2$ | 0.00 | 0.12 | 0.06 | 0.01 | 0.00 | 0.00 | 0.01 | 0.01 |
| 168 | $HCO+O_2 \Leftrightarrow HO_2+CO$ | 0.02 | -0.07 | -0.11 | 0.00 | -0.10 | -0.04 | -0.04 | -0.04 |
| 159 | $2CH_3 \Leftrightarrow H+C_2H_5$ | 0.03 | 0.10 | 0.06 | -0.03 | 0.09 | 0.05 | 0.07 | 0.07 |
| 153 | $CH_2(S)+CO_2 \Leftrightarrow CO+CH_2O$ | -0.03 | -0.03 | 0.03 | -0.07 | -0.09 | -0.09 | -0.10 | -0.10 |
| 55 | $H+HCO \Leftrightarrow H_2+CO$ | 0.04 | 0.00 | 0.00 | 0.00 | -0.10 | -0.03 | -0.02 | -0.02 |
| 142 | $CH_2(S)+N_2 \Leftrightarrow CH_2+N_2$ | 0.05 | 0.01 | 0.05 | 0.02 | 0.09 | 0.06 | 0.05 | 0.04 |
| 273 | $HOCN+H \Leftrightarrow H+HNCO$ | 0.00 | 0.07 | 0.09 | 0.00 | 0.00 | 0.00 | 0.00 | 0.00 |
| 125 | $CH+O_2 \Leftrightarrow O+HCO$ | -0.08 | -0.03 | -0.04 | -0.03 | -0.09 | -0.06 | -0.05 | -0.05 |

by taking the ratio of the predicted sensitivity for peak NO concentration over that for peak OH concentration for each reaction. All reactions, with one exception which will be discussed later, for which this ratio was less than ten were included in this first group. The second group of reactions are those traditionally associated with prompt NO; specifically, the prompt initiation reaction as well as those reactions which affect CH concentration. Finally, the third group of reactions are those which involve the remaining nitrogenous compounds. This group includes NO reburn reactions as well as those reactions involved in the oxidation of HCN to NO.

These final two groups have the greatest import for the current study and thus have been separated and retabulated in Table 8.5. Looking first at the CH and prompt initiation chemistry, it is not surprising to find that the prompt initiation reaction (R240) has the highest sensitivity coefficient for all prompt-dominated flames. The remaining reactions impact CH concentration one way or another. Reactions R125, R126, and R127 balance the formation and destruction of CH. Meanwhile, reaction R135 provides an alternate route for $CH_2$ oxidation that avoids the production of CH. This reaction is the one mentioned previously whose peak NO concentration sensitivity was less than 10 times its peak OH concentration sensitivity and yet was not included in the first group of radical pool reactions. Specifically, the ratio of NO to OH sensitivity coefficients is ~5.0 for this reaction. However, reaction R135 does have a strong impact on CH concentration and seems to fit into this category. Furthermore, both reactions R126 and R135 become more significant for the prediction of prompt-NO contributions in lean-premixed flames and thus should be included in any optimization of the prompt NO pathway. From Table 8.5, it becomes clear that the remaining two reactions (R97 and R142) have considerably higher sensitivity coefficients for NO concentration in the counterflow-diffusion flames than in the rich premixed flames. Their higher sensitivity derives from their impact on the formation of $CH_2$ from $CH_3$ by way of the $CH_2(S)$ intermediate, which is the primary source of $CH_2$ in these flames.

The other group of reactions in Table 8.5 represents those directly involving the nitrogenous molecules HCN, NH, $NH_2$, HOCN, HCNO, HNCO, N, HNO, $H_2CN$ and

Table 8.5: Peak NO concentration sensitivity coefficients for reactions directly involved in prompt NO chemistry for prompt-dominated flames.

| Rxn | Description | Sensitivity Coefficients | | | | | | | |
|---|---|---|---|---|---|---|---|---|---|
| | Case # | 3 | 6 | 9 | 12 | 13 | 14 | 15 | 16 |
| CH Chemistry | | | | | | | | | |
| 240 | $CH+N_2 \Leftrightarrow HCN+N$ | 0.63 | 0.95 | 0.94 | 0.70 | 0.85 | 0.60 | 0.55 | 0.52 |
| 127 | $CH+H_2O \Leftrightarrow H+CH_2O$ | -0.40 | -0.55 | -0.50 | -0.56 | -0.59 | -0.44 | -0.42 | -0.39 |
| 126 | $CH+H_2 \Leftrightarrow H+CH_2$ | 0.19 | 0.50 | 0.48 | 0.40 | 0.45 | 0.32 | 0.32 | 0.30 |
| 97 | $OH+CH_3 \Leftrightarrow CH_2(S)+H_2O$ | 0.04 | 0.02 | 0.06 | 0.04 | 0.24 | 0.15 | 0.14 | 0.14 |
| 135 | $CH_2+O_2 \Leftrightarrow OH+HCO$ | -0.13 | -0.20 | -0.23 | -0.18 | -0.12 | -0.06 | -0.05 | -0.04 |
| 142 | $CH_2(S)+N_2 \Leftrightarrow CH_2+N_2$ | 0.05 | 0.01 | 0.05 | 0.02 | 0.09 | 0.06 | 0.05 | 0.04 |
| 125 | $CH+O_2 \Leftrightarrow O+HCO$ | -0.08 | -0.03 | -0.04 | -0.03 | -0.09 | -0.06 | -0.05 | -0.05 |
| Nitrogen Chemistry | | | | | | | | | |
| 202 | $NH_2+H \Leftrightarrow NH+H_2$ | 0.00 | 0.20 | 0.06 | 0.00 | 0.00 | 0.00 | 0.00 | 0.00 |
| 255 | $CH_3+NO \Leftrightarrow HCN+H_2O$ | 0.00 | -0.19 | -0.06 | 0.00 | 0.00 | -0.01 | -0.01 | -0.01 |
| 234 | $HCN+OH \Leftrightarrow HOCN+H$ | 0.00 | 0.14 | 0.17 | 0.00 | 0.00 | 0.00 | 0.00 | 0.00 |
| 274 | $HCCO+NO \Leftrightarrow HCNO+CO$ | 0.00 | -0.17 | -0.03 | 0.00 | -0.02 | -0.02 | -0.02 | -0.03 |
| 275 | $CH_3+N \Leftrightarrow H_2CN+H$ | 0.00 | -0.13 | -0.07 | 0.00 | -0.01 | 0.00 | 0.00 | 0.00 |
| 197 | $NH+H_2O \Leftrightarrow HNO+H_2$ | 0.00 | 0.12 | 0.06 | 0.01 | 0.00 | 0.00 | 0.01 | 0.01 |
| 273 | $HOCN+H \Leftrightarrow H+HNCO$ | 0.00 | 0.07 | 0.09 | 0.00 | 0.00 | 0.00 | 0.00 | 0.00 |

NO. These reactions include both those associated with NO reburn as well as those involved in HCN oxidation. However, the pertinent reactions all have one thing in common. They only exhibit high sensitivities in the two richest premixed flames studied (cases #6 and #9). The reason for this behavior was discussed previously with respect to the QRPD analysis for these flames. Specifically, the low concentrations of certain oxidizing molecules $(O, O_2, OH)$ leads to bottlenecks in the $N \rightarrow H_2CN \rightarrow HCN \rightarrow HOCN \rightarrow HNCO \rightarrow NH_2 \rightarrow NH \rightarrow HNO \rightarrow NO$ oxidation chain. These bottlenecks, in conjunction with the enhanced reburn contributions caused by the higher concentrations of hydrocarbon radicals, result in greater concentrations of HCN and $NH_3$ and thus reduced predictions of NO concentration in these flames. Errors in the rate coefficients for these particular reactions may thus help explain why predictions of NO concentrations in these two flames are the worst of all the cases studied in this chapter.

### 8.3.5 Parametric Study of GRI Mechanism in Prompt-Dominated Flames

The above kinetic analysis has clearly described the processes and key reactions involved in prompt NO formation via the GRI reaction mechanism (version 2.11). In this section, an attempt will be made to incorporate some modifications to the GRI mechanism which have been proposed by other researchers as well as a few which seem to be indicated by the results of the current analysis. Comparisons will then be made between modeling and experimental data to evaluate whether a few small changes to selected rate coefficients of the GRI mechanism can significantly improve its predictive capabilities with respect to prompt NO formation, without altering the initial reaction list or thermodynamic database.

Recently, two studies (Sick *et al.*, 1998; Juchmann *et al.*, 1998) have compared modeling predictions utilizing the GRI reaction mechanism with both experimental data and alternate predictions using a modified reaction sequence based on the comprehensive mechanism of Lindstedt and coworkers (Lindstedt and Skevis, 1997; Lindstedt *et al.*, 1994; 1995). The experimental work of Juchmann *et al.* (1998) consisted of LIF

measurements of CH and CN in an NO-doped, stoichiometric, premixed, $CH_4/O_2$ flame at a pressure of 10 Torr. Similarly, the experimental work of Sick *et al.* (1998) contained LIF measurements of NO concentration in both NO and $NH_3$ doped, as well as undoped, $CH_4$/air counterflow diffusion flames at atmospheric pressure. In a manner similar to that presented above, these authors utilized sensitivity analyses to identify key reactions for NO formation and destruction and then performed an in-depth review of the kinetic literature to bolster their development of the Lindstedt mechanism. During this process, they documented several discrepancies between the rate coefficients utilized in the GRI mechanism and those supported by their experimental work. The results of these two studies are summarized in this section with respect to the key CH reactions of Table 8.5.

The rate coefficient of reaction R125, $CH+O_2 \Leftrightarrow O+HCO$, was used as an optimization variable in the GRI mechanism, version 2.11. However, its rate coefficient was not modified from its initial value of $3.3 \times 10^{13}$ $cm^3$/mol·s. Juchmann *et al.* (1998) summarized recent kinetic studies which suggest this rate coefficient is probably a factor of 2-3 too low. This finding was independently verified by the work of Woiki *et al.* (1998) who determined that a factor of three increase in this reaction rate coefficient led to improved agreement between modeling predictions and their measurements of CH concentration.

The rate coefficient of reaction R126, $CH+H_2 \Leftrightarrow H+CH_2$, was also used as an optimization variable in the GRI mechanism. In this case, however, the optimization resulted in a factor of three decrease in the initial rate coefficient taken from the kinetics literature. Both Juchmann *et al.* (1998) and Sick *et al.* (1998) commented that the initial rate coefficient chosen for this reaction represented the high end of recent kinetic measurements. Furthermore, their studies indicated that the factor of three decrease brought on by the GRI optimization process actually produced a value consistent with most recent studies; however, considerable uncertainty continues to exist with respect to this reaction rate coefficient.

The rate coefficient for reaction R127, $CH+H_2O \Leftrightarrow H+CH_2O$, was another optimization variable for the GRI mechanism. In this case, the pre-exponential factor was

increased by a factor of three during the optimization process. Sick *et al.* (1998) found that introduction of this enhanced rate coefficient led to significant deterioration in the level of agreement between their NO predictions and experiments. Hence, they suggested the use of a rate coefficient more in line with the original, unoptimized, GRI rate coefficient for reaction R127.

The rate coefficient for reaction R135, $CH_2+O_2 \Leftrightarrow OH+HCO$, was decreased by a factor of 1.73 from its literature value during the optimization process for the GRI mechanism. The revised mechanism developed by Sick *et al.* (1998) and Juchmann *et al.* (1998) reduced this rate coefficient even further to about an order of magnitude below that used in the GRI mechanism. However, sufficient scatter exists in the experimental data to support either rate coefficient for this reaction.

Finally, reaction R240, $CH+N_2 \Leftrightarrow HCN+N$, features both one of the most sensitive rate coefficients with respect to NO formation as well as one of the most widely debated in the literature. The rate coefficient for this reaction was also an optimization variable for the GRI reaction mechanism and was reduced by a factor of 1.41 from its previous literature value. Recent work by several authors have suggested that this reduced rate coefficient is much too low. Berg *et al.* (1998) recommended an increase in the pre-exponential factor of this reaction by a factor of 2.1-2.3. Meanwhile, both Sick *et al.* (1998) and Ravikrishna and Laurendeau (1999) recommended a factor of 2.5 increase in this reaction rate coefficient based on their studies in counterflow diffusion flames. Thus, the general consensus seems to be that the reduced rate used in the GRI mechanism is too low, although discrepancies still exist with respect to the exact amount of underprediction in NO concentration.

Based on the above discussion as well as the kinetic analysis of the current work, two initial strategies were pursued for improving the predictive capabilities of the GRI mechanism with respect to prompt NO. In the first study, a simple variation of the pre-exponential factor for reaction R240 was assessed using techniques similar to Ravikrishna and Laurendeau (1999). In the second study, a more in-depth series of changes was evaluated. Specifically, the pre-exponential factor of reaction R125 was increased by a

factor of three, while the pre-exponential factor of reaction R127 was decreased by a factor of three to its original literature value. The rate coefficients for reactions R240 and R135, which are more widely disputed, were used as optimization variables for matching the prompt-dominated cases studied in this investigation. This second study also incorporated the reduced rate coefficient of Charlston-Goch (1999) for the NNH reaction R208.

The ultra-rich flames, for which reburn is most significant, were initially excluded from this optimization process to avoid confusing effects of reburn and CH chemistry. Furthermore, agreement was sought first for the atmospheric data, with the high-pressure results taking on a secondary role. Hence, agreement was sought first for cases #3 and #13 with cases #12 and #14-16 used for subsequent optimization in the second study. Based on these restrictions, optimized pre-exponential factors for reaction R240 were found to be 2.5 and 2.0 times the GRI mechanism value for the first and second studies, respectively. In the second study, it was also found that the pre-exponential factor for reaction R135 was best left unchanged.

The results of this work are summarized in Table 8.6. In this table, predicted peak NO concentrations are provided, using several different modeling strategies, for comparison with measurements of peak NO concentration. For all of the counterflow flames, both premixed and non-premixed, radiation correction routines were included in the kinetic modeling. This accounts for the small differences in the predicted NO concentrations for the counterflow premixed flames of Table 8.6 as compared to those of Table 8.2. In addition to the predictions for the standard GRI mechanism, predictions are shown using reaction mechanisms from each of the above two studies. For each of these three mechanisms, the sum of the three major product species, NO, HCN and $NH_3$ are also listed for comparitive purposes. Peak calculated NO concentrations based on two additional studies are also provided, as discussed in detail later in this chapter. A list of key reaction rate coefficients modified for the first three studies is provided in Table 8.7.

Starting with the first study, we note that NO predictions can be improved for some cases by simply increasing the rate coefficient for reaction R240 by a factor of 2.5.

Table 8.6: Predicted and measured concentrations for peak NO and the sum of NO+HCN+NH₃ for prompt-dominated CH₄/O₂/N₂ flames. Five different reaction mechanisms were used in the modeling: the unmodified GRI reaction mechanism, version 2.11, and four modified GRI reaction mechanisms based on the four kinetic studies of this section.

| Concentrations (ppm) | | | | | | | | |
|---|---|---|---|---|---|---|---|---|
| | LIF | GRI | | Study 1 | | Study 2 | | Study 3 | Study 4 |
| # | NO | NO | SUM | NO | SUM | NO | SUM | NO | NO |
| 3 | 60 | 32.8 | 32.8 | 63.6 | 63.7 | 59.2 | 59.3 | 59.2 | 59.6 |
| 6 | 57 | 1.9 | 9.7 | 4.5 | 23.7 | 5.4 | 28.9 | 6.0 | 12.9 |
| 9 | 57 | 10.2 | 19.9 | 24.5 | 48.0 | 27.2 | 61.3 | 27.8 | 37.7 |
| 12 | 37 | 13.0 | 13.3 | 26.2 | 26.8 | 35.2 | 36.0 | 35.3 | 35.9 |
| 13 | 22 | 11.6 | 12.4 | 23.6 | 25.4 | 23.7 | 26.7 | 24.1 | 27.0 |
| 14 | 56 | 12.4 | 13.2 | 24.0 | 25.7 | 24.0 | 25.9 | 24.4 | 27.3 |
| 15 | 44 | 12.6 | 13.1 | 22.6 | 23.7 | 22.7 | 23.8 | 23.2 | 25.8 |
| 16 | 34 | 12.1 | 12.5 | 21.1 | 22.0 | 21.1 | 22.1 | 21.6 | 24.1 |

Table 8.7: Reaction rate coefficients varied in the kinetic studies of Table 8.6. Rate coefficients in the form $k_f = AT^n \exp(-E_a/RT)$. Study 4 is identical to Study 3 with reactions R244-R256 and R274 removed.

| | | GRI Mechanism 2.11 | | | Study 1 | Study 2 | Study 3 |
|---|---|---|---|---|---|---|---|
| | | $A$ | $n$ | $E_a$ | $A$ | $A$ | $A$ |
| Rxn | Description | $cm^3/gmol \cdot s$ | | cal/gmol | $cm^3/gmol \cdot s$ | $cm^3/gmol \cdot s$ | $cm^3/gmol \cdot s$ |
| 125 | CH+O$_2$⇔O+HCO | 3.300E+13 | 0.00 | 0 | 3.300E+13 | 9.900E+13 | 9.900E+13 |
| 127 | CH+H$_2$O⇔H+CH$_2$O | 1.713E+13 | 0.00 | -755 | 1.713E+13 | 5.710E+12 | 5.710E+12 |
| 208 | NNH+O⇔NH+NO | 7.000E+13 | 0.00 | 0 | 7.000E+13 | 1.000E+12 | 1.000E+12 |
| 240 | CH+N$_2$⇔HCN+N | 2.857E+08 | 1.10 | 20400 | 7.143E+08 | 5.714E+08 | 5.714E+08 |
| 274 | HCCO+NO ⇔HCNO+CO | 2.350E+13 | 0.00 | 0 | 2.350E+13 | 2.350E+13 | 9.000E+12 |

Specifically, the atmospheric-pressure, near-stoichiometric premixed and non-premixed cases (#3 and #13) show excellent agreement between modeling and predictions for this case. However, this agreement does not extend to the high-pressure, near-stoichiometric premixed and non-premixed cases (#12, #14-16). Even more difficulties are found in the extension of this approach to the ultra-rich premixed flames (#6, #9). In both cases, we note that in addition to the predicted NO concentration being considerably below the experimental value, the sum of the three product species is also below the measured NO value. This disagreement indicates that even drastic changes in the sensitive rate coefficients for the reburn and nitrogen chemistry of these flames, as listed in the bottom half of Table 8.5, will be unlikely to result in successful matching of the experimental data.

The results of the second study were a bit more promising than those of the first, as can be seen in Table 8.6. This mechanism, with its modified CH chemistry, is better able to predict NO concentrations in near-stoichiometric premixed flames, not only at atmospheric pressure but at elevated pressures as well. This agreement can be seen in the modeling predictions for cases #3 and #12. Furthermore, predictions remain good for the diffusion flame at atmospheric pressure (case #13). For the ultra-rich case at atmospheric pressure (#9), the NO prediction is still low, but the experimental concentration now falls between the NO prediction and the sum of the nitrogenous product species. This result indicates that proper modification of the reburn and nitrogen chemistry may result in adequate performance for this case. However, in both the diffusion and ultra-rich cases, this revised model still fails to predict the impact of pressure on NO concentration.

To examine the influence of NO reburn chemistry on these predictions, we undertook two additional kinetic analyses. In Study 3, the pre-exponential factor of reaction R274 was reduced by a factor of approximately 2.6. This reaction was identified in the sensitivity analysis of Table 8.5 and has recently been the subject of much critical review in the literature. In particular, Miller et al. (1998) used a flow-reactor to investigate the rate coefficient and branching ratio of the HCCO+NO reaction. Their results suggest a temperature dependent rate coefficient for this reaction that consistently

falls below that utilized in the GRI mechanism. Furthermore, in the final stages of the current study, a new version of the GRI mechanism (version 3.0) was released which uses this rate coefficient as an optimization parameter (Smith *et al.*, 1999). The final value from this latter work is consistent with that of Miller *et al.* (1998) for moderate flame temperatures and was chosen for the current study. The performance characteristics of the GRI mechanism, version 3.0, will be considered further in Section 8.4.

As a final attempt to gauge the impact of reburn chemistry on NO concentrations in these flames, all reactions involving the attack of hydrocarbon radicals on the NO molecule were removed from the modified GRI mechanism of Study 3. Furthermore, reaction R274 involving the HCCO radical was also removed. While these changes are clearly extreme, since NO reburn has been experimentally observed in hydrocarbon flames, many earlier mechanistic investigations ignored these reactions. An example of this approach is the Glarborg-Miller-Kee (Glarborg *et al.*, 1986) reaction mechanism as modified by Drake and Blint (1991) (GMK-DB). The GMK-DB mechanism was shown in Chapter 4 to exhibit better qualitative prediction of NO concentrations under rich, premixed conditions than the GRI mechanism. Thus, to determine if the addition of reburn chemistry could be at all responsible for the qualitative failure of the GRI mechanism under ultra-rich conditions, this modified mechanism, which we shall term Study 4, was applied to the prompt-dominated flames of this section.

The results of Studies 3 and 4 are presented in Table 8.6. Clearly, reburn reactions alone cannot explain the underpredictions observed in ultra-rich flames, although they may be a piece of the puzzle. The reduced reburn of Studies 3 and 4 did result in increased NO predictions for the ultra-rich premixed flames (#6, #9); however, the magnitude of these changes was inadequate to match the experimental measurements. Furthermore, these changes had no effect on the predicted pressure dependence of NO concentration in counterflow diffusion or ultra-rich premixed flames. As a final attempt to unravel this mystery, we doubled or halved (in such a way as to maximize NO production) the four most sensitive nitrogen reactions listed in the lower half of Table 8.5. Even with these dramatic changes, NO was underpredicted in ultra-rich flames and no improvement was

observed in the pressure dependence. We are thus left without a simple solution to the poor predictive capability of the GRI mechanism in high-pressure diffusion and ultra-rich flames.

In conclusion, we have attempted, without varying the reaction list or thermodynamic and transport properties of the GRI reaction mechanism (version 2.11), to modify the reaction rate coefficients of certain key reactions based on current suggestions in the literature. Employing a parametric approach, we obtained a reaction mechanism (Study 3), which we will heretofore refer to as the modified GRI mechanism, that provides clearly superior prediction of NO concentrations in near-stoichiometric, rich flames and atmospheric-pressure, counterflow diffusion flames. However, this approach was unable to produce a mechanism capable of predicting NO concentrations in ultra-rich flames or to predict the pressure dependence of NO formation in counterflow diffusion flames.

Several explanations can be offered for this finding. First of all, inaccuracies could exist outside of the CH and nitrogenous reactions that were evaluated here. Secondly, some rate coefficients undoubtedly have inadequate temperature and pressure sensitivities owing to the limited amount of high-quality data available for many important elementary reactions. Thirdly, key reactions and kinetic pathways may not even be included in the GRI reaction mechanism. The selection of a reaction set is a complicated and ongoing procedure that will be critical to the continued development of the GRI reaction mechanism. Fourthly, modeling uncertainties with regard to temperature profiles, thermodynamic data, transport data and buoyancy effects could have various degrees of impact on our modeling conclusions. A summary of some of these effects has been presented by Dong *et al.* (1999). In general, however, such effects are unlikely to cause the large-scale qualitative discrepancies observed in the ultra-rich flames of the current study.

### 8.3.6 Kinetic Analysis of Lean Premixed Flames

In the pathway analysis of Section 8.3.2, it was noted that the leanest, premixed flames exhibited strong contributions from the $N_2O$ intermediate pathway. In fact, the $N_2O$ intermediate pathway became increasingly dominant with decreases in equivalence ratio. In general, the NO concentrations in such flames are better predicted by the GRI reaction mechanism than those in prompt-dominated flames. However, because of the contributions from several mechanisms, it is difficult to tell whether this good behavior truly indicates accurate prediction of the $N_2O$ intermediate mechanism. In this section, we will first consider a quantitative reaction path diagram for one of these ultra-lean flames (case #7). This diagram will identify those intermediates that play a substantial role in lean flames. Furthermore, QRPD analysis will help us to isolate those reactions important to NO formation via the $N_2O$ intermediate and NNH pathways in such flames. We will then elaborate on these findings by examining sensitivity coefficients for relevant elementary reactions. Finally, we will review some recent literature concerning the uncertainties associated with the various reactions in the $N_2O$ intermediate mechanism and assess the impact of proposed changes from the previous section on NO predictions under lean-premixed conditions.

Figure 8.4 presents the quantitative reaction path diagram for case #7, a burner-stabilized, lean, premixed flame ($\phi=0.60$, $N_2/O_2=2.2$, P=1.00 atm). This diagram clearly demonstrates the dominance of the $N_2O$ intermediate pathway in this flame as well as the secondary roles played by the NNH and Zeldovich pathways. The lower concentrations of hydrocarbon radicals lead not only to a decrease in the importance of prompt NO kinetics, but also to a decrease in the importance of reburn kinetics. One immediate impact of this scenario is a reduction in the number of key intermediates in the NO formation process. As Fig. 8.4 shows, the N, NH and HNO radicals have become the only significant intermediates for NO formation in lean, premixed flames. This is a considerably simpler picture than in the case of prompt NO kinetics and perhaps helps to explain the much better agreement found between predictions and measurements of NO concentration in lean, premixed flames.

Figure 8.4: Quantitative reaction path diagram for OPPDIF predictions of NO formation in a CH₄/O₂/N₂ lean, premixed, burner-stabilized flame at atmospheric pressure ($\phi$=0.6, N₂/O₂=2.2, case #7). Predictions were obtained by using temperatures found via the coupled species and energy equations for the GRI mechanism.

At the bottom of Fig. 8.4, two additional QRPDs have been provided that illuminate the role of individual reactions involved in the formation and destruction of the two NO formation intermediates, $N_2O$ and NNH. In each case, several reactions display significant contributions that could affect NO formation by each of these pathways. In the case of the $N_2O$ intermediate pathway, two reactions exist which convert $N_2O$ into NO; several additional reactions could also influence $N_2O$ concentration. The NNH pathway contains only one NO forming reaction, but several reactions are available which could impact the NNH concentration, thereby affecting the overall rate of NO formation.

As was noted for prompt NO chemistry, the rate at which a specific elementary reaction occurs does not necessarily determine its sensitivity for NO concentration. Hence, a sensitivity analysis was required for these moderately- to highly-lean flames (cases #1, #7, #8, #10, and #11). For this analysis, we were interested only in the nitrogen chemistry involved in the NNH, $N_2O$ intermediate and Zeldovich pathways. Of particular interest were those reactions appearing in the smaller QRPDs of Fig. 8.4 and those reactions involving the breakdown of molecular nitrogen directly to N atoms. Table 8.8 presents the results of this analysis.

Considering first the NNH kinetics, only the reaction directly responsible for converting NNH into NO (R208) has a significant sensitivity with respect to NO formation. This somewhat surprising conclusion is directly opposite that for prompt NO formation, which is strongly influenced by additional reactions governing CH concentration. One plausible explanation for this behavior is that the reaction rates are so fast that nearly equilibrium concentrations of NNH are maintained in those regions most critical for NO formation. Indeed, an examination of our predictions shows that the peak NNH concentration in these lean flames is almost exactly that expected from chemical equilibrium with $N_2$ and H. Hence, concentrations are determined by equilibrium- or fast-chemistry effects rather than kinetic limitations. Consequently, rather large changes in the reaction rate coefficients for NNH would be needed to reduce the overall rates sufficiently to enter a kinetically controlled regime.

Table 8.8: Peak NO concentration sensitivity coefficients for reactions directly involved in NNH, $N_2O$ intermediate and Zeldovich NO chemistry for lean premixed flames.

| Rxn | Description | Sensitivity Coefficients | | | | | | | |
|---|---|---|---|---|---|---|---|---|---|
| | Case # | 1 | 2 | 4 | 5 | 7 | 8 | 10 | 11 |
| NNH Chemistry | | | | | | | | | |
| 208 | $NNH+O\Leftrightarrow NH+NO$ | 0.37 | 0.28 | 0.55 | 0.47 | 0.28 | 0.34 | 0.61 | 0.11 |
| $N_2O$ Intermediate Chemistry | | | | | | | | | |
| 185 | $N_2O(+M) \Leftrightarrow N_2+O(+M)$ | 0.35 | 0.11 | 0.18 | 0.19 | 0.06 | 0.04 | 0.15 | 0.16 |
| 182 | $N_2O+O\Leftrightarrow 2NO$ | 0.12 | 0.10 | 0.19 | 0.02 | 0.18 | 0.07 | 0.29 | 0.15 |
| 199 | $NH+NO\Leftrightarrow N_2O+H$ | 0.23 | 0.10 | 0.15 | 0.16 | 0.22 | 0.21 | 0.20 | 0.27 |
| 183 | $N_2O+H\Leftrightarrow N_2+OH$ | -0.25 | -0.09 | -0.15 | -0.16 | -0.24 | -0.20 | -0.13 | -0.18 |
| 181 | $N_2O+O\Leftrightarrow N_2+O_2$ | -0.02 | -0.00 | -0.00 | -0.00 | -0.03 | -0.01 | -0.02 | -0.01 |
| Zeldovich Chemistry | | | | | | | | | |
| 178 | $N+NO\Leftrightarrow N_2+O$ | 0.20 | 0.46 | 0.07 | 0.15 | 0.23 | 0.23 | 0.39 | 0.35 |

Looking again at Table 8.8, we see that unlike the NNH pathway, the $N_2O$ intermediate pathway exhibits strong sensitivity to two reactions involved in the formation and destruction of $N_2O$ (R185 and R183) as well as to two reactions directly responsible for NO formation (R182 and R199). These results are more intuitive based on the QRPD of Fig. 8.4 than are those for the NNH pathway since the more favored reaction paths correspond to the most sensitive elementary reactions. However, since $N_2O$ concentrations are kinetically determined, any proposed improvements to the kinetics of this pathway must consider several balancing reactions. This feature increases the difficulties associated with accurately predicting NO formation under these conditions.

Recently, Allen *et al.* (1995;1997;1998) developed an $N_2O$ mechanism based both on the chemical kinetics literature and on their flow-reactor experiments. Though their mechanism was developed primarily for the modeling of $N_2O$ as an oxidizer in hydrogen flames, the thorough analysis of $N_2O$ kinetics involved in this work is worth mentioning in the current context. For the most sensitive $N_2O$ intermediate reaction (R185), the authors found considerable scatter in predicted pressure sensitivity among various proposed rate coefficients. However, their experimental study at pressures up to 10 atm supported a final rate expression which is remarkably consistent with that used in the GRI reaction mechanism (Allen *et al.*, 1995). Likewise, while the rate coefficient for reaction R182 was found to vary by a factor of three, at the temperatures of their study, depending on the chosen rate constant recommendation from the literature, their final kinetic expression for this reaction was consistent with the expression used in the GRI mechanism. Regarding the remaining two significant reactions identified in Table 8.8 (R199, R183), over the range of conditions of interest to the authors, the various rate coefficients in the literature for each elementary reaction show a remarkable level of consistency. Typical variations between the various rate expressions for a given reaction were found to be only 10-20% when evaluated at a temperature of 1000 K. Although a strong uncertainty was also identified for the rate coefficient of reaction R181 in these studies, Table 8.8 predicts that the sensitivity of this rate coefficient for NO formation is quite low for lean premixed flames. In conclusion, these in-depth reviews of the $N_2O$ intermediate pathway identified

significant uncertainties within the literature regarding the rate coefficients of reactions R185, R182 and R181. However, their final recommendations result in overall rate expressions for each of the $N_2O$ intermediate reactions that are very similar to those adopted by the GRI reaction mechanism.

The above discussion, combined with the relatively good predictive ability of the GRI mechanism in lean, premixed flames, suggests that the $N_2O$ pathway is fairly well modeled by the current reaction mechanism. However, discrepancies in the corresponding rate coefficients could still account for some of the 30-50% underprediction of post-flame zone NO concentrations found for the lean-premixed flames of Chapter 4. Furthermore, because of the significant contributions of other NO formation pathways in these flames, it is difficult to make any definitive statements about the $N_2O$ kinetics at this time.

Table 8.2 indicates that the Zeldovich pathway provides a strong contribution in lean flames, which increases with flame temperature. The Zeldovich pathway contributes in two distinct ways to overall NO formation. In the flamefront, superequilibrium concentrations of O atoms enhance the rate of NO formation via reaction R178; in the post-flame zone, the reaction continues at a slower rate. While the post-flame zone contribution of this pathway can be minimized by rapidly diluting and thus quenching reactions in the post-flame zone, under most practical flame conditions, significant residence times at high temperature are unavoidable. Thus, the Zeldovich pathway has traditionally been the most important NO formation pathway affecting practical combustion devices.

Fortunately, the nitrogen kinetics involved in Zeldovich NO formation are fairly simple. As shown in Table 8.8, assuming O atom concentrations are well defined, reaction R178 is the only Zeldovich reaction displaying significant sensitivity with respect to NO predictions. Furthermore, this reaction has been recognized and studied from the earliest days of NO formation analysis (Zeldovich, 1946), and is quite well known. This conclusion is further verified by the good agreement found between the experimental and predicted, post-flame zone, NO concentration profiles presented in Chapter 4.

Despite the above comments regarding Zeldovich chemistry, it must be noted that for the GRI mechanism, version 2.11, the reaction rate coefficient for reaction R178 was used as an optimization variable and ultimately increased by a factor of 1.4 over the consensus, literature-based value (Bowman et al., 1995). This modified rate coefficient, which is used in the GRI reaction mechanism, lies at the top of the range of literature values. Thus, even the most well-known of reaction rate coefficients for NO displays a 40% uncertainty in the chemical kinetics literature. This underscores the difficulties involved in compiling an accurate, comprehensive reaction mechanism which can predict NO formation over a wide range of flame conditions.

Finally, it is instructive to compare the modeling predictions of NO concentration using the GRI reaction mechanism, version 2.11, with those using the modified reaction mechanism developed in Section 8.3.5 (Study 3). For the leanest flames studied, the principal difference between these two mechanisms is the considerably reduced reaction rate coefficient for the NNH pathway. In near stoichiometric, lean flames, the increased prompt NO reaction rate coefficients should gain in importance. Table 8.9 summarizes the modeling and experimental results of this chapter. For all of the counterflow flames studied, the radiation source term was included in these modeling results using the techniques discussed previously. These radiation losses account for the small differences found between this table and the GRI predictions of NO concentration in the counterflow, premixed flames of Table 8.2.

One key observation concerning the leanest flames listed in Table 8.9 is that the large reduction in pre-exponential factor for the NNH initiation reaction (R208) proposed by Charlston-Goch (1999) results in an increased underprediction of NO concentration at atmospheric pressure (case #7), while having little effect on NO predictions at higher-pressures (case #10). While the poorer predictions at atmospheric pressure could initially cause us to prefer the original mechanism, the differences in the pressure trends for the two mechanisms are worth a closer look. Table 8.9, as well as the results of Chapter 4, demonstrate that the percentage underprediction of NO concentration by the GRI reaction mechanism in these ultra-lean flames increases slightly from ~30% to ~45% with an

increase of pressure from 1.00 atm to 9.15 atm, and then remains relatively constant with respect to pressure. While the error bars on these measurements mitigate against this conclusion, the same trend is observed in a wide variety of the lean premixed flames reported in Chapter 4. For the modified reaction mechanism of Study 3, the underprediction remains at approximately 50% at both of these pressures. This tenuous finding lends some credibility to the notion that the contribution of the pressure-sensitive NNH pathway is indeed overemphasized by the GRI reaction mechanism for these lean premixed flames, while the $N_2O$ intermediate reaction mechanism is underpredicted for the same conditions. Furthermore, we see from Table 8.2 that the GRI mechanism's large NNH-pathway predictions are required to supplement the $N_2O$ intermediate pathway in order to provide the excellent predictions of NO concentration observed in the atmospheric-pressure, lean-premixed flames of Chapter 6 (e.g. case #1). Hence, overprediction of the NNH pathway, as has been suggested by Charlston-Goch (1999), could indeed be covering up for an underprediction of the $N_2O$ intermediate pathway in these flames.

## 8.4 GRI Mechanism Version 3.0

During the final stages of preparation of this report, the Gas Research Institute released a new version of their kinetic mechanism labeled GRI-Mech., version 3.0 (Smith et al., 1999). During the development of this new version, additional targets were added to the optimization process and a variety of changes were made to both the selection of reactions as well as their associated rate coefficients. However, this latest round of optimizations still lacks significant high-pressure flame targets such as those presented in this investigation. The most significant change from GRI-Mech., version 2.11, that affects the current work is a large increase in the rate coefficient for the prompt NO initiation reaction (R240) in line with that proposed by Ravikrishna and Laurendeau (1999) and Berg et al. (1998). Additionally, small changes were made to virtually all of the reactions involved in CH formation and destruction. The authors did not, however, significantly

modify the reburn chemistry except to reduce the rate coefficient for reaction R274 by a factor of approximately 2.6. This modified rate coefficient is the same as that used in Study 3 of Section 8.3.5 and is inadequate, by itself, to rectify the inaccurate predictions of NO concentrations observed in ultra-rich premixed flames.

To gauge the improved predictive capabilities of this revised mechanism for the flame conditions of the present study, modeling predictions of NO concentration were obtained for each of the test cases of the current study. For this modeling, the thermodynamic and transport property databases provided with the new GRI mechanism were used in conjunction with the updated kinetics. All other parameters were kept identical to those used in the earlier GRI mechanism, version 2.11. The results of this analysis, along with a compendium of the results from this chapter, have been included in the modeling summary of Table 8.9.

Several interesting behaviors are noted while comparing the modeling predictions using the GRI reaction mechanism, version 3.0, with those of both the GRI mechanism, version 2.11, and the modified reaction mechanism of the current work (Study 3). For near-stoichiometric, rich premixed flames (cases #3 and #12), the GRI 3.0 predictions are higher at lower pressures and lower at higher pressures than those of the modified reaction mechanism. This results in slightly worse predictive capability for the new mechanism under these conditions, although it is still much better than the earlier GRI mechanism. Similar results are found for the non-premixed flames (cases #13-16). Under these conditions, the modified reaction mechanism scores slightly better than the GRI 3.0 mechanism at atmospheric pressure, and both outperform GRI 2.11. However, none of the mechanisms accurately predicts NO concentrations under high-pressure, non-premixed conditions. In addition, for highly rich, premixed flames (cases #6 and #9), none of the mechanisms adequately predict NO formation, particularly at high pressures.

In ultra-lean flames (cases #1,7,8,10,11), the NO predictions using GRI 3.0 are actually farther from the experimental values than those of version 2.11. This may be due in part to a decrease in the pre-exponential factor of reaction R183, one of the $N_2O$ intermediate reactions identified as being sensitive to NO formation. Another change in

Table 8.9: Predicted and measured concentrations for NO and the sum of NO+HCN+NH₃ for CH₄/O₂/N₂ flames. Three different reaction mechanisms were used in the modeling: the unmodified GRI reaction mechanism, version 2.11, a modified GRI reaction mechanism (Study 3), and a newly released version of the GRI reaction mechanism (3.0).

| Concentrations (ppm) | | | | | | | |
|---|---|---|---|---|---|---|---|
| | LIF | GRI 2.11 | | Study 3 | | GRI 3.0 | |
| # | NO | NO | SUM | NO | SUM | NO | SUM |
| 1 | 4.6 | 4.6 | 4.6 | 3.0 | 3.0 | 3.8 | 3.8 |
| 2 | 30 | 33.1 | 33.1 | 26.4 | 26.4 | 30.9 | 30.9 |
| 3 | 60 | 32.8 | 32.8 | 59.2 | 59.2 | 68.5 | 68.5 |
| 4 | 12 | 7.2 | 7.2 | 5.0 | 5.0 | 9.7 | 9.7 |
| 5 | 12 | 10.0 | 10.0 | 7.0 | 7.0 | 12.0 | 12.0 |
| 6 | 57 | 1.9 | 9.7 | 6.0 | 29.0 | 6.3 | 28.9 |
| 7 | 4.3 | 3.1 | 3.1 | 2.3 | 2.3 | 2.4 | 2.4 |
| 8 | 9.8 | 6.1 | 6.1 | 4.4 | 4.4 | 6.0 | 6.0 |
| 9 | 57 | 10.2 | 19.9 | 27.8 | 61.3 | 32.2 | 62.0 |
| 10 | 6.8 | 3.9 | 3.9 | 3.7 | 3.7 | 2.7 | 2.7 |
| 11 | 17 | 6.9 | 6.9 | 6.5 | 6.5 | 5.7 | 5.7 |
| 12 | 37 | 13.0 | 13.3 | 35.3 | 36.1 | 29.2 | 29.9 |
| 13 | 22 | 11.6 | 12.4 | 24.1 | 27.0 | 27.2 | 29.7 |
| 14 | 56 | 12.4 | 13.2 | 24.4 | 26.6 | 24.9 | 26.3 |
| 15 | 44 | 12.6 | 13.1 | 23.2 | 24.6 | 20.6 | 21.5 |
| 16 | 34 | 12.1 | 12.5 | 21.6 | 22.9 | 18.4 | 19.2 |

the revised mechanism is a decrease in the rate coefficient for the Zeldovich initiation reaction (R178). This reduction may also contribute to the lower predictions for these ultra-lean cases. One pathway which has not been changed in the new mechanism is the NNH pathway. Thus GRI 3.0 displays a similar decrease in predictive performance for lean flames at higher pressures as found for version 2.11. While the Study 3 mechanism displays worse predictive capabilities for atmospheric-pressure flames, its pressure trends are qualitatively better than the other two mechanisms, and in high-pressure, ultra-lean flames, it provides more accurate predictions than the revised GRI mechanism.

The place where the revised GRI mechanism out-performs both of the other two mechanisms is in the atmospheric-pressure, $\phi$=0.9, counterflow premixed flames of this study (cases #2, #4, and #5). Both quantitatively and qualitatively, the new mechanism is better able to model the influence of additional nitrogen dilution on NO formation in these near stoichiometric flames. This better prediction is possibly due to the changed Zeldovich rate coefficient which lies much nearer to the central range of literature values as compared to the previously optimized value from GRI 2.11.

## 8.5 Conclusions

In this chapter, we have compiled a variety of experimental measurements of NO concentration in $CH_4/O_2/N_2$ flames. Through the selection of a wide range of pressures, temperatures, flame structures and stoichiometries, the predictive capabilities of the GRI reaction mechanism, version 2.11, were exercised and areas were identified for which this mechanism performs well and for which room still remains for improvement. Pathway, quantitative reaction path and sensitivity analyses were used to further investigate these issues and to arrive at preliminary conclusions regarding specific causes for the mechanism's performance or lack thereof.

The most serious issues uncovered are concerned with the prediction of prompt NO formation. Modifications were proposed, based on literature suggestions and a sensitivity analysis of prompt-dominated flames, which significantly improved the

predictive capability of the GRI mechanism for moderately-rich premixed and atmospheric-pressure, non-premixed flames. However, in high-pressure, non-premixed flames as well as ultra-rich flames at all pressures, these changes proved insufficient to match the experimental results. This finding underscores the need for additional studies of prompt NO formation under similar flame conditions.

For atmospheric flames, the impact of the NNH mechanism was found to be considerable under almost all flame conditions. The validity of this strong contribution, from a relatively newly discovered and unknown pathway, has recently come under scrutiny (Charlston-Goch, 1999). To assess the impact of a lower NNH pathway contribution, the initiation rate coefficient for this pathway was lowered within the GRI mechanism. The results, while providing quantitatively inferior predictions at atmospheric pressure, were more consistent with the pressure trends of the experimental data than those of the GRI mechanism. These findings tentatively support the conclusion that NO formation via the NNH pathway is overestimated under these flame conditions. Clearly, however, the pressure and temperature trends of this pathway require further investigation.

The $N_2O$ intermediate and Zeldovich pathways were found to be the most consistently modeled of the NO formation mechanisms. However, considerable room still exists for modifications in the rate coefficients for even these relatively well-known pathways. Specifically, the current work seems to suggest that the $N_2O$ intermediate mechanism is slightly underpredicted by the GRI reaction mechanism, on the order of 20-50%. However, the pressure trends of this mechanism seem to be fairly well understood. While no definitive conclusions can be made regarding Zeldovich NO kinetics, the optimized rate coefficient for the Zeldovich initiation reaction was found to be surprisingly close to the upper limit of those proposed in the literature.

Finally, the performance of the most recent version of the GRI reaction mechanism, version 3.0, was analyzed and compared to both the previous version (2.11) as well as to the proposed, modified reaction mechanism of the current work (study 3). This new mechanism was found to offer superior predictions in near-stoichiometric, lean

premixed flames than either of the other two reaction mechanisms, possibly owing to better predictions of the Zeldovich NO pathway. Under other flame conditions, however, the results were mixed, indicating that much work remains to be done in optimizing this reaction mechanism for the prediction of NO formation over a wide range of flame conditions.

# 9. CONCLUSIONS AND FUTURE WORK

## 9.1 Conclusions

The work presented in this investigation has consisted of two primary tasks. The first of these tasks was the development of a database of quantitative NO concentration measurements over a wide range of $CH_4/O_2/N_2$ flame types, temperatures and pressures. This task required both the design and development of new combustion facilities as well as the continued improvement and expansion of the laser-induced fluorescence (LIF) technique for obtaining quantitative measurements of NO concentration over an ever-widening array of flame conditions. The second task was to use this database of NO concentration measurements to increase our understanding of NO formation in natural gas combustion. This goal required comparisons of experimental results to modeling predictions using the best-available kinetic mechanisms. Trends of the data were then used to point out both strengths and weaknesses in the various modeling schemes.

In pursuit of the first major task, previous work in our laboratory had produced NO concentration measurements in the post-flame zones of a wide range of premixed flames stabilized on a water-cooled McKenna burner. A limitation of these flames was that their highly non-adiabatic nature resulted in both lower flame temperatures and unrealistic dilution ratios in order to obtain ultra-lean conditions. Furthermore, it was impossible to obtain measurements of NO concentration beneath and through the flamefront of these flames owing to their close proximity to the surface of the burner. In response to these limitations, a counterflow burner was designed for use in our high-pressure facility. This burner proved capable of stabilizing flat, laminar, nearly adiabatic premixed and non-premixed flames over a wide range of atmospheric-pressure conditions. Furthermore, the burner proved useful to a more limited extent for studies of NO

formation at elevated pressure. Key limitations of this burner configuration included (1) the strong effect of buoyancy at elevated pressures, which prevented the study of ultra-lean, high-pressure premixed flames; and (2) the maximum-flow limitations caused by restrictions on the burner's maximum heat output and by irregularities in the flowfield which became apparent under high-pressure, high-velocity conditions.

Along with the new burner configuration came the challenge of developing a suitably accurate LIF technique to measure NO concentrations under these conditions. The first step of this task was improvement of the existing LIF facility. Specific new additions included an etalon system to minimize excitation wavelength drift and a spatial lock-on device to minimize the impact of beam drift on the LIF measurements. The second step was to develop a procedure for calibrating NO measurements in these flames and for assessing the impact of non-NO interferences under these flame conditions. Because these measurements were restricted to lower pressures, as compared to those for the earlier burner-stabilized flames, background interferences were not found to be as problematic. However, such interferences were significant enough to require an on- and off-line excitation calibration scheme to determine their magnitude at each pressure. This calibration technique, which involved doping known amounts of NO into each of the premixed reactant streams independently, was developed and demonstrated in counterflow premixed flames up to a pressure of 5.08 atm.

Employing these facilities and experimental procedures, NO concentration measurements were obtained in a series of counterflow, premixed, $CH_4/O_2/N_2$ flames at pressures ranging from 1.00 to 5.08 atm, temperatures from 1660 to 2070 K, and equivalence ratios from $\phi=0.60$ to $\phi=1.50$. These measurements were shown to follow trends similar to those for post-flame zone NO concentrations in previous burner-stabilized premixed flames; however, the higher temperatures typically resulted in greater overall NO concentrations. More importantly, the ability to probe under the flamefront provided valuable insight into the structure of these counterflow premixed flames.

The second major task of this investigation required comparisons of these NO concentration measurements with chemical kinetic predictions using the best available

kinetic model. The GRI reaction mechanism, version 2.11, was chosen for the majority of these comparisons. This relatively recent mechanism has been optimized for natural gas combustion and includes each of the four major NO formation pathways, i.e., NNH, $N_2O$ intermediate, prompt and Zeldovich. Thorough comparisons were made between predictions with this mechanism and the experimental measurements, both for the current counterflow premixed flames as well as for a variety of additional premixed and non-premixed flames from other studies in our laboratory. We found through this work that the inclusion of radiation correction routines in the modeling of counterflow flames had its greatest impact in diluted, non-premixed flames and had only a small impact on NO predictions in premixed flames.

Several tools were utilized in analyzing the predictive strength of the GRI reaction mechanism. A pathway analysis was used to indicate the relative importance of various pathways for different flame conditions. This analysis demonstrated, among other things, that the largest discrepancies between GRI predictions and experimental results occurred in those flames whose NO formation chemistry was dominated by the prompt NO mechanism. Quantitative reaction path diagrams were then used to analyze which intermediate species were predominantly involved in nitrogen oxidation. This analysis demonstrated some key changes in intermediate species sequences from one flame condition to another. Of particular interest was the shift in reaction path for prompt dominated, rich flames from an $HCN{\rightarrow}NCO{\rightarrow}NH{\rightarrow}N{\rightarrow}NO$ sequence to the sequence $HCN{\rightarrow}HOCN{\rightarrow}HNCO{\rightarrow}NH_2{\rightarrow}HNO{\rightarrow}NO$ with increasing equivalence ratio. Predictions based on the GRI mechanism also showed that a lack of oxidizing species combined with an enhanced reburn rate resulted in a buildup of HCN and $NH_3$ concentrations in the richest flames of this study.

The pathway and QRPD analyses identified, in a broad sense, how NO formation occurred in these flames. A further analysis was required, however, to determine those reactions for which small changes in rate coefficients would have the greatest impact on NO formation. A sensitivity analysis was used to obtain this information and to identify key reactions which may be responsible for the observed performance of the GRI

mechanism. From this analysis, key reactions were identified within both the CH and nitrogen chemistry whose rate coefficients were most critical in determining NO formation in those prompt-dominated flames for which NO had been severely underpredicted. Suggestions from the literature regarding the rate coefficients of these key reactions were then implemented to determine their impact on NO formation within the confines of the GRI mechanism. A modified mechanism was thus proposed with enhanced predictive capabilities in prompt-dominated flames. However, even this modified reaction mechanism was unable to predict NO concentrations in prompt-dominated, ultra-rich or high-pressure, non-premixed flames. Hence, additional work is clearly needed to define the optimum set of elementary reactions for NO formation, including their corresponding pressure sensitivities.

Regarding the other three NO formation pathways, a recent suggestion that the NNH pathway is overpredicted in the GRI mechanism was investigated relative to the current flame conditions. Tentative agreement was found with this conclusion, although the data are insufficient to firmly conclude that this is indeed the case. Clearly, more work is needed to clarify the pressure and temperature trends of this relatively poorly-known NO formation pathway. The experimental results also suggest, particularly if the NNH conclusion is correct, that the $N_2O$ intermediate reaction pathway is underpredicted within the GRI reaction mechanism. Several key reactions were identified for this mechanism, but no clear trends were found within the literature to indicate which changes might be required. Finally, although the GRI predictions for Zeldovich NO formation seem consistent with axial profiles of NO concentration in the post-flame zone of our flames, the rate coefficient of the initiation reaction for this mechanism was found to lie at the upper bounds of those proposed in the kinetics literature.

## 9.2 Recommendations for Future Work

The biggest conclusion from this investigation is that NO formation, and flame chemistry in general, is a complex and fascinating subject which is far from being

complete. The work funded by the Gas Research Institute to develop a comprehensive mechanism capable of modeling the widest possible range of flame conditions is a daunting task which should be applauded and respected. As has been pointed out in this work, many of the limitations of this mechanism are likely caused by the relative scarcity of high-quality data for high-pressure flame conditions and by the absence of such targets in their current optimization procedure. While the recent work of Purdue's Flame Diagnostics Laboratory has provided some of the first such sets of NO concentration data, more information is needed to enhance the utility of this data for code optimization. The following two suggestions would be useful in this regard.

First of all, accurate, non-intrusive temperature measurements are needed for these flame conditions. The thermocouples which have heretofore been used in the post-flame zone of burner-stabilized, premixed flames are incapable of accurately measuring temperatures in the critical flamefront region. Furthermore, uncertainties in radiation corrections often make the error bars on these measurements unacceptable for NO modeling studies. Refinement of a laser-based technique and application of such a technique to determine temperatures for the flame conditions of this study is thus a top priority.

Secondly, this study has demonstrated the need for better understanding of CH as well as HCN oxidation chemistry in rich-premixed and non-premixed flames. Accurate concentration measurements of CH would thus be very helpful in future mechanism development. Furthermore, measurements of HCN and $NH_3$ concentration in the post-flame zone of ultra-rich premixed flames are needed to validate whether or not the large buildup of these species as predicted by the GRI mechanism is indeed correct.

The LIF measurements of NO concentration require further work to improve the accuracy and portability of the calibration and background correction techniques, especially if LIF is applied to even higher pressure and temperature conditions, or is extended to flames containing more exotic species and/or multiple phases of matter. The analysis of other excitation/detection schemes for NO, many of which are currently limited by rather high detection limits, must continue, especially with respect to future work at

pressures above 15 atm. Finally, the validation and continued improvement of quenching correlations for LIF measurements of NO is much needed, particularly for flame conditions displaying large quenching variations.

On the modeling side, a more comprehensive study of errors associated with modeling uncertainties should be undertaken with an eye on minimizing such non-kinetic factors in future studies. In this work, radiation-correction routines were incorporated into the Sandia opposed diffusion flame code. This allowed the effect of radiation to be analyzed and incorporated into the model rather than just ignored. These corrections should be incorporated into the premixed code as well and the validity of the assumptions on which they are based should be analyzed for the variety of flame conditions studied here. Furthermore, several other sources of possible error which have been mentioned in this study (inclusion or non-inclusion of species thermal diffusivity, area profiles of burner-stabilized flames, etc.), as well as several more which could be uncovered in a thorough study of such effects, should be incorporated into a complete error analysis of the modeling predictions. Such an error analysis would serve not only to guide our interpretation of modeling conclusions, but would necessarily suggest further research projects to improve the quality of all modeling techniques.

LIST OF REFERENCES

LIST OF REFERENCES

Allen, M. G., McManus, K. R., and Sonnenfroh, D. M. (1995a). "PLIF imaging in spray flame combustors at elevated pressure," *AIAA paper 95-0172*. Thirty-third Aerospace Sciences Meeting, Reno, NV.

Allen, M. T., Yetter, R. A., and Dryer, F. L. (1995b). "The decomposition of nitrous oxide at $1.5 \leq P \leq 10.5$ atm and $1103 \leq T \leq 1173$ K," *Int. J. Chem. Kin.* **27**, 883-909.

Allen, M. T., Yetter, R. A., and Dryer, F. L. (1997). "High pressure studies of moist carbon monoxide/nitrous oxide kinetics," *Combust. and Flame* **109**, 449-470.

Allen, M. T., Yetter, R. A., and Dryer, F. L. (1998). "Hydrogen/Nitrous Oxide Kinetics-Implications of the $N_xH_y$ species," *Combust. and Flame* **112**, 302-311.

Avallone, E. A., and Baumeister, T., III (1987). *Mark's Standard Handbook for Mechanical Engineers, Ninth Edition*, McGraw hill, New York NY.

Battles, B. E., Seitzman, J. M., and Hanson, R. K. (1994). "Quantitative planar laser-induced fluorescence imaging of radical species in high pressure flames," *AIAA paper 94-0029*. Thirty-second Aerospace Sciences Meeting, Reno, NV.

Becker, K. H., Geiger, H., and Wiesen, P. (1996). "Kinetics of the reaction $CH + N_2 \rightarrow$ products in the range 10-620 torr and 298-1059 K," *Int. J. Chem. Kin.* **28**, 115-123.

Bengtsson, K. U., Benz, P., Scharen, R., and Frouzakis, C. E. (1998). "$N_yO_x$ formation in lean premixed combustion of methane in a high-pressure jet-stirred reactor," *Twenty-seventh Symposium (International) on Combustion*, The Combustion Institute, Pittsburgh, PA, 1393-1399.

Berg, P. A., Smith, G. P., Jeffries, J. B., and Crosley, D. R. (1998). "Nitric oxide formation and reburn in low-pressure methane flames," *Twenty-seventh Symposium (International) on Combustion*, The Combustion Institute, Pittsburgh, PA, 1337-1384.

Bian, J., Vandooren, J., and Van Tiggelen, P. J. (1990). "Experimental study of the formation of nitrous and nitric oxides in $H_2$-$O_2$-Ar flames seeded with NO and/or $NH_3$," *Twenty-Third Symposium (International) on Combustion*. The Combustion Institute, Pittsburgh, PA, 379-386.

Bockhorn, H., Chevalier, C., and Weyrauch, V. (1991). "Experimental investigation and modeling of prompt-NO formation in hydrocarbon flames," *Heat Transfer in Fire and Combustion Systems, HTD* **166**, ASME, 11-16.

Bowman, C. T., Hanson, R. K., Davidson, D. F., Gardiner, W. P., Jr., Lissianski, V., Smith, G. P., Golden, D. M., Frenklach, M., and Goldenberg, M. (1995). http://www.me.berkeley.edu/gri_mech/.

Bozzelli, J. W., and Dean, A. M. (1995). "O + NNH – A possible new route for $NO_x$ formation in flames," *Int. J. Chem. Kinet.* **27**, 1097-1109.

Bradley, D., and Matthews, K. J. (1968). "Measurement of high gas temperatures with fine wire thermocouples," *J. Mech. Eng. Sci.* **10**, 299-305.

Brugman, T. M., Stoffels, G. G. M., Dam, N., Meerts, W. L., and ter Meulen, J. J. (1997). "Imaging and post-processing of laser-induced fluorescence from NO in a diesel engine," *Appl. Phys. B* **64**, 717-724.

Carter, C. D., Salmon, J. T., King, G. B., and Laurendeau, N. M. (1987). "Feasibility of hydroxyl concentration measurements by laser-saturated fluorescence in high-pressure flames," *Appl. Opt.* **26**, 4551-4562.

Carter, C. D., King, G. B., and Laurendeau, N. M. (1989). "A combustion facility for high-pressure flame studies by spectroscopic methods," *Rev. Sci. Instrum.* **60**, 2606-2609.

Carter, C. D., King, G. B., and Laurendeau, N. M. (1991). "Quenching-corrected saturated fluorescence measurements of the hydroxyl radical in laminar, high-pressure $C_2H_6$/$O_2$/$N_2$ flames," *Combust. Sci. and Tech.* **78**, 247-264.

Carter, C. D., and Barlow, R. S. (1994). "Simultaneous measurements of NO, OH, and the major species in turbulent flames," *Opt. Lett.* **19**, 299-301.

Chao, B. H., Egolfopoulos, F. N., and Law, C. K. (1997). "Structure and propagation of premixed flame in nozzle-generated counterflow," *Combust. and Flame* **109**, 620-638.

Charlston-Goch, D., (1999). *Laser-based diagnostics and modeling of NO and its precursor NH3 in low specific energy gas flames*, PhD Thesis, Department of Chemistry, Faculty of Science, Monash University, Clayton, VIC, Australia.

Cooper, C. S., and Laurendeau, N. M. (1997). "Effect of pulsed dye laser wavelength stabilization on spectral overlap in atmospheric NO fluorescence studies," *Appl. Opt.* **36**, 5262-5265.

Corr, R. A., Malte, P. C., and Marinov, N. M. (1992). "Evaluation of $NO_x$ mechanisms for lean, premixed combustion," *ASME Journal of Engineering for Gas Turbines and Power* **114**, 425-434.

Correa, S. M., and Smooke, M. D. (1990). "$NO_x$ in parametrically varied methane flames," *Twenty-third Symposium (International) on Combustion*, The Combustion Institute, Pittsburgh, PA, 289-295.

Correa, S. M. (1992). "A review of $NO_x$ formation under gas-turbine combustion conditions," *Combust. Sci. and Tech.* **87**, 329-362.

Dean, A. J., Davidson, D. F., Hanson, R. K., and Bowman, C. T. (1988). "Development and application of CH laser absorption diagnostic for shock tube kinetic studies," *Western States Section/Combustion Institute Paper*, 88-91.

Diau, E. W., Halbgewachs, M. J., Smith, A. R., and Lin, M. C. (1995). "Thermal reduction of NO by $H_2$: kinetic measurment and computer modeling of the HNO + NO reaction," *Int. J. Chem. Kin.* **27**, 867-881.

Di Rosa, M. D., Klavuhn, K. G., and Hanson, R. K. (1996). "LIF spectroscopy of NO and $O_2$ in high-pressure flames," *Combust. Sci. and Tech.* **118**, 257-283.

Dixon-Lewis, G. (1990). "Structure of laminar flames," *Twenty-Third Symposium (International) on Combustion*, The Combustion Institute, Pittsburgh, PA, 305-324.

Dong, J., Smith, G. P., Jeffries, J. B., and Crosley, D. R. (1999). "Modeling $NO_x$ chemistry and heat release in a variety of hydrocarbon flames," *Joint Meeting of the U.S. Sections of the Combustion Institute*, Washington D.C.

Drake, M. C., Ratcliffe, J. W., Blint, R. J., Carter, C. D., and Laurendeau, N. M. (1990). "Measurements and modelling of flamefront NO formation and superequilibrium radical concentrations in laminar high-pressure premixed flames," *Twenty-third Symposium (International) on Combustion*, The Combustion Institute, Pittsburgh, PA, 387-395.

Drake, M. C., and Blint, R. J. (1991). "Calculations of $NO_x$ formation pathways in propagating laminar, high pressure premixed $CH_4$ flames," *Combust. Sci. and Tech.* **75**, 261-285.

Drake, M. C., and Blint, R. J. (1992). Personal Communication.

Dupont, V., and Williams, A. (1998). "$NO_x$ mechanisms in rich methane-air flames," *Combust. and Flame* **114**, 103-118.

Egolfopoulos, F. N., Zhu, D. L., and Law, C. K. (1990). "Experimental and numerical determination of laminar flame speeds: mixtures of $C_2$-hydrocarbons with oxygen and nitrogen," *Twenty-Third Symposium (International) on Combustion*, The Combustion Institute, Pittsburgh, PA, 471-478.

Fenimore, C. P. (1971). "Formation of nitric oxide in premixed hydrocarbon flames," *Thirteenth Symposium (International) on Combustion*, The Combustion Institute, Pittsburgh, PA, 373-380.

Flatness, S. A., and Kramlich, J. C. (1996). "Measurement of the branching ratio of NCO + NO into $N_2O$ at 1100-1400 K," *Twenty-Sixth Symposium (International) on Combustion*, The Combustion Institute, Pittsburgh, PA, 567-573.

Giovangigli, V., and Smooke, M. D. (1987). "Extinction of strained premixed laminar flames with complex chemistry," *Combust. Sci. and Tech.* **53**, 23-49.

Glarborg, P., Miller, J. A., and Kee, R. J. (1986). "Kinetic modeling and sensitivity analysis of nitrogen oxide formation in well-stirred reactors," *Combust. and Flame* **65**, 177-202.

Gore, J. P., Lim, J., Takeno, T., and Zhu, X. L. (1999). "A study of the effect of thermal radiation on the structure of methane-air counterflow diffusion flames using detailed chemical kinetics," *Proceedings of the 5th ASME/JSME Joint Thermal Engineering Conference*, San Diego, CA, Paper AJTE99-6311.

Guo, H., Ju, Y., Maruta, K., and Niioka, T. (1997). "Radiation extinction limit of counterflow premixed lean methane-air flames," *Combust. and Flame* **109**, 639-646.

Guo, H., Ju, Y., Maruta, K., Niioka, T., and Liu, F. (1998). "Numerical investigation of $CH_4/CO_2/Air$ and $CH_4/CO_2/O_2$ counterflow premixed flames with radiation reabsorption," *Combust. Sci. and Tech.* **135**, 49-64.

Hanson, R. K., and Salimian, S. (1984). "Survey of rate constants in the N/H/O system" in *Combustion Chemistry*, W.C. Gardiner Jr., ed., Springer-Verlag, New York.

Harrington, J. E., Smith, G. P., Berg, P. A., Noble, A. R., Jeffries, J. B., and Crosley, D. R. (1996). "Evidence for a new NO production mechanism in flames," *Twenty-Sixth Symposium (International) on Combustion*, The Combustion Institute, Pittsburgh, PA, 2133-2138.

Harris, J. M., Lytle, F. E., and McCain, T. C. (1976). "Squirrel-cage photomultiplier base design for measurements of nanosecond fluorescence decays," *Anal. Chem.* **48**, 2095-2098.

Haynes, B. S. (1977). "Reactions of ammonia and nitric oxide in the burnt gases of fuel-rich hydrocarbon-air flames," *Combust. and Flame* **28**, 81-91.

Heberling, P.V. (1976). ""Prompt NO" measurements at high pressures," *Sixteenth Symposium (International) on Combustion*, The Combustion Institute, Pittsburgh, PA, 159-168.

Im, H. G., Bechtold, J. K., and Law, C. K. (1996). "Response of counterflow premixed flames to oscillating strain rates," *Combust. and Flame* **105**, 358-372.

Juang, D. Y., Lee, J., and Wang, N. S. (1995). "Kinetics of the reactions of NCO with NO and $NO_2$," *Int. J. Chem. Kin.* **27**, 1111-1120.

Juchmann, W., Latzel, H., Shin, D. I., Peiter, G., Dreier, T., Volpp, H.-R., Wolfrum, J., Lindstedt, R. P., and Leung, K. M. (1998). "Absolute radical concentration measurements and modeling of low-pressure $CH_4/O_2/NO$ flames," *Twenty-seventh Symposium (International) on Combustion*, The Combustion Institute, Pittsburgh, PA, 469-476.

Kee, R. J., Grcar, J. F., Smooke, M. D., and Miller, J. A. (1985). "A fortran program for modeling steady laminar one-dimensional premixed flames," Sandia National Laboratories, *Sandia Report SAND85-8240*.

Kee, R. J., Dixon-Lewis Jr., G., Warnatz, J., Coltrin, M. E., and Miller, J. A. (1986). "A fortran computer code package for the evaluation of gas-phase multicomponent transport properties," Sandia National Laboratories, *Sandia Report SAND86-8246*.

Kee, R.J., Rupley, F. M., and Miller, J. A. (1987). "A chemical thermodynamic data base," Sandia National Laboratories, *Sandia Report SAND87-8215*.

Kee, R.J., Rupley, F. M., and Miller, J. A. (1989). "CHEMKIN-II: A fortran chemical kinetics package for the analysis of gas-phase chemical kinetics," Sandia National Laboratories, *Sandia Report SAND89-8009*.

Klassen, M. S., Thomsen, D. D., Reisel, J. R., and Laurendeau, N. M. (1995). "Laser-induced fluorescence measurements of nitric oxide formation in high-pressure premixed methane flames," *Combust. Sci. and Tech.* **110-111**, 229-247.

Konnov, A. A., Idir, M., Delfau, J. L., and Vovelle, C. (1996). "Experimental study of extinction of nonadiabatic counterflow premixed flames," *Combust. and Flame* **105**, 308-320.

Krupenie, P. H. (1972). "The spectrum of molecular oxygen," *J. Phys. Chem. Ref. Data,* **1**, 423-534.

Kuhl, C. (1996). Personal Communication.

Kuligowski, F. F. (1997). *An experimental assessment of quantitative LIF techniques for nitric oxide concentration measurements in high-pressure flames,* Master of Science in Mechanical Engineering Thesis, School of Mechanical Engineering, Purdue University, West Lafayette, IN.

Kuligowski, F. F., and Laurendeau, N. M. (1998). "An experimental assessment of quantitative LIF techniques for nitric oxide concentration measurements in high-pressure flames," *Central States Section/Combustion Institute, Spring Technical Meeting,* Lexington, Kentucky.

Laurendeau, N. M., and Goldsmith, J. E. M. (1989). "Comparison of hydroxyl concentration profiles using five laser-induced fluorescence methods in a lean subatmospheric-pressure $H_2/O_2/Ar$ flame," *Combust. Sci. and Tech.* **63**, 139-152.

Law, C. K., Sung, C. J., Yu, G., and Axelbaum, R. L. (1994). "On the structural sensitivity of purely strained planar premixed flames to strain rate variations," *Combust. and Flame* **98**, 139-154.

Lee, M. P., and Hanson, R. K. (1986). "Calculations of $O_2$ absorption and fluorescence at elevated temperatures for a broadband argon-fluoride laser source at 193 nm," *J. Quant. Spectrosc. Radiat. Transfer* **36**, 425-440.

Lefebvre, A. H. (1995). "The role of fuel preparation in low-emission combustion," *ASME Journal of Engineering for Gas Turbines and Power* **117**, 617-654.

Leonard, G., and Correa, S. (1990). "$NO_x$ formation in premixed high-pressure lean methane flames," *2nd ASME Fossil Fuel Combustion Symposium,* New Orleans, Louisiana, ASME/PD **30**, Singh, S.N. Ed., 69-74.

Lim, J. (1998). *A study of the effects of preheat and steam addition on the flame structure and NO formation in laminar counterflow flames*, PhD Thesis, School of Mechanical Engineering, Purdue University, West Lafayette, IN.

Lindstedt, R. P., Lockwood, F. C., Selim, M. A. (1994). "Detailed kinetic modelling of chemistry and temperature effects on ammonia oxidation," *Combust. Sci. and Tech.* **99**, 253-276.

Lindstedt, R. P., Lockwood, R. C., and Selim, M. A. (1995). *A Review of Detailed Kinetics of NO$_x$ Formation and Removal in C/N/H/O System*, Thermofluids Report TF/95/3, Mar. 1995, Imperial College, London.

Lindstedt, R. P., and Skevis, G. (1997). "Chemistry of acetylene flames," *Combust. Sci. and Tech.* **125**, 73-137.

Lutz, A. E., Kee, R. J., and Grcar, J. F. (1996). "OPPDIF: A fortran program for computing opposed-flow diffusion flames," Sandia National Laboratories, *Sandia Report SAND96-8243*.

Malte, P. C., and Pratt, D. T. (1974). "The role of energy-releasing kinetics in NO$_x$ formation: fuel-lean, jet-stirred CO-air combustion," *Combust. Sci. and Tech.* **9**, 221-231.

Marinov, N. M., Curran, H. J., Pitz, W. J., and Westbrook, C. K. (1998). "Chemical kinetic modeling of hydrogen under conditions found in internal combustion engines," *Energy and Fuels* **12**, 78-82.

Markus, M. W., Roth, P., and Just, T. (1996). "A shock tube study of the reactions of CH with CO$_2$ and O$_2$," *Int. J. Chem. Kinet.* **28**, 171-179.

Mebel, A. M., Lin, M. C., Morokuma, K., and Melius, C. F. (1996). "Theoretical study of reactions of N$_2$O with NO and OH radicals," *Int. J. Chem. Kin.* **28**, 693-703.

Miller, J. A., and Bowman, C. T. (1989). "Mechanism and modeling of nitrogen chemistry in combustion," *Prog. Energy Combust. Sci.* **15**, 287-338.

Miller, J. A., Branch, M. C., McLean, D. W., Chandler, D. W., Smooke, M. D., and Lee, R. J. (1984). "The conversion of HCN to NO and N$_2$ in H$_2$-O$_2$-HCN-Ar flames at low pressure," *Nineteenth Symposium (International) on Combustion*, The Combustion Institute, Pittsburgh, PA, 673-684.

Miller, J. A., Durant, J. L., and Glarborg, P. (1998). "Some chemical kinetics issues in reburning: the branching fraction of the HCCO+NO reaction," *Twenty-seventh*

*Symposium (International) on Combustion*, The Combustion Institute, Pittsburgh, PA, 235-243.

Miller, J. A., and Fisk, G. A. (1987). "Combustion chemistry," *Chem. Eng. News* **65**;35, 22-46.

Miller, J. A., and Melius, C. F. (1992). "Kinetic and thermodynamic issues in the formation of aromatic compounds in flames of aliphatic fuels," *Combust. & Flame* **91**, 21-39.

Miller, J. A., and Walch, S. P. (1997). "Prompt NO: theoretical prediction of the high-temperature rate coefficient for CH + N₂ → HCN + N," *Int. J. Chem. Kin.* **29**, 253-259.

Morley, C. (1981). "The mechanism of NO formation from nitrogen compounds in hydrogen flames studied by laser fluorescence," *Eighteenth Symposium (International) on Combustion*, The Combustion Institute, Pittsburgh, PA, 23-32.

Nicol, D. G., Steele, R. C., Marinov, N. M., and Malte, P. C. (1993). "The importance of the nitrous oxide pathway to NOₓ in lean-premixed combustion," *ASME Paper 93-GT-342*.

Nishioka, M., Kondoh, Y., and Takeno, T. (1996). "Behavior of key reactions on NO formation in methane-air flames," *Twenty-Sixth Symposium (International) on Combustion*, The Combustion Institute, Pittsburgh, PA 2130-2145.

Partridge, W. P., Jr., Klassen, M. S., Thomsen, D. D., and Laurendeau, N. M. (1996). "Experimental assessment of O₂ interferences on LIF measurements of NO in high-pressure, lean premixed flames using narrow-band and broad-band detection," *Appl. Opt.* **34**, 4890-4904.

Paul, P. H., Carter, C. D., Gray, J. A., Durant, Jr., J. L., Thoman, J. W., and Furlanetto, M. R. (1995). *Correlations for the NO A²Σ⁺ Electronic Quenching Cross-section*, Sandia National Laboratories, *Sandia Report SAND94-8237*.

Ravikrishna, R. V., and Laurendeau, N. M. (1998). "Laser-saturated fluorescence measurements of nitric oxide in laminar counterflow diffusion flames," *Combust. and Flame* **113**, 473-475.

Ravikrishna, R. V. (1999). *Laser-induced fluorescence measurements and modeling of nitric oxide in counterflow diffusion flames*, PhD Thesis, School of Mechanical Engineering, Purdue University, West Lafayette, IN.

Ravikrishna, R. V., and Laurendeau, N. M. (1999). "Laser-induced fluorescence measurements and modeling of nitric oxide in methane-air and ethane-air counterflow diffusion flames," *Combust. and Flame*, in press.

Reisel, J. R., Carter, C.D., Laurendeau, N. M., and Drake, M. C. (1993). "Laser-saturated fluorescence measurements of nitric oxide in laminar, flat, $C_2H_6/O_2/N_2$ flames at atmospheric pressure," *Combust. Sci. and Tech.* **91**, 271-295.

Reisel, J. R., and Laurendeau, N. M. (1994a). "Laser-induced fluorescence measurements and modeling of nitric oxide formation in high-pressure flames," *Combust. Sci. and Tech.* **98**, 137-160.

Reisel, J. R., and Laurendeau, N. M. (1994b). "Quantitative LIF measurements of nitric oxide in laminar high-temperature flames," *Energy & Fuels* **8**, 1115-1122.

Reisel, J. R., and Laurendeau, N. M. (1995). "Quantitative LIF measurements and modeling of nitric oxide in high-pressure $C_2H_4/O_2/N_2$ flames," *Combust. and Flame* **101**, 141-152.

Reisel, J. R., Partridge, W. P., Jr., and Laurendeau, N. M. (1995). "Transportability of a laser-induced fluorescence calibration for NO at high pressure," *J. Quant. Spectrosc. Radiat. Transfer* **53**, 165-178.

Reisel, J. R. (1998). "Trends of NO formation in low-temperature hydrocarbon flames," *Combust. and Flame* **112**, 275-277.

Rodgers, A. S., and Smith, G. P. (1996). "Pressure and temperature dependence of the reactions of CH with $N_2$," *Chem. Phys. Lett.*, **253**, 313-321.

Rohrig, M., Petersen, E. L., Davidson, D. F., and Hanson, R. K. (1996). "The pressure dependence of the thermal decomposition of $N_2O$," *Int. J. Chem. Kin.* **28**, 599-608.

Romming, H.-J., and Wagner, H. GG. (1996). "A kinetic study of the reactions of $NH(X^3\Sigma^-)$ with $O_2$ and NO in the temperature range from 1200 to 2200 K," *Twenty-Sixth Symposium (International) on Combustion*, The Combustion Institute, Pittsburgh, PA, 559-566.

Sato, J. (1982). "Effects of Lewis number on extinction behavior of premixed flames in a stagnation flow," *Nineteenth Symposium (International) on Combustion*, The Combustion Institute, Pittsburgh, PA, 1541.

Schulz, C., Sick, V., Heinze, J., and Stricker, W. (1997). "Laser-induced-fluorescence detection of nitric oxide in high-pressure flames with $A$-$X$(0,2) excitation," *Appl. Opt.* **36**, 3227-3232.

Schulz, C., Sick, V., Meier, U. E., Heinze, J., and Stricker, W. (1999). "Quantification of NO $A$-$X$(0,2) laser-induced fluorescence: investigation of calibration and collisional influences in high-pressure flames," *Appl. Opt.* **38**, 1434-1443.

Seery, D. J., and Zabielski, M. F. (1977). "Mass spectrometer probing of a $CO/NH_3/O_2$ flame," *Combust. Sci. and Tech.* **28**, 93-99.

Seitzman, J. M. (1991). *Quantitative applications of fluorescence imaging in combustion*, Ph.D. Thesis, Department of Mechanical Engineering, Stanford University, Palo Alto, CA.

Sick, V., Decker, M., Heinze, J., and Stricker, W. (1996). "Collisional processes in the $O_2$ B $^3\Sigma_u^-$ state," *Chem. Phys. Lett.* **249**, 335-340.

Sick, V., Hildenbrand, F., Lindstedt, P. (1998). "Quantitative laser-based measurements and detailed chemical kinetic modelling of nitric oxide concentrations in methane/air counterflow diffusion flames," *Twenty-seventh Symposium (International) on Combustion*, The Combustion Institute, Pittsburgh, PA, 1401-1409.

Smith, G. P., Golden, D. M., Frenklach, M., Moriarty, N. W., Eiteneer, B., Goldenberg, M., Bowman, C. T., Hanson, R., Song, S., Gardiner, W. C., Jr., Lissianski, V., and Qin, Z. (1999). http://www.me.berkeley.edu/gri_mech/.

Smyth, K. C. (1996). "NO production and destruction in a methane/air diffusion flame," *Combust. Sci. and Tech.* **115**, 151-176.

Steele, R. C., Malte, P. C., Nicol, D. G., and Kramlich, J. C. (1995). "$NO_x$ and $N_2O$ in lean-premixed jet-stirred flames," *Combust. and Flame* **100**, 440-449.

Sun, C. J., Sung, C. J., Zhu, D. L., and Law, C. K. (1996). "Response of counterflow premixed and diffusion flames to strain rate variations at reduced and elevated pressures," *Twenty-Third Symposium (International) on Combustion*, The Combustion Institute, Pittsburgh, PA, 1111-1120.

Sung, C. J., Liu, J. B., and Law, C. K. (1996). "On the scalar structure of nonequidiffusive premixed flames in counterflow," *Combust. and Flame* **106**, 168-183.

Thomsen, D. D. (1996). *Measurements and modeling of nitric oxide formation in high-pressure, premixed CH₄/O₂/N₂ flames*, M.S.E. Thesis, School of Mechanical Engineering, Purdue University, West Lafayette, IN.

Thomsen, D. D., Kuligowski, F. F., and Laurendeau, N. M. (1997). "Background corrections for laser-induced-fluorescence measurements of nitric oxide in lean, high-pressure, premixed methane flames," *Appl. Opt.* **36**, 3244-3252.

Tomeczek, J., and Gradon, B. (1997). "The role of nitrous oxide in the mechanism of thermal nitric oxide formation within the flame temperature range," *Combust. Sci. and Tech.* **125**, 159-180.

Turns, S. R. (1996). *An Introduction to Combustion, Concepts and Applications*, McGraw hill, New York NY.

Upschulte, B. L., Allen, M. G., and McManus, K. R. (1996). "Fluorescence imaging of NO, O₂, and fuel vapor in a high-pressure spray flame combustor," *AIAA paper 96-0536*. Thirty-Fourth Aerospace Sciences Meeting, Reno, NV.

Vandooren, J. (1992). "Comparison of the experimental structure of an ammonia seeded rich-hydrogen-oxygen-argon flame with the calculated ones along several reaction mechanisms," *Combust. Sci. and Tech.* **84**, 335-344.

Vranos, A., and Hall, R. J. (1993). "Influence of radiative loss on nitric oxide formation in counterflow diffusion flames at high pressure," *Combust. and Flame* **93**, 230-238.

Vyrodov, A. O., Heinze, J., Dillmann, M., Meier, U. E., and Stricker, W. (1995). "Laser-induced fluorescence thermometry and concentration measurements on NO A-X (0-0) transitions in the exhaust gas of high pressure CH₄/air flames," *Appl. Phys. B* **61**, 409-414.

Williams, B. A., and Pasternack, L. (1997). "The effect of nitric oxide on premixed flames of CH₄, C₂H₆, C₂H₄, and C₂H₂," *Combust. and Flame* **111**, 87-110.

Woiki, D., Votsmeier, M., Davidson, D. F., Hanson, R. K., and Bowman, C. T. (1998). "CH-radical concentration measurements in fuel-rich CH₄/O₂/AR and CH₄/O₂/NO/Ar mixtures behind shock waves," *Combust. and Flame* **113**, 624-626.

Wooldridge, S. T., Hanson, R. K., and Bowman, C. T. (1995). "Simultaneous laser absorption measurements of CN and OH in a shock tube study of HCN + OH → products," *Int. J. Chem. Kin.* **27**, 1075-1087.

Wooldridge, S. T., Hanson, R. K., and Bowman, C. T. (1996a). "A shock tube study of reactions of CN with HCN, OH, and $H_2$ using CN and OH laser absorption," *Int. J. Chem. Kin.* **28**, 245-258.

Wooldridge, S. T., Hanson, R. K., and Bowman, C. T. (1996b). "A shock tube study of CO + OH $\rightarrow$ $CO_2$ + H and HNCO + OH $\rightarrow$ products via simultaneous laser absorption measurements of OH and $CO_2$," *Int. J. Chem. Kin.* **28**, 361-372.

Wysong, I. J., Jeffries, J. B., and Crosley, D. R. (1989). "Laser-induced fluorescence of $O(3p^3P)$, $O_2$, and NO near 226 nm: photolytic interferences and simultaneous excitation in flames," *Opt. Lett.* **14**, 767-769.

Zeldovich, J. (1946). "The oxidation of nitrogen in combustion and explosions," *ACTA Physicochem. URSS* **21**, 577-628.

APPENDICES

## Appendix A: GMK-DB Reaction Mechanism

This appendix contains the chemical kinetics input for the elementary reaction mechanism referred to as the GMK-DB mechanism. The bulk of the mechanism was developed by Glarborg, Miller, and Kee (1986). However, Drake and Blint (1991) modified the GMK mechanism using the results of Hanson and Salimian (1984) and Dean et al. (1988). A propane mechanism has also been added to the GMK scheme, but that most likely has little influence on our results for $CH_4/O_2/N_2$ flames.

The chemical kinetics input consists of three sections. The first section is simply a list of the elements considered in the computations. It is worth noting that argon is not included in either the modeling or the experimental flames of this study. The second section consists of a list of the species considered. Finally, the last section contains a list of the elementary reactions for the GMK-DB mechanism with their associated rate coefficients. The three numbers listed after each reaction represent the constants $A$, $n$, and $E_a$, respectively, in the Arrhenius equation

$$k_f = AT^n \exp\left\{\frac{-E_a}{RT}\right\},$$

(A.1)

where $k_f$ is the forward rate coefficient for the reaction, $T$ is the temperature (K) and $R$ is the ideal gas constant (cal/gmol·K). A second line follows some of the termolecular reactions which involve a third-body species (M). This line contains the major species expected to play the role of the third body in the reaction as well as their corresponding enhancement efficiencies. These third-body efficiencies represent the amount that the rate coefficients are multiplied by for a particular third-body species. In some cases the value 0.0 is entered for a species efficiency; this simply tells the code that a separate reaction is included to account for the termolecular reaction with that species acting as a third-body.

The following kinetics input file was written for a pressure of 14.6 atm. Four reaction rate coefficients are influenced by changes in pressure. Their modified values are tabulated in the work by Reisel (1994).

ELEMENTS
 H C O N
END

SPECIES
 N2 CO CO2 O2 H2O H2 OH O H HO2 H2O2
 CH4 CH3 CH2 CH C CH2O HCO
 C2H6 C2H5 C2H4 C2H3 C2H2 C2H
 C3H6 C3H2
 CH3O CH2CO HCCO C3H8 C3H7(N) C3H7(I)
 NO N NO2 HNO NH3 NH2 NH N2H2 NNH N2O
 HCN CN
 NCO HNCO  HCNO  HOCN  C2N2
END

REACTIONS

| | | | |
|---|---|---|---|
| H+O2=O+OH | 5.10E+16 | -0.820 | 16510.0 |
| H2+O=H+OH | 1.80E+10 | 1.000 | 8830.0 |
| H2+OH=H2O+H | 1.20E+09 | 1.300 | 3630.0 |
| OH+OH=H2O+O | 6.00E+08 | 1.300 | 0.0 |
| H+OH+M=H2O+M | 7.50E+23 | -2.600 | 0.0 |
| H2O/20.0/ | | | |
| O2+M=O+O+M | 1.90E+11 | 0.500 | 95560.0 |
| H+H+M=H2+M | 1.00E+18 | -1.000 | 0.0 |
| H2/0./ H2O/0./ CO2/0./ | | | |
| H+H+H2=H2+H2 | 9.20E+16 | -0.600 | 0.0 |
| H+H+H2O=H2+H2O | 6.00E+19 | -1.250 | 0.0 |
| H+H+CO2=H2+CO2 | 5.50E+20 | -2.000 | 0.0 |
| H2+O2=OH+OH | 1.70E+13 | 0.000 | 47780.0 |
| H+O2+O2=HO2+O2 | 6.70E+19 | -1.420 | 0.0 |
| H+O2+N2=HO2+N2 | 6.70E+19 | -1.420 | 0.0 |
| HO2+H=H2+O2 | 2.50E+13 | 0.000 | 700.0 |
| HO2+H=OH+OH | 2.50E+14 | 0.000 | 1900.0 |
| HO2+O=OH+O2 | 4.80E+13 | 0.000 | 1000.0 |
| HO2+OH=H2O+O2 | 5.00E+13 | 0.000 | 1000.0 |
| HO2+HO2=H2O2+O2 | 2.00E+12 | 0.000 | 0.0 |
| H2O2+M=OH+OH+M | 1.20E+17 | 0.000 | 45500.0 |
| H2O2+H=HO2+H2 | 1.70E+12 | 0.000 | 3750.0 |
| H2O2+OH=H2O+HO2 | 1.00E+13 | 0.000 | 1800.0 |
| CO+O+M=CO2+M | 3.20E+13 | 0.000 | -4200.0 |
| CO+O2=CO2+O | 2.50E+12 | 0.000 | 47700.0 |
| CO+OH=CO2+H | 1.50E+07 | 1.300 | -760.0 |
| CO+HO2=CO2+OH | 5.80E+13 | 0.000 | 22930.0 |

| | | | |
|---|---|---|---|
| HCO+M=CO+H+M | 1.60E+14 | 0.000 | 14700.0 |
| HCO+H=CO+H2 | 4.00E+13 | 0.000 | 0.0 |
| HCO+O=CO+OH | 3.00E+13 | 0.000 | 0.0 |
| HCO+O=CO2+H | 3.00E+13 | 0.000 | 0.0 |
| HCO+OH=CO+H2O | 5.00E+12 | 0.000 | 0.0 |
| HCO+O2=CO+HO2 | 3.30E+13 | -0.400 | 0.0 |
| CH2O+M=HCO+H+M | 3.30E+16 | 0.000 | 81000.0 |
| CH2O+H=HCO+H2 | 2.20E+08 | 1.770 | 10500.0 |
| CH2O+O=HCO+OH | 1.80E+13 | 0.000 | 3080.0 |
| CH2O+OH=HCO+H2O | 3.40E+09 | 1.180 | -447.0 |
| CH4+H=CH3+H2 | 2.20E+04 | 3.000 | 8750.0 |
| CH4+O=CH3+OH | 1.20E+07 | 2.080 | 7630.0 |
| CH4+OH=CH3+H2O | 3.50E+03 | 3.080 | 2000.0 |
| CH4+CH2=CH3+CH3 | 1.30E+13 | 0.000 | 9500.0 |
| CH3+M=CH2+H+M | 1.90E+16 | 0.000 | 91600.0 |
| CH3+H=CH2+H2 | 9.00E+13 | 0.000 | 15100.0 |
| CH3+O=CH2O+H | 6.80E+13 | 0.000 | 0.0 |
| CH3+O=CH2+OH | 5.00E+13 | 0.000 | 12000.0 |
| CH3+OH=CH2+H2O | 1.50E+13 | 0.000 | 5000.0 |
| CH3+OH=CH2O+H2 | 1.00E+12 | 0.000 | 0.0 |
| CH3+O2=CH2O+OH | 5.20E+13 | 0.000 | 34570.0 |
| CH2+H=CH+H2 | 7.30E+17 | -1.560 | 0.0 |
| CH2+O=CO+H+H | 3.00E+13 | 0.000 | 0.0 |
| CH2+O=CO+H2 | 5.00E+13 | 0.000 | 0.0 |
| CH2+O=CH+OH | 5.00E+13 | 0.000 | 12000.0 |
| CH2+OH=CH2O+H | 3.00E+13 | 0.000 | 0.0 |
| CH2+OH=CH+H2O | 4.50E+13 | 0.000 | 3000.0 |
| CH2+O2=CO2+H+H | 1.60E+12 | 0.000 | 1000.0 |
| CH2+O2=CO2+H2 | 6.90E+11 | 0.000 | 500.0 |
| CH2+O2=CO+H2O | 1.90E+10 | 0.000 | -1000.0 |
| CH2+O2=CO+OH+H | 8.60E+10 | 0.000 | -500.0 |
| CH2+O2=HCO+OH | 4.30E+10 | 0.000 | -500.0 |
| CH2+O2=CH2O+O | 2.00E+13 | 0.000 | 9000.0 |
| CH2+CO2=CO+CH2O | 1.10E+11 | 0.000 | 1000.0 |
| CH+H=C+H2 | 1.50E+14 | 0.000 | 0.0 |
| CH+O=CO+H | 5.70E+13 | 0.000 | 0.0 |
| CH+OH=HCO+H | 3.00E+13 | 0.000 | 0.0 |
| CH+O2=HCO+O | 3.30E+13 | 0.000 | 0.0 |
| CH+CO2=HCO+CO | 3.40E+12 | 0.000 | 690.0 |
| C+CH4=CH+CH3 | 5.00E+13 | 0.000 | 24000.0 |
| C+OH=CO+H | 5.00E+13 | 0.000 | 0.0 |
| C+O2=CO+O | 2.00E+13 | 0.000 | 0.0 |
| C+CO2=CO+CO | 6.00E+08 | 0.000 | 0.0 |
| CH3+O2=CH3O+O | 7.00E+12 | 0.000 | 25650.0 |

| | | | |
|---|---|---|---|
| CH3O+M=CH2O+H+M | 1.00E+14 | 0.000 | 25000.0 |
| CH3O+H=CH2O+H2 | 2.00E+13 | 0.000 | 0.0 |
| CH3O+O=CH2O+OH | 1.00E+13 | 0.000 | 0.0 |
| CH3O+OH=CH2O+H2O | 1.00E+13 | 0.000 | 0.0 |
| CH3O+O2=CH2O+HO2 | 6.30E+10 | 0.000 | 2600.0 |
| CH2CO+M=CH2+CO+M | 3.60E+15 | 0.000 | 59300.0 |
| CH2CO+H=CH3+CO | 1.10E+13 | 0.000 | 3430.0 |
| CH2CO+H=HCCO+H2 | 7.50E+13 | 0.000 | 8000.0 |
| CH2CO+O=CH2O+CO | 2.00E+13 | 0.000 | 0.0 |
| CH2CO+O=HCCO+OH | 5.00E+13 | 0.000 | 8000.0 |
| CH2CO+OH=CH2O+HCO | 2.80E+13 | 0.000 | 0.0 |
| CH2CO+OH=HCCO+H2O | 7.50E+12 | 0.000 | 3000.0 |
| HCCO+H=CH2+CO | 1.10E+14 | 0.000 | 0.0 |
| HCCO+O=CO+CO+H | 1.10E+14 | 0.000 | 0.0 |
| HCCO+OH=HCO+CO+H | 1.00E+13 | 0.000 | 0.0 |
| HCCO+O2=CO+CO+OH | 1.50E+12 | 0.000 | 2500.0 |
| CH2+CH=C2H2+H | 4.00E+13 | 0.000 | 0.0 |
| CH2+CH2=C2H2+H2 | 3.20E+13 | 0.000 | 0.0 |
| CH+CH3=C2H3+H | 3.00E+13 | 0.000 | 0.0 |
| CH+CH4=C2H4+H | 6.00E+13 | 0.000 | 0.0 |
| CH+C2H2=C3H2+H | 1.30E+14 | 0.000 | 0.0 |
| C+CH3=C2H2+H | 5.00E+13 | 0.000 | 0.0 |
| C+CH2=C2H+H | 5.00E+13 | 0.000 | 0.0 |
| CH3+CH2=C2H4+H | 3.00E+13 | 0.000 | 0.0 |
| C2H6+H=C2H5+H2 | 5.40E+02 | 3.500 | 5200.0 |
| C2H6+O=C2H5+OH | 2.50E+13 | 0.000 | 6360.0 |
| C2H6+OH=C2H5+H2O | 8.70E+09 | 1.050 | 1810.0 |
| C2H6+CH3=C2H5+CH4 | 5.50E-01 | 4.000 | 8280.0 |
| C2H6+CH2=CH3+C2H5 | 2.20E+13 | 0.000 | 8660.0 |
| C2H5+O2=C2H4+HO2 | 3.20E+12 | 0.000 | 5020.0 |
| C2H4+H=C2H3+H2 | 1.10E+14 | 0.000 | 8500.0 |
| C2H4+O=HCO+CH3 | 1.60E+09 | 1.200 | 746.0 |
| C2H4+OH=C2H3+H2O | 4.80E+12 | 0.000 | 1230.0 |
| C2H4+OH=CH2O+CH3 | 2.00E+12 | 0.000 | 960.0 |
| C2H3+H=C2H2+H2 | 4.00E+13 | 0.000 | 0.0 |
| C2H3+O=CH2CO+H | 3.30E+13 | 0.000 | 0.0 |
| C2H3+OH=C2H2+H2O | 5.00E+12 | 0.000 | 0.0 |
| C2H3+O2=HCO+CH2O | 4.00E+12 | 0.000 | -250.0 |
| C2H3+CH2=C2H2+CH3 | 3.00E+13 | 0.000 | 0.0 |
| C2H3+C2H=C2H2+C2H2 | 3.00E+13 | 0.000 | 0.0 |
| C2H2+M=C2H+H+M | 4.20E+16 | 0.000 | 107000.0 |
| C2H+H2=C2H2+H | 4.10E+05 | 2.390 | 860.0 |
| C2H2+O=CH2+CO | 2.20E+10 | 1.000 | 2580.0 |
| C2H2+O=HCCO+H | 3.60E+04 | 2.700 | 1390.0 |

| | | | |
|---|---|---|---|
| C2H2+O=C2H+OH | 3.20E+15 | -0.600 | 15000.0 |
| C2H2+OH=CH2CO+H | 3.20E+11 | 0.000 | 200.0 |
| C2H2+OH=C2H+H2O | 6.00E+12 | 0.000 | 7000.0 |
| HCCO+CH2=C2H+CH2O | 1.00E+13 | 0.000 | 2000.0 |
| HCCO+CH2=C2H3+CO | 3.00E+13 | 0.000 | 0.0 |
| HCCO+HCCO=C2H2+CO+CO | 1.00E+13 | 0.000 | 0.0 |
| C2H+O=CH+CO | 5.00E+13 | 0.000 | 0.0 |
| C2H+OH=HCCO+H | 2.00E+13 | 0.000 | 0.0 |
| C2H+O2=CO+HCO | 2.40E+12 | 0.000 | 0.0 |
| C2H+O2=HCCO+O | 6.00E+11 | 0.000 | 0.0 |
| HNO+M=H+NO+M | 1.50E+16 | 0.000 | 48680.0 |
| H2O/6.0/ H2/2.0/ O2/2./ N2/2./ | | | |
| HNO+H=H2+NO | 5.00E+12 | 0.000 | 0.0 |
| HNO+OH=NO+H2O | 3.60E+13 | 0.000 | 0.0 |
| NH3+M=NH2+H+M | 1.40E+16 | 0.060 | 90600.0 |
| NH3+H=NH2+H2 | 7.00E+06 | 2.390 | 10171.0 |
| NH3+O=NH2+OH | 2.10E+13 | 0.000 | 9000.0 |
| NH3+OH=NH2+H2O | 2.04E+06 | 2.040 | 566.0 |
| NH2+H=NH+H2 | 6.90E+13 | 0.000 | 3650.0 |
| NH2+O=NH+OH | 6.80E+12 | 0.000 | 0.0 |
| NH2+O=HNO+H | 6.60E+14 | -0.500 | 0.0 |
| NH2+OH=NH+H2O | 4.50E+12 | 0.000 | 2200.0 |
| NH2+N=N2+H+H | 7.20E+13 | 0.000 | 0.0 |
| NH2+NO=N2+H2O | 3.80E+15 | -1.250 | 0.0 |
| NH+H=N+H2 | 3.00E+13 | 0.000 | 0.0 |
| NH+O=NO+H | 2.00E+13 | 0.000 | 0.0 |
| NH+OH=HNO+H | 2.00E+13 | 0.000 | 0.0 |
| NH+OH=N+H2O | 5.00E+11 | 0.500 | 2000.0 |
| NH+O2=HNO+O | 1.00E+13 | 0.000 | 12000.0 |
| NH+O2=NO+OH | 1.40E+11 | 0.000 | 2000.0 |
| NH+N=N2+H | 3.00E+13 | 0.000 | 0.0 |
| N+O2=NO+O | 6.40E+09 | 1.000 | 6280.0 |
| N+OH=NO+H | 3.80E+13 | 0.000 | 0.0 |
| N+CO2=NO+CO | 1.90E+11 | 0.000 | 3400.0 |
| NO+HO2=NO2+OH | 2.10E+12 | 0.000 | -480.0 |
| NO2+M=NO+O+M | 1.10E+16 | 0.000 | 66000.0 |
| NO2+H=NO+OH | 3.50E+14 | 0.000 | 1500.0 |
| NO2+O=NO+O2 | 1.00E+13 | 0.000 | 600.0 |
| N2H2+M=NNH+H+M | 5.00E+16 | 0.000 | 50000.0 |
| N2H2+H=NNH+H2 | 5.00E+13 | 0.000 | 1000.0 |
| NNH+M=N2+H+M | 2.00E+14 | 0.000 | 20000.0 |
| NNH+H=N2+H2 | 3.70E+13 | 0.000 | 3000.0 |
| NNH+NO=N2+HNO | 5.00E+13 | 0.000 | 0.0 |
| NH2+NH=N2H2+H | 5.00E+13 | 0.000 | 0.0 |

| | | | |
|---|---|---|---|
| NH2+NO=NNH+OH | 8.80E+15 | -1.250 | 0.0 |
| NH+NO=N2O+H | 4.30E+14 | -0.500 | 0.0 |
| N2O+H=N2+OH | 7.60E+13 | 0.000 | 15200.0 |
| N2O+O=NO+NO | 1.00E+14 | 0.000 | 28200.0 |
| N2O+O=N2+O2 | 1.00E+14 | 0.000 | 28200.0 |
| CH+NO=HCN+O | 1.10E+14 | 0.000 | 0.0 |
| CH2+N2=HCN+NH | 1.00E+13 | 0.000 | 74000.0 |
| CH+NH2=HCN+H+H | 3.00E+13 | 0.000 | 0.0 |
| CH+NH=HCN+H | 5.00E+13 | 0.000 | 0.0 |
| CH2+NH=HCN+H+H | 3.00E+13 | 0.000 | 0.0 |
| CH+N=CN+H | 1.30E+13 | 0.000 | 0.0 |
| CH2+N=HCN+H | 5.00E+13 | 0.000 | 0.0 |
| CH3+N=HCN+H+H | 5.00E+13 | 0.000 | 0.0 |
| CH4+N=NH+CH3 | 1.00E+13 | 0.000 | 24000.0 |
| HCN+O=CN+OH | 2.70E+09 | 1.580 | 26600.0 |
| HCN+O=NH+CO | 3.50E+03 | 2.640 | 4980.0 |
| HCN+OH=CN+H2O | 1.50E+13 | 0.000 | 10929.0 |
| CN+O=CO+N | 1.80E+13 | 0.000 | 0.0 |
| CN+H2=HCN+H | 3.00E+05 | 2.450 | 2237.0 |
| C+NO=CN+O | 6.60E+13 | 0.000 | 0.0 |
| C+N2O=CN+NO | 1.00E+13 | 0.000 | 0.0 |
| N+HCCO=HCN+CO | 5.00E+13 | 0.000 | 0.0 |
| HCN+OH=HNCO+H | 4.80E+11 | 0.000 | 11000.0 |
| NCO+H2=HNCO+H | 8.60E+12 | 0.000 | 9000.0 |
| HOCN+H=HNCO+H | 1.00E+13 | 0.000 | 0.0 |
| HNCO+H=NH2+CO | 2.00E+13 | 0.000 | 3000.0 |
| CH2+NO=HCNO+H | 1.40E+12 | 0.000 | -1100.0 |
| HCNO+H=HCN+OH | 5.00E+13 | 0.000 | 12000.0 |
| HCN+OH=HOCN+H | 9.20E+12 | 0.000 | 15000.0 |
| C2N2+OH=HOCN+CN | 1.90E+11 | 0.000 | 2900.0 |
| HCN+O=NCO+H | 1.40E+04 | 2.640 | 4980.0 |
| CN+OH=NCO+H | 6.00E+13 | 0.000 | 0.0 |
| CN+O2=NCO+O | 5.60E+12 | 0.000 | 0.0 |
| CN+NO2=NCO+NO | 3.00E+13 | 0.000 | 0.0 |
| CN+N2O=NCO+N2 | 1.00E+13 | 0.000 | 0.0 |
| NCO+M=N+CO+M | 3.10E+16 | -0.500 | 48000.0 |
| NCO+H=NH+CO | 5.00E+13 | 0.000 | 0.0 |
| NCO+O=NO+CO | 5.60E+13 | 0.000 | 0.0 |
| NCO+OH=NO+CO+H | 1.00E+13 | 0.000 | 0.0 |
| NCO+N=N2+CO | 2.00E+13 | 0.000 | 0.0 |
| NCO+NO=N2O+CO | 1.00E+13 | 0.000 | -390.0 |
| HCN+CN=C2N2+H | 2.00E+13 | 0.000 | 0.0 |
| C2N2+O=NCO+CN | 4.60E+12 | 0.000 | 8880.0 |
| N+NO=N2+O | 3.30E+12 | 0.300 | 0.0 |

| | | | |
|---|---|---|---|
| N2O=N2+O | 9.40E+16 | -1.794 | 62509.0 |
| CH+N2=HCN+N | 4.20E+12 | 0.000 | 20400.0 |
| C2H5+CH3=C3H8 | 2.00E+13 | 0.000 | 0.0 |
| H+C3H8=H2+C3H7(N) | 1.30E+14 | 0.000 | 9700.0 |
| H+C3H8=H2+C3H7(I) | 1.00E+14 | 0.000 | 8360.0 |
| O+C3H8=OH+C3H7(N) | 3.00E+13 | 0.000 | 5760.0 |
| O+C3H8=OH+C3H7(I) | 2.60E+13 | 0.000 | 4440.0 |
| OH+C3H8=H2O+C3H7(N) | 3.70E+12 | 0.000 | 1650.0 |
| OH+C3H8=H2O+C3H7(I) | 2.80E+12 | 0.000 | 860.0 |
| C3H7(N)=C2H4+CH3 | 3.00E+14 | 0.000 | 33030.0 |
| C3H7(I)=C3H6+H | 2.00E+14 | 0.000 | 38740.0 |
| C3H7(N)=C3H6+H | 1.00E+14 | 0.000 | 37330.0 |
| C3H8+HO2=C3H7(N)+H2O2 | 5.00E+12 | 0.000 | 18000.0 |
| C3H8+HO2=C3H7(I)+H2O2 | 5.00E+12 | 0.000 | 18000.0 |
| H+O2+M=HO2+M | 2.10E+18 | -1.000 | 0.0 |
| H2O/21.0/ CO2/5./ H2/3.3/ CO/2./ O2/0./ N2/0./ | | | |
| C2H5+H=CH3+CH3 | 4.00E+13 | 0.000 | 0.0 |
| CH3+CH3=C2H4+H2 | 2.10E+14 | 0.000 | 19200.0 |
| CH4=CH3+H | 8.90E+30 | -5.030 | 105166.0 |
| C2H6=CH3+CH3 | 1.40E+29 | -3.360 | 91082.0 |
| C2H5=C2H4+H | 1.80E+20 | -2.197 | 41756.0 |
| C2H3+M=C2H2+H+M | 3.00E+15 | 0.000 | 32027.0 |
| C2H4+M=C2H2+H2+M | 2.60E+17 | 0.000 | 79350.0 |
| C2H4+M=C2H3+H+M | 2.60E+17 | 0.000 | 96600.0 |
| END | | | |

Appendix B: GRI Reaction Mechanism Version 2.11

This appendix contains the chemical kinetics input for the elementary reaction mechanism developed by the Gas Research Institute (GRI), which has been optimized for the modeling of natural gas combustion (Bowman *et al*, 1995). This reaction mechanism (version 2.11) considers 49 species and 277 reactions and was used without modification. Hereafter, this kinetic mechanism will be referred to as the GRI reaction mechanism. During the final stages of this study an updated version (3.00) of the GRI mechanism was released (Smith *et al*, 1999). Its kinetics were not used in the bulk of this report and thus will not be included as a separate appendix. When referred to in the text, this updated mechanism will explicitly be referred to as the GRI reaction mechanism, version 3.00.

The chemical kinetics input consists of three sections. The first section is simply a list of the elements considered in the computations. The second section consists of a list of the species considered. Finally, the last section contains a list of the elementary reactions for the GRI mechanism with their associated rate coefficients. The three numbers listed after each reaction represent the constants $A$, $n$, and $E_a$, respectively, in the Arrhenius equation

$$k_f = AT^n \exp\left\{\frac{-E_a}{RT}\right\}, \tag{B.1}$$

where $k_f$ is the forward rate coefficient for the reaction, $T$ is the temperature (K) and $R$ is the ideal gas constant (cal/gmol·K). A second line follows some of the termolecular reactions which involve a third-body species (M). This line contains the major species expected to play the role of the third body in the reaction as well as their corresponding enhancement efficiencies. These third-body efficiencies represent the amount that the rate coefficients are multiplied by for a particular third-body species. In some cases the value 0.0 is entered for a species efficiency; this simply tells the code that a separate reaction is included to account for the termolecular reaction with that species acting as a third-body. In the case that a single Arrhenius expression is inadequate to describe the temperature sensitivity of a given reaction, multiple Arrhenius equations are included through the use

of the DUPLICATE keyword. Finally, for some reactions, pressure sensitivity is added
using the LOW and TROE keywords.

ELEMENTS
O  H  C  N  AR
END

SPECIES
H2    H      O      O2     OH     H2O    HO2    H2O2
C     CH     CH2    CH2(S) CH3    CH4    CO     CO2
HCO   CH2O   CH2OH  CH3O   CH3OH  C2H    C2H2   C2H3
C2H4  C2H5   C2H6   HCCO   CH2CO  HCCOH  N      NH
NH2   NH3    NNH    NO     NO2    N2O    HNO    CN
HCN   H2CN   HCNN   HCNO   HOCN   HNCO   NCO    N2
AR
END

REACTIONS
2O+M<=>O2+M                          1.200E+17      -1.000         .00
H2/ 2.40/ H2O/15.40/ CH4/ 2.00/ CO/ 1.75/ CO2/ 3.60/ C2H6/ 3.00/ AR/ .83/
O+H+M<=>OH+M                         5.000E+17      -1.000         .00
H2/2.00/ H2O/6.00/ CH4/2.00/ CO/1.50/ CO2/2.00/ C2H6/3.00/ AR/ .70/
O+H2<=>H+OH                          5.000E+04       2.670     6290.00
O+HO2<=>OH+O2                        2.000E+13        .000         .00
O+H2O2<=>OH+HO2                      9.630E+06       2.000     4000.00
O+CH<=>H+CO                          5.700E+13        .000         .00
O+CH2<=>H+HCO                        8.000E+13        .000         .00
O+CH2(S)<=>H2+CO                     1.500E+13        .000         .00
O+CH2(S)<=>H+HCO                     1.500E+13        .000         .00
O+CH3<=>H+CH2O                       8.430E+13        .000         .00
O+CH4<=>OH+CH3                       1.020E+09       1.500     8600.00
O+CO+M<=>CO2+M                       6.020E+14        .000     3000.00
H2/2.00/ O2/6.00/ H2O/6.00/ CH4/2.00/ CO/1.50/ CO2/3.50/ C2H6/3.00/ AR/ .50/
O+HCO<=>OH+CO                        3.000E+13        .000         .00
O+HCO<=>H+CO2                        3.000E+13        .000         .00
O+CH2O<=>OH+HCO                      3.900E+13        .000     3540.00
O+CH2OH<=>OH+CH2O                    1.000E+13        .000         .00
O+CH3O<=>OH+CH2O                     1.000E+13        .000         .00
O+CH3OH<=>OH+CH2OH                   3.880E+05       2.500     3100.00
O+CH3OH<=>OH+CH3O                    1.300E+05       2.500     5000.00
O+C2H<=>CH+CO                        5.000E+13        .000         .00

| | | | |
|---|---|---|---|
| O+C2H2<=>H+HCCO | 1.020E+07 | 2.000 | 1900.00 |
| O+C2H2<=>OH+C2H | 4.600E+19 | -1.410 | 28950.00 |
| O+C2H2<=>CO+CH2 | 1.020E+07 | 2.000 | 1900.00 |
| O+C2H3<=>H+CH2CO | 3.000E+13 | .000 | .00 |
| O+C2H4<=>CH3+HCO | 1.920E+07 | 1.830 | 220.00 |
| O+C2H5<=>CH3+CH2O | 1.320E+14 | .000 | .00 |
| O+C2H6<=>OH+C2H5 | 8.980E+07 | 1.920 | 5690.00 |
| O+HCCO<=>H+2CO | 1.000E+14 | .000 | .00 |
| O+CH2CO<=>OH+HCCO | 1.000E+13 | .000 | 8000.00 |
| O+CH2CO<=>CH2+CO2 | 1.750E+12 | .000 | 1350.00 |
| O2+CO<=>O+CO2 | 2.500E+12 | .000 | 47800.00 |
| O2+CH2O<=>HO2+HCO | 1.000E+14 | .000 | 40000.00 |
| H+O2+M<=>HO2+M | 2.800E+18 | -.860 | .00 |

O2/ .00/ H2O/ .00/ CO/ .75/ CO2/1.50/ C2H6/1.50/ N2/ .00/ AR/ .00/

| | | | |
|---|---|---|---|
| H+2O2<=>HO2+O2 | 3.000E+20 | -1.720 | .00 |
| H+O2+H2O<=>HO2+H2O | 9.380E+18 | -.760 | .00 |
| H+O2+N2<=>HO2+N2 | 3.750E+20 | -1.720 | .00 |
| H+O2+AR<=>HO2+AR | 7.000E+17 | -.800 | .00 |
| H+O2<=>O+OH | 8.300E+13 | .000 | 14413.00 |
| 2H+M<=>H2+M | 1.000E+18 | -1.000 | .00 |

H2/ .00/ H2O/ .00/ CH4/2.00/ CO2/ .00/ C2H6/3.00/ AR/ .63/

| | | | |
|---|---|---|---|
| 2H+H2<=>2H2 | 9.000E+16 | -.600 | .00 |
| 2H+H2O<=>H2+H2O | 6.000E+19 | -1.250 | .00 |
| 2H+CO2<=>H2+CO2 | 5.500E+20 | -2.000 | .00 |
| H+OH+M<=>H2O+M | 2.200E+22 | -2.000 | .00 |

H2/ .73/ H2O/3.65/ CH4/2.00/ C2H6/3.00/ AR/ .38/

| | | | |
|---|---|---|---|
| H+HO2<=>O+H2O | 3.970E+12 | .000 | 671.00 |
| H+HO2<=>O2+H2 | 2.800E+13 | .000 | 1068.00 |
| H+HO2<=>2OH | 1.340E+14 | .000 | 635.00 |
| H+H2O2<=>HO2+H2 | 1.210E+07 | 2.000 | 5200.00 |
| H+H2O2<=>OH+H2O | 1.000E+13 | .000 | 3600.00 |
| H+CH<=>C+H2 | 1.100E+14 | .000 | .00 |
| H+CH2(+M)<=>CH3(+M) | 2.500E+16 | -.800 | .00 |

   LOW / 3.200E+27 -3.140 1230.00/

   TROE/ .6800 78.00 1995.00 5590.00 /

H2/2.00/ H2O/6.00/ CH4/2.00/ CO/1.50/ CO2/2.00/ C2H6/3.00/ AR/ .70/

| | | | |
|---|---|---|---|
| H+CH2(S)<=>CH+H2 | 3.000E+13 | .000 | .00 |
| H+CH3(+M)<=>CH4(+M) | 1.270E+16 | -.630 | 383.00 |

   LOW / 2.477E+33 -4.760 2440.00/

   TROE/ .7830 74.00 2941.00 6964.00 /

H2/2.00/ H2O/6.00/ CH4/2.00/ CO/1.50/ CO2/2.00/ C2H6/3.00/ AR/ .70/

| | | | |
|---|---|---|---|
| H+CH4<=>CH3+H2 | 6.600E+08 | 1.620 | 10840.00 |
| H+HCO(+M)<=>CH2O(+M) | 1.090E+12 | .480 | -260.00 |

   LOW / 1.350E+24 -2.570 1425.00/

```
     TROE/ .7824 271.00 2755.00 6570.00 /
H2/2.00/ H2O/6.00/ CH4/2.00/ CO/1.50/ CO2/2.00/ C2H6/3.00/ AR/ .70/
H+HCO<=>H2+CO                       7.340E+13        .000          .00
H+CH2O(+M)<=>CH2OH(+M)              5.400E+11        .454       3600.00
     LOW / 1.270E+32  -4.820  6530.00/
     TROE/ .7187 103.00 1291.00 4160.00 /
H2/2.00/ H2O/6.00/ CH4/2.00/ CO/1.50/ CO2/2.00/ C2H6/3.00/
H+CH2O(+M)<=>CH3O(+M)               5.400E+11        .454       2600.00
     LOW / 2.200E+30  -4.800  5560.00/
     TROE/ .7580  94.00 1555.00 4200.00 /
H2/2.00/ H2O/6.00/ CH4/2.00/ CO/1.50/ CO2/2.00/ C2H6/3.00/
H+CH2O<=>HCO+H2                     2.300E+10       1.050       3275.00
H+CH2OH(+M)<=>CH3OH(+M)             1.800E+13        .000          .00
     LOW / 3.000E+31  -4.800  3300.00/
     TROE/ .7679 338.00 1812.00 5081.00 /
H2/2.00/ H2O/6.00/ CH4/2.00/ CO/1.50/ CO2/2.00/ C2H6/3.00/
H+CH2OH<=>H2+CH2O                   2.000E+13        .000          .00
H+CH2OH<=>OH+CH3                    1.200E+13        .000          .00
H+CH2OH<=>CH2(S)+H2O                6.000E+12        .000          .00
H+CH3O(+M)<=>CH3OH(+M)              5.000E+13        .000          .00
     LOW / 8.600E+28  -4.000  3025.00/
     TROE/ .8902 144.00 2838.00 45569.00 /
H2/2.00/ H2O/6.00/ CH4/2.00/ CO/1.50/ CO2/2.00/ C2H6/3.00/
H+CH3O<=>H+CH2OH                    3.400E+06       1.600          .00
H+CH3O<=>H2+CH2O                    2.000E+13        .000          .00
H+CH3O<=>OH+CH3                     3.200E+13        .000          .00
H+CH3O<=>CH2(S)+H2O                 1.600E+13        .000          .00
H+CH3OH<=>CH2OH+H2                  1.700E+07       2.100       4870.00
H+CH3OH<=>CH3O+H2                   4.200E+06       2.100       4870.00
H+C2H(+M)<=>C2H2(+M)                1.000E+17      -1.000          .00
     LOW / 3.750E+33  -4.800  1900.00/
     TROE/ .6464 132.00 1315.00 5566.00 /
H2/2.00/ H2O/6.00/ CH4/2.00/ CO/1.50/ CO2/2.00/ C2H6/3.00/ AR/ .70/
H+C2H2(+M)<=>C2H3(+M)               5.600E+12        .000       2400.00
     LOW / 3.800E+40  -7.270  7220.00/
     TROE/ .7507  98.50 1302.00 4167.00 /
H2/2.00/ H2O/6.00/ CH4/2.00/ CO/1.50/ CO2/2.00/ C2H6/3.00/ AR/ .70/
H+C2H3(+M)<=>C2H4(+M)               6.080E+12        .270        280.00
     LOW / 1.400E+30  -3.860  3320.00/
     TROE/ .7820 207.50 2663.00 6095.00 /
H2/2.00/ H2O/6.00/ CH4/2.00/ CO/1.50/ CO2/2.00/ C2H6/3.00/ AR/ .70/
H+C2H3<=>H2+C2H2                    3.000E+13        .000          .00
H+C2H4(+M)<=>C2H5(+M)               1.080E+12        .454       1820.00
     LOW / 1.200E+42  -7.620  6970.00/
```

```
      TROE/  .9753  210.00  984.00  4374.00 /
H2/2.00/ H2O/6.00/ CH4/2.00/ CO/1.50/ CO2/2.00/ C2H6/3.00/ AR/ .70/
H+C2H4<=>C2H3+H2                 1.325E+06      2.530     12240.00
H+C2H5(+M)<=>C2H6(+M)            5.210E+17      -.990      1580.00
      LOW / 1.990E+41  -7.080  6685.00/
      TROE/  .8422  125.00  2219.00  6882.00 /
H2/2.00/ H2O/6.00/ CH4/2.00/ CO/1.50/ CO2/2.00/ C2H6/3.00/ AR/ .70/
H+C2H5<=>H2+C2H4                 2.000E+12      .000        .00
H+C2H6<=>C2H5+H2                 1.150E+08      1.900      7530.00
H+HCCO<=>CH2(S)+CO               1.000E+14      .000        .00
H+CH2CO<=>HCCO+H2                5.000E+13      .000       8000.00
H+CH2CO<=>CH3+CO                 1.130E+13      .000       3428.00
H+HCCOH<=>H+CH2CO                1.000E+13      .000        .00
H2+CO(+M)<=>CH2O(+M)             4.300E+07      1.500     79600.00
      LOW / 5.070E+27  -3.420  84350.00/
      TROE/  .9320  197.00  1540.00  10300.00 /
H2/2.00/ H2O/6.00/ CH4/2.00/ CO/1.50/ CO2/2.00/ C2H6/3.00/ AR/ .70/
OH+H2<=>H+H2O                    2.160E+08      1.510      3430.00
2OH(+M)<=>H2O2(+M)               7.400E+13      -.370       .00
      LOW / 2.300E+18  -.900  -1700.00/
      TROE/  .7346  94.00  1756.00  5182.00 /
H2/2.00/ H2O/6.00/ CH4/2.00/ CO/1.50/ CO2/2.00/ C2H6/3.00/ AR/ .70/
2OH<=>O+H2O                      3.570E+04      2.400     -2110.00
OH+HO2<=>O2+H2O                  2.900E+13      .000       -500.00
OH+H2O2<=>HO2+H2O                1.750E+12      .000        320.00
DUPLICATE
OH+H2O2<=>HO2+H2O                5.800E+14      .000       9560.00
DUPLICATE
OH+C<=>H+CO                      5.000E+13      .000        .00
OH+CH<=>H+HCO                    3.000E+13      .000        .00
OH+CH2<=>H+CH2O                  2.000E+13      .000        .00
OH+CH2<=>CH+H2O                  1.130E+07      2.000      3000.00
OH+CH2(S)<=>H+CH2O               3.000E+13      .000        .00
OH+CH3(+M)<=>CH3OH(+M)           6.300E+13      .000        .00
      LOW / 2.700E+38  -6.300  3100.00/
      TROE/  .2105  83.50  5398.00  8370.00 /
H2/2.00/ H2O/6.00/ CH4/2.00/ CO/1.50/ CO2/2.00/ C2H6/3.00/
OH+CH3<=>CH2+H2O                 5.600E+07      1.600      5420.00
OH+CH3<=>CH2(S)+H2O              2.501E+13      .000        .00
OH+CH4<=>CH3+H2O                 1.000E+08      1.600      3120.00
OH+CO<=>H+CO2                    4.760E+07      1.228        70.00
OH+HCO<=>H2O+CO                  5.000E+13      .000        .00
OH+CH2O<=>HCO+H2O                3.430E+09      1.180       -447.00
OH+CH2OH<=>H2O+CH2O              5.000E+12      .000        .00
```

| | | | |
|---|---|---|---|
| OH+CH3O<=>H2O+CH2O | 5.000E+12 | .000 | .00 |
| OH+CH3OH<=>CH2OH+H2O | 1.440E+06 | 2.000 | -840.00 |
| OH+CH3OH<=>CH3O+H2O | 6.300E+06 | 2.000 | 1500.00 |
| OH+C2H<=>H+HCCO | 2.000E+13 | .000 | .00 |
| OH+C2H2<=>H+CH2CO | 2.180E-04 | 4.500 | -1000.00 |
| OH+C2H2<=>H+HCCOH | 5.040E+05 | 2.300 | 13500.00 |
| OH+C2H2<=>C2H+H2O | 3.370E+07 | 2.000 | 14000.00 |
| OH+C2H2<=>CH3+CO | 4.830E-04 | 4.000 | -2000.00 |
| OH+C2H3<=>H2O+C2H2 | 5.000E+12 | .000 | .00 |
| OH+C2H4<=>C2H3+H2O | 3.600E+06 | 2.000 | 2500.00 |
| OH+C2H6<=>C2H5+H2O | 3.540E+06 | 2.120 | 870.00 |
| OH+CH2CO<=>HCCO+H2O | 7.500E+12 | .000 | 2000.00 |
| 2HO2<=>O2+H2O2 | 1.300E+11 | .000 | -1630.00 |
| DUPLICATE | | | |
| 2HO2<=>O2+H2O2 | 4.200E+14 | .000 | 12000.00 |
| DUPLICATE | | | |
| HO2+CH2<=>OH+CH2O | 2.000E+13 | .000 | .00 |
| HO2+CH3<=>O2+CH4 | 1.000E+12 | .000 | .00 |
| HO2+CH3<=>OH+CH3O | 2.000E+13 | .000 | .00 |
| HO2+CO<=>OH+CO2 | 1.500E+14 | .000 | 23600.00 |
| HO2+CH2O<=>HCO+H2O2 | 1.000E+12 | .000 | 8000.00 |
| C+O2<=>O+CO | 5.800E+13 | .000 | 576.00 |
| C+CH2<=>H+C2H | 5.000E+13 | .000 | .00 |
| C+CH3<=>H+C2H2 | 5.000E+13 | .000 | .00 |
| CH+O2<=>O+HCO | 3.300E+13 | .000 | .00 |
| CH+H2<=>H+CH2 | 1.107E+08 | 1.790 | 1670.00 |
| CH+H2O<=>H+CH2O | 1.713E+13 | .000 | -755.00 |
| CH+CH2<=>H+C2H2 | 4.000E+13 | .000 | .00 |
| CH+CH3<=>H+C2H3 | 3.000E+13 | .000 | .00 |
| CH+CH4<=>H+C2H4 | 6.000E+13 | .000 | .00 |
| CH+CO(+M)<=>HCCO(+M) | 5.000E+13 | .000 | .00 |

   LOW / 2.690E+28 -3.740 1936.00/
   TROE/ .5757 237.00 1652.00 5069.00 /
H2/2.00/ H2O/6.00/ CH4/2.00/ CO/1.50/ CO2/2.00/ C2H6/3.00/ AR/ .70/

| | | | |
|---|---|---|---|
| CH+CO2<=>HCO+CO | 3.400E+12 | .000 | 690.00 |
| CH+CH2O<=>H+CH2CO | 9.460E+13 | .000 | -515.00 |
| CH+HCCO<=>CO+C2H2 | 5.000E+13 | .000 | .00 |
| CH2+O2<=>OH+HCO | 1.320E+13 | .000 | 1500.00 |
| CH2+H2<=>H+CH3 | 5.000E+05 | 2.000 | 7230.00 |
| 2CH2<=>H2+C2H2 | 3.200E+13 | .000 | .00 |
| CH2+CH3<=>H+C2H4 | 4.000E+13 | .000 | .00 |
| CH2+CH4<=>2CH3 | 2.460E+06 | 2.000 | 8270.00 |
| CH2+CO(+M)<=>CH2CO(+M) | 8.100E+11 | .500 | 4510.00 |

   LOW / 2.690E+33 -5.110 7095.00/

```
    TROE/ .5907 275.00 1226.00 5185.00 /
H2/2.00/ H2O/6.00/ CH4/2.00/ CO/1.50/ CO2/2.00/ C2H6/3.00/ AR/ .70/
CH2+HCCO<=>C2H3+CO                    3.000E+13        .000            .00
CH2(S)+N2<=>CH2+N2                    1.500E+13        .000         600.00
CH2(S)+AR<=>CH2+AR                    9.000E+12        .000         600.00
CH2(S)+O2<=>H+OH+CO                   2.800E+13        .000            .00
CH2(S)+O2<=>CO+H2O                    1.200E+13        .000            .00
CH2(S)+H2<=>CH3+H                     7.000E+13        .000            .00
CH2(S)+H2O(+M)<=>CH3OH(+M)            2.000E+13        .000            .00
    LOW / 2.700E+38  -6.300  3100.00/
    TROE/ .1507 134.00 2383.00 7265.00 /
H2/2.00/ H2O/6.00/ CH4/2.00/ CO/1.50/ CO2/2.00/ C2H6/3.00/
CH2(S)+H2O<=>CH2+H2O                  3.000E+13        .000            .00
CH2(S)+CH3<=>H+C2H4                   1.200E+13        .000         -570.00
CH2(S)+CH4<=>2CH3                     1.600E+13        .000         -570.00
CH2(S)+CO<=>CH2+CO                    9.000E+12        .000            .00
CH2(S)+CO2<=>CH2+CO2                  7.000E+12        .000            .00
CH2(S)+CO2<=>CO+CH2O                  1.400E+13        .000            .00
CH2(S)+C2H6<=>CH3+C2H5               4.000E+13        .000         -550.00
CH3+O2<=>O+CH3O                       2.675E+13        .000       28800.00
CH3+O2<=>OH+CH2O                      3.600E+10        .000        8940.00
CH3+H2O2<=>HO2+CH4                    2.450E+04       2.470        5180.00
2CH3(+M)<=>C2H6(+M)                   2.120E+16       -.970         620.00
    LOW / 1.770E+50  -9.670  6220.00/
    TROE/ .5325 151.00 1038.00 4970.00 /
H2/2.00/ H2O/6.00/ CH4/2.00/ CO/1.50/ CO2/2.00/ C2H6/3.00/ AR/ .70/
2CH3<=>H+C2H5                         4.990E+12        .100       10600.00
CH3+HCO<=>CH4+CO                      2.648E+13        .000            .00
CH3+CH2O<=>HCO+CH4                    3.320E+03       2.810        5860.00
CH3+CH3OH<=>CH2OH+CH4                 3.000E+07       1.500        9940.00
CH3+CH3OH<=>CH3O+CH4                  1.000E+07       1.500        9940.00
CH3+C2H4<=>C2H3+CH4                   2.270E+05       2.000        9200.00
CH3+C2H6<=>C2H5+CH4                   6.140E+06       1.740       10450.00
HCO+H2O<=>H+CO+H2O                    2.244E+18      -1.000       17000.00
HCO+M<=>H+CO+M                        1.870E+17      -1.000       17000.00
H2/2.00/ H2O/ .00/ CH4/2.00/ CO/1.50/ CO2/2.00/ C2H6/3.00/
HCO+O2<=>HO2+CO                       7.600E+12        .000         400.00
CH2OH+O2<=>HO2+CH2O                   1.800E+13        .000         900.00
CH3O+O2<=>HO2+CH2O                    4.280E-13       7.600       -3530.00
C2H+O2<=>HCO+CO                       5.000E+13        .000        1500.00
C2H+H2<=>H+C2H2                       4.070E+05       2.400         200.00
C2H3+O2<=>HCO+CH2O                    3.980E+12        .000         -240.00
C2H4(+M)<=>H2+C2H2(+M)                8.000E+12        .440       88770.00
    LOW / 7.000E+50  -9.310  99860.00/
```

TROE/ .7345 180.00 1035.00 5417.00 /
H2/2.00/ H2O/6.00/ CH4/2.00/ CO/1.50/ CO2/2.00/ C2H6/3.00/ AR/ .70/

| | | | |
|---|---|---|---|
| C2H5+O2<=>HO2+C2H4 | 8.400E+11 | .000 | 3875.00 |
| HCCO+O2<=>OH+2CO | 1.600E+12 | .000 | 854.00 |
| 2HCCO<=>2CO+C2H2 | 1.000E+13 | .000 | .00 |
| N+NO<=>N2+O | 3.500E+13 | .000 | 330.00 |
| N+O2<=>NO+O | 2.650E+12 | .000 | 6400.00 |
| N+OH<=>NO+H | 7.333E+13 | .000 | 1120.00 |
| N2O+O<=>N2+O2 | 1.400E+12 | .000 | 10810.00 |
| N2O+O<=>2NO | 2.900E+13 | .000 | 23150.00 |
| N2O+H<=>N2+OH | 4.400E+14 | .000 | 18880.00 |
| N2O+OH<=>N2+HO2 | 2.000E+12 | .000 | 21060.00 |
| N2O(+M)<=>N2+O(+M) | 1.300E+11 | .000 | 59620.00 |

LOW / 6.200E+14 .000 56100.00/
H2/2.00/ H2O/6.00/ CH4/2.00/ CO/1.50/ CO2/2.00/ C2H6/3.00/ AR/ .70/

| | | | |
|---|---|---|---|
| HO2+NO<=>NO2+OH | 2.110E+12 | .000 | -480.00 |
| NO+O+M<=>NO2+M | 1.060E+20 | -1.410 | .00 |

H2/2.00/ H2O/6.00/ CH4/2.00/ CO/1.50/ CO2/2.00/ C2H6/3.00/ AR/ .70/

| | | | |
|---|---|---|---|
| NO2+O<=>NO+O2 | 3.900E+12 | .000 | -240.00 |
| NO2+H<=>NO+OH | 1.320E+14 | .000 | 360.00 |
| NH+O<=>NO+H | 5.000E+13 | .000 | .00 |
| NH+H<=>N+H2 | 3.200E+13 | .000 | 330.00 |
| NH+OH<=>HNO+H | 2.000E+13 | .000 | .00 |
| NH+OH<=>N+H2O | 2.000E+09 | 1.200 | .00 |
| NH+O2<=>HNO+O | 4.610E+05 | 2.000 | 6500.00 |
| NH+O2<=>NO+OH | 1.280E+06 | 1.500 | 100.00 |
| NH+N<=>N2+H | 1.500E+13 | .000 | .00 |
| NH+H2O<=>HNO+H2 | 2.000E+13 | .000 | 13850.00 |
| NH+NO<=>N2+OH | 2.160E+13 | -.230 | .00 |
| NH+NO<=>N2O+H | 4.160E+14 | -.450 | .00 |
| NH2+O<=>OH+NH | 7.000E+12 | .000 | .00 |
| NH2+O<=>H+HNO | 4.600E+13 | .000 | .00 |
| NH2+H<=>NH+H2 | 4.000E+13 | .000 | 3650.00 |
| NH2+OH<=>NH+H2O | 9.000E+07 | 1.500 | -460.00 |
| NNH<=>N2+H | 3.300E+08 | .000 | .00 |
| NNH+M<=>N2+H+M | 1.300E+14 | -.110 | 4980.00 |

H2/2.00/ H2O/6.00/ CH4/2.00/ CO/1.50/ CO2/2.00/ C2H6/3.00/ AR/ .70/

| | | | |
|---|---|---|---|
| NNH+O2<=>HO2+N2 | 5.000E+12 | .000 | .00 |
| NNH+O<=>OH+N2 | 2.500E+13 | .000 | .00 |
| NNH+O<=>NH+NO | 7.000E+13 | .000 | .00 |
| NNH+H<=>H2+N2 | 5.000E+13 | .000 | .00 |
| NNH+OH<=>H2O+N2 | 2.000E+13 | .000 | .00 |
| NNH+CH3<=>CH4+N2 | 2.500E+13 | .000 | .00 |
| H+NO+M<=>HNO+M | 8.950E+19 | -1.320 | 740.00 |

H2/2.00/ H2O/6.00/ CH4/2.00/ CO/1.50/ CO2/2.00/ C2H6/3.00/ AR/ .70/

| | | | |
|---|---|---|---|
| HNO+O<=>NO+OH | 2.500E+13 | .000 | .00 |
| HNO+H<=>H2+NO | 4.500E+11 | .720 | 660.00 |
| HNO+OH<=>NO+H2O | 1.300E+07 | 1.900 | -950.00 |
| HNO+O2<=>HO2+NO | 1.000E+13 | .000 | 13000.00 |
| CN+O<=>CO+N | 7.700E+13 | .000 | .00 |
| CN+OH<=>NCO+H | 4.000E+13 | .000 | .00 |
| CN+H2O<=>HCN+OH | 8.000E+12 | .000 | 7460.00 |
| CN+O2<=>NCO+O | 6.140E+12 | .000 | -440.00 |
| CN+H2<=>HCN+H | 2.100E+13 | .000 | 4710.00 |
| NCO+O<=>NO+CO | 2.350E+13 | .000 | .00 |
| NCO+H<=>NH+CO | 5.400E+13 | .000 | .00 |
| NCO+OH<=>NO+H+CO | 2.500E+12 | .000 | .00 |
| NCO+N<=>N2+CO | 2.000E+13 | .000 | .00 |
| NCO+O2<=>NO+CO2 | 2.000E+12 | .000 | 20000.00 |
| NCO+M<=>N+CO+M | 8.800E+16 | -.500 | 48000.00 |

H2/2.00/ H2O/6.00/ CH4/2.00/ CO/1.50/ CO2/2.00/ C2H6/3.00/ AR/ .70/

| | | | |
|---|---|---|---|
| NCO+NO<=>N2O+CO | 2.850E+17 | -1.520 | 740.00 |
| NCO+NO<=>N2+CO2 | 5.700E+18 | -2.000 | 800.00 |
| HCN+M<=>H+CN+M | 1.040E+29 | -3.300 | 126600.00 |

H2/2.00/ H2O/6.00/ CH4/2.00/ CO/1.50/ CO2/2.00/ C2H6/3.00/ AR/ .70/

| | | | |
|---|---|---|---|
| HCN+O<=>NCO+H | 1.107E+04 | 2.640 | 4980.00 |
| HCN+O<=>NH+CO | 2.767E+03 | 2.640 | 4980.00 |
| HCN+O<=>CN+OH | 2.134E+09 | 1.580 | 26600.00 |
| HCN+OH<=>HOCN+H | 1.100E+06 | 2.030 | 13370.00 |
| HCN+OH<=>HNCO+H | 4.400E+03 | 2.260 | 6400.00 |
| HCN+OH<=>NH2+CO | 1.600E+02 | 2.560 | 9000.00 |
| H+HCN+M<=>H2CN+M | 1.400E+26 | -3.400 | 1900.00 |

H2/2.00/ H2O/6.00/ CH4/2.00/ CO/1.50/ CO2/2.00/ C2H6/3.00/ AR/ .70/

| | | | |
|---|---|---|---|
| H2CN+N<=>N2+CH2 | 6.000E+13 | .000 | 400.00 |
| C+N2<=>CN+N | 6.300E+13 | .000 | 46020.00 |
| CH+N2<=>HCN+N | 2.857E+08 | 1.100 | 20400.00 |
| CH+N2(+M)<=>HCNN(+M) | 3.100E+12 | .150 | .00 |

    LOW / 1.300E+25  -3.160   740.00/

    TROE/  .6670  235.00  2117.00  4536.00 /

H2/2.00/ H2O/6.00/ CH4/2.00/ CO/1.50/ CO2/2.00/ C2H6/3.00/ AR/ .70/

| | | | |
|---|---|---|---|
| CH2+N2<=>HCN+NH | 1.000E+13 | .000 | 74000.00 |
| CH2(S)+N2<=>NH+HCN | 1.000E+11 | .000 | 65000.00 |
| C+NO<=>CN+O | 1.900E+13 | .000 | .00 |
| C+NO<=>CO+N | 2.900E+13 | .000 | .00 |
| CH+NO<=>HCN+O | 5.000E+13 | .000 | .00 |
| CH+NO<=>H+NCO | 2.000E+13 | .000 | .00 |
| CH+NO<=>N+HCO | 3.000E+13 | .000 | .00 |
| CH2+NO<=>H+HNCO | 3.100E+17 | -1.380 | 1270.00 |

| | | | |
|---|---|---|---|
| CH2+NO<=>OH+HCN | 2.900E+14 | -.690 | 760.00 |
| CH2+NO<=>H+HCNO | 3.800E+13 | -.360 | 580.00 |
| CH2(S)+NO<=>H+HNCO | 3.100E+17 | -1.380 | 1270.00 |
| CH2(S)+NO<=>OH+HCN | 2.900E+14 | -.690 | 760.00 |
| CH2(S)+NO<=>H+HCNO | 3.800E+13 | -.360 | 580.00 |
| CH3+NO<=>HCN+H2O | 9.600E+13 | .000 | 28800.00 |
| CH3+NO<=>H2CN+OH | 1.000E+12 | .000 | 21750.00 |
| HCNN+O<=>CO+H+N2 | 2.200E+13 | .000 | .00 |
| HCNN+O<=>HCN+NO | 2.000E+12 | .000 | .00 |
| HCNN+O2<=>O+HCO+N2 | 1.200E+13 | .000 | .00 |
| HCNN+OH<=>H+HCO+N2 | 1.200E+13 | .000 | .00 |
| HCNN+H<=>CH2+N2 | 1.000E+14 | .000 | .00 |
| HNCO+O<=>NH+CO2 | 9.800E+07 | 1.410 | 8500.00 |
| HNCO+O<=>HNO+CO | 1.500E+08 | 1.570 | 44000.00 |
| HNCO+O<=>NCO+OH | 2.200E+06 | 2.110 | 11400.00 |
| HNCO+H<=>NH2+CO | 2.250E+07 | 1.700 | 3800.00 |
| HNCO+H<=>H2+NCO | 1.050E+05 | 2.500 | 13300.00 |
| HNCO+OH<=>NCO+H2O | 4.650E+12 | .000 | 6850.00 |
| HNCO+OH<=>NH2+CO2 | 1.550E+12 | .000 | 6850.00 |
| HNCO+M<=>NH+CO+M | 1.180E+16 | .000 | 84720.00 |
| H2/2.00/ H2O/6.00/ CH4/2.00/ CO/1.50/ CO2/2.00/ C2H6/3.00/ AR/ .70/ | | | |
| HCNO+H<=>H+HNCO | 2.100E+15 | -.690 | 2850.00 |
| HCNO+H<=>OH+HCN | 2.700E+11 | .180 | 2120.00 |
| HCNO+H<=>NH2+CO | 1.700E+14 | -.750 | 2890.00 |
| HOCN+H<=>H+HNCO | 2.000E+07 | 2.000 | 2000.00 |
| HCCO+NO<=>HCNO+CO | 2.350E+13 | .000 | .00 |
| CH3+N<=>H2CN+H | 6.100E+14 | -.310 | 290.00 |
| CH3+N<=>HCN+H2 | 3.700E+12 | .150 | -90.00 |
| NH3+H<=>NH2+H2 | 5.400E+05 | 2.400 | 9915.00 |
| NH3+OH<=>NH2+H2O | 5.000E+07 | 1.600 | 955.00 |
| NH3+O<=>NH2+OH | 9.400E+06 | 1.940 | 6460.00 |
| END | | | |

## Appendix C:  Counterflow Burner Design Schematics

This appendix contains design schematics for the counterflow burner used in this report.  Details about the design criteria and method as well as the operational capabilities of this burner can be found in Chapter 5.  In the following schematics, all dimensions are in inches unless otherwise specified.  The complete counterflow burner assembly consists of two identical burners, as described in this section, as well as appropriate mounting hardware and plumbing fittings.  A sketch of the complete apparatus, which demonstrates how the two burners are mounted in a counterflow configuration, is shown in Figure 5.1.
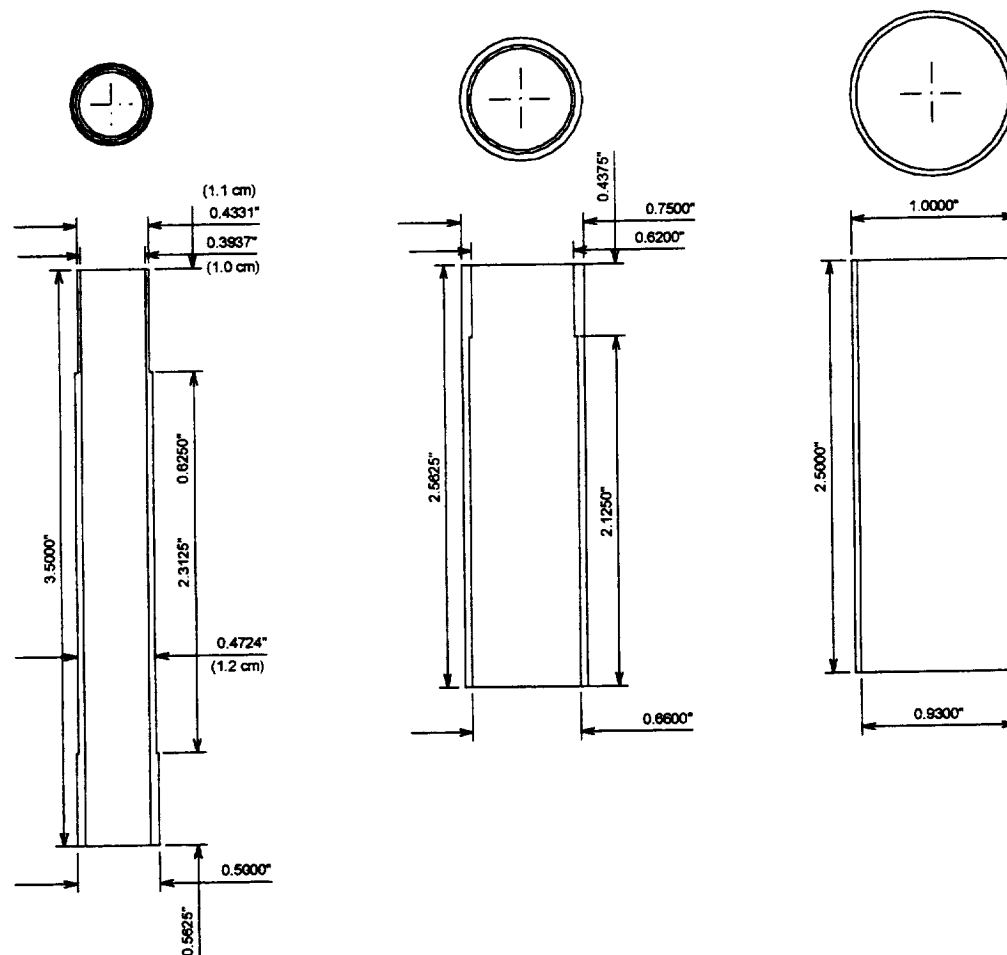
Figure C.1: Counterflow burner design schematics: stainless steel flow tubes.

(Break Edges With File to Fit in Rings)

0.0625"

1.0000"

0.6200"

0.0900"

0|0625"

0.7500"

0.03125"

0.0625"

0.9300"

(6 parts)→

2.3125"
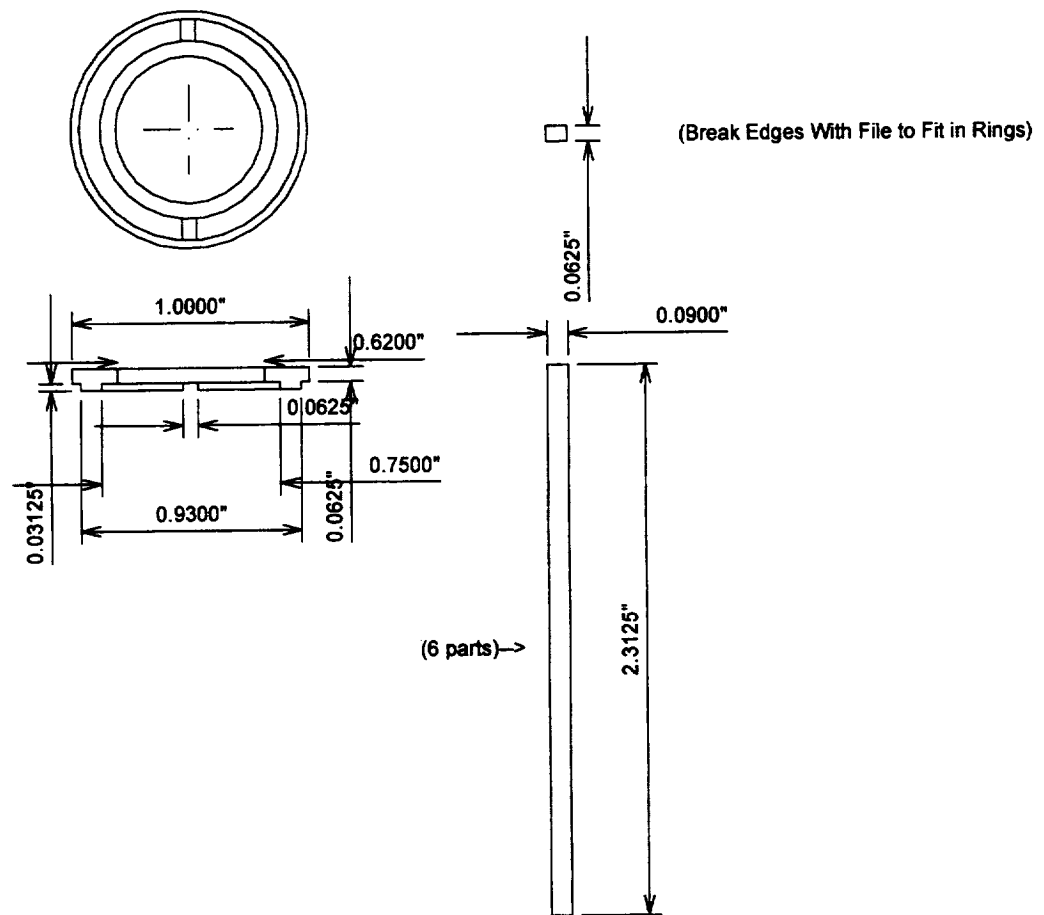
Figure C.2: Counterflow burner design schematics: stainless steel cap and flow guides.
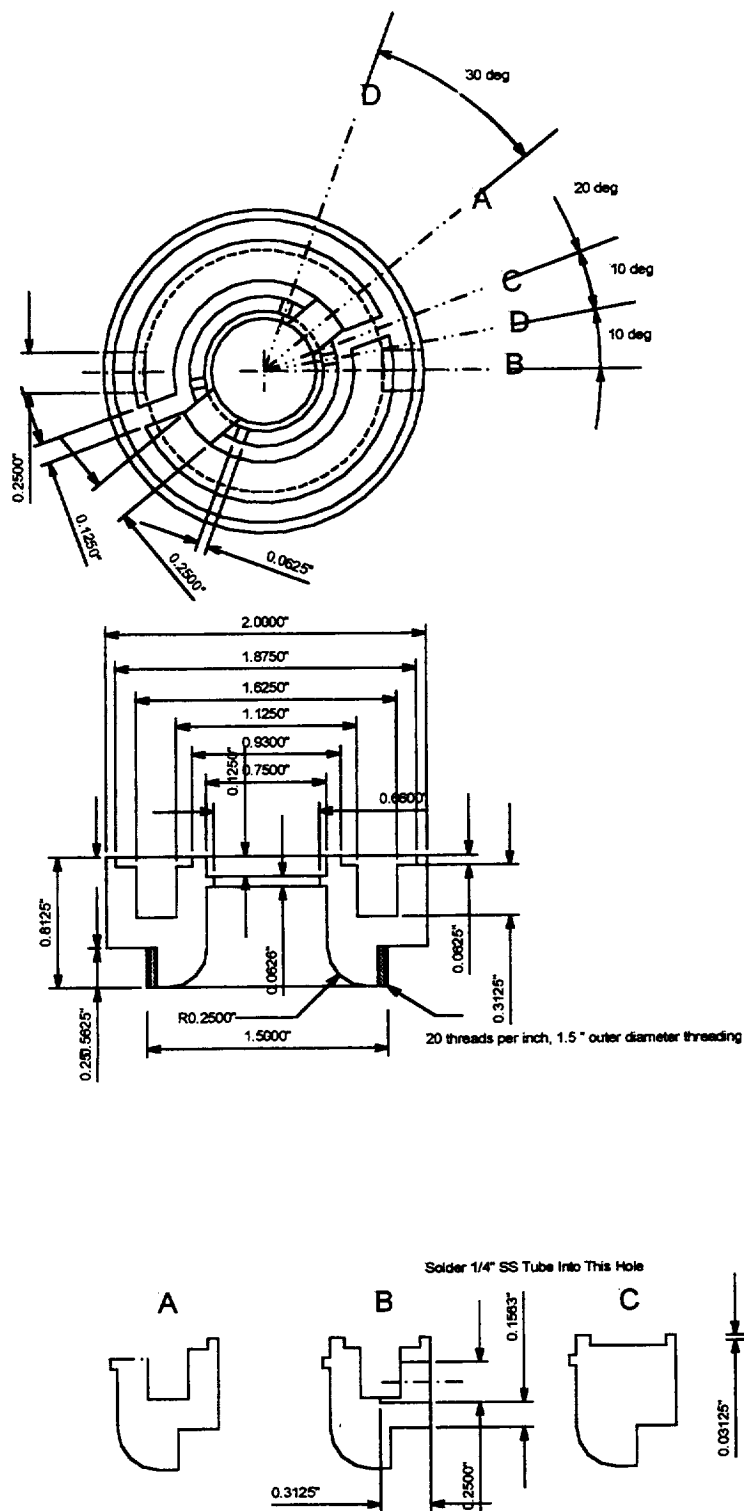
Figure C.3: Counterflow burner design schematics: stainless steel tube base.
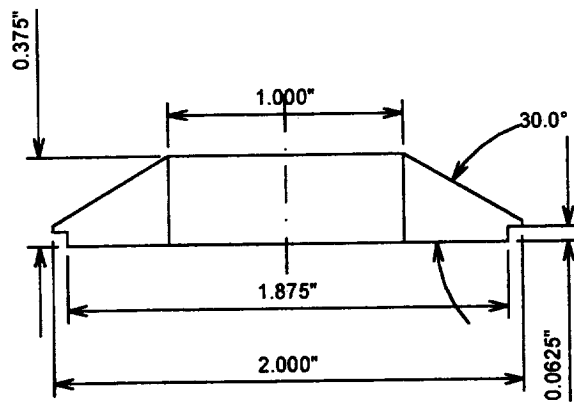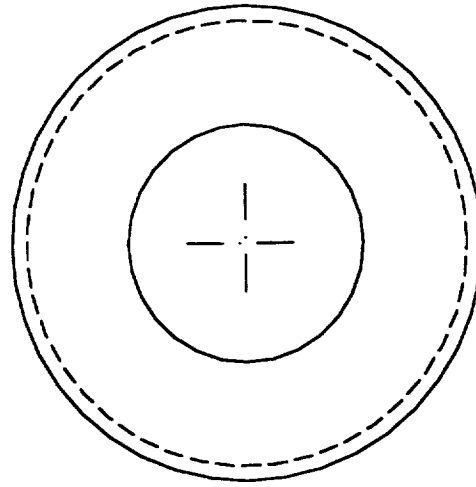
Figure C.4: Counterflow burner design schematics: stainless steel water cap.
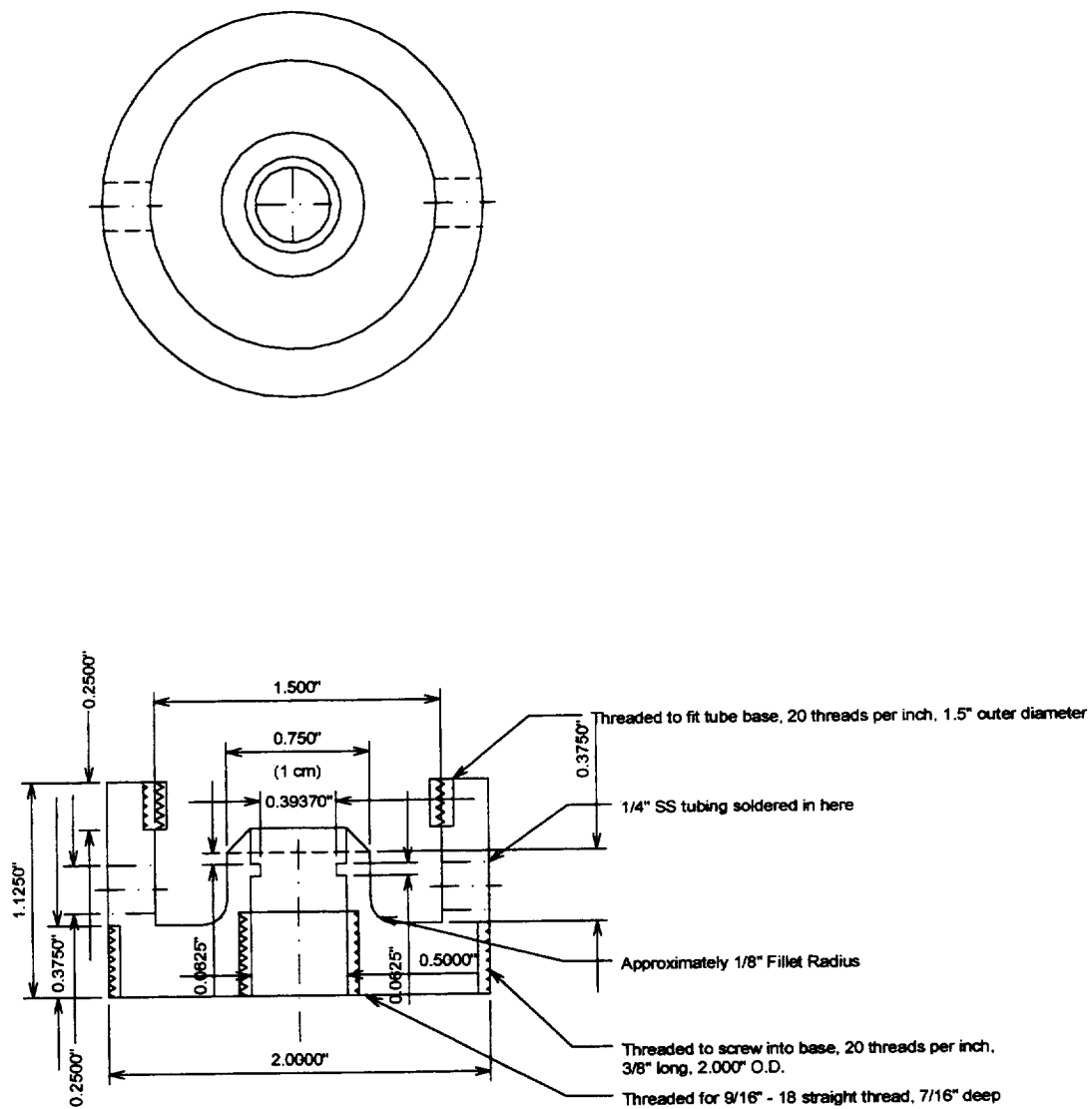
Figure C.5: Counterflow burner design schematics: stainless steel base.

## Sintered Stainless Plugs
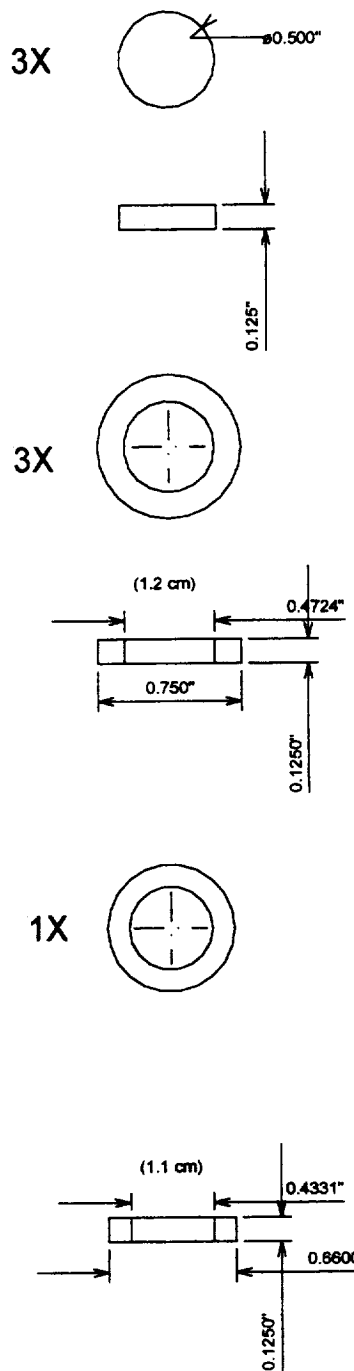
## Hastaloy Honeycomb Plug

**3X**

ø0.500"

(1.0 cm)

0.3937"

0.125"

0.7500"

**3X**

(1.2 cm)

0.4724"

0.750"

0.1250"

**1X**

(1.1 cm)

0.4331"

0.6600"

0.1250"
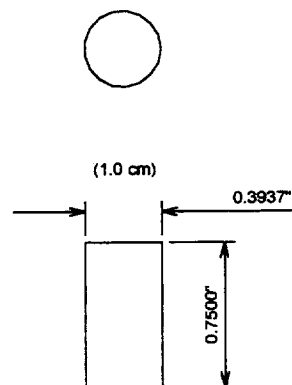
Figure C.6: Counterflow burner design schematics: plugs.
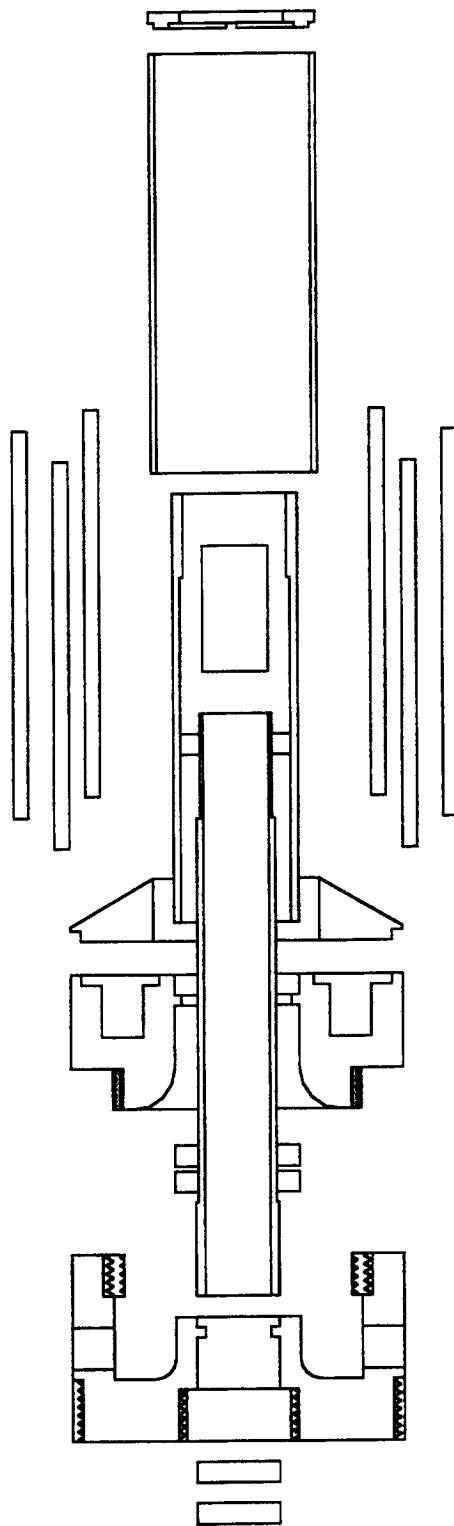
Figure C.7: Counterflow burner design schematics: exploded view.
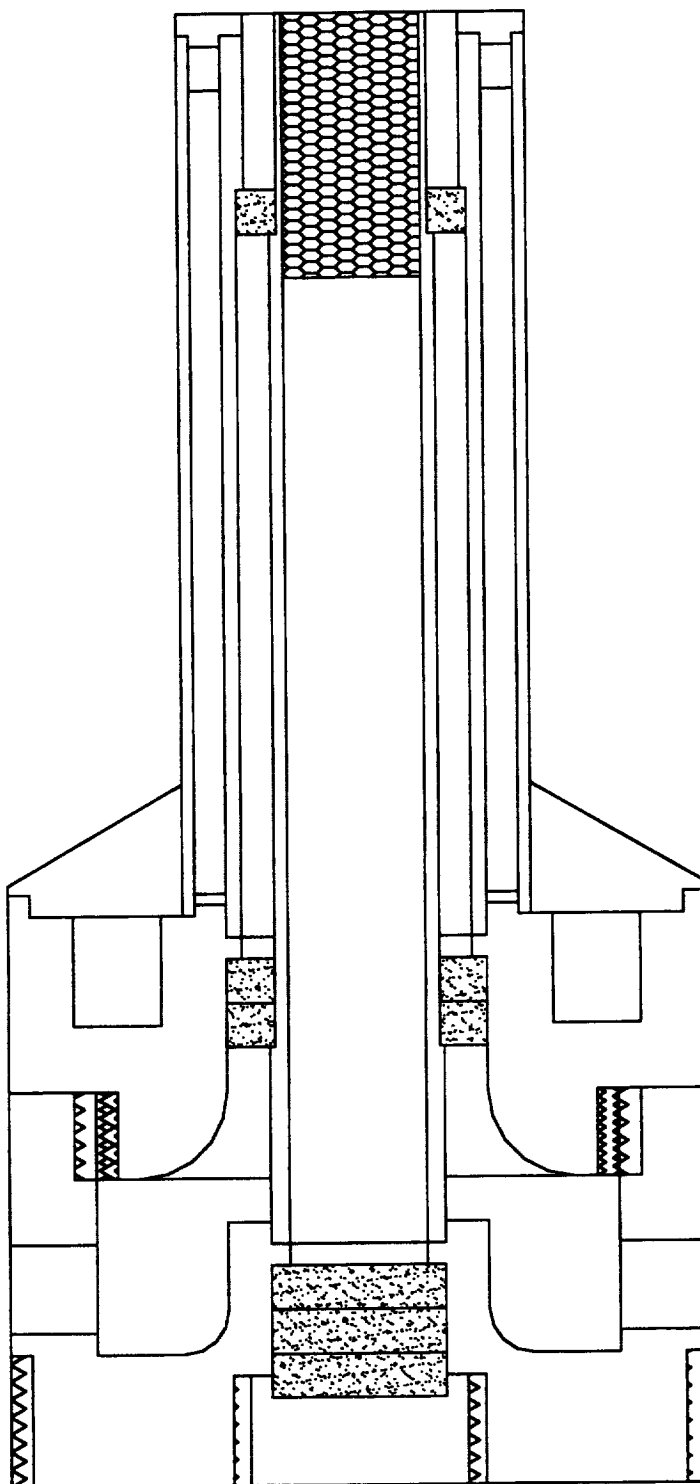
Figure C.8: Counterflow burner design schematics: assembled view.
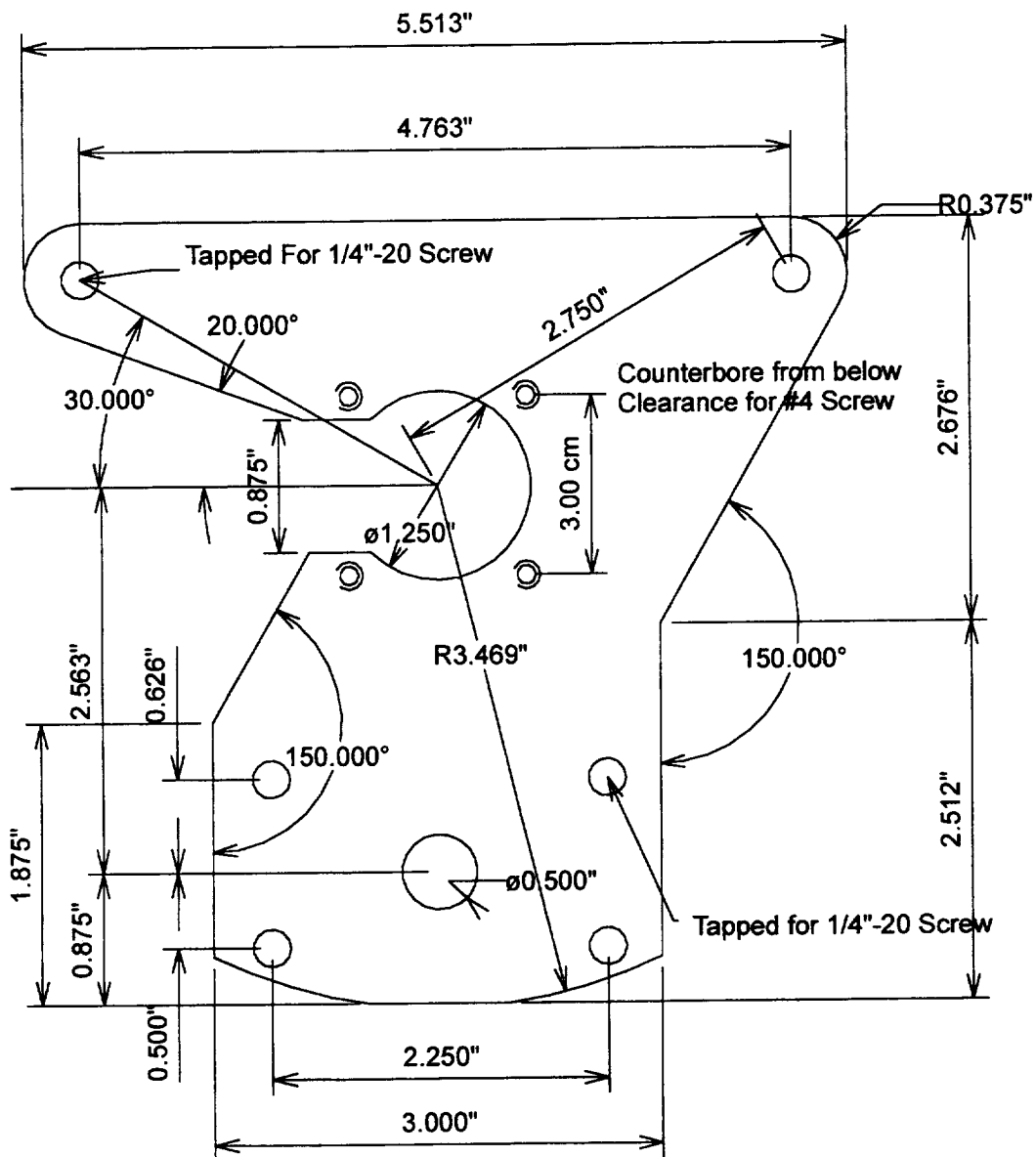
Figure C.9: Counterflow burner design schematics: aluminum bottom mounting plate.
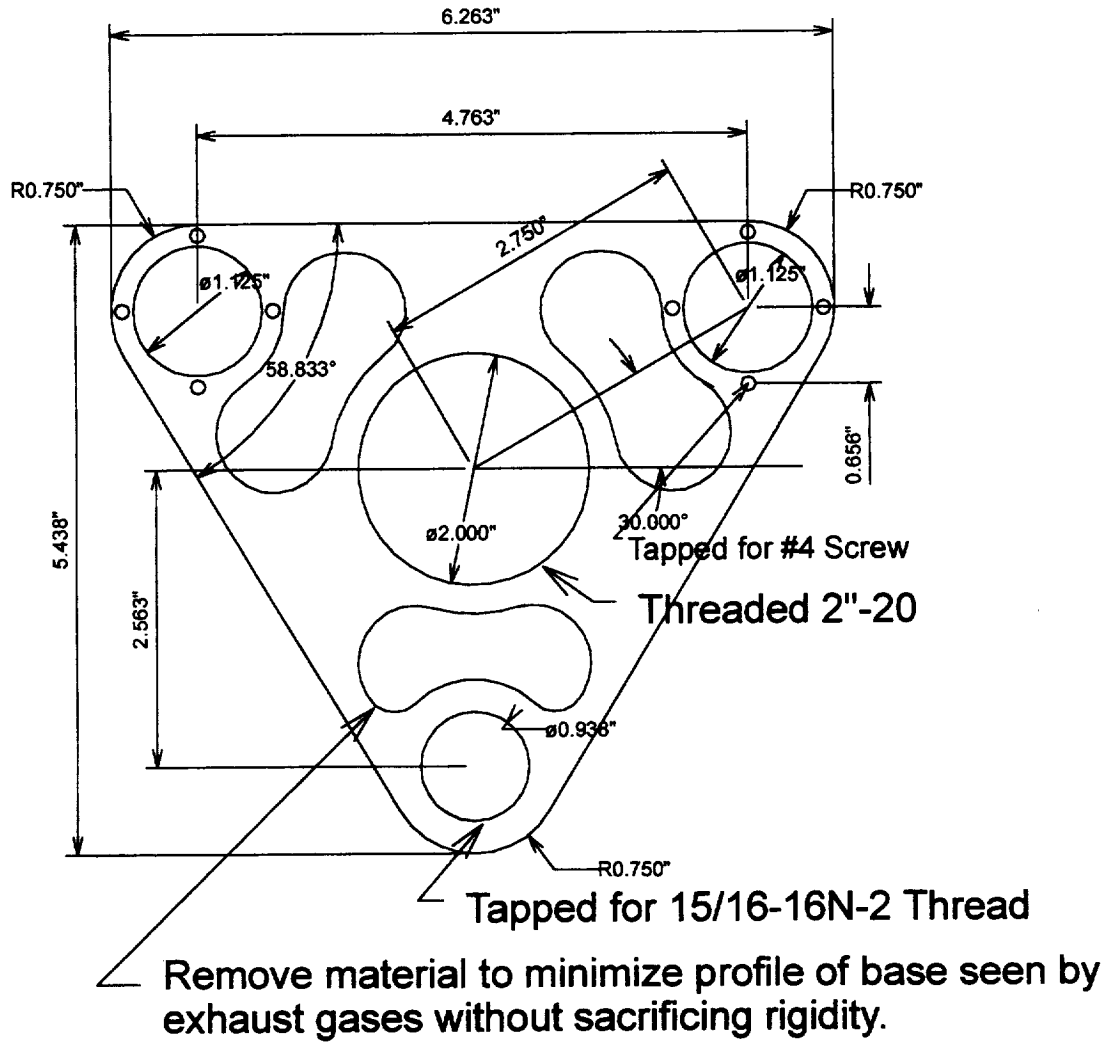
Figure C.10: Counterflow burner design schematics: stainless steel top mounting plate.

ø0.938"

ø1.125"

ø0.750"

ø1.500"

ø0.875"

ø1.313"

Clearance for #4 Screw

0.500"

0.188"

0.250"

0.250"

0.250"

0.500"

2.875"

Threaded 20 threads per inch
Outer diameter = 1.125"
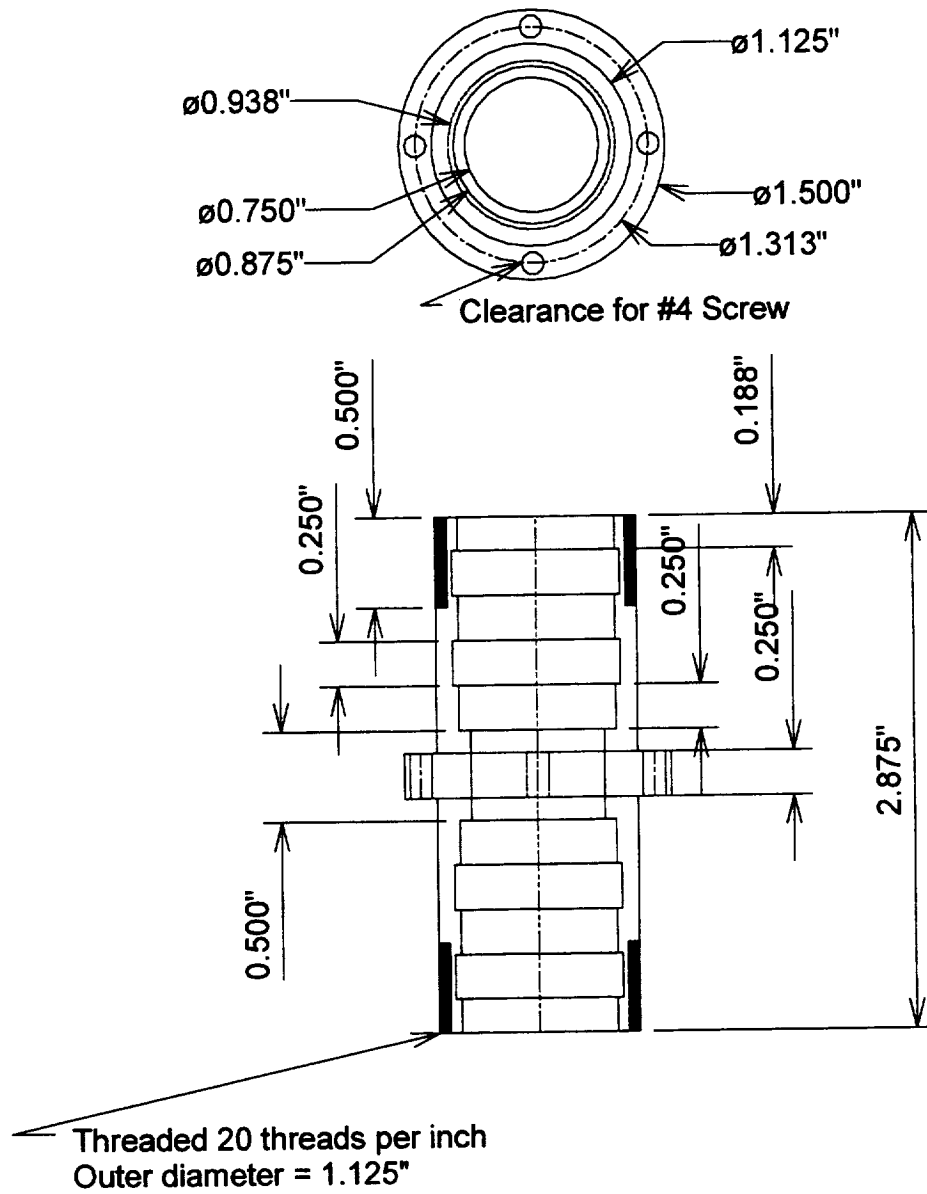
Figure C.11: Counterflow burner design schematics: stainless steel bearing holder.

ø1.500"

ø0.625"

Threaded 20 threads per inch
Outer diameter=1.125"

0.500"

Knurled end for grasping

0.750"
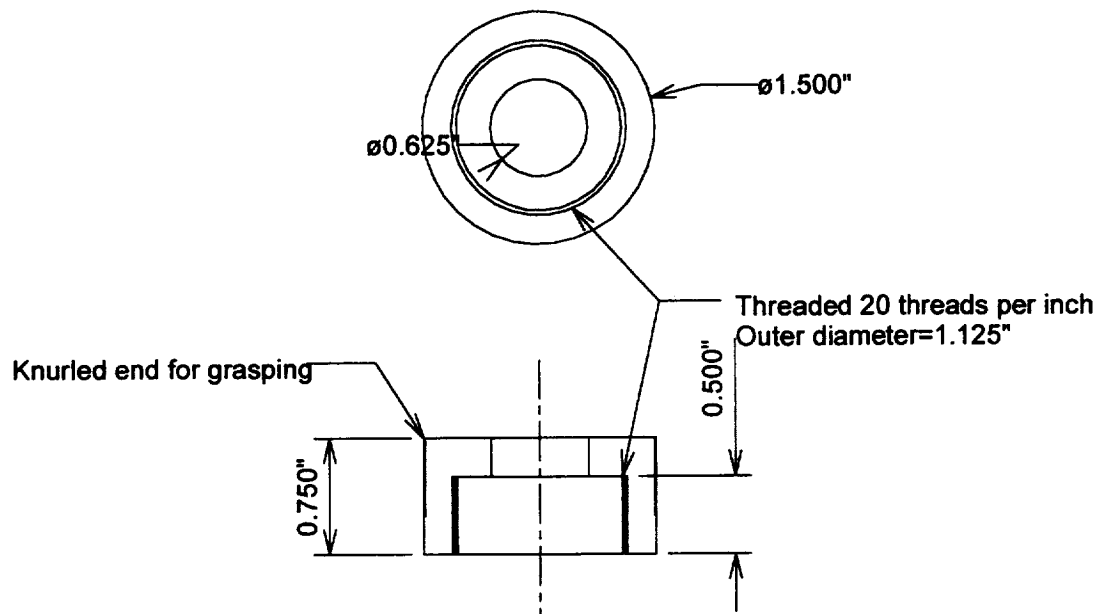
Figure C.12: Counterflow burner design schematics: stainless steel bearing cap.

Appendix D: Error Analysis

All experimental measurements contain a certain amount of uncertainty that must be analyzed to determine the accuracy and precision of the resulting data. Precision is a measure of the repeatability of an experiment. It accounts for random fluctuations within an experiment and gives us an indication of how large these fluctuations are compared to the quantity we are trying to measure. Thus, precision determines both the detection limit and the reproducibility of our experiments. However, even if we could somehow eliminate all noise from our measurements, it must be determined if any systematic errors have crept into the data which would cause our results to differ from the actual values that we are attempting to measure. To account for these systematic errors we must look at the accuracy of the measurements. Accuracy is a measure of how close the result of an experiment compares to the true value. Precision can often be improved simply by repeating an experiment several times. Improving accuracy, however, requires a careful look at the limiting assumptions and components within a given experiment.

Errors in LIF measurements of NO can occur at several stages, from control of the doping concentration in the calibration flames to dark noise within the PMT. This appendix investigates the uncertainties associated with each of these stages as well as their influence on the overall precision and accuracy of the LIF measurements. Some conclusions are then made regarding possible ways to improve these measurements. All uncertainties are based on a 95% confidence interval.

## D.1 Propagation of Errors

To determine the effect of the uncertainty in one portion of a measurement scheme on the uncertainty of the measurement as a whole, we use the method of propagation of errors (Taylor, 1982). This method states that the uncertainty in a function $q(x, ..., z)$, where $x, ..., z$ are independent, random, measured quantities with respective uncertainties $\delta x, ..., \delta z$, is given by the equation

$$\delta q = \sqrt{\left(\frac{\partial q}{\partial x}\delta x\right)^2 + \cdots + \left(\frac{\partial q}{\partial z}\delta z\right)^2}.$$ (D.1)

On the other hand, if the uncertainties in the measured quantities are not independent of one another or are not random, a more conservative error estimate should be used, of the form

$$\delta q = \left|\frac{\partial q}{\partial x}\right|\delta x + \cdots + \left|\frac{\partial q}{\partial z}\right|\delta z.$$ (D.2)

For the special case where each uncertainty only appears once in the equation for q, some simple formulas can be used to combine the uncertainties of the measured quantities. Specifically, for sums and differences of the form $q = x + \cdots + z - (u + \cdots + v)$, Equations (D.1) and (D.2) reduce to

$$\delta q = \sqrt{(\delta x)^2 + \cdots + (\delta y)^2 + (\delta u)^2 + \cdots + (\delta v)^2}$$ (D.3)

and

$$\delta q = \delta x + \cdots + \delta z + \delta u + \cdots + \delta v.$$ (D.4)

Furthermore, for products and quotients of the form $q = \dfrac{x \times \cdots \times z}{u \times \cdots \times v}$, these equations reduce to

$$\frac{\delta q}{|q|} = \sqrt{\left(\frac{\delta x}{x}\right)^2 + \cdots + \left(\frac{\delta z}{z}\right)^2 + \left(\frac{\delta u}{u}\right)^2 + \cdots + \left(\frac{\delta v}{v}\right)^2},$$ (D.5)

and

$$\frac{\delta q}{|q|} = \frac{\delta x}{x} + \cdots + \frac{\delta z}{z} + \frac{\delta u}{u} + \cdots + \frac{\delta v}{v}.$$ (D.6)

The above equations will be used extensively in the remainder of this appendix for combining the errors associated with our LIF measurement scheme.

## D.2 Calibration Technique and Uncertainties

Starting with an individual LIF signal, the measured voltage will have random errors associated with noise from the PMT and electronics, fluctuations in the laser beam power and position, and fluctuations within the flame environment itself. These errors will all be manifested as random fluctuations in the LIF signal. By averaging our signal over many shots, we can obtain a more accurate mean value for each condition. In these experiments, both the signal and relative laser power for each condition are averaged over 600 shots. The corresponding standard deviation of the mean for these measurements accounts for all of the random uncertainties mentioned above. Since we are interested in the 95% confidence interval, twice this standard deviation of the mean will represent the random uncertainty in the LIF signal.

For high-pressure, linear LIF measurements, the laser-power corrected fluorescence signal is of most interest. This signal is found from

$$S = \frac{V - V_b}{V_l - V_{l,b}} \ ,$$ 
(D.7)

where $V$ and $V_b$ represent the LIF voltages corresponding to the NO and blocked-beam background signals, respectively, while $V_l$ and $V_{l,b}$ represent the voltages corresponding to the laser power and its background signal, respectively. Several additional experimental uncertainties that could affect this corrected fluorescence signal are pdl drift and beam steering, as well as PMT and photodiode non-linearities. Pdl drift is a serious concern that can potentially affect the precision of each measurement. As discussed in Chapter 3, the measurements presented here utilized a wavelength locking procedure to minimize this effect, thus limiting the corresponding relative error, $\varepsilon(pdl)$, to less than 2%. This error is both random and independent of the previous uncertainties. Beam steering is another source of error in LIF measurements as small shifts in beam position can impact the optical yield and thus alter the measured LIF signals. As discussed in Chapter 3, a beam locking apparatus employing a pinhole aperture and a photodiode were used to minimize the untoward effects of beam steering. For purposes of this error analysis, the remaining uncertainty associated with beam steering, $\varepsilon(bs)$, is approximated as 2%. PMT and

photodiode linearities are avoided by operating well within each instrument's linear range, and thus can be neglected in the error analysis. Considering the above effects, the relative uncertainty of the corrected signal, $\varepsilon(S)$, can be calculated via a combination of Equations (D.3), (D.5) and (D.7) to give

$$\varepsilon(S) = \frac{\delta S}{S} = \sqrt{\left(\frac{\sqrt{(\delta V)^2 + (\delta V_b)^2}}{V - V_b}\right)^2 + \left(\frac{\sqrt{(\delta V_l)^2 + (\delta V_{l,b})^2}}{V_l - V_{l,b}}\right)^2 + \varepsilon(pdl)^2 + \varepsilon(bs)^2} \quad , \text{(D.8)}$$

where $\delta V$ and $\delta V_l$ are twice the standard deviation of the mean of the LIF voltage and laser-power voltage, respectively.

These corrected signals are plotted on the calibration curve for varying amounts of doped NO in the flames. Each point on this calibration curve contains an additional uncertainty owing to uncertainties in the gas delivery systems for NO. Thus, to obtain a modified uncertainty for the signal at each NO concentration on the calibration curve, the uncertainty in NO concentration must be multiplied by the slope of the curve as described by Bevington and Robinson (1992). Regression analysis could then be used with the data points and their associated errors to determine the slope and y-intercept of the best-fit line for the calibration data, as well as the associated uncertainties in these two parameters.

Alternatively, a least-squares fit could be applied to the corrected fluorescence signals, and the standard error of the slope and y-intercept determined by the goodness of the corresponding fit. This latter method, which provides a more conservative estimate of the errors, should account for all of the above mentioned uncertainties, as well as any other unforeseen random errors which might corrupt the measurements. Because of its greater robustness, this method was chosen for the determination of the calibration slope and its relative precision, $\varepsilon(m_p)$, which was set at twice the standard error of the calibration slope. This technique is thus used for both on- and off-line excitation to obtain a calibration plot such as that shown in Figure 7.3.

In addition to the above uncertainties, which affect the precision of the calibration curve, two more errors can affect the accuracy of the on- and off-line calibration slopes, $m$ and $m'$ respectively. The first of these is the accuracy of the calibration gas used to

obtain a calibration curve. Tests within our laboratory, using chemiluminescent detection to compare six different calibration bottles from two different gas suppliers, have shown that the relative NO concentration ($NO_{measured}/NO_{listed}$) in these bottles all fall within 3% of each other. Thus, a relative error, $\varepsilon(NO_b)$, of 3% is used to account for this error in determining the slopes of the calibration curves. This error source is both random and independent of the uncertainties associated with the above precision analysis.

The second possible factor affecting the accuracy of the slope for the calibration is the destruction of doped NO as it passes through the flamefront. Kinetic modeling of these doped flames using the GMK-DB model (Drake and Blint, 1991) and the Sandia steady, laminar, one-dimensional, premixed flame code (Kee et. al., 1985) predicts that this NO destruction will increase with pressure. For our conditions, the maximum predicted NO destruction at 14.6 atm is ~3%. Since the pressures studied in the counterflow premixed flames of this report are considerably lower than this value, a conservative estimate of 3% relative error, $\varepsilon(NO_d)$, in the calculated slope owing to this effect has been assumed in this work to account for both the destruction of NO and the uncertainty of the modeling predictions. It is worth noting that this error could be reduced by the application of a suitable correction. However, since our purpose is to use these measurements to verify the modeling schemes, it seems injudicious to use data from the modeling schemes to vary our measured concentrations. Finally, this source of error, though independent of the errors previously studied, is not random in nature. Because of this feature, the associated 3% error must be added to the accuracy measurements via Equation (D.6).

Based on the above discussion, and on the inverse relationship between the slope of the calibration curve and the amount of doped NO, we can calculate the relative accuracy associated with the measurement of this slope. Combining Equations (D.1) and (D.2) we get

$$\varepsilon(m_a) = \frac{\delta m}{m} = \sqrt{\varepsilon(NO_b)^2 + \varepsilon(m_p)^2} + \varepsilon(NO_d). \qquad \text{(D.9)}$$

Equation (D.9) holds for the slopes of both the on- and off-line calibration curves. Thus, the uncertainty in the slope ratio $f = m'/m$ can now be calculated. While the accuracies of $m$ and $m'$ are not entirely independent owing to the NO destruction term which will be the same for both, this dependence would have the net effect of slightly reducing the relative error in $f$ from that predicted by Equation (D.5). Thus, the following equations give us conservative estimates for the precision and accuracy of the slope ratio $f = m'/m$:

$$\varepsilon(f_p) = \sqrt{\varepsilon(m_p')^2 + \varepsilon(m_p)^2} , \qquad (D.10)$$

$$\varepsilon(f_a) = \sqrt{\varepsilon(m_a')^2 + \varepsilon(m_a)^2} . \qquad (D.11)$$

The final parameters needed for the calibration equations are the on- and off-line, undoped, corrected fluorescence signals. While we could simply use one measurement with its corresponding accuracy given by Equation (D.8), better results can be obtained by averaging several corrected measurements. Since these uncertainties tend to dominate the uncertainty calculations for the NO concentration in the calibration flame, between two and four measurements were obtained for each of these values. The uncertainty of these averaged values was then given by

$$\delta S_u = \frac{\sqrt{(\delta S_1)^2 + \cdots + (\delta S_N)^2}}{N} , \qquad (D.12)$$

where $N$ is the number of averaged measurements. A similar equation was used to calculate $\delta S_u'$.

This brings us to the calculation of our corrected background signal $C_b$ from

$$C_b = \frac{(S_u' - f \cdot S_u)}{(1 - f)} . \qquad (D.13)$$

In this equation, $S_u$ and $S_u'$ are the on- and off-line, laser-power corrected fluorescence signals obtained in the calibration flame without additional NO doping. Since $f$ shows up in both the numerator and denominator of Equation (D.13), we must use Equation (D.1) to calculate the corresponding precision and accuracy of the above equation. Carefully evaluating the partial derivatives of Equation (D.13), we obtain for the precision of $C_b$,

$$\delta C_{b,p} = \sqrt{\left(\frac{\delta S_u'}{1-f}\right)^2 + \left(\frac{f \cdot \delta S_u}{1-f}\right)^2 + \left(\frac{(S_u' - S_u) \cdot \delta f_p}{(1-f)^2}\right)^2} \ . \qquad \text{(D.14)}$$

A similar expression could be used for the accuracy of $C_b$ except for the fact that a non-random term exists in the equation for $\delta f_a$. Fortunately, the random terms dominate the calculation of $\delta C_{b,a}$, and thus, any underestimation of this error from adding the component errors in quadrature should be more than accounted for by the previous conservative assumptions within this analysis. Hence, Equation (D.14) was also used, with appropriate accuracy uncertainties, to calculate the accuracy of the background signal.

At this point, the corrected NO fluorescence signal owing to undoped NO in the calibration flame can be calculated as simply

$$S_{NO_u} = S_u - C_b \ . \qquad \text{(D.15)}$$

The associated precision is thus

$$\delta S_{NO_u,p} = \sqrt{\left(\delta S_u\right)^2 + \left(\delta C_{b,p}\right)^2} \ . \qquad \text{(D.16)}$$

The accuracy, $\delta S_{NO_u,a}$, is once again calculated with an analogous expression. Finally, the calibration flame NO concentration, in ppm, can be calculated using the expression

$$NO_u = \frac{S_{NO_u}}{m} \ . \qquad \text{(D.17)}$$

The final relative precision of the calibration concentration is thus

$$\varepsilon\left(NO_{u,p}\right) = \sqrt{\varepsilon\left(S_{NO_u,p}\right)^2 + \varepsilon\left(m_p\right)^2} \ . \qquad \text{(D.18)}$$

Unfortunately, we need to account for non-linearities in the calculations for the slope accuracy; thus, the accuracy of the calibration concentration becomes

$$\varepsilon\left(NO_{u,a}\right) = \sqrt{\varepsilon\left(S_{NO_u,a}\right)^2 + \varepsilon(m_p)^2 + \varepsilon(NO_b)^2 + \varepsilon(NO_d)} \ . \qquad \text{(D.19)}$$

Finally, in applying the conversion from ppm to number density, which is the quantity directly measured by the LIF technique, it is necessary to account for uncertainties in both the pressure and temperature of the calibration flame. In the current analysis, these errors,

$\varepsilon(T_c)$ and $\varepsilon(P_c)$, were approximated at 2% each. Thus the number density precision and accuracy in the calibration flame become:

$$\varepsilon\!\left([NO]_{u,p}\right) = \sqrt{\varepsilon\!\left(NO_{u,p}\right)^2 + \varepsilon\!\left(P_c\right)^2 + \varepsilon\!\left(T_c\right)^2} \qquad (D.20)$$

$$\varepsilon\!\left([NO]_{u,a}\right) = \sqrt{\varepsilon\!\left([NO]_{u,p}\right)^2 + \varepsilon(NO_b)^2 + \varepsilon(NO_d)} \qquad (D.21)$$

### D.3 LIF Measurement Uncertainties

When taking measurements at conditions other than the calibration condition, the first step is to calculate laser-power corrected fluorescence signals based on the data using Eqs. (D.7) and (D.15). At this point, in addition to the previously mentioned sources of error, three new sources can affect the accuracy of the calculation. The first source is the variation in quenching rate coefficient between the calibration and measurement conditions. For the relative number density profiles presented in Chapters 6 and 7, the modeling was "uncorrected" for quenching rate effects by using the quenching correlations of Paul et al. (1995) and thus the accuracy and precision of the plotted data is properly unaffected by this term. However, the accuracy of the entire approach must be considered within the context of the modeling predictions. In general, the resulting uncertainties will have their largest impact at conditions with significantly different quenching environments than found at the calibration point, such as the low-temperature preheat region of our counterflow premixed flames. For the corrected measurements of Chapter 7, an approximated value of $\varepsilon(q) = 3\%$ was applied to this relative error in order to account for both uncertainty in the temperature and major species concentrations used for the quenching calculation as well as uncertainties in the quenching cross-sections themselves.

The second source of error arises from variations in the absorption rate coefficient owing both to changes in the ground state Boltzmann fraction as well as to changes in the excitation overlap fraction. These effects have been modeled using the absorption code of Seitzman (1991). As in the case of the quenching code, this modeling was used to

"uncorrect" the code results, and thus is not properly included in the uncertainties for the uncorrected number density measurements. However, it must again be considered when comparing modeling predictions with our measurements. This uncertainty, as for quenching, will have little impact on peak, post-flame zone NO concentration measurements but could impact NO measurements in the preheat region. As discussed in Chapters 7 and 8, there is strong evidence to support the validity of the absorption correction technique utilized in this work; thus, for the corrected NO concentration measurements of Chapter 7, only a 3% error $\varepsilon(b)$ was included based on these effects.

The third source of error in these flames arises from variations in the background fluorescence signal. Owing to the relatively low background signal in these flames as well as the unknown variation of background with location, the LIF profiles obtained in this study were not directly corrected for background interferences. During calibration, backgrounds were determined in the post-flame zone of the calibration flames. These background signals were used as a basis for estimating the overall uncertainty associated with ignoring background contributions at each pressure. Assuming that a background signal up to 10% higher than the calibration background could be present at any point in the flame, appropriate uncertainties were added for each measurement. Hence, the absolute uncertainty in the corrected fluorescence signal was set at $\delta(C_{phi})=1.10*C_b$ for each pressure. In the atmospheric pressure flames the background was not explicitly solved for using the on- and off-line calibration scheme described previously. For these cases the background uncertainty was set at $\delta(C_{phi})=1.10*S_u'$ where $S_u'$ is simply the overall signal measured in the calibration flame using off-line excitation. Thus, in the absence of a calculated value for a given error contribution, a more conservative estimate is applied in its place to maintain the integrity of the technique. By applying the background signal error in an absolute sense, a strong relative impact occurs on the measurements of low NO concentrations in the preheat zone. If pressures higher than those studied here were to be examined, a more direct subtraction technique would need to be incorporated to minimize these errors.

While the above three errors are independent, they are clearly not random in nature. This could cause us to add these errors directly rather than in quadrature when calculating the total accuracy of our measurements. However, at least two of these errors, the quenching and absorption effects, tend to counteract each other in many cases. Hence, adding these errors directly would be too conservative. Based on this observation, the quenching and absorption terms are added in quadrature to determine the total error for the corrected concentration measurements of Chapter 7. For both the corrected and uncorrected NO concentration measurements, the background error is conservatively added in an absolute sense to the associated accuracy error bars.

For the uncorrected number density measurements, the NO concentration was determined by using

$$[NO] = \frac{[NO]_u \cdot S}{S_c}.$$

(D.22)

Here, the subscript $c$ is used to denote measurements obtained for the calibration flame during the same experimental session as for the non-subscripted data. In comparison, the subscript $u$ represents measurements for the undoped calibration flame during the development of the calibration plot. The need for the $c$ subscript arises from attempts to minimize the effects of PDL drift, as well as other changes in the experimental apparatus, that may have occurred between the times that the calibration curve and the relevant data were taken. In Eq. (D.22), $S_c$ is a corrected fluorescence signal corresponding to the calibration condition employed just prior to the measurement of $S$.

Based on our previous discussions the relative precision and accuracy of these measurements thus become:

$$\varepsilon\left([NO]_p\right) = \sqrt{\varepsilon\left(S_p\right)^2 + \varepsilon\left(S_{c,p}\right)^2 + \varepsilon\left([NO]_{u,p}\right)}$$

(D.23)

and

$$\varepsilon\left([NO]_a\right) = \sqrt{\varepsilon\left([NO]_p\right)^2 + \varepsilon\left(NO_b\right)^2 + \varepsilon\left(NO_d\right) + \frac{\delta\left(C_{phi}\right)}{S}}.$$

(D.24)

We are finally ready to calculate the NO concentration in ppm for each of our corrected measurements. In the conversion back to ppm, temperature and pressure effects will again enter these calculations. The equation for determining the measured NO concentration in ppm can be expressed as

$$NO \propto \frac{[NO] \cdot T}{P} \cdot \frac{q}{b}$$

(D.25)

where $q$ and $b$ are quenching and absorption ratios, respectively, between the measured and calibration conditions. The proportionality constant is based on the ideal gas law and includes the universal gas constant and unit conversions to obtain the NO concentration in ppm. Based on this equation, the precision and accuracy of these corrected NO concentration measurements become

$$\varepsilon(NO_p) = \sqrt{\varepsilon([NO]_p)^2 + \varepsilon(T)^2 + \varepsilon(P)^2}$$

(D.26)

and

$$\varepsilon(NO_a) = \sqrt{\varepsilon(NO_p)^2 + \varepsilon(NO_b)^2 + \varepsilon(b)^2 + \varepsilon(q)^2 + \varepsilon(NO_d) + \frac{\delta(C_{phi})}{S}}.$$

(D.27)

## D.4 Results and Conclusions

Using the above equations, precisions and accuracies were calculated for all of the LIF measurements presented in this report. Relative accuracies and precisions were found to vary from 12% to 27% and from 7% to 10%, respectively, in the post-flame zone and were strongly influenced by the overall NO concentration, with higher concentrations being measured with greater certainty as would be expected. The results of this analysis are presented as error bars in the various figures of Chapters 6 and 7.

As expected, the accuracy of our results becomes worse at higher pressures. This is due primarily to the increasing role of the background uncertainty in these high-pressure flames. In general, the accuracy of these flames could be improved by the incorporation of a background correction technique such as that described by Thomsen et al. (1997).

However, the careful application of such a technique is complicated by the changing background contribution in these flames and was deemed unnecessary for these relatively low-pressure conditions.

As an example, Table D.1 contains the important parameters used in the error analysis for the LIF measurements in the $\phi$=0.75, 2.02 atm and $\phi$=0.60, 4.06 atm counterflow premixed flames of Chapter 7. These two cases represent the most- and least-accurate, respectively, post-flame zone measurements presented in this report.

Table D.1: Parameters used in error analysis for LIF measurements of NO in 2.02 atm, $\phi$=0.75 and 4.06 atm, $\phi$=0.60 $CH_4/O_2/N_2$ counterflow premixed flames. Temperatures are in K, signals in volts, concentrations in ppm, and number densities in molecules/$cm^3$.

| Parameter | $\phi$=0.75 2.02 atm | $\phi$=0.60 4.06 atm | Parameter | $\phi$=0.75 2.02 atm | $\phi$=0.60 4.06 atm |
|---|---|---|---|---|---|
| $\varepsilon(pdl)$ | 0.020 | 0.020 | $S_{NO_u}$ | 0.799 | 0.619 |
| $\varepsilon(bs)$ | 0.020 | 0.020 | $\varepsilon(S_{NO_u,p})$ | 0.025 | 0.021 |
| $S_u$ | 0.814 | 0.642 | $\varepsilon(S_{NO_u,a})$ | 0.025 | 0.022 |
| $\varepsilon(S_u)$ | 0.023 | 0.019 | $NO_u$ | 7.798 | 8.042 |
| $S'_u$ | 0.055 | 0.071 | $\varepsilon(NO_{u,p})$ | 0.031 | 0.042 |
| $\varepsilon(S'_u)$ | 0.091 | 0.061 | $\varepsilon(NO_{u,a})$ | 0.073 | 0.082 |
| $\varepsilon(NO_b)$ | 0.030 | 0.030 | $[NO]_u$ | 6.28E+13 | 1.30E+14 |
| $\varepsilon(NO_d)$ | 0.030 | 0.030 | $\varepsilon(P_c)$ | 0.020 | 0.020 |
| $m$ | 0.102 | 0.077 | $\varepsilon(T_c)$ | 0.020 | 0.020 |
| $\varepsilon(m_p)$ | 0.019 | 0.037 | $\varepsilon([NO]_{u,p})$ | 0.042 | 0.051 |
| $\varepsilon(m_a)$ | 0.075 | 0.078 | $\varepsilon([NO]_{u,a})$ | 0.081 | 0.089 |
| $m'$ | 0.005 | 0.006 | | | |
| $\varepsilon(m'_p)$ | 0.000 | 0.000 | $\varepsilon(C_{phi})$ | 0.020 | 0.040 |
| $\varepsilon(m'_a)$ | 0.060 | 0.060 | $S_c$ | 0.804 | 0.064 |
| $f$ | 0.050 | 0.078 | $\varepsilon(S_c)$ | 0.039 | 0.022 |
| $\varepsilon(f_p)$ | 0.018 | 0.037 | $S$ | 1.318 | 0.195 |
| $\varepsilon(f_a)$ | 0.088 | 0.098 | $\varepsilon(S)$ | 0.045 | 0.082 |
| $C_b$ | 0.015 | 0.023 | $[NO]$ | 1.03E+14 | 3.99E+13 |
| $\varepsilon(C_{b,p})$ | 0.361 | 0.223 | $\varepsilon([NO]_p)$ | 0.072 | 0.099 |
| $\varepsilon(C_{b,a})$ | 0.423 | 0.284 | $\varepsilon([NO]_a)$ | 0.120 | 0.265 |

# REPORT DOCUMENTATION PAGE

| 1. AGENCY USE ONLY (*Leave blank*) | 2. REPORT DATE | 3. REPORT TYPE AND DATES COVERED |
|---|---|---|
| | February 2000 | Final Contractor Report |

**4. TITLE AND SUBTITLE**

Measurements and Modeling of Nitric Oxide Formation in Counterflow, Premixed $CH_4/O_2/N_2$ Flames

**6. AUTHOR(S)**

D. Douglas Thomsen and Normand M. Laurendeau

**5. FUNDING NUMBERS**

WU–714–02–40–00
NAG3–1782
NAG3–2251

**7. PERFORMING ORGANIZATION NAME(S) AND ADDRESS(ES)**

Purdue University
West Lafayette, Indiana 47907

**8. PERFORMING ORGANIZATION REPORT NUMBER**

E–12110

**9. SPONSORING/MONITORING AGENCY NAME(S) AND ADDRESS(ES)**

National Aeronautics and Space Administration
John H. Glenn Research Center at Lewis Field
Cleveland, Ohio 44135–3191

**10. SPONSORING/MONITORING AGENCY REPORT NUMBER**

NASA CR—2000-209804

**11. SUPPLEMENTARY NOTES**

**12a. DISTRIBUTION/AVAILABILITY STATEMENT**

Unclassified - Unlimited
Subject Categories: 09, 23, 34, and 35          Distribution: Nonstandard

This publication is available from the NASA Center for AeroSpace Information, (301) 621–0390.

**12b. DISTRIBUTION CODE**

**13. ABSTRACT (Maximum 200 words)**

Laser-induced fluorescence (LIF) measurements of NO concentration in a variety of $CH_4/O_2/N_2$ flames are used to evaluate the chemical kinetics of NO formation. The analysis begins with previous measurements in flat, laminar, premixed $CH_4/O_2/N_2$ flames stabilized on a water-cooled McKenna burner at pressures ranging from 1 to 14.6 atm, equivalence ratios from 0.5 to 1.6, and volumetric nitrogen/oxygen dilution ratios of 2.2, 3.1 and 3.76. These measured results are compared to predictions to determine the capabilities and limitations of the comprehensive kinetic mechanism developed by the Gas Research Institute (GRI), version 2.11. The model is shown to predict well the qualitative trends of NO formation in lean-premixed flames, while quantitatively underpredicting NO concentration by 30-50%. For rich flames, the model is unable to even qualitatively match the experimental results. These flames were found to be limited by low temperatures and an inability to separate the flame from the burner surface. In response to these limitations, a counterflow burner was designed for use in opposed premixed flame studies. A new LIF calibration technique was developed and applied to obtain quantitative measurements of NO concentration in laminar, counterflow premixed, $CH_4/O_2/N_2$ flames at pressures ranging from 1 to 5.1 atm, equivalence ratios of 0.6 to 1.5, and an $N_2/O_2$ dilution ratio of 3.76. The counterflow premixed flame measurements are combined with measurements in burner-stabilized premixed flames and counterflow diffusion flames to build a comprehensive database for analysis of the GRI kinetic mechanism. Pathways, quantitative reaction path and sensitivity analyses are applied to the GRI mechanism for these flame conditions. The prompt NO mechanism is found to severely underpredict the amount of NO formed in rich premixed and nitrogen-diluted diffusion flames. This underprediction is traced to uncertainties in the CH kinetics as well as in the nitrogen oxidation chemistry. Suggestions are made which significantly improve the predictive capability of the GRI mechanism in near-stoichiometric, rich, premixed flames and in atmospheric-pressure, diffusion flames. However, the modified reaction mechanism is unable to model the formation of NO in ultra-rich, premixed or in high-pressure, nonpremixed flames, thus indicating the need for additional study under these conditions.

| 14. SUBJECT TERMS | | 15. NUMBER OF PAGES |
|---|---|---|
| Premixed combustion; Optical measurements; Laser-induced fluorescence | | 285 |
| | | **16. PRICE CODE** A13 |

| 17. SECURITY CLASSIFICATION OF REPORT | 18. SECURITY CLASSIFICATION OF THIS PAGE | 19. SECURITY CLASSIFICATION OF ABSTRACT | 20. LIMITATION OF ABSTRACT |
|---|---|---|---|
| Unclassified | Unclassified | Unclassified | |